Modular Design and Synthetic Tuning of Ternary Molecular Nanoclusters

Sebastian Krajewski

A dissertation

submitted in partial fulfillment of the

requirements for the degree of

Doctor of Philosophy

University of Washington

2025

Reading Committee:

Alexandra Velian, Chair

Brandi Cossairt

Forrest Michael

Program Authorized to Offer Degree:

Chemistry

University of Washington

Abstract

Modular Design and Synthetic Tuning of Ternary Molecular Nanoclusters

Sebastian Krajewski

Chair of the Supervisory Committee:
Alexandra Velian
Department of Chemistry

The understanding of the nature of the metal/support interaction in catalytic systems is central to designing better and more sustainable catalysts. The characterization of heterogeneous interfaces most relevant to catalysis is challenging and relies on techniques that provide limited atom-level information on processes at the surface. To better understand this complex chemistry, atomically precise nanoclusters can be used as a molecular analogue to study such surface chemistry with high precision. Here the chemistry of $Co_6Se_8L_6$ (L = Ph_2PR, Ph = phenyl) is studied as a means of reaching this goal by facilitating the formation of ternary nanoclusters with metal edge sites which sit upon the cluster core and are akin to single-atom catalysts on a surface. In the first chapter, the synthesis of a series of Cu/Co/Se molecular clusters is described, and their properties probed extensively through a bevy of techniques. Four highly isostructural clusters varying in overall charge from –3 to 0 are synthesized and found to exhibit robust charge separation between the copper edge sites and Co/Se core. The electronic interactions and redistribution of charge between the copper(I) edge sites and the electronically flexible core glean insights into the nature of the dopant/support interaction.

In Chapter 2, synthetic explorations are undertaken to expand the scope of the supporting phosphine ligands on the cluster, elucidating the approaches and challenges associated with developing new ligand platforms of this type. By varying the identity of the R-group on the phosphine Ph_2PR used in cluster syntheses, a library of homoleptic clusters $Co_6Se_8L_6$ ($L = Ph_2PR$) with various heteroatom functionalities is created. It is found that many functional groups will tolerate the conditions of cluster formation, allowing for the facile synthesis of several clusters with contrasting functionalities. The utility of these clusters is limited by their solubility profiles and challenges with metalation, but they serve as a promising example of synthetic versatility of Co_6Se_8 nanoclusters and hybrid phosphine ligands while providing important lessons for the future design of ternary nanocluster systems.

TABLE OF CONTENTS

List of Figures v

List of Schemes xi

List of Tables xi

Chapter 1. Exploring Charge Redistribution At the Cu/Co_6Se_8 Interface 1

1.1 Abstract 1

1.2 Introduction 1

1.3 Results and discussion 3

1.3.1 A Cu/[Co_6Se_8] Redox Series 5

1.3.2 Isostructurality and helical chirality across the redox series 8

1.3.3 Solution Magnetism and Paramagnetic ^{31}P NMR Studies to Elucidate Spin State Changes In Redox Series 9

1.3.4 X-ray Absorption Spectroscopy Probes Electronic Changes at Se 11

1.3.5 Insights into Electronic Structure via DFT Calculations 12

1.4 Conclusion 13

1.5 Synthetic Details and Characterization of products 13

1.5.1 General Experimental Considerations 13

1.5.2 Computational Methods 15

1.5.3 Synthesis of [Li(thf)$_4$][1-Cu_3] 16

1.5.4 Synthesis of [Li(thf)$_4$][Cp_2Co][1-Cu_3] 23

1.5.5 Synthesis of [Li(CH_3CN)$_4$][Cp^*_2Co]$_2$[1-Cu_3] 25

1.5.6 Synthesis of 1-Cu_3 27
1.5.7 Synthesis of $[Li(thf)_4]_2[1\text{-}Cu_3]$ 29
1.5.8 Synthesis of [TBA][1-Cu_3] 29
1.5.9 Synthesis of $[Ru(bpy)_3][1\text{-}Cu_3]$ 32
1.5.10 Oxidation of [TBA][1-Cu_3] 35
1.5.11 Ligand coordination studies with [TBA][1-Cu_3] 35
1.6 Electronic Paramagnetic Resonance Spectroscopy 35
1.7 Paramagnetic ^{31}P NMR Studies 36
1.8 Selenium X-ray Absorption Studies 44
1.9 X-ray Diffraction Studies 49
1.9.1 $[Li(thf)_4][1\text{-}Cu_3]$ 50
1.9.2 $[Li(thf)_4][Cp^*_2Co]_2[1\text{-}Cu_3]$ 50
1.9.3 1-Cu_3 50
1.9.4 $[Ru(bpy)_3][1\text{-}Cu_3]$ 51
1.10 DFT Calculations 57
1.10.1 Example inputs 57
1.10.2 Selected calculation results 58
1.11 References 59

Chapter 2. Probing the synthetic limits of the $Co_6Se_8L_6$ system with Bifunctional Phosphine ligands 68

2.1 Abstract 68
2.2 Introduction 68
2.3 Results and Discussion 69

2.3.1 Motivation and selection of phosphines 69
2.3.2 Synthetic Approaches to $Co_6Se_8L_6$ Formation 70
2.3.3 General Properties of the Nanoclusters 70
2.3.4 Structural Parameter Comparison 72
2.3.5 Challenges with cluster deprotonation and transmetallation 73
2.4 Conclusion 74
2.5 Synthetic Details and Characterization of Products 74
2.5.1 General Information 74
2.5.2 Synthesis of Ph_2PCH_2NHTol 76
2.5.3 Synthesis of Ph_2PSeCH_2OH 78
2.5.4 Synthesis of $Ph_2PSeCH_2CH_2OH$ 79
2.5.5 Synthesis of Ph_2PSTol 81
2.5.6 Synthesis of $Ph_2P(Se)STol$ 83
2.5.7 Synthesis of $Co_6Se_8(Ph_2PCH_2NHTol)_6$ 84
2.5.8 Synthesis of $Co_6Se_8(Ph_2PCH_2OH)_6$ 86
2.5.9 Synthesis of $Co_6Se_8(Ph_2PCH_2OSiMe_3)_6$ 88
2.5.10 Synthesis of $[Co_6Se_8(Ph_2PCH_2OSiMe_3)_6][PF_6]$ 89
2.5.11 Synthesis of $Co_6Se_8(Ph_2PCH_2OCH_3)_6$ 91
2.5.12 Synthesis of $Co_6Se_8(Ph_2PCH_2CH_2OH)_6$ 92
2.5.13 Synthesis of $[Co_6Se_8(Ph_2PCH_2CH_2OH)_6][PF_6]$ 94
2.5.14 Synthesis of $Co_6Se_8(Ph_2PCH_2CH_2O(SiMe_3))_6$ 96
2.5.15 Synthesis of $Co_6Se_8(Ph_2PH)_6$ 98
2.5.16 Synthesis of $[Co_6Se_8(Ph_2PH)_6][PF_6]$ 100

2.5.17 Synthesis of $Co_6Se_8(Ph_2PSTol)_6$ 100

2.5.18 Synthesis of $Co_6Se_8(Ph_2PCH_2(C_4H_7O))_6$ 102

2.6 X-ray Diffraction Studies 104

2.6.1 $Co_6Se_8(Ph_2PCH_2NHTol)_6$ 105

2.6.2 $Co_6Se_8(Ph_2PCH_2OH)_6$ 106

2.6.3 $Co_6Se_8(Ph_2PCH_2OCH_3)_6$ 107

2.6.4 $[Co_6Se_8(Ph_2PCH_2OSi(CH_3)_3)_6][PF_6]$ 108

2.6.5 $[Co_6Se_8(Ph_2PCH_2OSi(CH_3)_3)_6][FeCl_4]_2$ 109

2.6.6 $Co_6Se_8(Ph_2PCH_2CH_2OH)_6$ 110

2.6.7 $Co_6Se_8(Ph_2PCH_2CH_2OSi(CH_3)_3)_6$ 111

2.6.8 $Co_6Se_8(Ph_2PH)_6$ 112

2.6.9 $[Co_6Se_8(Ph_2PH)_6][PF_6]$ 113

2.6.10 $Co_6Se_8(Ph_2PSTol)_6$ 114

2.6.11 $Co_6Se_8(Ph_2PCH_2C_4H_7O)_6$ 115

2.7 References 120

LIST OF FIGURES

Figure 1. The ternary nanoclusters **1**-M_3 feature three edge sites (M^{2+}) anchored on a diamagnetic cluster core $[Co_6Se_8]^0$. Spontaneous edge/core electron transfer occurs when Cu^{2+} edge sites are installed. 3

Figure 2. Comparison of the single crystal solid-state structures of (a) **1**-Cu_3, (b) $[Li(thf)_4][$**1**-$Cu_3]$, (c) $[Ru(bpy)_3][$**1**-$Cu_3]$, and (d) $[CoCp^*_2]_2[Li(thf)_4][$**1**-$Cu_3]$, with carbon atoms and cations truncated for clarity. Thermal ellipsoids are drawn at the 50% probability level. 4

Figure 3. a) Cyclic voltammograms of **1**-H_6 and $[Li(thf)_4][$**1**-$Cu_3]$ (0.1 M $TBAPF_6$ in THF, at scan rates of 200 and 25 mV/s, respectively, currents are normalized). b) UV-vis absorption spectra of [**1**-$Li_6(thf)_6$], **1**-Cu_3, $[Li(thf)_4][$**1**-$Cu_3]$, $[Li(thf)_4]_2[$**1**-$Cu_3]$, $[CoCp^*_2]_2[Li(thf)_4][$**1**-$Cu_3]$ acquired in THF. 5

Figure 4. Comparison of bonding parameters obtained via crystallography as a function of cluster core oxidation state. Error bars represent the standard error of each data point. 8

Figure 5. a) Curie behavior of $[$**1**-$Cu_3]^n$ (n = 0, –1, –2) reflected in the linear dependence of the ^{31}P NMR shifts with the inverse of temperature (290 – 330 K). b) Se XANES spectra of **1**-Cu_3, $[CoCp^*_2]_2[Li(THF)_4][$**1**-$Cu_3]$, **1**-H_6 and Se foil. The signal for the Se foil is scaled to enable comparison to the clusters. 11

Figure 6. (a) Molecular orbital diagrams for $[$**1**-$Cu_3]^n$ (n = 0, –1, –2, –3) calculated at B3LYP+/ccPVTZ level of theory. Alpha (*a*) and beta (*b*) orbitals for the open-shell clusters are colored red and blue, respectively, and (b) corresponding partial density of states plots. To facilitate comparisons, each top occupied orbital is normalized to a value of 0 eV. 12

Figure 7. ^1H NMR (CD_3CN, 25 °C, 500 MHz) spectrum of $[Li(thf)_4][$**1**-$Cu_3]$ 17

Figure 8. $^{31}P\{^1H\}$ NMR (CD_3CN, 25 °C, 283 MHz) spectrum of $[Li(thf)_4][$**1**-$Cu_3]$ 17

Figure 9. ^7Li NMR (CD_3CN, 25 °C, 194 MHz) spectrum of $[Li(thf)_4][$**1**-$Cu_3]$ 18

Figure 10. $^{31}P\{^1H\}$ NMR (C_6D_6, 25 °C, 202 MHz) spectrum of $[Li(thf)_4][$**1**-$Cu_3]$ 19

Figure 11. ^7Li NMR (C_6D_6, 25 °C, 194 MHz) spectrum of $[Li(thf)_4][$**1**-$Cu_3]$ 19

Figure 12. $^{13}C\{^{1}H\}$ NMR (acetonitrile-d_3, 25 °C, 126 MHz) spectrum of $[Li(thf)_4][\mathbf{1}\text{-}Cu_3]$20
Figure 13. Cyclic voltammogram of $[Li(thf)_4][\mathbf{1}\text{-}Cu_3]$ (Tetrahydrofuran, 0.1 M $TBAPF_6$, 25 mV/s)..... 20
Figure 14. Scan rate dependence in the cyclic voltammetry of $[Li(thf)_4][\mathbf{1}\text{-}Cu_3]$ (Tetrahydrofuran, 0.1 M $TBAPF_6$)..... 21
Figure 15. FT-IR spectrum of $[Li(thf)_4][\mathbf{1}\text{-}Cu_3]$ 22
Figure 16. Mass spectrum obtained via ESI-MS of direct injection of a solution of $[Li(thf)_4][\mathbf{1}\text{-}Cu_3]$ in acetonitrile, showing fragmentation to $[Co_6Se_8(Ph_2PNHTol)_6]^{n+}$ 22
Figure 17. ^{1}H NMR (CD_3CN, 25 °C, 500 MHz) spectrum of $[Li(thf)_4][Cp_2Co][\mathbf{1}\text{-}Cu_3]$. 24
Figure 18. $^{31}P\{^{1}H\}$NMR (CD_3CN, 25 °C, 202 MHz) spectrum of $[Li(thf)_4][Cp_2Co][\mathbf{1}\text{-}Cu_3]$ 25
Figure 19. ^{1}H NMR (CD_3CN, 25 °C, 500 MHz) spectrum of $[Li(CH_3CN)_4][Cp^*_2Co]_2[\mathbf{1}\text{-}Cu_3]$ 26
Figure 20. $^{31}P\{^{1}H\}$NMR (CD_3CN, 25 °C, 202 MHz) spectrum of $[Li(CH_3CN)_4][Cp^*_2Co]_2[\mathbf{1}\text{-}Cu_3]$ 26
Figure 21. ^{1}H NMR (CD_2Cl_2, 25 °C, 500 MHz) spectrum of $\mathbf{1}\text{-}Cu_3$ 28
Figure 22. $^{31}P\{^{1}H\}$NMR (CD_2Cl_2, 25 °C, 283 MHz) spectrum of $\mathbf{1}\text{-}Cu_3$..... 28
Figure 23. $^{13}C\{^{1}H\}$NMR (CD_2Cl_2, 25 °C, 126 MHz) spectrum of $\mathbf{1}\text{-}Cu_3$ 29
Figure 24. ^{1}H NMR (CD_2Cl_2, 25 °C, 500 MHz) spectrum of $[TBA][\mathbf{1}\text{-}Cu_3]$..... 31
Figure 25. $^{31}P\{^{1}H\}$NMR (CD_2Cl_2, 25 °C, 283 MHz) spectrum of $[TBA][\mathbf{1}\text{-}Cu_3]$ 31
Figure 26. $^{13}C\{^{1}H\}$NMR (CD_2Cl_2, 25 °C, 126 MHz) spectrum of $[TBA][\mathbf{1}\text{-}Cu_3]$..... 32
Figure 27. ^{1}H NMR (DMSO-d_6, 25 °C, 500 MHz) spectrum of $[Ru(bpy)_3][\mathbf{1}\text{-}Cu_3]$..... 33
Figure 28. $^{31}P\{^{1}H\}$NMR (DMSO-d_6, 25 °C, 202 MHz) spectrum of $[Ru(bpy)_3][\mathbf{1}\text{-}Cu_3]$ 33
Figure 29. $^{13}C\{^{1}H\}$NMR (DMSO-d_6, 25 °C, 126 MHz) spectrum of $[Ru(bpy)_3][\mathbf{1}\text{-}Cu_3]$ 34
Figure 30. UV-Vis spectrum of $[Ru(bpy)_3][\mathbf{1}\text{-}Cu_3]$ in dimethylformamide 34
Figure 31. EPR spectra of $\mathbf{1}\text{-}Cu_3$ and $[TBA][\mathbf{1}\text{-}Cu_3]$ in toluene at 100 K..... 36
Figure 32. Results of inversion recovery experiments performed to determine the ^{31}P T_1 relaxation time of $\mathbf{1}\text{-}H_6$ (chloroform-d, 25 °C, 283 MHz). 37
Figure 33. Results of inversion recovery experiments performed to determine the ^{31}P T_1 relaxation time of $[Li(thf)_4]_2[\mathbf{1}\text{-}Cu_3]$ (acetonitrile-d_3, 25 °C, 283 MHz) 38

Figure 34. Results of inversion recovery experiments performed to determine the ^{31}P T_1 relaxation time of [TBA][**1**-Cu_3] (acetonitrile-d_3, 25 °C, 283 MHz)..... 39
Figure 35. Results of inversion recovery experiments performed to determine the ^{31}P T_1 relaxation time of **1**-Cu_3 (dichloromethane-d_2, 25 °C, 283 MHz) 40
Figure 36. Variable-temperature ^{31}P NMR (Toluene, 202 MHz) spectra of **1**-Cu_3..... 41
Figure 37. Variable-temperature ^{31}P NMR (acetonitrile-d_3, 202 MHz) spectra of [TBA][**1**-Cu_3] 41
Figure 38. Variable-temperature ^{31}P NMR (THF, 202 MHz) spectra of [TBA][**1**-Cu_3] .. 42
Figure 39. Plot of chemical shifts from ^{31}P VT-NMR (202 MHz, 190-340K) of [TBA][**1**-Cu_3]. 43
Figure 40. Variable-temperature ^{31}P NMR (acetonitrile-d_3, 202 MHz) spectra of $[Li(thf)_4]_2$[**1**-Cu_3] 44
Figure 41. Overlaid selenium X-ray absorption spectra of selected cluster compounds.. 46
Figure 42. Difference plot of selenium X-ray absorption spectra of selected cluster compounds 47
Figure 43. Fitted selenium X-ray absorption spectrum of **1**-H_6..... 48
Figure 44. Fitted selenium X-ray absorption spectrum of **1**-Cu_3..... 48
Figure 45. Fitted selenium X-ray absorption spectrum of [**1**-Cu_3]$^{3-}$ 49
Figure 46. Solid-state structure of $[Li(thf)_4]$[**1**-Cu_3] with thermal ellipsoids shown at a 50% probability level. All hydrogen atoms and isolated co-crystallized solvent molecules omitted for clarity..... 51
Figure 47. Solid-state structure of **1**-Cu_3 with thermal ellipsoids shown at a 50% probability level. All hydrogen atoms and co-crystallized solvent molecules omitted for clarity.52
Figure 48. Solid-state structure of $[Li(thf)_4][Cp_2*Co]_2$[**1**-Cu_3] with thermal ellipsoids shown at a 30% probability level. All hydrogen atoms and co-crystallized solvent molecules are omitted for clarity. Due to extensive disorder, the $[Li(thf)_4]^+$ ion could not be located definitively. 53
Figure 49. Solid -state structure of $[Ru(bpy)_3]$[**1**-Cu_3] with thermal ellipsoids shown at a 50% probability level. All hydrogen atoms and co-crystallized solvent molecules are omitted for clarity 54

Figure 50. The LUMO of [**1**-Cu_3]$^-$ calculated at the DFT uB3LYP+/cc-PVTZ level of theory with hydrogen atoms omitted for clarity. Surface plotted at an isovalue of 0.05. 58
Figure 51. The pseudo-degenerate HOMO/HOMO-1 orbitals of [**1**-Cu_3]$^-$ calculated at the DFT uB3LYP+/cc-PVTZ level of theory with hydrogen atoms omitted for clarity. The orbitals on the left and right belong to the alpha and beta spin manifolds, respectively. Surfaces plotted at an isovalue of 0.05. 59
Figure 52. ^{1}H NMR (C_6D_6, 25 °C, 500 MHz) spectrum of Ph_2PCH_2NHTol..... 77
Figure 53. ^{31}P NMR (C_6D_6, 25 °C, 202 MHz) spectrum of Ph_2PCH_2NHTol 77
Figure 54. ^{31}P NMR ($CDCl_3$, 25 °C, 202 MHz) spectrum of Ph_2PSeCH_2OH 78
Figure 55. ^{1}H NMR (C_6D_6, 25 °C, 300 MHz) spectrum of $Ph_2PSeCH_2CH_2OH$ 80
Figure 56. ^{31}P NMR (C_6D_6, 25 °C, 101 MHz) spectrum of $Ph_2PSeCH_2CH_2OH$..... 80
Figure 57. ^{1}H NMR ($CDCl_3$, 25 °C, 500 MHz) spectrum of Ph_2PSTol 82
Figure 58. ^{31}P NMR ($CDCl_3$, 25 °C, 202 MHz) spectrum of Ph_2PSTol 82
Figure 59. ^{1}H NMR ($CDCl_3$, 25 °C, 500 MHz) spectrum of $Ph_2P(Se)STol$ 83
Figure 60. ^{31}P NMR ($CDCl_3$, 25 °C, 202 MHz) spectrum of $Ph_2P(Se)STol$ 84
Figure 61. ^{1}H NMR (C_6D_6, 25 °C, 300 MHz) spectrum of $Co_6Se_8(Ph_2PCH_2NHTol)_6$ 85
Figure 62. ^{31}P NMR (C_6D_6, 25 °C, 121 MHz) spectrum of $Co_6Se_8(Ph_2PCH_2NHTol)_6$ ... 86
Figure 63. ^{1}H NMR (DMSO-d_6, 25 °C, 500 MHz) spectrum of $Co_6Se_8(Ph_2PCH_2OH)_6$.. 87
Figure 64. ^{31}P NMR (DMSO-d_6, 25 °C, 121 MHz) spectrum of $Co_6Se_8(Ph_2PCH_2OH)_6$. 87
Figure 65. ^{1}H NMR (benzene-d_6, 25 °C, 300 MHz) spectrum of $Co_6Se_8(Ph_2PCH_2OSiMe_3)_6$ 88
Figure 66. ^{31}P NMR (benzene-d_6, 25 °C, 121 MHz) spectrum of $Co_6Se_8(Ph_2PCH_2OSiMe_3)_6$ 89
Figure 67. ^{1}H NMR ($CDCl_3$, 25 °C, 300 MHz) spectrum of $[Co_6Se_8(Ph_2PCH_2OSiMe_3)_6][PF_6]$ 90
Figure 68. ^{31}P NMR ($CDCl_3$, 25 °C, 121 MHz) spectrum of $[Co_6Se_8(Ph_2PCH_2OSiMe_3)_6][PF_6]$ 90
Figure 69. ^{1}H NMR (CD_2Cl_2, 25 °C, 500 MHz) spectrum of $Co_6Se_8(Ph_2PCH_2OCH_3)_6$ .. 91
Figure 70. ^{31}P NMR ($CDCl_3$, 25 °C, 202 MHz) spectrum of $Co_6Se_8(Ph_2PCH_2OCH_3)_6$... 92
Figure 71. ^{1}H NMR (DMSO-d_6, 25 °C, 300 MHz) spectrum of $Co_6Se_8(Ph_2PCH_2CH_2OH)_6$93

Figure 72. ^{31}P NMR (DMSO-d_6, 25 °C, 121 MHz) spectrum of $Co_6Se_8(Ph_2PCH_2CH_2OH)_6$ 94
Figure 73. ^{1}H NMR (CD_3CN, 25 °C, 300 MHz) spectrum of $[Co_6Se_8(Ph_2PCH_2CH_2OH)_6][PF_6]$ 95
Figure 74. ^{31}P NMR (CD_3CN, 25 °C, 121 MHz) spectrum of $[Co_6Se_8(Ph_2PCH_2CH_2OH)_6][PF_6]$ 96
Figure 75. ^{1}H NMR ($CDCl_3$, 25 °C, 300 MHz) spectrum of $Co_6Se_8(Ph_2PCH_2CH_2O(SiMe_3))_6$ 97
Figure 76. ^{31}P NMR ($CDCl_3$, 25 °C, 121 MHz) spectrum of $Co_6Se_8(Ph_2PCH_2CH_2O(SiMe_3))_6$ 97
Figure 77. ^{1}H NMR ($CDCl_3$, 25 °C, 500 MHz) spectrum of $Co_6Se_8(Ph_2PH)_6$ 99
Figure 78. ^{31}P NMR ($CDCl_3$, 25 °C, 202 MHz) spectrum of $Co_6Se_8(Ph_2PH)_6$..... 99
Figure 79. ^{31}P NMR (Tetrahydrofuran, 25 °C, 500 MHz) spectrum of $[Co_6Se_8(Ph_2PH)_6][PF_6]$ 100
Figure 80. ^{1}H NMR (CD_2Cl_2, 25 °C, 500 MHz) spectrum of $Co_6Se_8(Ph_2PSTol)_6$ 101
Figure 81. ^{31}P NMR (CD_2Cl_2, 25 °C, 202 MHz) spectrum of $Co_6Se_8(Ph_2PSTol)_6$ 102
Figure 82. ^{1}H NMR (CD_2Cl_2, 25 °C, 500 MHz) spectrum of $Co_6Se_8(Ph_2PCH_2(C_4H_7O))_6$103
Figure 83. ^{31}P NMR (CD_2Cl_2, 25 °C, 202 MHz) spectrum of $Co_6Se_8(Ph_2PCH_2(C_4H_7O))_6$104
Figure 84. Solid-state structure of $Co_6Se_8(Ph_2PCH_2NHTol)_6$ with thermal ellipsoids shown at a 50% probability level. All hydrogen atoms and co-crystallized solvent molecules omitted for clarity. 105
Figure 85. Solid-state structure of $Co_6Se_8(Ph_2PCH_2OH)_6$ with thermal ellipsoids shown at a 50% probability level. All hydrogen atoms and co-crystallized solvent molecules omitted for clarity. 106
Figure 86. Solid-state structure of $Co_6Se_8(Ph_2PCH_2OCH_3)_6$ with thermal ellipsoids shown at a 50% probability level. All hydrogen atoms and co-crystallized solvent molecules omitted for clarity. 107
Figure 87. Solid-state structure of $Co_6Se_8(Ph_2PCH_2OSi(CH_3)_3)_6$ with thermal ellipsoids shown at a 50% probability level. All hydrogen atoms and co-crystallized solvent molecules omitted for clarity. 108

Figure 88. Solid-state structure of $Co_6Se_8(Ph_2PCH_2OSi(CH_3)_3)_6$ with thermal ellipsoids shown at a 50% probability level. All hydrogen atoms and co-crystallized solvent molecules omitted for clarity. 109
Figure 89. Solid-state structure of $Co_6Se_8(Ph_2PCH_2CH_2OH)_6$ with thermal ellipsoids shown at a 50% probability level. All hydrogen atoms and co-crystallized solvent molecules omitted for clarity. 110
Figure 90. Solid-state structure of $Co_6Se_8(Ph2PCH_2CH2OSi(CH_3)_3)_6$ with thermal ellipsoids shown at a 50% probability level. All hydrogen atoms and co-crystallized solvent molecules omitted for clarity. 111
Figure 91. Solid-state structure of $Co_6Se_8(Ph_2PH)_6$ with thermal ellipsoids shown at a 50% probability level. All hydrogen atoms and co-crystallized solvent molecules omitted for clarity, except for P-H hydrogen atoms (drawn as 2D spheres). 112
Figure 92. Solid-state structure of $[Co_6Se_8(Ph_2PH)_6][PF_6]$ with thermal ellipsoids shown at a 50% probability level. All hydrogen atoms and co-crystallized solvent molecules omitted for clarity, except for P-H hydrogen atoms (drawn as 2D spheres)..... 113
Figure 93. Solid-state structure of $Co_6Se_8(Ph_2PSTol)_6$ with thermal ellipsoids shown at a 50% probability level. All hydrogen atoms and co-crystallized solvent molecules omitted for clarity. 114
Figure 94. Solid-state structure of $Co_6Se_8(Ph_2PCH_2C_4H_7O)_6$ with thermal ellipsoids shown at a 30% probability level. All hydrogen atoms and co-crystallized solvent molecules omitted for clarity. Only a single enantiomer of the disordered phosphine is shown. 115

LIST OF SCHEMES

Scheme 1. Synthesis of $[Li(thf)_4][\mathbf{1}\text{-}Cu_3]$ and $[Li(thf)_4]_2[\mathbf{1}\text{-}Cu_3]$. 4

Scheme 2. a) Synthesis of the redox series $[\mathbf{1}\text{-}Cu_3]^n$, n = 0, −2, −3 via chemical oxidation and reduction of $[\mathbf{1}\text{-}Cu_3]^-$, and b) the proposed oxidation state of the Co/Se cluster. 6

Scheme 3. Generalized Synthesis of $Co_6Se_8(Ph_2R)_6$ clusters. 70

LIST OF TABLES

Table 1. Parameters from the linear fit of ^{31}P VT-NMR of $[\mathbf{1}\text{-}Cu_3]^{n-}$ 37

Table 2. Calculated parameters from fitted Se XAS data 49

Table 3. Crystallographic information for $[Li(thf)_4][\mathbf{1}\text{-}Cu_3]$, $[Li(thf)_4][Cp^*_2Co]_2[\mathbf{1}\text{-}Cu_3]$, and **1**-$Cu_3$ 55

Table 4. Crystallographic information for $[Ru(bpy)_3][\mathbf{1}\text{-}Cu_3]$ 56

Table 5. DFT optimized interatomic distances and angles for $[\mathbf{1}\text{-}Cu_3]^n$ (n = 0,–1,–2,–3) 58

Table 6. Structural parameters for homoleptic clusters with general formula $Co_6Se_8L_6$. Some clusters were crystallized in oxidized form and are marked accordingly. 72

Table 7. Crystallographic information for $Co_6Se_8(Ph_2PCH_2NHTol)_6$, $Co_6Se_8(Ph_2PCH_2OH)_6$, and $Co_6Se_8(Ph_2PCH_2CH_2OH)_6$ 116

Table 8. Crystallographic information for $Co_6Se_8(Ph_2PCH_2OCH_3)_6$, $[Co_6Se_8(Ph_2PCH_2OSi(CH_3)_3)_6][PF_6]$, and $[Co_6Se_8(Ph_2PCH_2OSi(CH_3)_3)_6][PF_6]$ ... 117

Table 9. Crystallographic information for $Co_6Se_8(Ph_2PCH_2CH_2OSi(CH_3)_3)_6$, $Co_6Se_8(Ph_2PCH_2C_4H_7O)_6$, $Co_6Se_8(Ph_2PSTol)_6$ 118

Table 10. Crystallographic information for $Co_6Se_8(Ph_2PH)_6$ and $[Co_6Se_8(Ph_2PH)_6][PF_6]$ 119

ACKNOWLEDGEMENTS

I must first thank the graduate students whose friendliness and expertise convinced me to join the Velian lab in the first place: Jon Kephart, Ben Mitchell, and Kendahl Walz were all amazing to work with in lab, and I could not have survived those initial COVID years without their kindness and guidance. Many years from now, I'll still appreciate Jon for helping me adopt my cat in my first year.

Alongside me all these years, Daniel Zhou and Rob Love have been my main men on the cluster project through the many highs and lows of graduate school. Whether it was messing around in lab or agonizing over some synthetic problem, I was glad you two were with me. On the other side of lab, I had Andrei Draguicevic, who is always good company despite his acrid takes on sports, and Mike Riehs, who is a materials wizard. I also must thank Emily Miura-Stempel, who is basically an honorary Velian group member.

Of course, Alexandra herself has been a primary catalyst for my growth and development as a chemist and communicator. Her mentorship and keen eye never failed to help me move forward as a scientist, and I can't wait to see what future chemistry emerges from the Velian lab with her guidance. The next generation of students - Ella Spurlock, Lauren Peck, Hailey Akins, and Natacha Oget - has the future of the lab in good hands.

I've thoroughly enjoyed working with Werner Kaminsky over the years, and his wisdom as a crystallographer cannot be overstated. I also give thanks to Dylan Rogers and Paige Gannon, who served as the crystallography assistants prior to my tenure. I will really miss the X-ray lab once I'm gone, plants and all.

My committee, which has included Prof. Cossairt, Prof. Michael, Prof. Xiao, Prof. Holmberg, and Prof. Seidler, deserve many thanks for their insightful questions and comments.

I never would have been able to pursue my passion for crystallography and synthesis without my undergraduate advisor Michael Marshak, whose enthusiasm and knowledge of inorganic chemistry were infectious. Likewise, Emily Hopkins and Aaron Crossman were two of the most helpful graduate student mentors I had at my time in Boulder and the Marshak Lab.

The Seattle Chapter of the ARCS foundation and the Clean Energy Institute of UW both provided crucial financial support to me during my time here.

I feel obligated to acknowledge the city itself, with Seattle truly becoming one of my favorite places to be, rain or shine. There's so much to love about this beautiful and dynamic region, where the mountains and evergreen forests meet the sea.

I owe so much to Mom and Dad, who have always supported me on my scientific journey from Arlington to Boulder to Seattle. I'm lucky to have such a thoughtful family, and I hope one day I can repay you for everything.

To Mom

Chapter 1. Exploring Charge Redistribution At the Cu/Co_6Se_8 Interface

1.1 Abstract

[1]This study investigates the electronic interactions and charge redistribution at the dopant/support interface using a Cu/Co_6Se_8 cluster construct. Specifically, the redox cluster series $[Cu_3Co_6Se_8L_6]^n$ ([**1**-Cu_3]^n; n = 0, –1, –2, –3; L = Ph_2PNTol^-, Ph = phenyl, Tol = *p*-tolyl) spanning four distinct oxidation states is synthesized and characterized using a multitude of techniques, including multinuclear NMR, UV-Vis, XANES, and X-ray crystallography. Structural investigations indicate that the clusters are isostructural and chiral, adopting a pseudo-D_3 symmetry. Paramagnetic ^{31}P NMR spectroscopy and solution phase magnetic measurements together with DFT calculations are employed to interrogate the electronic structure and spin state changes across the [**1**-Cu_3]$^{3-}$ to **1**-Cu_3 redox series, revealing that the copper edge sites retain a +1 oxidation state while the Co/Se core becomes increasingly oxidized, yielding a highly zwitterionic cluster.

1.2 Introduction

Redox-active dopants can dramatically impact the catalytic activity of transition metal chalcogenide materials, but a detailed, atomic-level understanding of how the structural and electronic interactions at the dopant/host interface modulates reactivity remains elusive.[1–3] For example, introducing Cu(II) centers in MoS_2 materials stunts hydrodesulfurization and has little impact on hydrogen evolution, whereas Co(II) or Ni(II) improve both.[2,3] This promoter/inhibitor effect of the dopants (M) is still not completely understood, and has been correlated with the ability of the dopants to reduce or oxidize the molybdenum, the strength of the M—S bonds, and to the impact of dopants on the morphology of the catalyst, the reactivity of sulfur active sites, and the substrate chemisorption energies.[2–5]

---

[1]Reproduced with permission from:

Krajewski, S. M. et al., *Inorg. Chem.* **2024**, 63, 43, 20388–20397. Copyright 2024 American Chemical Society.

In contrast to the structurally complex M-Mo-S materials, transition metal chalcogenide molecular clusters can be prepared with precise and uniform structures and compositions, offering the potential to investigate specific motifs found within heterogeneous catalysts.[6–17]

Our group introduced a family of transition metal chalcogenide clusters that bear resemblance to edge-decorated active sites of M-Mo-S catalysts[18] and ternary M/Mo_6S_8 Chevrel phases,[19] and contain well-defined active sites.[3] Specifically, nanoclusters $M_3Co_6Se_8L_6$ (**1**-M_3; M = Cr, Fe, Co, Zn, Me_2Sn; L = Ph_2PNTol^-) and $MCo_6Se_8(PEt_3)_4L_2$ (**2**-M, M = Cr—Co, Cu, Zn) contain low-coordinate edge site "dopants" (M) which can double as active sites, anchored on a redox-active, diamagnetic [Co_6Se_8] superatomic cluster "support" (Figure 1).[8,20–25] These structurally modular, catalytically active clusters enabled us to pursue systematic structure/function studies to map the role of metal/support interactions and inter-active site (allosteric) interactions in catalysis. Mapping charge redistribution across multiple metals, particularly in response to chemical events, remains a topic of intense investigations in the molecular cluster community.[26–30] The M/Co_6Se_8 interface in our clusters is unique as it enables probing charge redistribution between a metal dopant and a superatomic support unit, and its impact in catalysis. Prior investigations have revealed the presence of distinct regimes of metal/support cooperativity.[10,23,31] For instance, in a redox independent regime, holes are localized exclusively on the edge site during an oxidative reaction. This is the case in $CrCo_6Se_8(PEt_3)_4L_2$ (**2**-Cr) where the Cr(II) is significantly more reducing than the Co/Se cluster.[10] In contrast, in a redox cooperative regime, the edge and the [Co_6Se_8] cluster have similar reducing power and good orbital overlap. The edge metal and the [Co_6Se_8] cluster can therefore share the burden of oxidation, as in $CoCo_6Se_8(PEt_3)_4L_2$ (**2**-Co).[10] Spontaneous charge transfer can also occur between the edge and support. For example, the single edge cluster $CuCo_6Se_8(PEt_3)_4L_2$ (**2**-Cu) is synthesized from a Cu(II) source and a neutral Co_6Se_8 cluster, and yet **2**-Cu is best described as a Cu(I) edge installed on a mono-oxidized $[Co_6Se_8]^+$ unit.[10]

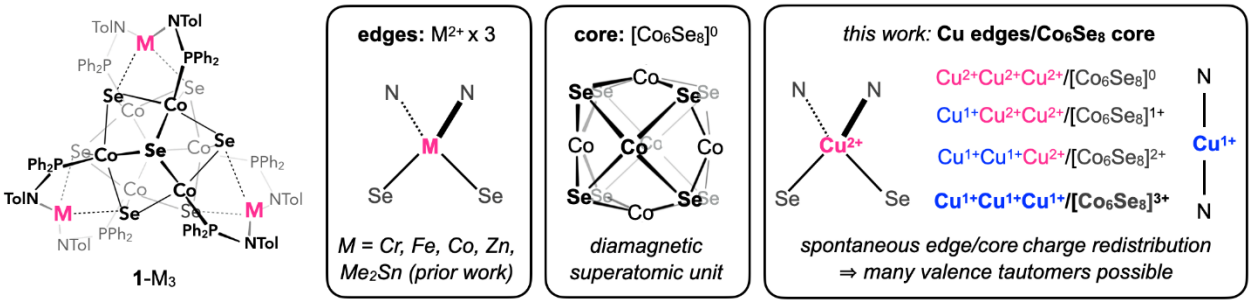

Figure 1. The ternary nanoclusters **1**-M_3 feature three edge sites (M^{2+}) anchored on a diamagnetic cluster core $[Co_6Se_8]^0$. Spontaneous edge/core electron transfer occurs when Cu^{2+} edge sites are installed.

Here, the limits of the spontaneous charge redistribution at the metal/support interface of a molecular cluster are tested by increasing the number of Cu centers on the $[Co_6Se_8]$ unit from one to three. The presence of multiple edge sites in a putative tricopper cluster could have interesting electronic consequences (Figure 1). Two scenarios are envisioned, which could co-exist via valence tautomerism.[32–34] In the first, three electron transfer events occur to produce a tricopper cluster in which three Cu(I) edge sites are installed on the elusive tri-oxidized $[Co_6Se_8]^{3+}$ unit.[8,20,35] The second scenario would illustrate a redox allostery of the edge sites,[23,24] producing a mixture of Cu(I)/Cu(II) edge sites anchored on an oxidized $[Co_6Se_8]^n$ unit (n = +1, +2). Our findings suggest that the former scenario is favored, and no clear evidence of valence tautomerism is observed across a wide window of redox states.

1.3 Results and Discussion

Treatment of the hexalithiated salt $Li_6(py)_6Co_6Se_8L_6$ (**1**-$Li_6(py)_6$; py = pyridine) with copper(I) bromide dimethyl sulfide (6.1 equiv) produces a single, paramagnetic cluster over the course of 16 h. This compound is isolated as a dark brown crystalline solid following a standard solvent workup (Scheme 1a). In solution, the product is symmetrical and contains no bound solvent. NMR spectroscopy analysis reveals a single ^{1}H environment for the amidophosphine ligand and a broad ^{31}P peak at −1065 ppm ($\nu_{1/2}$ = 1180 Hz), indicative of paramagnetism (Figures 7-8).

Single crystal X-ray diffraction analysis identified this species as the tricopper cluster salt $[Li(thf)_4][$**1**-$Cu_3]$ (thf = tetrahydrofuran), where each of the three edge sites are occupied by a single copper atom free of bound exogeneous ligands. The linear N—Cu—N geometry (Figure 2b, Table

S1) is suggestive of a +1 oxidation state.[10,36] Formally, the anionic cluster [**1**-Cu_3]$^-$ contains three Cu(I) edge sites anchored on a doubly oxidized $[Co_6Se_8]^{2+}$ cluster core. Given the relatively weak oxidizing capability of copper (I), we propose the starting material disproportionates *in situ* upon heating and forms multiple equivalents of copper(II), which is able to oxidize the $[Co_6Se_8]^0$ cluster core twice.[37,38]

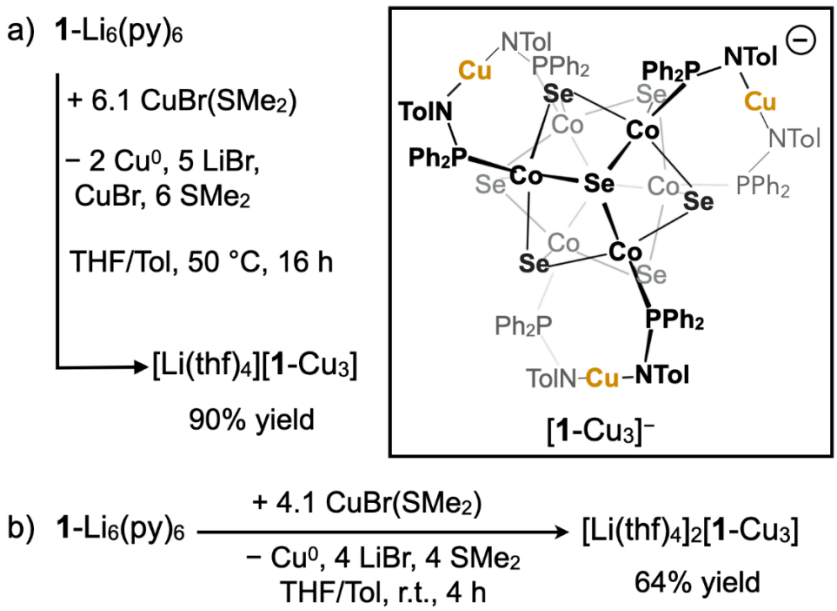

Scheme 1. Synthesis of [Li(thf)$_4$][**1**-Cu_3] and [Li(thf)$_4$]$_2$[**1**-Cu_3].

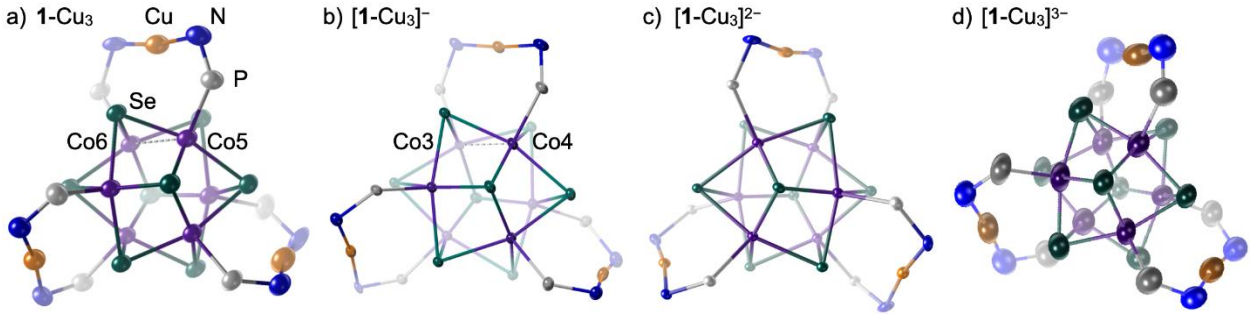

Figure 2. Comparison of the single crystal solid-state structures of (a) **1**-Cu_3, (b) [Li(thf)$_4$][**1**-Cu_3], (c) [Ru(bpy)$_3$][**1**-Cu_3], and (d) [CoCp*$_2$]$_2$[Li(thf)$_4$][**1**-Cu_3], with carbon atoms and cations truncated for clarity. Thermal ellipsoids are drawn at the 50% probability level.

If the **1**-Li_6(py)$_6$ cluster is treated instead with four equivalents of CuBr(SMe$_2$) and kept at room temperature during the reaction, then the cluster core is only oxidized once during transmetallation, yielding the dianionic salt [Li(thf)$_4$]$_2$[**1**-Cu_3] (Scheme 1b). The independent synthesis and characterization of [**1**-Cu_3]$^{2-}$ by reduction of [**1**-Cu_3]$^-$ is discussed in a later section. Treatment of

1-$Li_6(py)_6$ with copper(II) chloride (3 equiv) does not produce a tricopper cluster, instead leading to complex reactivity beyond the scope of this work.

The monoanionic tricopper(I) cluster [**1**-Cu_3]$^-$ has no observable affinity for exogenous ligands (e.g. THF, py, CO; SI 1.1), and in contrast to other **1**-M_3 clusters, it does not undergo hydrolysis in the presence of water (3 M in CH_3CN, 24 h, room temperature; Section S1.1). The increased stability and low reactivity of linear Cu(I) bisamides is documented, and has been attributed to the strong σ-donating ability of the supporting ligands and high covalency of the Cu—N bonds.[29-31] Solid-state analysis of [**1**-Cu_3]$^-$ reveals the Cu–N distances (1.90(1) Å avg.) are consistent with the average bond reported in the CCDC database of 2.0(1) Å,[42] and those in the mono-metallated cluster **2**-Cu of 1.893(4) Å.[10]

1.3.1 *A Cu/[Co_6Se_8] Redox Series*

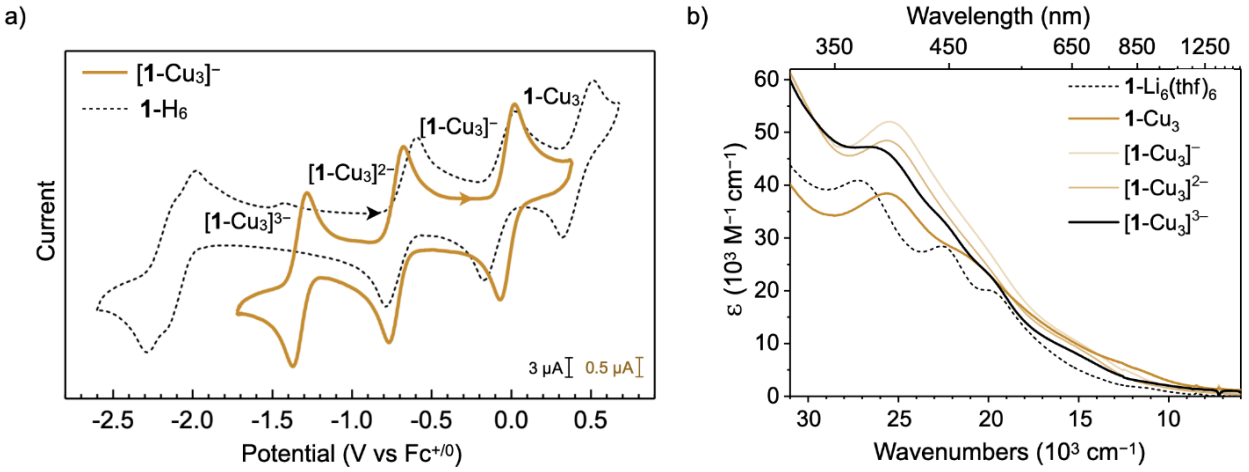

Figure 3. a) Cyclic voltammograms of **1**-H_6 and [$Li(thf)_4$][**1**-Cu_3] (0.1 M $TBAPF_6$ in THF, at scan rates of 200 and 25 mV/s, respectively, currents are normalized). b) UV-vis absorption spectra of [**1**-$Li_6(thf)_6$], **1**-Cu_3, [$Li(thf)_4$][**1**-Cu_3], [$Li(thf)_4$]$_2$[**1**-Cu_3], [$CoCp^*_2$]$_2$[$Li(thf)_4$][**1**-Cu_3] acquired in THF.

The electronic structure of the cluster is probed chemically and electrochemically. Cyclic voltammetry analysis of [**1**-Cu_3]$^-$ indicates three quasireversible, single electron events: two reductions and one oxidation at −1.33, −0.72, and −0.02 V vs $Fc^{+/0}$ respectively (Figures 3a and 14). The large separation between these redox events indicate that all the individual members of the [**1**-Cu_3]^n (n = 0 to −3) series might be stable towards isolation. Indeed, chemical one- and two-

electron reduction, as well as one-electron oxidation of [**1**-Cu_3]$^-$ is successfully accomplished using reagents of appropriate redox strength and enabled the independent isolation of all the members of the redox series (Scheme 2).[38] One-electron reduction of [**1**-Cu_3]$^-$ with $CoCp_2$ (Cp = C_5H_5; 1 equiv) yields the [$CoCp_2$][$Li(thf)_4$][**1**-Cu_3] salt, and two-electron reduction with $CoCp^*_2$ (Cp^* = C_5Me_5; 2 equiv) produces [$CoCp^*_2$]$_2$[$Li(thf)_4$][**1**-Cu_3]. The dianionic cluster [**1**-Cu_3]$^{2-}$ has also been isolated as the [$Ru(bpy)_3$][**1**-Cu_3] (bpy = 2,2'-bipyridine) salt following cation exchange, enabling its characterization by single crystal X-ray diffraction (Figure 2c). Cyclic voltammetry reveals that the trianionic cluster [**1**-Cu_3]$^{3-}$ is significantly more reducing than the isoelectronic **1**-H_6 cluster, ostensibly due to the presence of the anionic copper-bisamido unit edge sites (Figure 3a).[43]

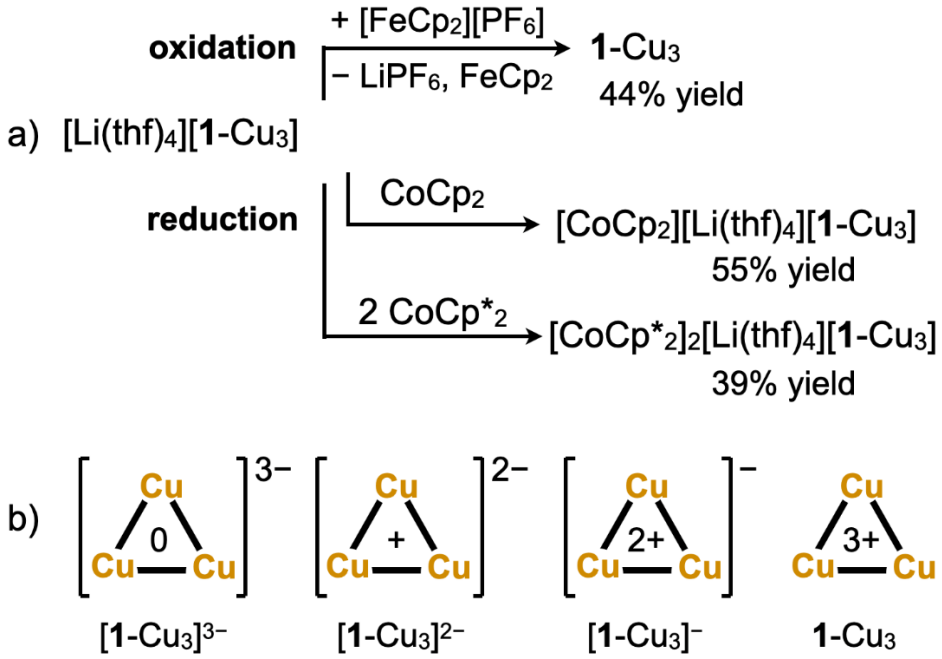

Scheme 2. a) Synthesis of the redox series [**1**-Cu_3]^n, n = 0, −2, −3 via chemical oxidation and reduction of [**1**-Cu_3]$^-$, and b) the proposed oxidation state of the Co/Se cluster.

In contrast to chemical reduction, the success of chemical mono-oxidation of [**1**-Cu_3]$^-$ is strongly dependent on the coordinating ability of the solvent and the identity of the counterion. While one-electron oxidation with [$FeCp_2$][PF_6] (1.0 equiv) occurs readily in THF to produce the neutral cluster **1**-Cu_3, no reaction occurs in CH_2Cl_2 even with strong oxidizing agents such as $AgPF_6$, [$N(C_6H_4Br\text{-}4)_3$][$SbCl_6$] or WCl_6.[38] Meanwhile, one-electron oxidation of [TBA][**1**-Cu_3], obtained via cation exchange from [$Li(thf)_4$][**1**-Cu_3] and [TBA]Cl, with [$FeCp_2$][PF_6] proceeds with or

without a coordinating ligand present. We attribute this solvent dependance to the association of lithium cation with the cluster. Indeed, NMR analysis indicates that the symmetry of the [Li(thf)$_4$][**1**-Cu$_3$] cluster lowers dramatically when dissolved in non-coordinating solvents (i.e., C_6D_6, CD_2Cl_2), suggesting ion association. In benzene-d_6, three distinct amidophosphine ligand environments are observable by ^{1}H and ^{31}P NMR spectroscopy, and two lithium signals are detected by ^{7}Li NMR spectroscopy – one at 0.4 ppm attributed to a Li(thf)$_4^+$ ion, and another broad peak at 16.7 ppm ($\nu_{1/2}$ = 200 Hz), attributed to Li(thf)$_x^+$ ions associating with the paramagnetic cluster core, likely at N or Se sites (Figures 8-11). We hypothesize that this ion pairing with the Lewis-acidic lithium cation depletes the cluster of electron density, making it more resistant to oxidation.

The [**1**-Cu$_3$]^n are strong absorbers and have UV-vis-nIR spectral profiles characteristic of the **1**-M$_3$ and **1**-Li$_6$(thf)$_6$ clusters. As illustrated in Figure 3b, all the clusters have a main feature with λ_{max} (ε) ranging from 389 nm (36,000 M^{-1}cm^{-1}) for [Li(thf)$_4$][**1**-Cu$_3$] to 392 nm (50,000 M^{-1}cm^{-1}) for [Li(thf)$_4$][Cp$_2$Co][**1**-Cu$_3$], and absorption tails that extend into near-IR. The absorption in the near-IR region redshifts as electrons are removed from the system, with lowest energy values for **1**-Cu$_3$. However, the significance of this trend in connection to the observation of intervalence charge transfer bands is currently little understood (Figure 3b).

With three Cu(I) edge sites and a trioxidized Co/Se core, **1**-Cu$_3$ represents the first reported example of a [Co$_6$Se$_8$]$^{3+}$ cluster. In agreement with this oxidation state assignment, electron paramagnetic resonance spectroscopy of **1**-Cu$_3$ at 100 K does not indicate the presence of Cu(II) (Figure 2). **1**-Cu$_3$ is resistant to further oxidation, highlighting the difficulty of directly oxidizing the Cu(I) sites to Cu(II) in this system. It also suggests that the tetraoxidized form of the Co/Se core is not synthetically accessible with standard reagents. Valence tautomerization is not observed in **1**-Cu$_3$, although three electron-rich copper(I) sites are placed on a highly oxidizing [Co$_6$Se$_8$]$^{3+}$ cluster. **1**-Cu$_3$ is thermally stable (24 h, 80 °C) and does not convert to a new species (e.g., **1**-Cu^{II}Cu$^{I}_2$) even in the presence of coordinating ligands (THF, py, PMe$_3$, ^{t}BuCN, CO). The reorganization energy cost associated with this putative inner-sphere electron transfer that would oversee a linear Cu(I) convert to a pseudo-tetrahedral or square planar Cu(II) center could be prohibitive,[39] whereas there is minimal entropic cost associated with the oxidation or reduction of the Co$_6$Se$_8$ core. A limited number of two-coordinate linear copper(II) amido complexes are known, but they are not synthesized through the oxidation of a linear copper(I) complex.[44–46]

1.3.2 *Isostructurality and helical chirality across the redox series*

The solid-state structures of the tricopper cluster redox series [**1**-Cu_3]^n (n = 0, –1, –2, –3) are obtained using single crystal X-ray diffraction analysis (Figure 2). Whereas the data sets for **1**-Cu_3, [$Li(thf)_4$][**1**-Cu_3] and [$Ru(bpy)_3$][**1**-Cu_3] are sufficiently high quality to enable a bond metric comparison, the crystal structure of [$CoCp^*_2$]$_2$[$Li(thf)_4$][**1**-Cu_3] is fraught with extensive cation and solvent disorder, precluding a bond metrics discussion. The Cu/Co/Se clusters retain a pseudo-D_3 symmetry across the redox series. The copper (I) amidophosphine units remain relatively rigid and nearly linear, with ∠NCuN angles ranging from 168.0(3) to 175.0(3)°, and an average Cu…Se distance of 2.80 Å, indicating no binding interaction is present (Table 1).[47]

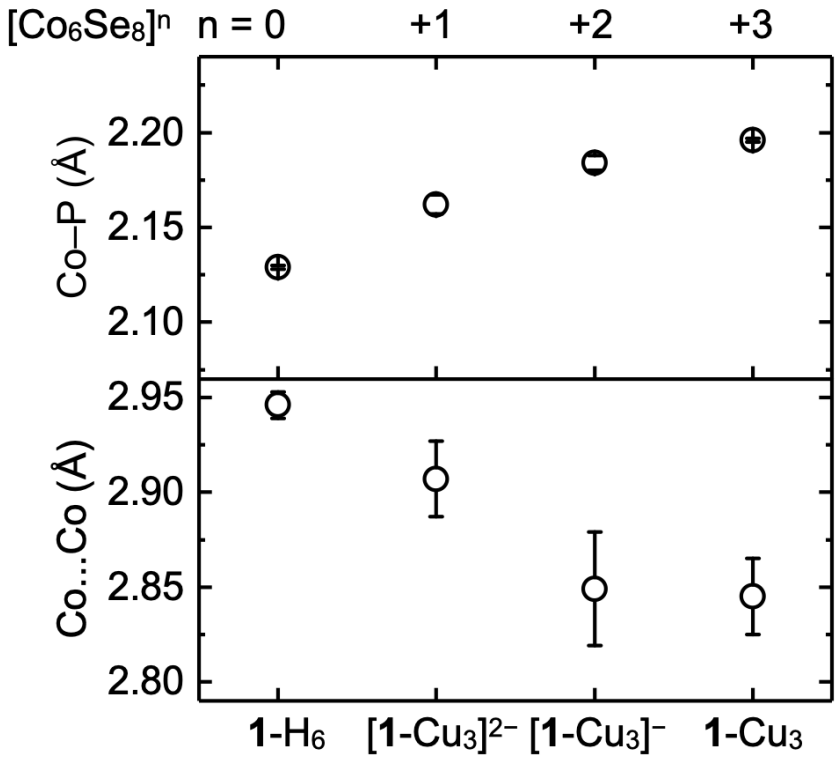

Figure 4. Comparison of bonding parameters obtained via crystallography as a function of cluster core oxidation state. Error bars represent the standard error of each data point.

A bond metric comparison informs on the distribution of electron density between the copper edge sites and the Co/Se core, lending support to the proposal that while copper maintains a +1 oxidation state, [Co_6Se_8] is the locus of redox state changes, ranging from +3 in **1**-Cu_3 to neutral in [**1**-Cu_3]$^{3–}$. Whereas the Co—Se, Cu…Se and Cu—N interatomic distances do not vary significantly with

oxidation state changes, the Co…Co and Co—P interatomic distances are informative (Figure 4). A basic molecular diagram of the Co_6Se_8 cluster core[48] predicts that as electrons are removed from it, antibonding Co…Co orbitals are depopulated and the Co…Co bonding character increases. Indeed, a contraction in the Co…Co distances in the Co/Se core has been empirically associated with oxidation.[20,49] Figure 4 reflects this trend: as one, two and three electrons are removed from the Co/Se cluster, the Co…Co average distances contract from 2.946(7) Å in the neutral Co_6Se_8 core of **1**-H_6 to 2.85(2) Å in **1**-Cu_3 and [**1**-Cu_3]$^-$. In fact, **1**-Cu_3 and [**1**-Cu_3]$^-$ feature one short Co…Co distance of 2.683(3) and 2.682(2) Å, respectively, consistent with a weak Co—Co bonding interaction.[50] Density functional theory calculations indicate Mayer bond orders of 0.44 and 0.12 for the Co/Co pairs with short and long contacts in [**1**-Cu_3]$^-$, respectively.[51] The average Co–P distances in the redox series oppose the trend of the Co…Co distances, increasing with oxidation of the Co/Se core from 2.129(1) Å (avg.) in **1**-H_6 to 2.162(5) Å in [**1**-Cu_3]$^{2-}$ to 2.196(1) Å in **1**-Cu_3. As electrons are removed from the Co_6Se_8 cluster, the cobalt atoms participate in weaker back-bonding with the phosphines.[52]

The propeller-like arrangement of the copper-amidophosphine units on the surface of the Co/Se core results in inherent helical chirality for the cluster.[53] While all **1**-M_3 clusters are helically chiral, [Li(thf)$_4$][**1**-Cu_3] represents the first example to enantioseparate upon crystallization. The presence of individual single crystals of a single handedness is confirmed experimentally by X-ray crystallography; [Li(thf)$_4$][**1**-Cu_3] crystallizes in the chiral space group $P2_12_12_1$. Spontaneous chiral resolution by crystallization is a relatively rare phenomenon.[54] However, efforts to access enantiomerically pure samples of the cluster at scale have been unfruitful.

1.3.3 *Solution Magnetism and Paramagnetic ^{31}P NMR Studies to Elucidate Spin State Changes In Redox Series*

Solution magnetic susceptibility measurements of [Li(thf)$_4$][**1**-Cu_3] using Evans' method[55] produce an overall magnetic moment of 2.1 Bohr magnetons, intermediate to the expected spin-only magnetic moment values of 1.73 and 2.83 Bohr magnetons for the spin states of S = ½ and 1, respectively. The [**1**-Cu_3]$^-$ cluster has an even number of electrons and therefore would nominally be expected to have either a closed-shell or triplet ground state (S = 0 or 1). Meanwhile, the Evans' method measurements for [Li(thf)$_4$]$_2$[**1**-Cu_3] and **1**-Cu_3 result in effective magnetic moments of 1.6 Bohr magnetons, which are consistent with an S = ½ spin state. Molecular orbital theory

predicts that the HOMO in a Co_6Se_8 system is triply degenerate,[48] and DFT calculations on the homoleptic cluster $Co_6Se_8(PEt_3)_6$ similarly predicts a doubly degenerate HOMO level followed closely by the HOMO-1 only 0.02 eV lower in energy.[43] Both situations would theoretically yield a $[Co_6Se_8]^{2+}$ cluster core in an S=1 state.

^{31}P NMR spectroscopy analysis of the redox series [**1**-Cu_3]^n (n = 0, –1, –2, –3) indicates that all four compounds remain nominally D_3 symmetric in coordinating solvents. While ^{1}H NMR chemical shifts are relatively unremarkable and span the diamagnetic window, the ^{31}P nuclei serve as diagnostic reporters on the electronic state of the clusters,[10] featuring chemical shifts that undergo dramatic changes with the redox state. The ^{31}P NMR chemical shifts range from 80 ppm for the diamagnetic [**1**-Cu_3]$^{3-}$ to –1160 ppm in **1**-Cu_3 (Figure 5). As expected, the paramagnetic centers greatly reduce the relaxation times of the ^{31}P signals, from 162(2) ms in **1**-H_6 to 1.6(1)—3.4(1) ms in [**1**-Cu_3]^n, n = 0, –1, –2 (Figures 32-35).

Paramagnetic NMR chemical shifts (δ_T^{obs}) are a result of diamagnetic (δ^{dia}) and paramagnetic contributions (δ^{para}), as described by Eq. 1.[56] Since δ^{para} depends on the total spin and temperature, variable-temperature ^{31}P NMR measurements can inform on the electronic structure of the compounds measured. Plotting the ^{31}P NMR chemical shifts of [**1**-Cu_3]^n (n = 0, –1, –2) vs the inverse of temperature (T = 290 – 330 K; Figure 5a) confirms a linear Curie-Weiss relationship, and rules out any unexpected behavior of the clusters such as ferromagnetism.[57] The temperature-independent ^{31}P NMR chemical shifts (δ^{TIP}) can further inform on the spin state of the clusters. These originate from temperature-independent sources of paramagnetism such as Van Vleck or Pauli susceptibilities,[57] the former of which is proportional to the number of unpaired spins.[58] In particular, Van Vleck susceptibilities have been previously observed in oxidized Co_6Te_8 clusters, and could be relevant in the [**1**-Cu_3]^n series.[59,60] Here, temperature-independent chemical shifts were estimated by extrapolating the linear fits of the observed ^{31}P NMR chemical shift to infinite temperature. The δ^{TIP} values obtained for [**1**-Cu_3]$^{2-}$ and **1**-Cu_3 are near-equivalent, of 190(13) and 182(27) ppm, respectively, lending support to the equivalent spin state attribution of S = 1/2. Meanwhile, the δ^{TIP} for [**1**-Cu_3]$^-$ is calculated to be 354(25) ppm, nearly twice that of the other clusters, suggestive of an S = 1 spin state. The behavior of [**1**-Cu_3]$^-$ was further probed by ^{31}P VT-NMR experiments at an extended temperature range (340-200 K). No deviations from linearity (indicative of spin crossover) were observed in this temperature window (Figure 39).[61]

1.3.4 *X-ray Absorption Spectroscopy Probes Electronic Changes at Se*

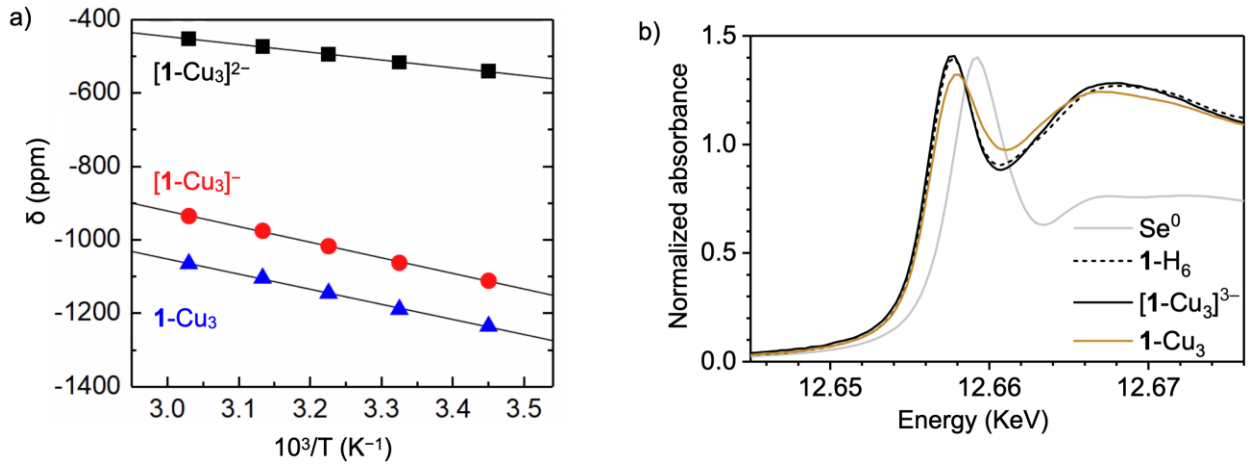

Figure 5. a) Curie behavior of [**1**-Cu_3]^n (n = 0, –1, –2) reflected in the linear dependence of the ^{31}P NMR shifts with the inverse of temperature (290 – 330 K). b) Se XANES spectra of **1**-Cu_3, $[CoCp^*_2]_2[Li(THF)_4]$[**1**-Cu_3], **1**-H_6 and Se foil. The signal for the Se foil is scaled to enable comparison to the clusters.

To further understand the electronic changes within the cluster core, **1**-H_6, [**1**-Cu_3]$^{3–}$ and **1**-Cu_3 were analyzed via selenium K-edge X-ray absorption near edge structure spectroscopy (XANES; Figure 5b, Table 2). The pre-edge feature (Se 1s to 4p; 12.657 keV) is similar to that seen in transition metal selenides (12.657 keV in $Cu_2Mo_6Se_8$,, 12.656 keV in CdSe),[62–64] and is consistent with a Se(–2) oxidation state. The pre-edge feature shifts by 0.3 eV between [**1**-Cu_3]$^{3–}$ and **1**-Cu_3, indicating a slight increase in the oxidation state of the Se sites as the Co/Se cluster undergoes a three-electron oxidation.[65] For comparison, the one electron oxidation of the cationic cluster $[Fe_2Se_2]^{+1/+2}$ is associated with a positive shift of 0.6 eV of the pre-edge feature.[66] In this instance, the larger magnitude could be attributed to the increased charge per Se atom (1 $e^–$/2 Fe, 2 Se) compared to the Co_6Se_8 cluster (3 $e^–$/6 Co, 8 Se). The Se XANES data also reflect the similarity between the isoelectronic **1**-H_6 and [**1**-Cu_3]$^{3–}$ clusters, which feature neutral Co_6Se_8 cores. (Figure 42).

1.3.5 *Insights into Electronic Structure via DFT Calculations*

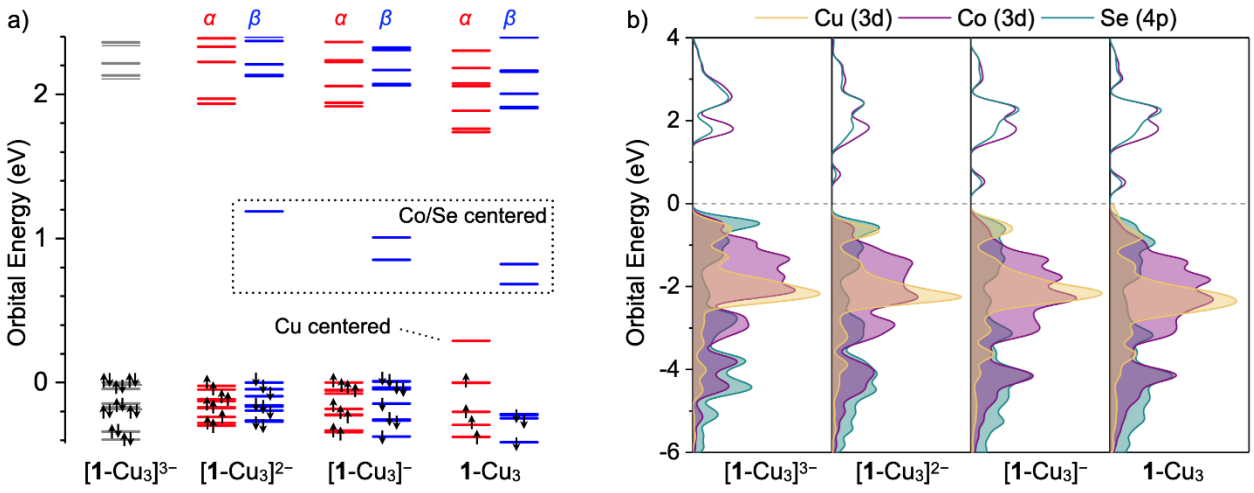

Figure 6. (a) Molecular orbital diagrams for [**1**-Cu_3]^n (n = 0, –1, –2, –3) calculated at B3LYP+/ccPVTZ level of theory. Alpha (*a*) and beta (*b*) orbitals for the open-shell clusters are colored red and blue, respectively, and (b) corresponding partial density of states plots. To facilitate comparisons, each top occupied orbital is normalized to a value of 0 eV.

The electronic structure of the [**1**-Cu_3]^n (n = 0,–1,–2,–3) redox series was modeled using Density Functional Theory (DFT; Sections 1.5.2 and 1.10). The optimized geometries reflect experimentally observed trends in Co–P and Co…Co distances (Table 5). As expected, the closed-shell cluster [**1**-Cu_3]$^{3-}$ features a an electronic structure resembling that of $Co_6Se_8(PEt_3)_6$, with a near-triply degenerate highest occupied molecular orbital (HOMO), and a doubly degenerate lowest unoccupied molecular orbital (LUMO; Figure 6a).[43]

The frontier electronic states are plotted as molecular orbital diagrams (Figure 6a), but also as density of states plots which better illustrate elemental contributions (Figure 6b).[67] The neutral and dianionic clusters both have a singly occupied molecular orbital (SOMO) that is significantly higher in energy than the other occupied frontier orbitals, consistent with the observed S = ½ spin state, while the monoanionic cluster has a more ambiguous electronic structure with several pseudo-degenerate orbitals at the frontier. Considering both the alpha (α) and beta (β) manifolds in [**1**-Cu_3]$^-$, the three occupied orbitals that are highest in energy are separated by only 0.01 eV in total. Their pseudo-degeneracy is possibly a consequence of the deviations from idealized D_3 geometry in the optimized structure, which results in slight energy differences in nominally

equivalent orbitals. Jahn-Teller type distortions could be responsible for the partially quenched magnetic moment of [**1**-Cu_3]$^-$, as observed experimentally by Evans' method.[68]

Density of states plots indicate that the copper character in the occupied frontier orbitals increases substantially as electrons are removed from [**1**-Cu_3]$^{3-}$ until it becomes exclusively copper centered in **1**-Cu_3 (Figures 6b and 51). This is aligned with our earlier interpretation of the experimental data: as 1, 2, and 3 electrons are removed from [**1**-Cu_3]$^{3-}$, the copper edge sites retain their +1 oxidation state while the Co/Se core becomes increasingly oxidized. Indeed, even in the highly oxidized cluster **1**-Cu_3, there is little contribution from copper to the unoccupied electronic states, corroborating the experimentally observed absence of copper(II) or any intermediate oxidation state in the clusters. Correspondingly, the LUMO and LUMO+1 orbitals are localized on the Co/Se core for all members of the redox series, consistent with experimental results suggesting core-based oxidation.[10] Additionally, as the cluster increases in oxidation state, the selenium character of the occupied frontier states gradually diminishes. We attribute this to the partial oxidation of the Se, in line with the Se XANES data discussed above.

1.4 Conclusion

Atomically precise and entropically robust, the [**1**-Cu_3]^n (n = 0, –1, –2, –3) clusters enable detailed mapping of the structural and electronic interactions at the Cu/Co_6Se_8 dopant/support interface. Experimental and DFT investigations suggest that as electrons are removed from [**1**-Cu_3]$^{3-}$ cluster, the copper edge sites retain a +1 oxidation state while the Co/Se core becomes increasingly oxidized. The series culminates with the formation of **1**-Cu_3, a highly zwitterionic species with three Cu(I) edge sites anchored but not binding directly to the triply oxidized [Co_6Se_8]$^{3+}$ core. The reluctance of the copper(I) edge sites to undergo oxidation and the absence of any apparent valence tautomerism may be attributed to the large entropic cost of entering a tetracoordinate coordination geometry favorable to copper(II).

1.5 Synthetic Details and Characterization of Products

1.5.1 *General Experimental Considerations*

All syntheses were conducted under a dinitrogen atmosphere using a standard Schlenk line or an LC Technology Solutions glovebox equipped with a freezer set to −35 °C. All glassware was dried

at 160 °C for a minimum of 12 h prior to use. Solvents were purchased from Fisher Scientific and degassed, dried, and purified using solvent purification columns housed in a stainless-steel cabinet and dispensed by a stainless-steel Schlenk line manufactured by JC Meyer Solvent Systems. Tetrahydrofuran (THF), diethyl ether (Et_2O), acetonitrile, and methylene chloride (DCM) are passed through two packed columns of neutral alumina. *n*-Pentane, benzene, and toluene are passed through a column packed with alumina, and one containing Q5 reactant, a copper(II) oxide oxygen scavenger. All solvents were passed through an in-line, 2 μm filter, then stored over activated 3Å molecular sieves in the glovebox. 3Å molecular sieves were purchased from Sigma Aldrich and activated under vacuum at 300 °C for 48 h. Anhydrous pyridine (99.8% purity) was purchased from Sigma Aldrich and stored over activated 3Å molecular sieves for 72 h prior to use. Copper(I) bromide dimethylsulfide (99% purity), tetrabutylammonium chloride (97+% purity), decamethylcobaltocene, and tris(4-bromophenyl)ammoniumyl hexachloroantimonate (technical grade) were purchased from Sigma Aldrich and used without further purification. Cobaltocene (98+% purity) was purchased from Strem Chemicals and used without further purification. Tris(bipyridine)ruthenium(II) chloride hexahydrate (99.95% purity) was purchased from Sigma Aldrich and converted to the iodide salt via a literature procedure.[69] **1**-H_6 and **1**-$Li_6(py)_6$ were synthesized according to literature procedures.[8] Tetra(*n*-butyl)ammonium hexafluorophosphate ($TBAPF_6$, 98%) was purchased from Sigma Aldrich and recrystallized from ethanol upon cooling from 78 to –35 °C three times followed by removal of volatiles under reduced pressure at 110 °C for 24 h prior to its use.

Deuterated solvents were purchased from Sigma Aldrich or Cambridge Isotope Labs, degassed and dried over activated 3Å molecular sieves in the glovebox for a minimum of 72 h.

UV-vis-*n*IR absorption spectra were acquired using a Varian Cary 5000 UV-Vis-*n*IR spectrophotometer, in *n*IR quartz cuvettes (Spectrocell Inc., 10 mm path length, 220–3500 nm spectral window). Attenuated total reflectance infrared (ATR-IR) spectra were recorded on a Bruker Alpha IR instrument equipped with a Platinum ATR accessory housed within a nitrogen glovebox. NMR spectra were acquired at 25 °C unless indicated otherwise on Bruker 300, 500, or 700 MHz spectrometers. ^{1}H NMR spectra were referenced to residual deuterated solvent peaks. ^{7}Li NMR spectra were referenced to aqueous lithium chloride, and ^{31}P NMR spectra referenced to 85% phosphoric acid. Heteronuclear NMR experiments were not proton-decoupled unless

specified otherwise. Solution magnetic susceptibilities were determined by the Evans method in acetonitrile-d_3 or dichloromethane-d_2 using 5% dimethylformamide or dichloromethane as internal standards, respectively.[70]

Cyclic voltammetry was conducted using a μAutolabbIII/FRA2 potentiostat by Metrohm and a Gamry Interface 1010B potentiostat. A three-electrode cell setup was used with a glassy carbon disk working electrode, a platinum wire counter electrode, and a silver wire pseudo-reference electrode. All potentials were referenced Fc/Fc^+ redox couple by adding a small amount of ferrocene after each measurement. All electrochemical measurements were conducted under a dinitrogen atmosphere at room temperature.

Samples were prepared for elemental analysis by crushing crystalline material into a powder and then removing volatiles under reduced pressure for 12 h. Co, Se, P elemental analysis was conducted using a Perkin-Elmer Nexion 2000B inductively-coupled plasma mass spectrometer (ICP-MS). Prior to ICP-MS analysis, samples were digested in neat nitric acid (Fisher Scientific, ICP-MS grade) at 50 °C, and serial dilutions were performed with Milli-Q reference water.

Mass spectrometry was carried out via direct injection of acetonitrile solutions of the analyte using a Bruker Esquire mass spectrometer. Mass spectra were collected in positive mode using the extended m/z scanning range (400-3400 m/z) to locate the parent ion peaks.

1.5.2 *Computational Methods*

All DFT calculations were performed using Gaussian 16, Revision A.03 quantum chemistry program package for the Linux operating system.[71] The initial starting point geometries were obtained by using the crystallographically obtained structure of $[Li(thf)_4][\mathbf{1}\text{-}Cu_3]$ as a starting point and optimizing to a minimum, followed by analytical frequency calculations (Hessian) to confirm that no imaginary frequencies were present. Prior to optimization, the cation was omitted from the structure and the methyl groups on the tolyl groups of the aminophosphine ligands were replaced with hydrogen atoms to reduce computation time. The geometry optimizations were performed using unrestricted DFT calculations (except for $[\mathbf{1}\text{-}Cu_3]^{3-}$ which was restricted) at a pure GGA functional level using Becke's 1988 gradient-corrected exchange functional and Perdew's 1986 electron correlation functional (uBPV86) and def2SVP basis set. The optimized geometry of the $[\mathbf{1}\text{-}Cu_3]^-$ anion was used as the starting point for optimization of the other clusters in the series.

Using the optimized geometries, single point calculations were performed at the uB3LYP+/cc-pVTZ that were used for orbital energy diagrams and spin density calculations. Doublet spin states were assumed for [**1**-Cu_3]$^{2-}$ and **1**-Cu_3, while [**1**-Cu_3]$^{-}$ was modeled as a triplet. Multiwfn was used to generate partial density of states plots and calculate Mayer bond orders.[67] This level of theory and approach has been previously utilized to reproduce defining experimental features of the **1**-M_3 and **2**-M clusters.[10,25]

1.5.3 *Synthesis of [Li(thf)$_4$][1-Cu$_3$]*

Inside the glovebox, a 200 mL Schlenk flask with Teflon-coated stir bar was charged with **1**-$Li_6(py)_6$ (5.500 g, 1.7 mmol) and copper(I) bromide dimethylsulfide (2.127 g, 10.3 mmol). Toluene (70 mL) and tetrahydrofuran (25 mL) are added to the flask, resulting in a dark brown solution upon mixing. The flask is capped with a rubber septum and heated in an oil bath to 50 °C for 16 hours. The flask is cooled and returned to the glovebox, and the solvent was removed from the reaction mixture by applying vacuum. The dark brown residue was dissolved in minimal tetrahydrofuran, combined with toluene (50 mL) and pentane (50 mL), and left to sit at room temperature for 12 hours. The resulting crystals are isolated by vacuum filtration over a medium-pore frit and washed with toluene (50 mL) and pentane (30 mL). The product is obtained as a black crystalline solid after removing volatiles *in vacuo* (4.770 g, 1.58 mmol, 87%). The compound can be handled in air and does not hydrolyze if treated with water in acetonitrile at 25 °C (3 M) for a period of at least 12 hours. ^{1}H NMR (acetonitrile-d_3, 500 MHz) δ: 8.74 (s, 6H, -Ph), 8.31 (d, *J*=7.4 Hz, 12H, -Ph), 7.35 (t, *J*=7.3 Hz, 6H, -Ph), 7.04 (t, *J*=7.4 Hz, 12H, -Ph), 6.72 – 6.66 (d, *J*=7.4 Hz, 12H, -C_6H_4-p-Me), 6.58 (d, *J*=7.8 Hz, 24 Hz, -Ph), 5.04 (d, *J*=7.3 Hz, 12H, -C_6H_4-p-Me), 1.99 (s, 18H,-CH_3). ^{31}P NMR (acetonitrile-d_3, 283 MHz) δ: -1065.8 ($\nu_{1/2}$ = 1200 Hz, T_1 = 3.4 ms). ^{31}P NMR (benzene-d_6, 283 MHz) δ: -960.9 ($\nu_{1/2}$ = 900 Hz), -990.8 ($\nu_{1/2}$ = 650 Hz), -1033.2 ($\nu_{1/2}$ = 2000 Hz). ^{7}Li NMR (acetonitrile-d_3, 194 MHz) δ: -2.45 ($\nu_{1/2}$ = 18 Hz). ^{7}Li NMR (benzene-d_6, 194 MHz) δ: 16.68 ($\nu_{1/2}$ = 180 Hz), 0.38 ($\nu_{1/2}$ = 45 Hz). ^{13}C NMR (acetonitrile-d_3, 126 MHz) δ: 134.42, 133.17, 131.78, 131.66, 128.56, 125.77, 124.83, 124.80, 121.25, 120.93, 20.70. μ_{eff} (Evans Method, CD_3CN, 298 K): 2.06 μ_B. UV-Vis (acetonitrile): λ_{max} (ε) 389 nm (36,000 $M^{-1}cm^{-1}$). Elemental Analysis (ICP-MS): Experimental (Calculated for $C_{130}H_{134}Co_6Cu_3LiN_6O_4P_6Se_8$) Co 11.00 (11.11) Se 19.90 (19.66) P 5.82 (5.78).

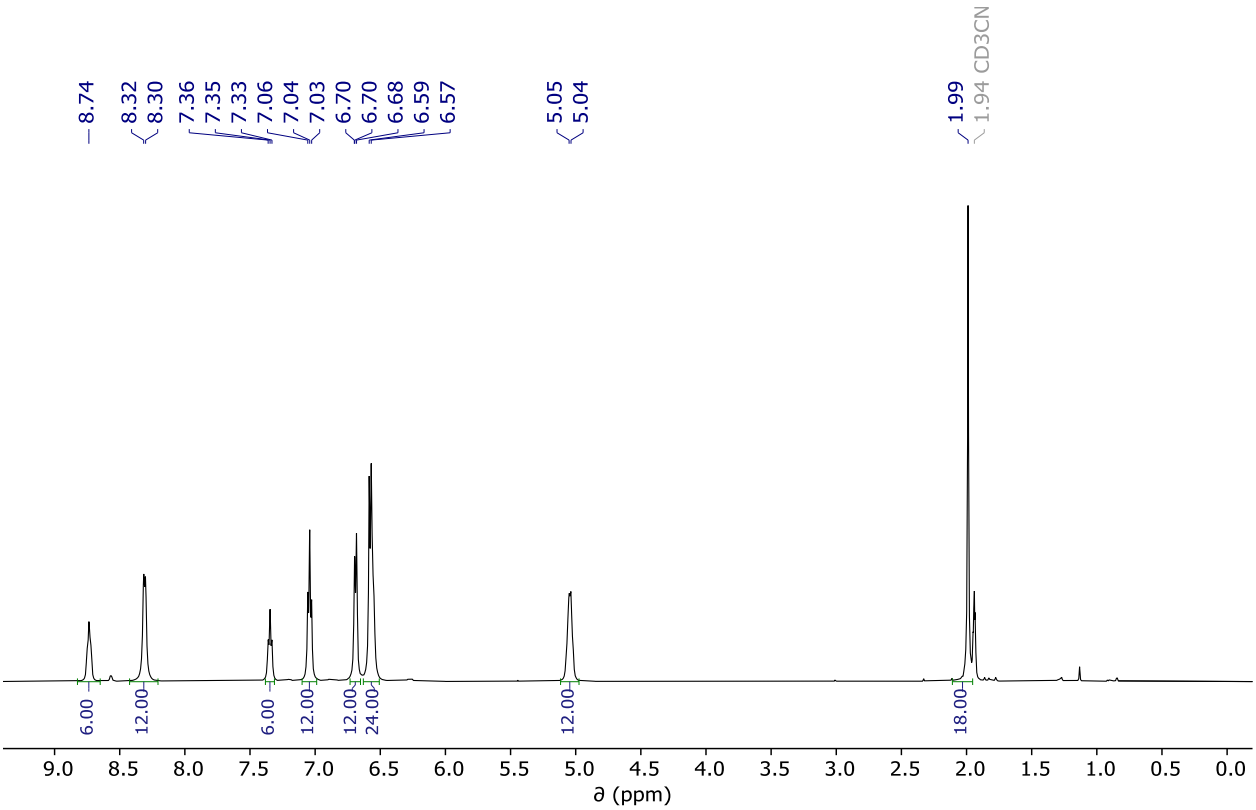

Figure 7. ^{1}H NMR (CD_3CN, 25 °C, 500 MHz) spectrum of [Li(thf)$_4$][**1**-Cu$_3$]

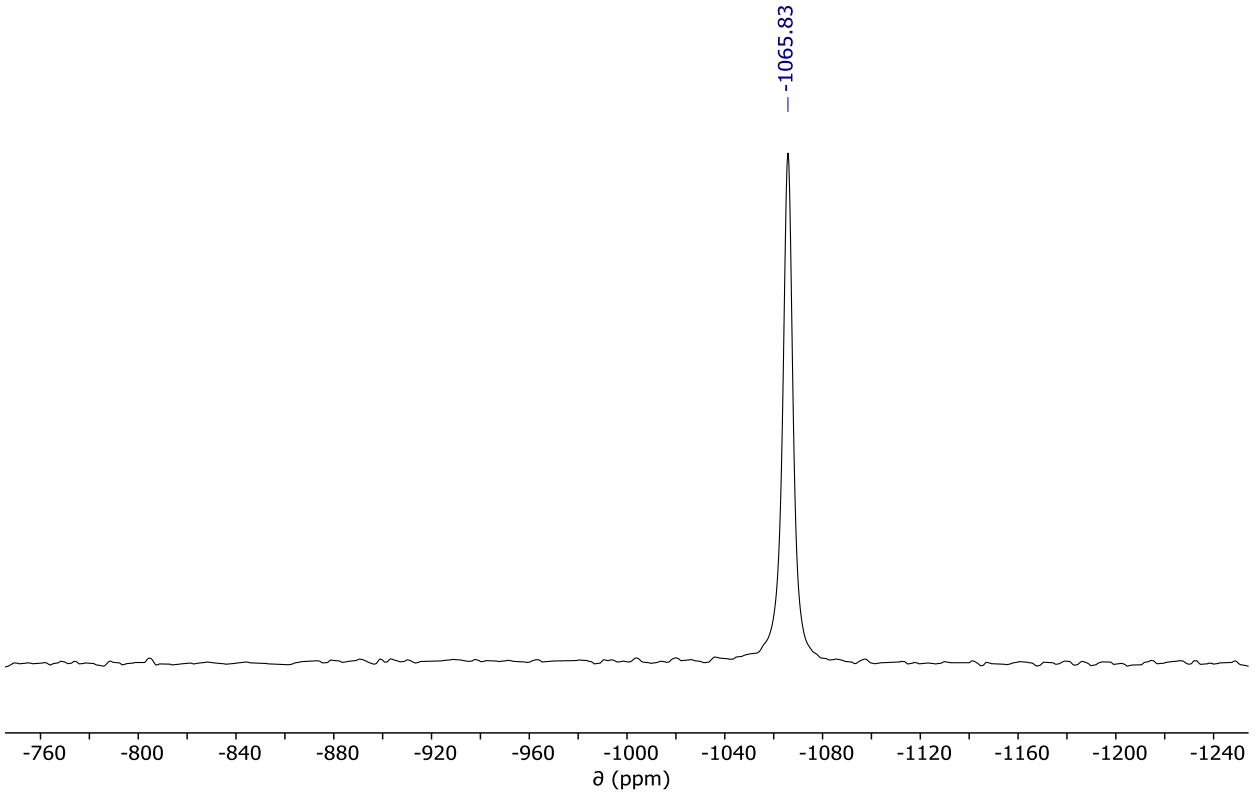

Figure 8. ^{31}P{^{1}H} NMR (CD_3CN, 25 °C, 283 MHz) spectrum of [Li(thf)$_4$][**1**-Cu$_3$]

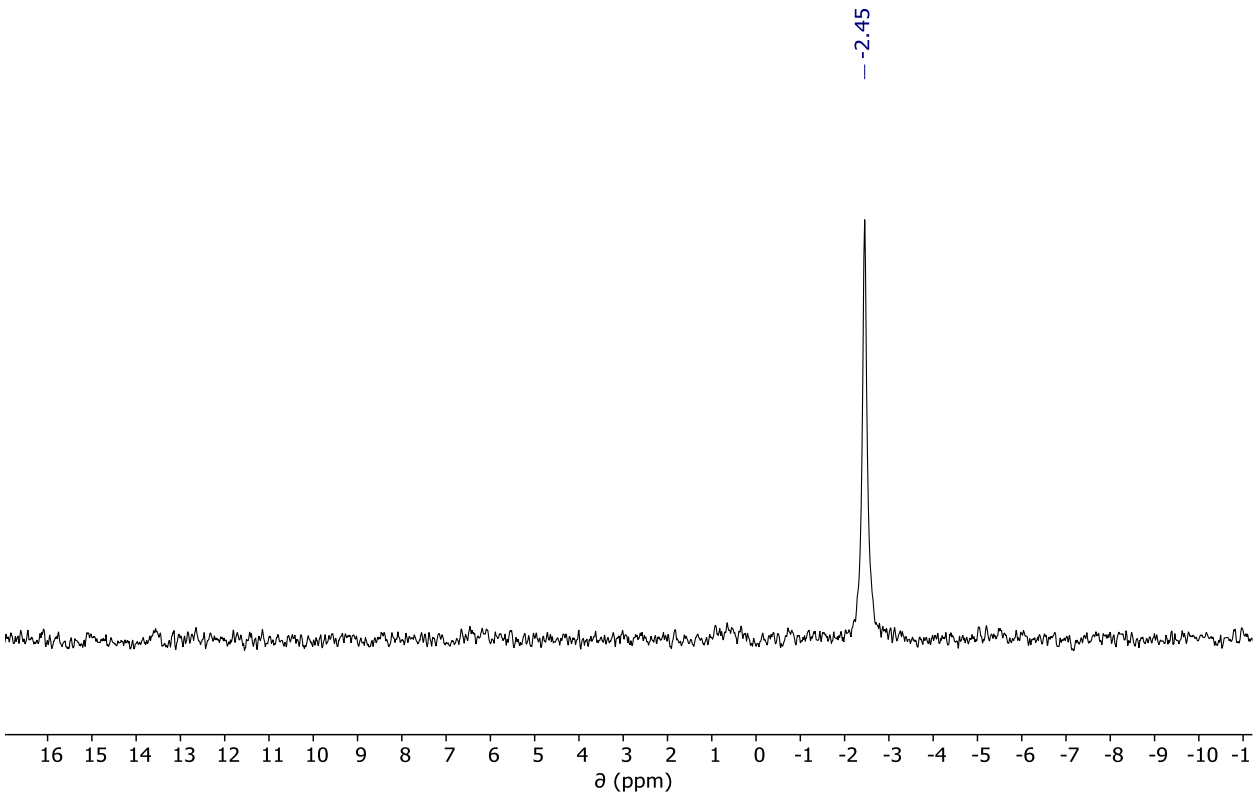

Figure 9. ^{7}Li NMR (CD_3CN, 25 °C, 194 MHz) spectrum of $[Li(thf)_4][\mathbf{1}\text{-}Cu_3]$

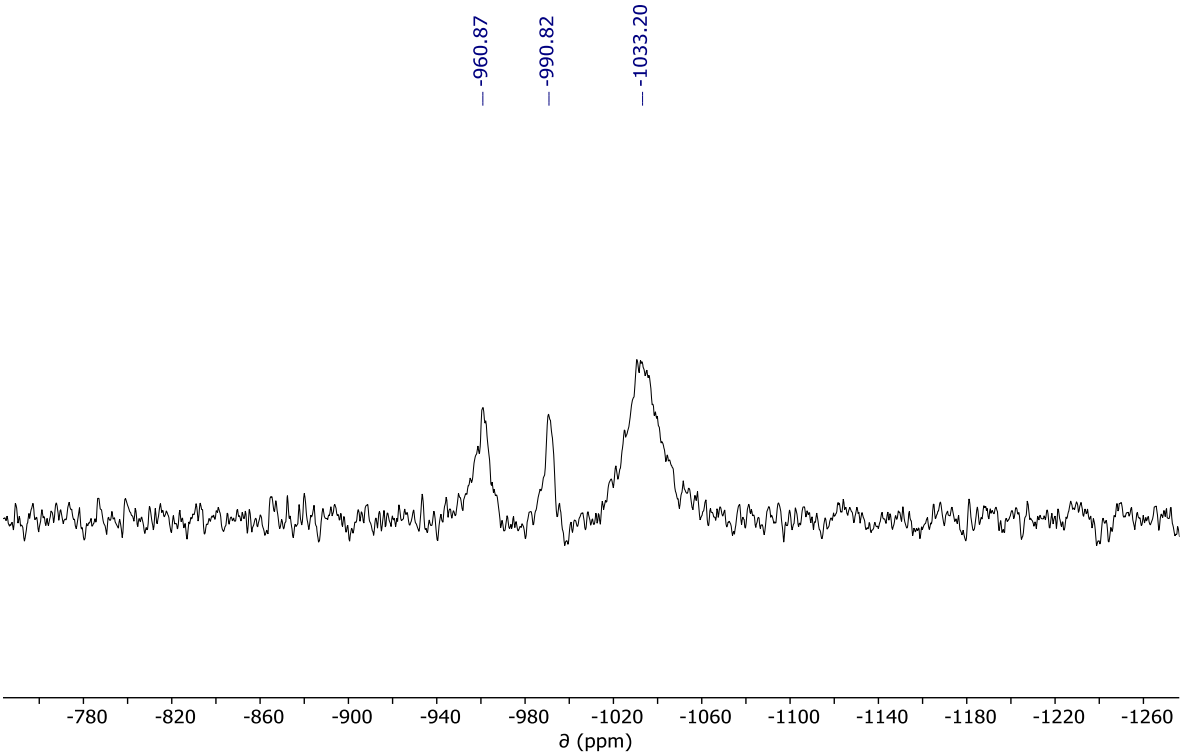

Figure 10. $^{31}P\{^{1}H\}$ NMR (C_6D_6, 25 °C, 202 MHz) spectrum of [Li(thf)$_4$][**1**-Cu$_3$]

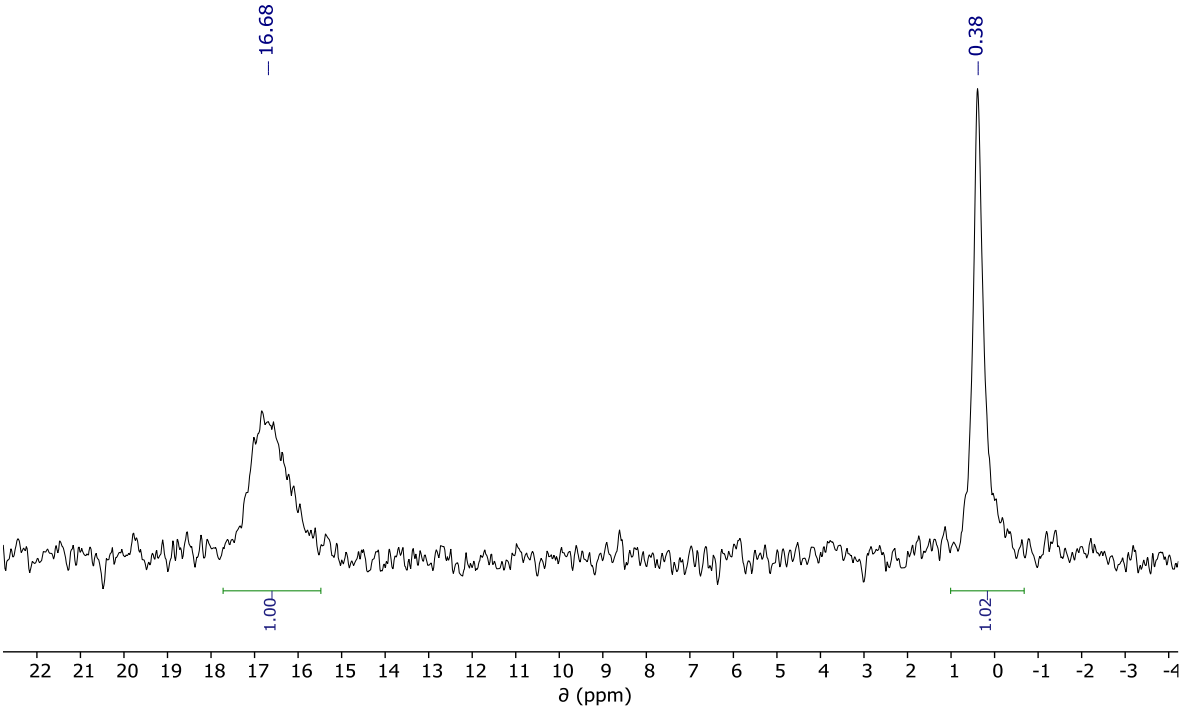

Figure 11. ^{7}Li NMR (C_6D_6, 25 °C, 194 MHz) spectrum of [Li(thf)$_4$][**1**-Cu$_3$]

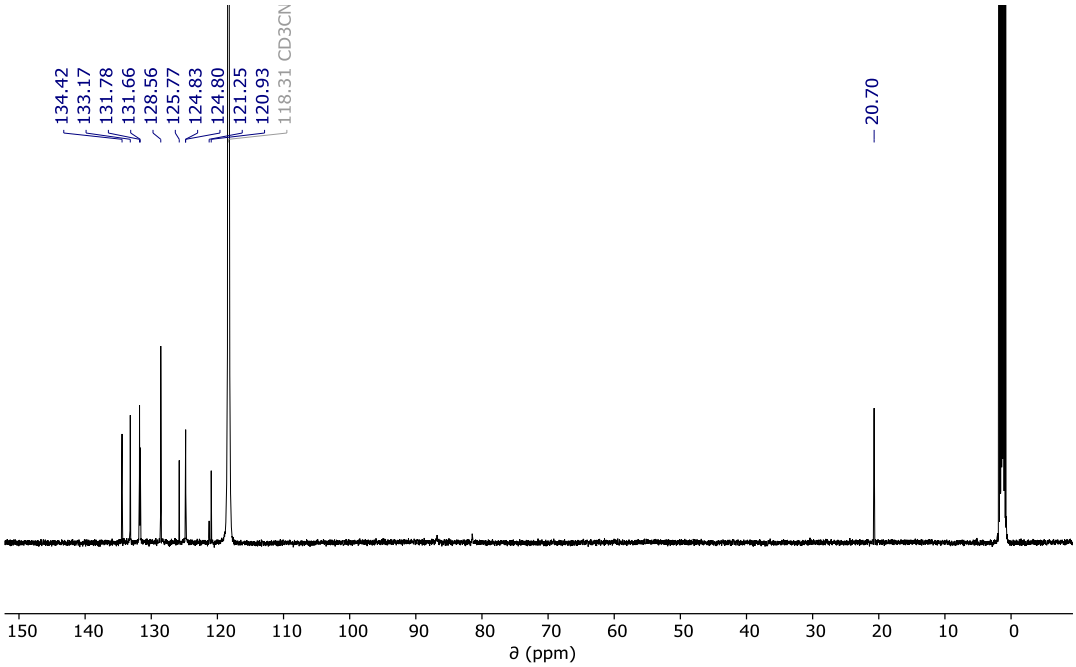

Figure 12. $^{13}C\{^{1}H\}$ NMR (acetonitrile-d_3, 25 °C, 126 MHz) spectrum of $[Li(thf)_4][\mathbf{1}\text{-}Cu_3]$

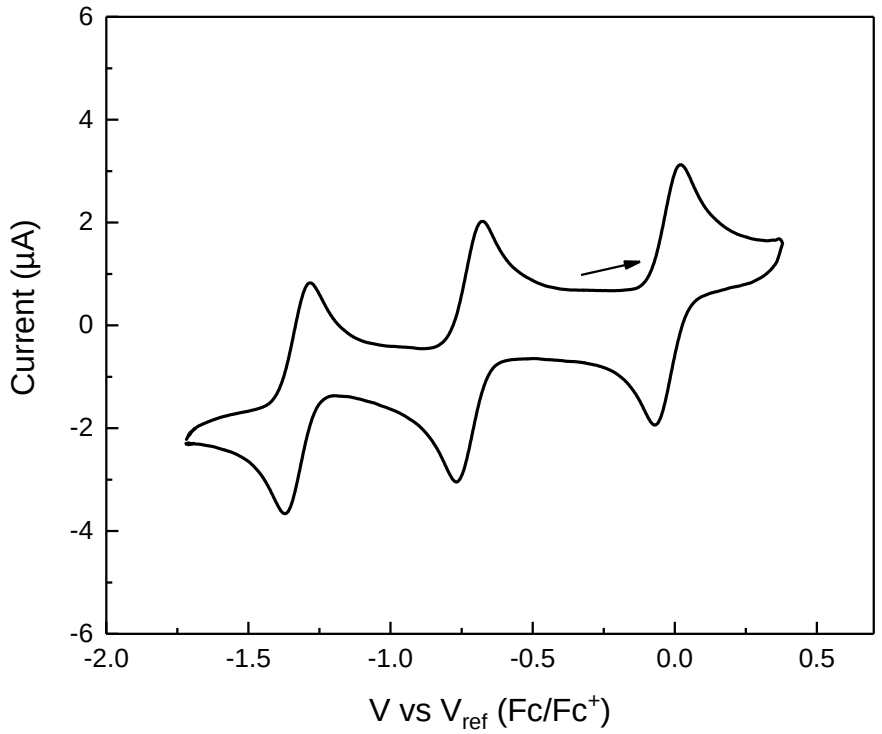

Figure 13. Cyclic voltammogram of $[Li(thf)_4][\mathbf{1}\text{-}Cu_3]$ (Tetrahydrofuran, 0.1 M $TBAPF_6$, 25 mV/s)

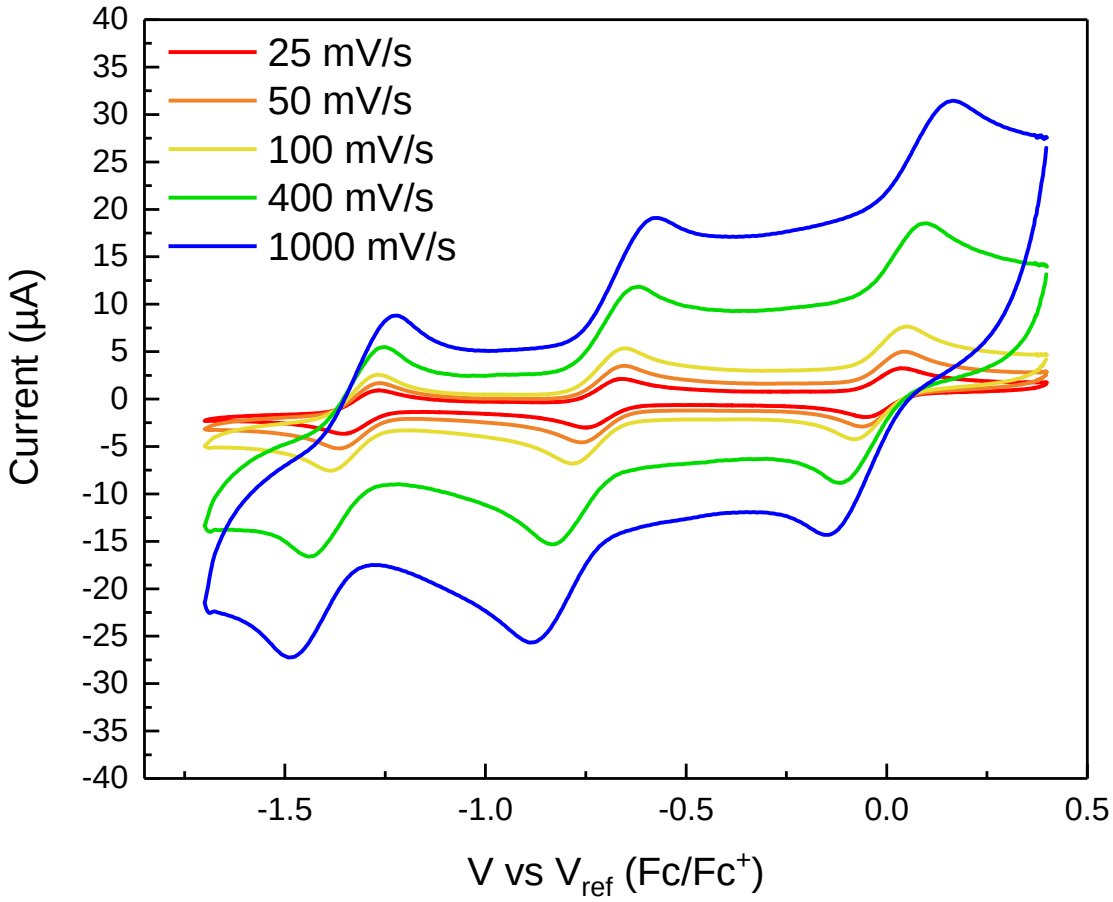

Figure 14. Scan rate dependence in the cyclic voltammetry of $[Li(thf)_4][\mathbf{1}\text{-}Cu_3]$ (Tetrahydrofuran, 0.1 M $TBAPF_6$)

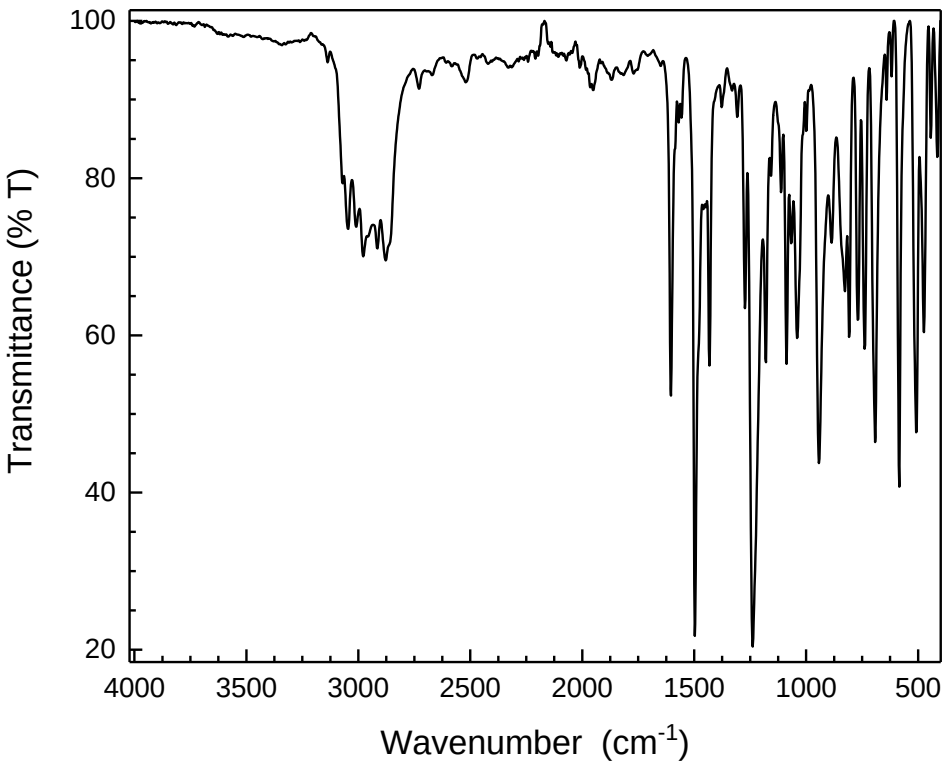

Figure 15. FT-IR spectrum of $[Li(thf)_4][\mathbf{1}\text{-}Cu_3]$

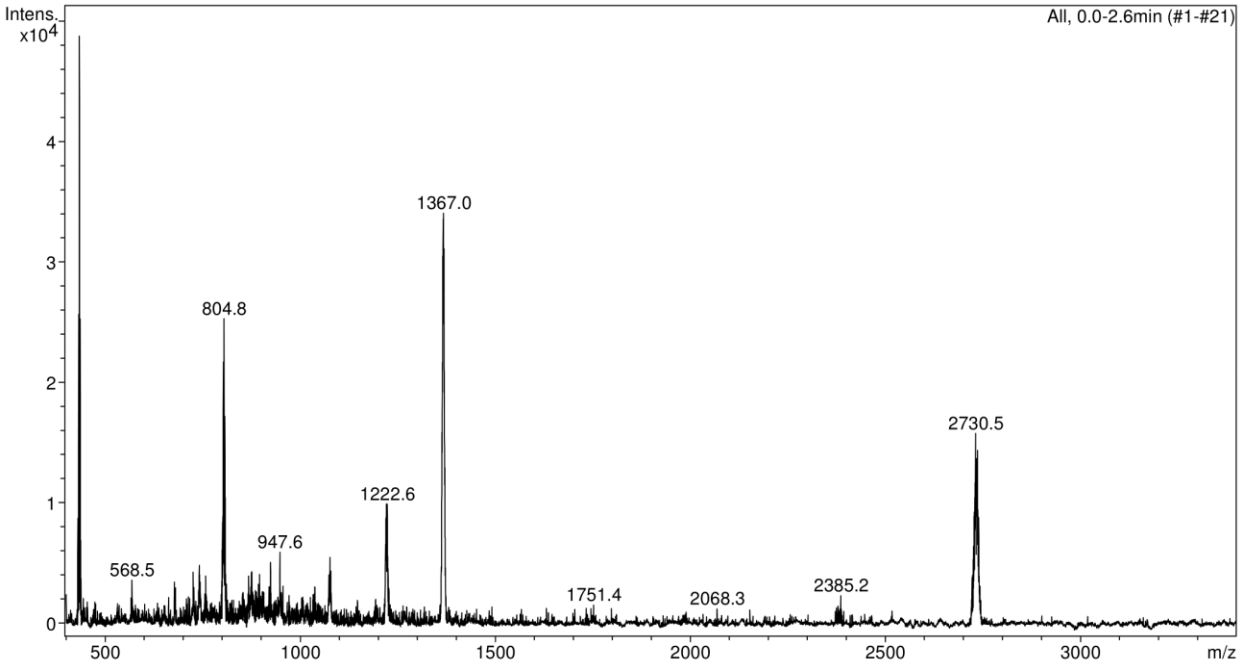

Figure 16. Mass spectrum obtained via ESI-MS of direct injection of a solution of $[Li(thf)_4][\mathbf{1}\text{-}Cu_3]$ in acetonitrile, showing fragmentation to $[Co_6Se_8(Ph_2PNHTol)_6]^{n+}$

1.5.4 *Synthesis of [Li(thf)$_4$][Cp$_2$Co][1-Cu$_3$]*

Inside the glovebox, a 100 mL round bottom flask is charged with [Li(thf)$_4$][**1**-Cu$_3$] (0.622 g, 0.19 mmol) and a Teflon-coated stirbar. Tetrahydrofuran (30 mL) is added to the flask and the mixture is stirred until a homogeneous solution is formed. Cobaltocene (0.038 g, 0.20 mmol) is weighed out into a vial and dissolved in tetrahydrofuran (10 mL), and the solution is added to the flask while stirring. Within a few minutes, dark brown precipitate is seen on the inside of the flask. After stirring for 12 hours, the product is isolated via vacuum filtration over a medium-pore frit and washed with diethyl ether (50 mL). After removing volatiles under vacuum, the product is obtained as a black, spectroscopically pure powder (0.360 g, 0.106 mmol, 55%). ^{1}H NMR (acetonitrile-d_3, 500 MHz) δ: 8.12-8.06 (m, 18H, -Ph), 7.62 (s, 6H, -Ph), 7.18 (s, 12H, -Ph), 6.91 (s, 12H), 6.79 (s, 12H, -Ph), 6.21 (s, 12H, -C$_6$*H*$_4$-p-Me), 6.12 (s, 12H, -C$_6$*H*$_4$-p-Me), 5.63 (s, Cp), 1.78 (s, 18H,-Me). ^{31}P NMR (acetonitrile-d_3, 283 MHz) δ: -522.6 ($\nu_{1/2}$=3600 Hz). ^{7}Li NMR (acetonitrile-d_3, 194 MHz) δ: -2.47 ($\nu_{1/2}$=10 Hz). μ_{eff} (Evans Method, CD$_3$CN, 298 K): 1.65 μ_B. UV-Vis (acetonitrile): λ_{max} (ε) 392 nm (50,000 M^{-1}cm^{-1}). Elemental Analysis (ICP-MS): Experimental (Calculated for C$_{140}$H$_{144}$Co$_7$Cu$_3$LiN$_6$O$_4$P$_6$Se$_8$) Co 10.31 (12.12) Se 18.70 (18.57) P 5.36 (5.46).

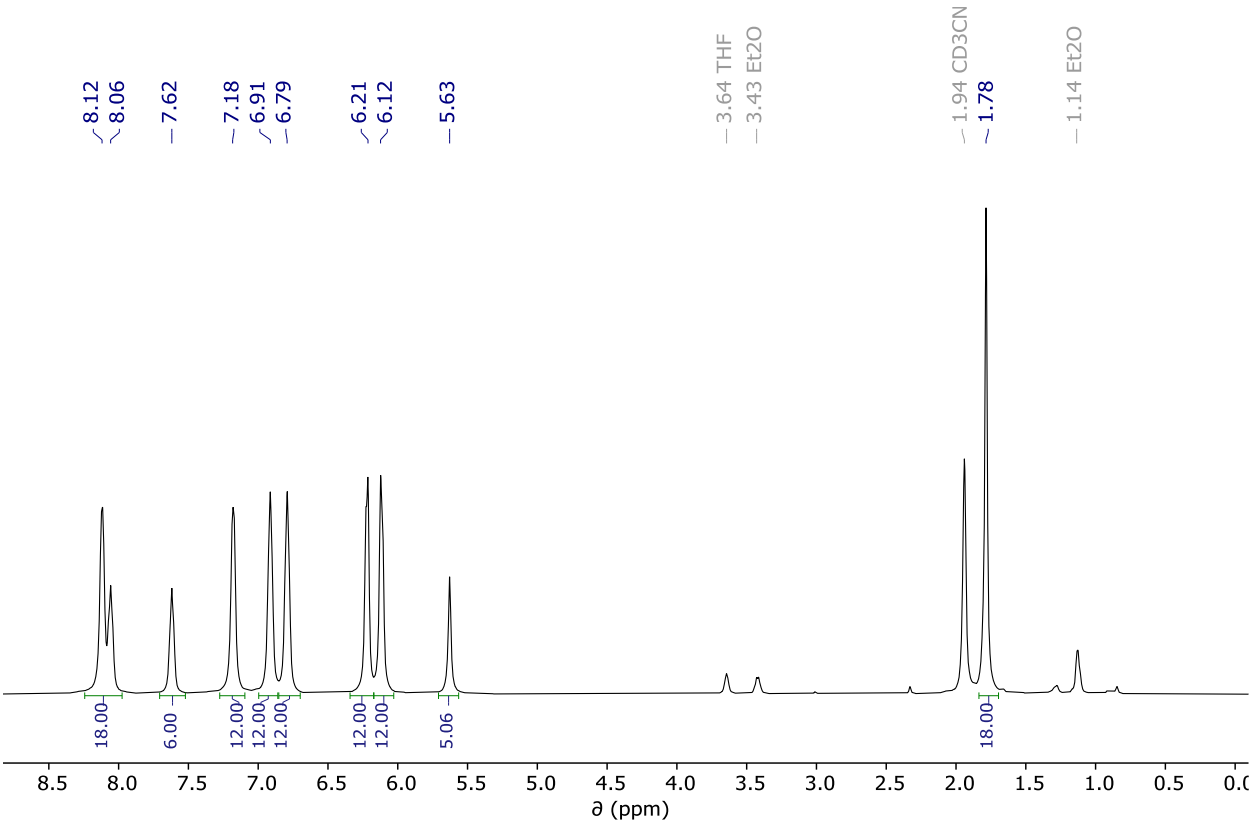

Figure 17. ^{1}H NMR (CD_3CN, 25 °C, 500 MHz) spectrum of $[Li(thf)_4][Cp_2Co][\mathbf{1}\text{-}Cu_3]$

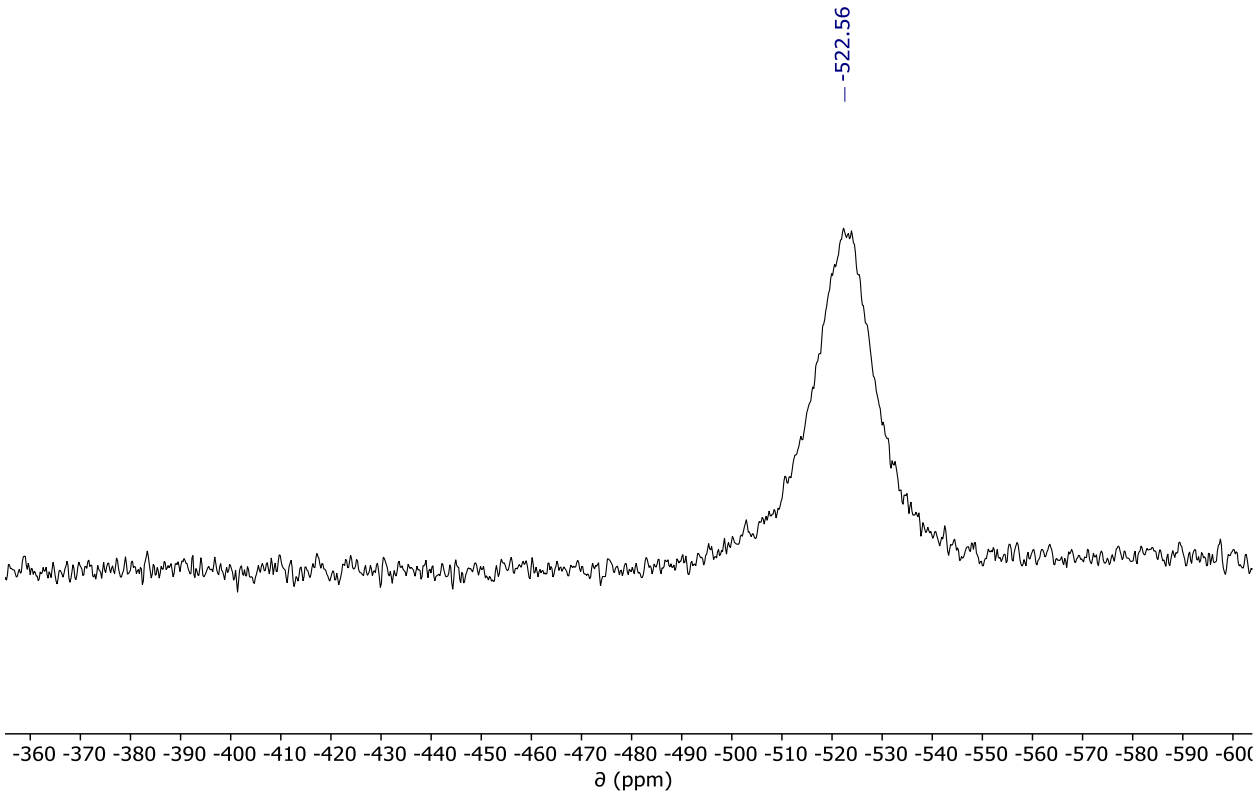

Figure 18. $^{31}P\{^{1}H\}$NMR (CD_3CN, 25 °C, 202 MHz) spectrum of $[Li(thf)_4][Cp_2Co][\mathbf{1}\text{-}Cu_3]$

1.5.5 *Synthesis of $[Li(CH_3CN)_4][Cp^*_2Co]_2[1\text{-}Cu_3]$*

Inside the glovebox, $[Li(thf)_4][\mathbf{1}\text{-}Cu_3]$ (0.350 g, 0.11 mmol) is weighed out into a vial with Teflon-coated stirbar and dissolved in acetonitrile (10 mL). Decamethylcobaltocene (0.072 g, 0.22 mmol) is weighed out into a separate vial and added directly to the flask, resulting in color change of the solution to dark red brown. After stirring for 12 hours, the solution is concentrated to half the initial volume and mixed with diethyl ether (30 mL). The resulting precipitate is isolated by vacuum filtration over a medium-pore frit and washed with diethyl ether (30 mL). After removing volatiles under vacuum, the product is obtained as a black powder (0.162 g, 0.042 mmol, 39%). The product is unstable towards halogenated solvents such as dichloromethane. ^{1}H NMR (acetonitrile-d_3, 500 MHz) δ: 7.55-7.04 (m 66H), 6.33 (s, 24H), 1.72 (s, 60H, Cp*). ^{31}P NMR (acetonitrile-d_3, 283 MHz) δ: 86.2 ($\nu_{1/2}$ = 850 Hz). UV-Vis (THF): λ_{max} (ε) 373 nm (48,000 $M^{-1}cm^{-1}$). Experimental (Calculated for $C_{170}H_{194}Co_8Cu_3LiN_6O_4P_6Se_8$) Co 10.19 (12.18) Se 16.43 (16.32) P 4.74 (4.80).

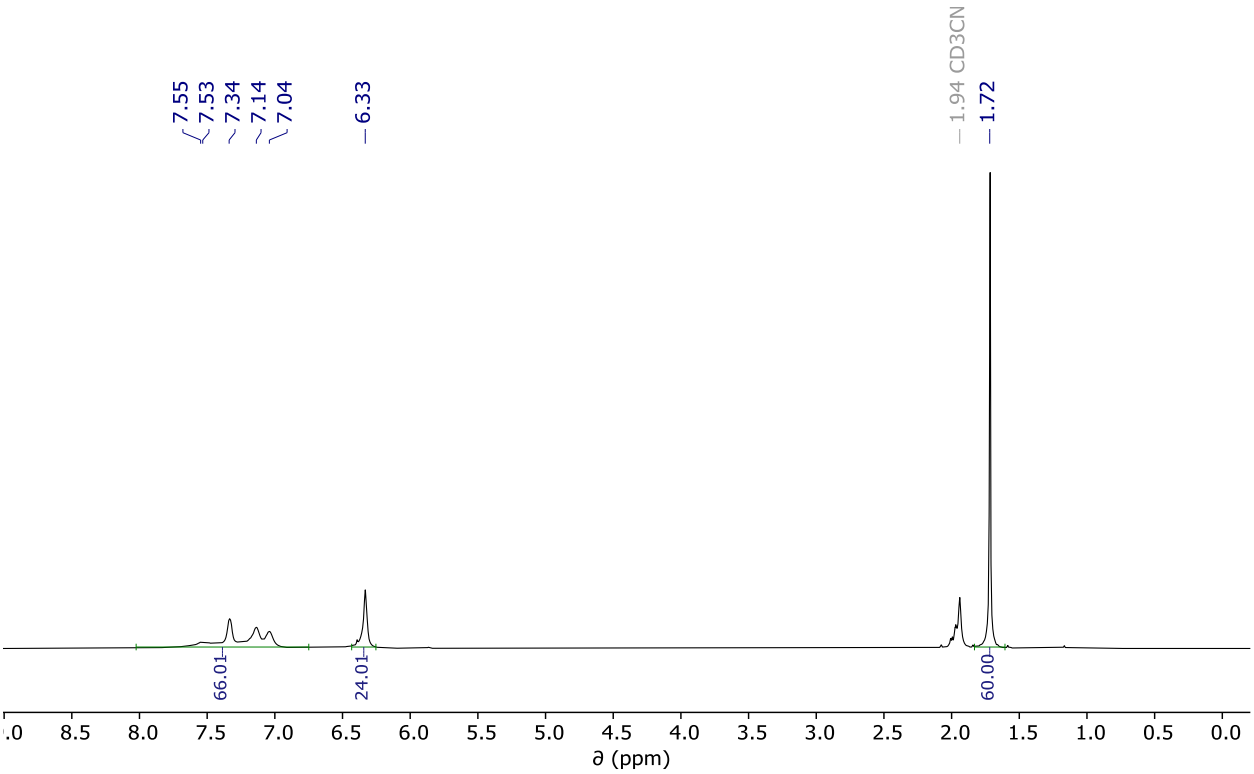

Figure 19. ^{1}H NMR (CD_3CN, 25 °C, 500 MHz) spectrum of $[Li(CH_3CN)_4][Cp^*_2Co]_2[$**1**-$Cu_3]$

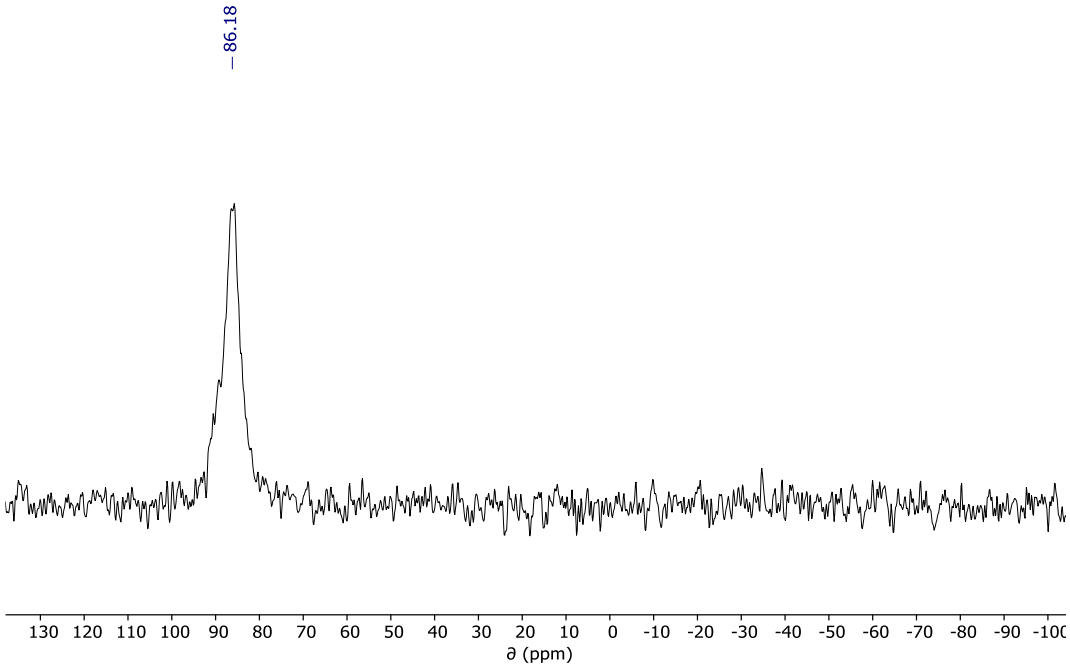

Figure 20. ^{31}P{^{1}H}NMR (CD_3CN, 25 °C, 202 MHz) spectrum of $[Li(CH_3CN)_4][Cp^*_2Co]_2[$**1**-$Cu_3]$

1.5.6 *Synthesis of 1-Cu_3*

Inside the glovebox, [Li(thf)$_4$][**1**-Cu_3] (1.500 g, 0.47 mmol) is weighed out into a 100 mL Schlenk flask and dissolved in dichloromethane (35 mL). Tris(4-bromophenyl)ammoniumyl hexachloroantimonate (0.400 g, 0.49 mmol) is weighed out into a vial and dissolved in tetrahydrofuran (10 mL). The solution is then added to the reaction mixture, which is left to stir at room temperature for 1 hour. The reaction mixture is then concentrated to dryness under vacuum, redissolved in dichloromethane, and concentrated to dryness again to remove residual tetrahydrofuran. After dissolving the residue in dichloromethane once again, the solution is filtered through Celite and the solvent removed from the filtrate under vacuum. The residue is redissolved in tetrahydrofuran, layered with diethyl ether, and left to sit at room temperature overnight. The next day, the resulting precipitate is isolated via vacuum filtration through a medium pore frit (0.596 g, 0.204 mmol, 44%). ^{1}H NMR (dichloromethane-d_2, 500 MHz) δ: 9.23 (d, 12H, -Ph), 9.02 (t, 6H, -Ph), 7.78 (t, 6H, -Ph), 7.18 (d, 12H, -Ph), 6.81 (d, 24H -Ph), 5.96 (d, 12H -C_6H_4-p-Me), 5.35, (t, 12H, -Ph), 2.64 (s, 18H, -Me). ^{31}P NMR (dichloromethane-d_2, 283 MHz) δ: -1159.92 ($\nu_{1/2}$= 1200 Hz). ^{13}C NMR (dichloromethane-d_2, 126 MHz) δ: 135.30, 133.93, 133.06, 132.32, 131.98, 130.69, 129.23, 126.38, 123.14, 121.42, 112.19, 19.38. μ_{eff} (Evans Method, CD_2Cl_2, 298 K): 1.68 μ_B. UV-Vis (THF): λ_{max} (ε) 390 nm (38,000 $M^{-1}cm^{-1}$). Elemental Analysis (ICP-MS): Experimental (Calculated for $C_{114}H_{102}Co_6Cu_3N_6P_6Se_8$) Co 12.47 (12.11) Se 21.25 (21.65) P 6.27 (6.37).

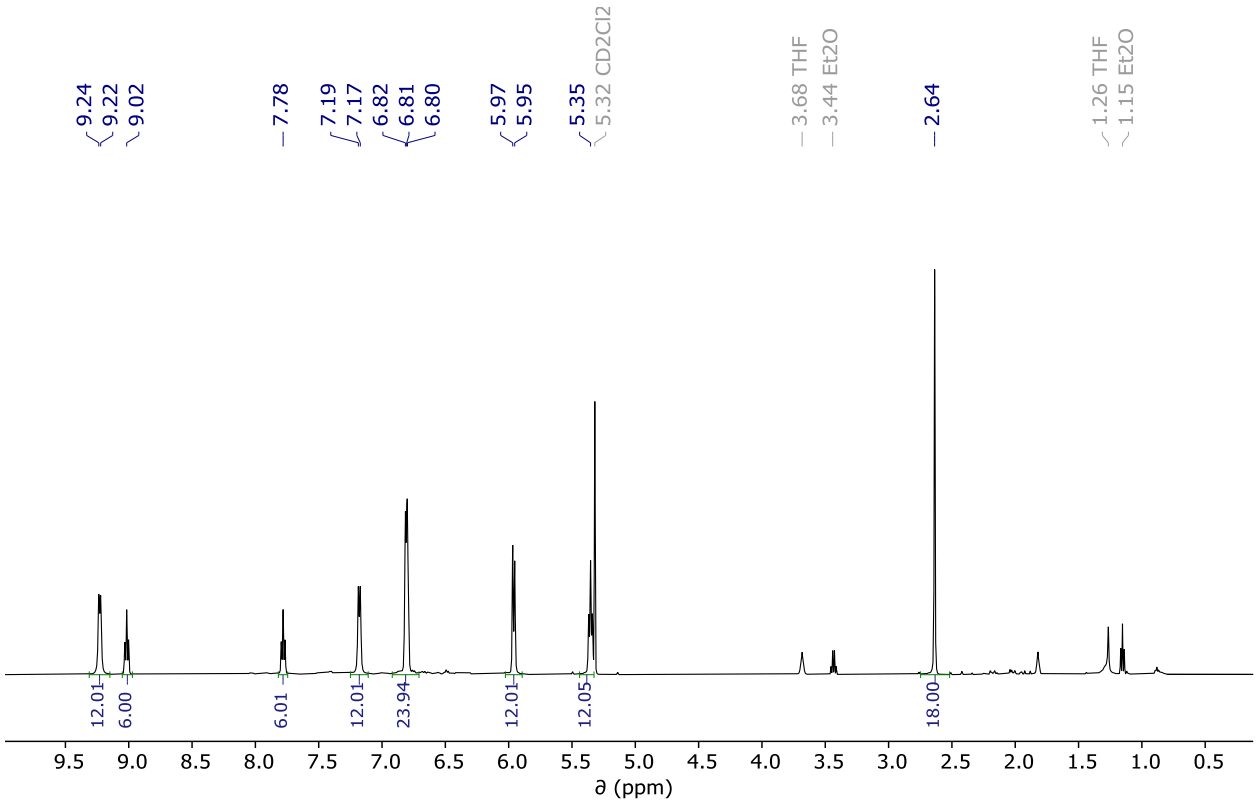

Figure 21. ^{1}H NMR (CD_2Cl_2, 25 °C, 500 MHz) spectrum of **1**-Cu_3

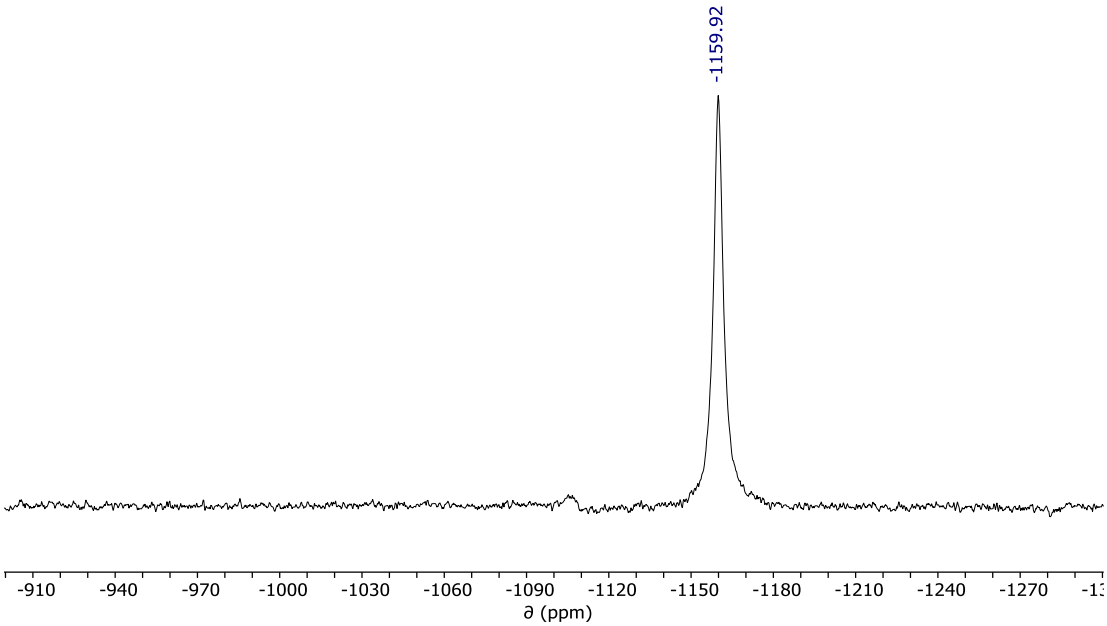

Figure 22. ^{31}P{^{1}H}NMR (CD_2Cl_2, 25 °C, 283 MHz) spectrum of **1**-Cu_3

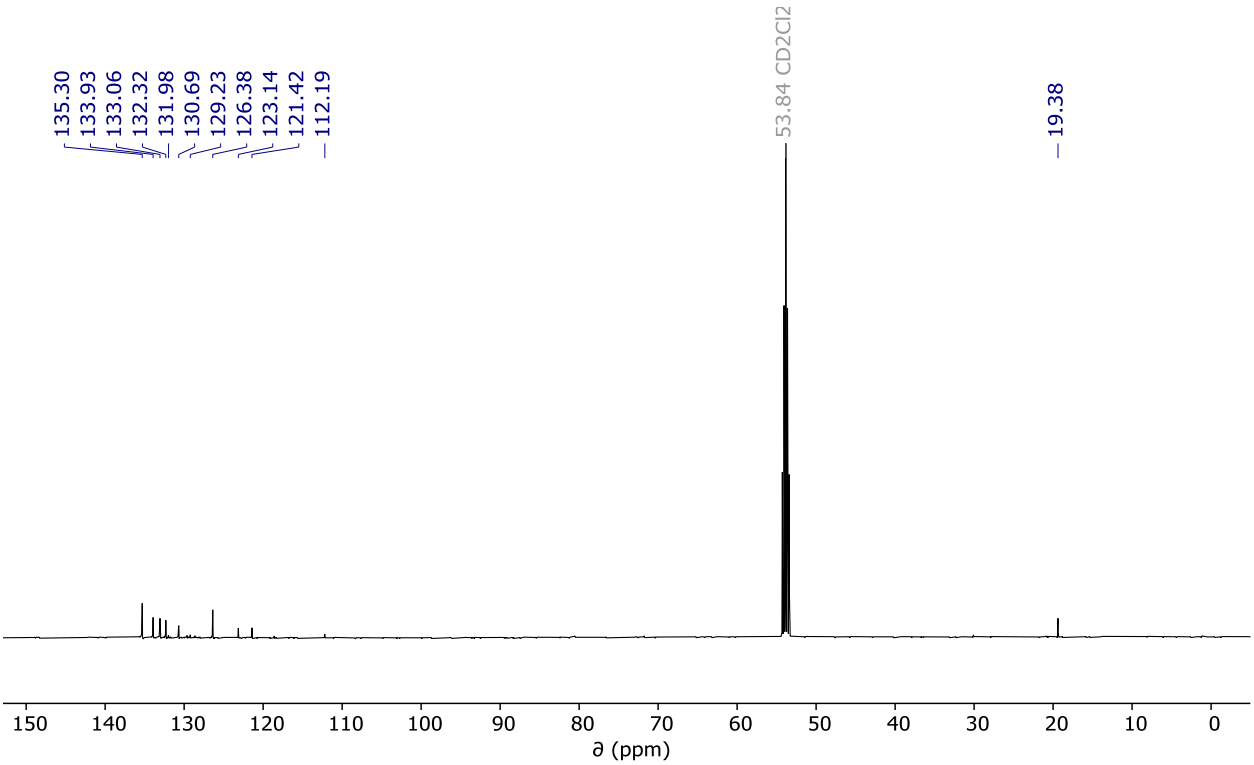

Figure 23. $^{13}C\{^{1}H\}$NMR (CD_2Cl_2, 25 °C, 126 MHz) spectrum of **1**-Cu_3

1.5.7 *Synthesis of [Li(thf)$_4$]$_2$[1-Cu$_3$]*

Inside the glovebox, a 100 mL Schlenk flask with Teflon-coated stirbar was charged with **1**-$Li_6(py)_6$ (2.440 g, 0.75 mmol) and copper(I) bromide dimethylsulfide (0.480 g, 2.33 mmol). Toluene (70 mL) and tetrahydrofuran (25 mL) are added to the flask, resulting in a dark brown solution upon mixing. After stirring the reaction mixture at 25 °C for 16 hours, the resulting slurry is filtered through a medium pore frit, and the solids on the frit are washed with toluene (20 mL), diethyl ether (50 mL), and pentane (50 mL). After collecting the solids and removing residual volatiles under vacuum, the product is obtained as a fine brown powder (1.660 g, 0.516 mmol, 64%). The spectroscopic data matches that of the product synthesized by one-electron reduction of [Li(thf)$_4$][**1**-Cu_3] (see S1.2). Elemental Analysis (ICP-MS): Experimental (Calculated for $C_{146}H_{166}Co_6Cu_3Li_2N_6O_8P_6Se_8$) Co 10.39 (10.07) Se 17.70 (18.00) P 5.05 (5.30).

1.5.8 *Synthesis of [TBA][1-Cu$_3$]*

Inside the glovebox, a 100 mL Schlenk flask with Teflon-coated stirbar was charged with [Li(thf)$_4$][**1**-Cu_3] (1.500 g, 0.47 mmol) and tetrabutylammonium chloride (0.143 g, 0.51 mmol).

Dichloromethane (25 mL) was added to the flask, and the reaction was stirred at room temperature for 1 hour to afford a dark brown solution. The solvent was removed from the reaction mixture under vacuum, and the residue redissolved in dichloromethane (15 mL). This step was repeated once more, and the solution filtered through a medium-pore frit filled with Celite. After removing the solvent from the filtrate, the residue was dissolved in tetrahydrofuran (15 mL). After layering the solution with pentane (40 mL) and leaving the mixture to sit overnight, the dark brown microcrystalline material precipitates from the solution. The product is isolated via vacuum filtration through a medium pore frit, and after washing with diethyl ether (20 mL) and pentane (20 mL), the compound is obtained as dark brown crystals (1.203 g, 0.381 mmol, 82%). ^{1}H NMR (dichloromethane-d_2, 500 MHz) δ: 8.69 (t, J = 7.4 Hz, 6H), 8.37 (d, J = 7.3 Hz, 12H), 7.31 (t, J = 7.3 Hz, 6H), 6.97 (t, J = 7.4 Hz, 12H), 6.73 (dd, J = 7.8, 5.3 Hz, 24H), 6.62 (d, J = 7.9 Hz, 12H), 5.05 (t, J = 7.5 Hz, 12H), 3.31 – 3.01 (m, 9H), 2.04 (s, 18H), 1.61 (dq, J = 11.9, 7.7 Hz, 9H), 1.46 (h, J = 7.3 Hz, 9H), 1.06 (t, J = 7.3 Hz, 12H). ^{31}P NMR (acetonitrile-d_3, 283 MHz) δ: -1071.2 ($\nu_{1/2}$ = 1000 Hz). ^{13}C NMR (dichloromethane-d_2, 126 MHz) δ: 134.06, 132.30, 131.36, 131.07, 127.73, 124.88, 124.64, 123.75, 121.23, 119.72, 59.52, 24.30, 20.77, 20.16, 13.77. Elemental Analysis (ICP-MS): Experimental (Calculated for $C_{130}H_{138}Co_6Cu_3N_7P_6Se_8$) Co 11.47 (11.17) Se 19.90 (19.96) P 5.69 (5.87).

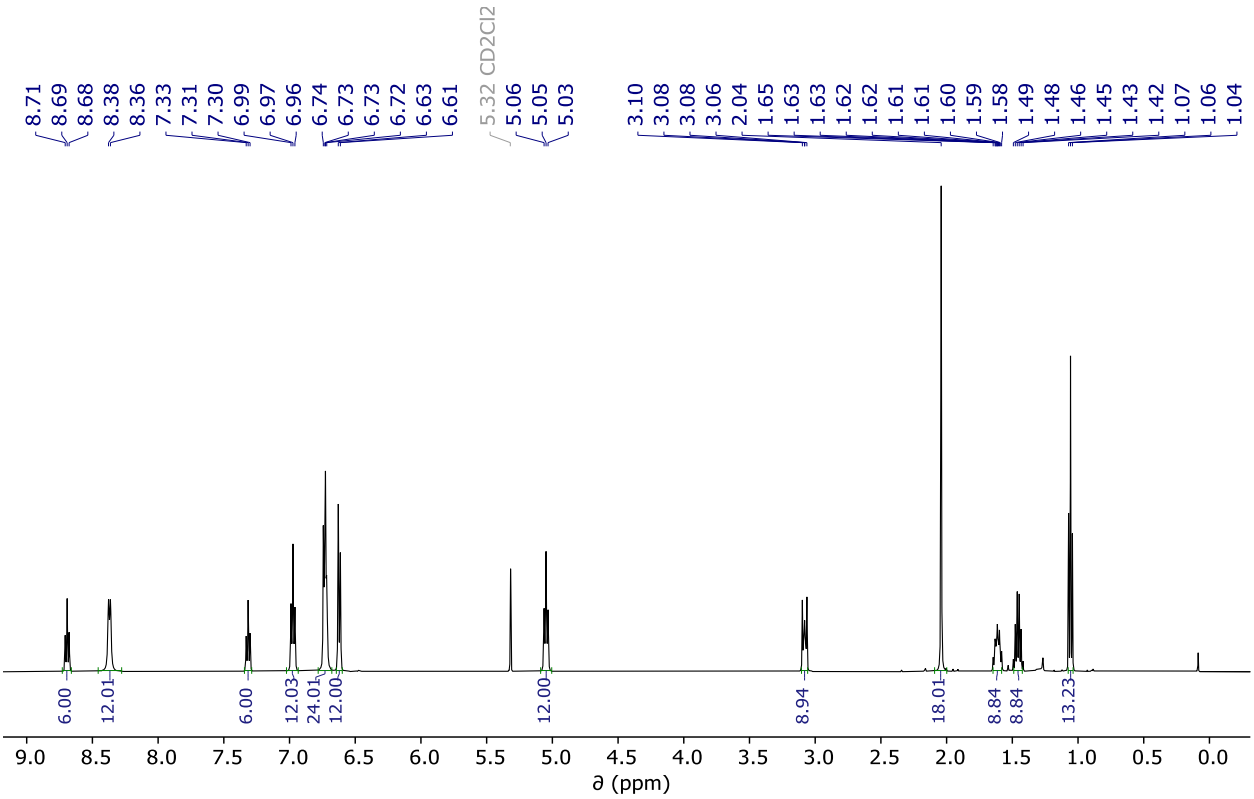

Figure 24. ^{1}H NMR (CD_2Cl_2, 25 °C, 500 MHz) spectrum of [TBA][**1**-Cu_3]

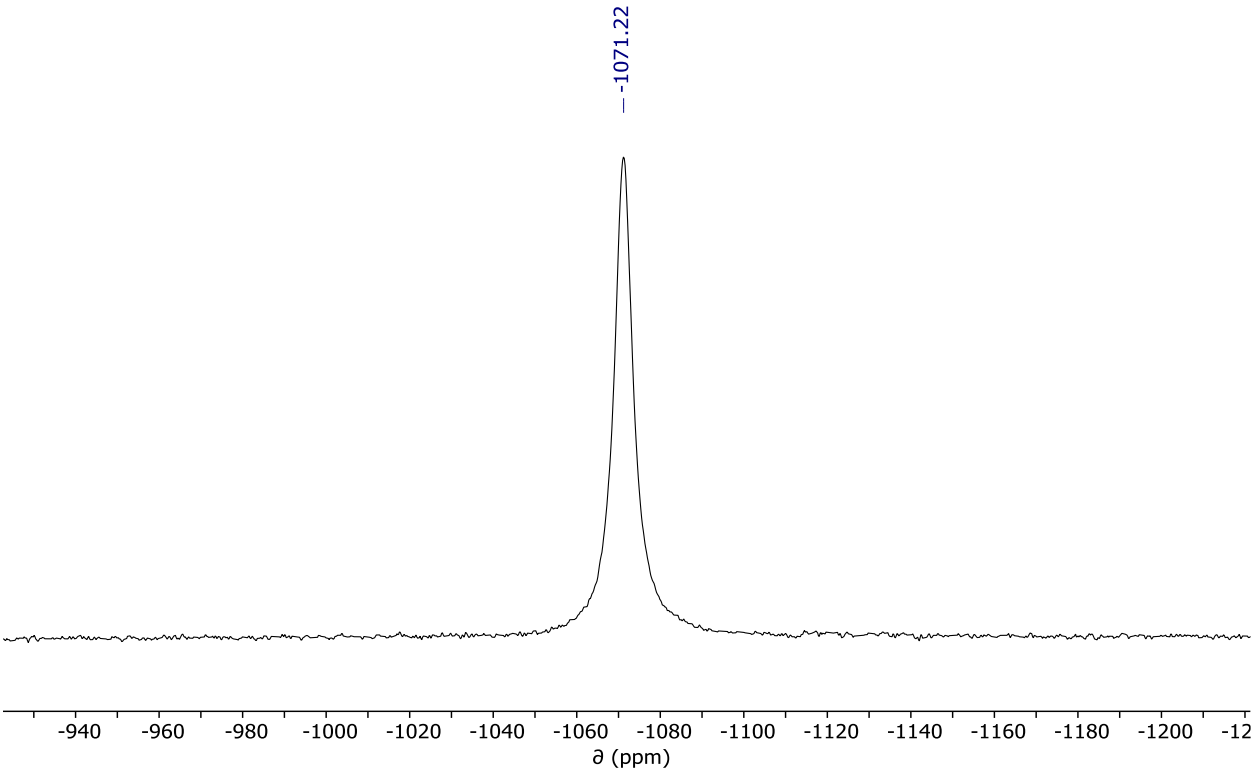

Figure 25. $^{31}P\{^{1}H\}$NMR (CD_2Cl_2, 25 °C, 283 MHz) spectrum of [TBA][**1**-Cu_3]

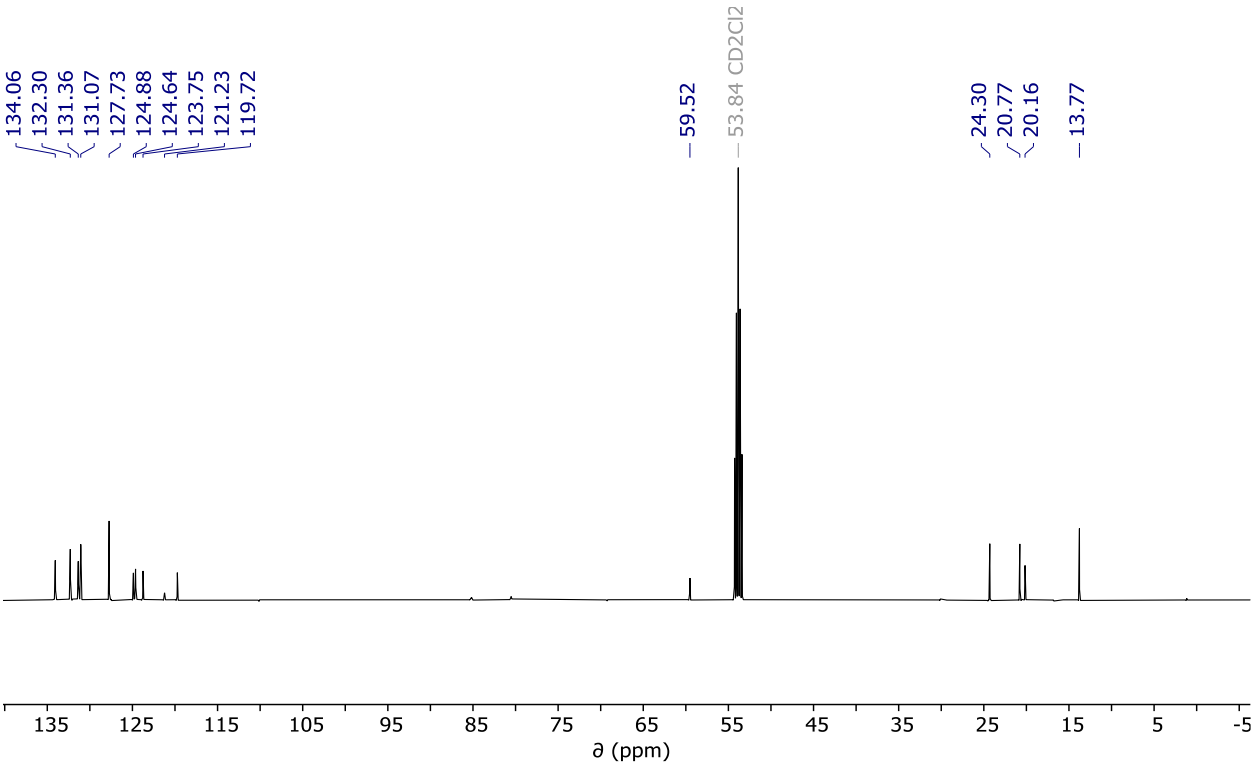

Figure 26. $^{13}C\{^{1}H\}$NMR (CD_2Cl_2, 25 °C, 126 MHz) spectrum of [TBA][**1**-Cu_3]

1.5.9 *Synthesis of [Ru(bpy)$_3$][1-Cu$_3$]*

Inside the glovebox, $[Li(THF)_4]_2$[**1**-Cu_3] (0.511 g, 0.146 mmol) and $Ru(bpy)_3I_2$ (0.120 g, 0.146 mmol) were dissolved in separate vials in acetonitrile (7 mL each) with stirring. The orange solution of ruthenium complex was transferred to the vial containing the cluster solution while stirring, which quickly led to the formation of a brown precipitate. After stirring vigorously for 30 minutes, the resulting slurry was filtered through a fine-pore frit, and the resulting solids on the frit washed with warm acetonitrile (10 mL) and diethyl ether (10 mL). The product is obtained as a brown powder that has poor solubility in acetonitrile but is moderately soluble in dimethyl sulfoxide and dimethylformamide (0.349 g, 0.100 mmol, 69%). ^{1}H NMR (DMSO-d_6, 500 MHz) δ: 8.82, 8.80, 8.15, 8.05, 7.70, 7.51, 7.50, 7.13, 6.87, 6.72, 6.16, 6.14, 6.09, 2.07, 1.75. ^{31}P NMR (DMSO-d_6, 25 °C, 202 MHz) -522.4 ($\nu_{1/2}$ = 1750 Hz). ^{13}C NMR (DMSO-d_6, 126 MHz) δ: 156.47, 151.10, 137.87, 133.69, 130.98, 129.87, 127.84, 127.16, 126.71, 124.62, 124.46, 122.83, 121.32, 120.42, 20.06. UV-Vis (Dimethylformamide): λ_{max} (ε) 388 nm.

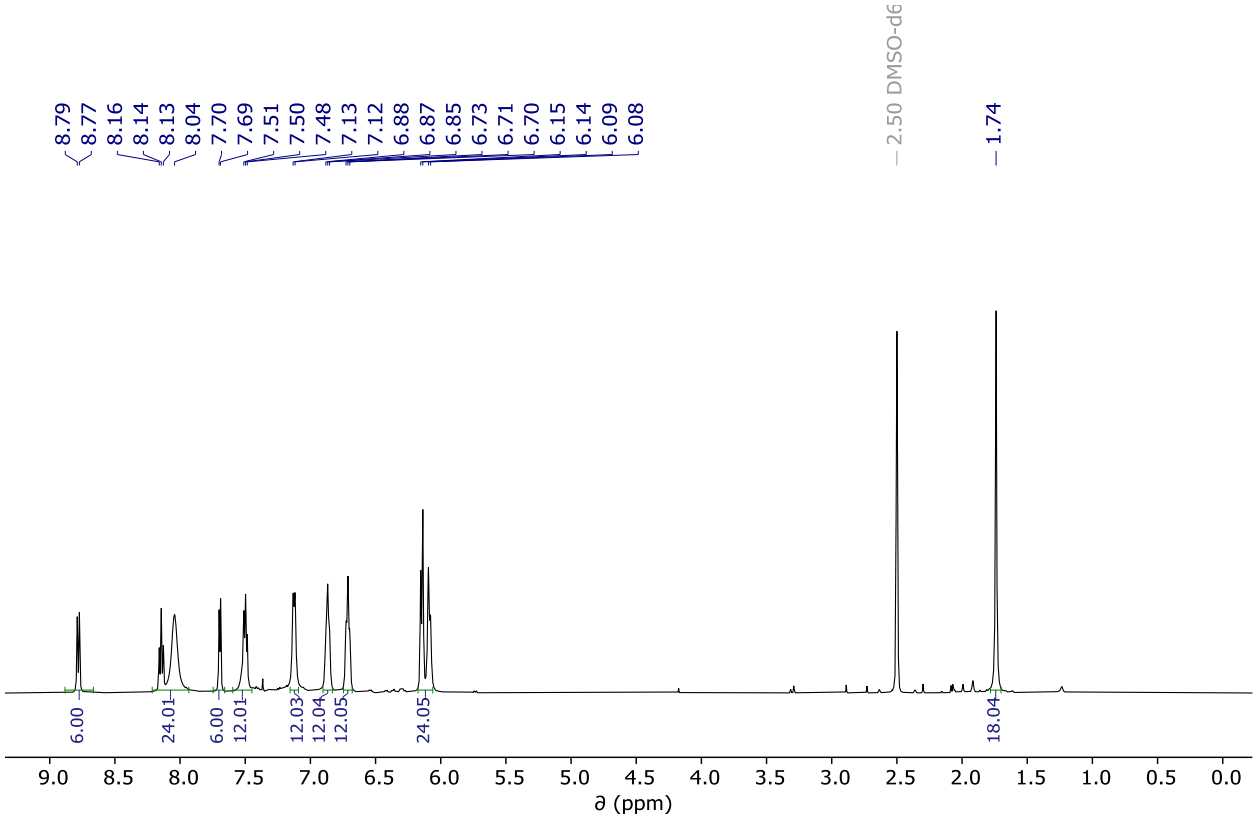

Figure 27. ^{1}H NMR (DMSO-d_6, 25 °C, 500 MHz) spectrum of [Ru(bpy)$_3$][**1**-Cu$_3$]

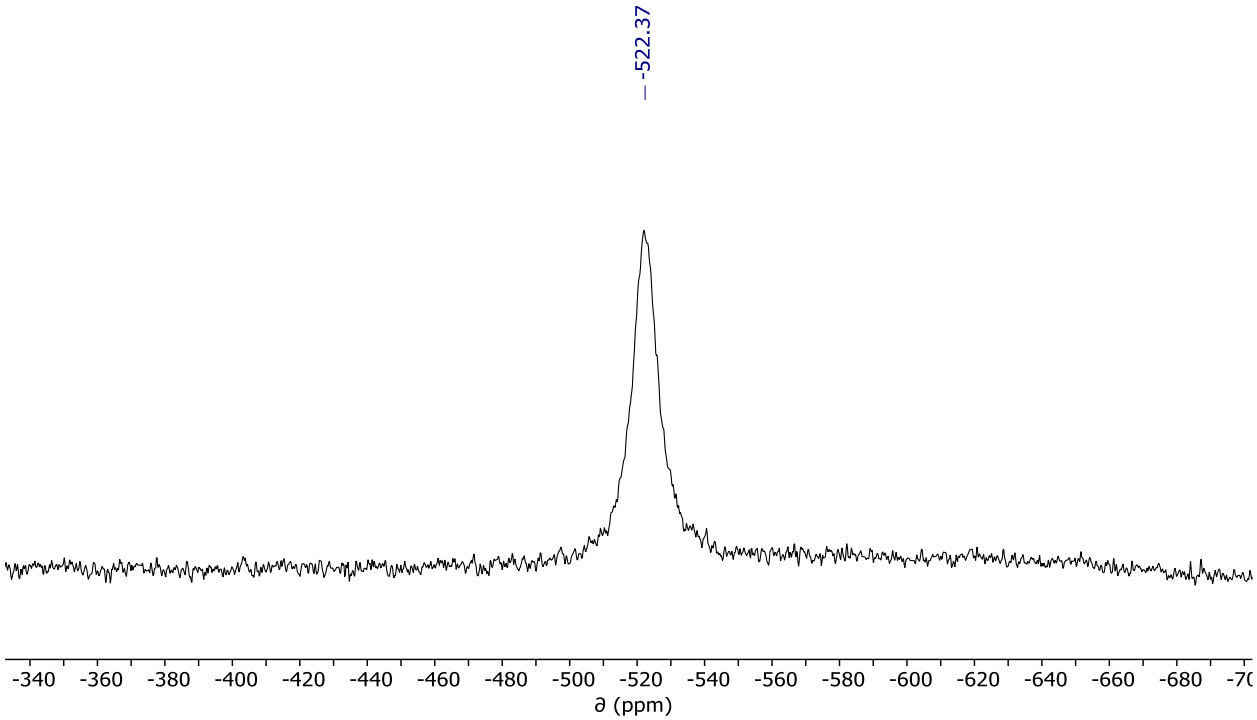

Figure 28. ^{31}P{^{1}H}NMR (DMSO-d_6, 25 °C, 202 MHz) spectrum of [Ru(bpy)$_3$][**1**-Cu$_3$]

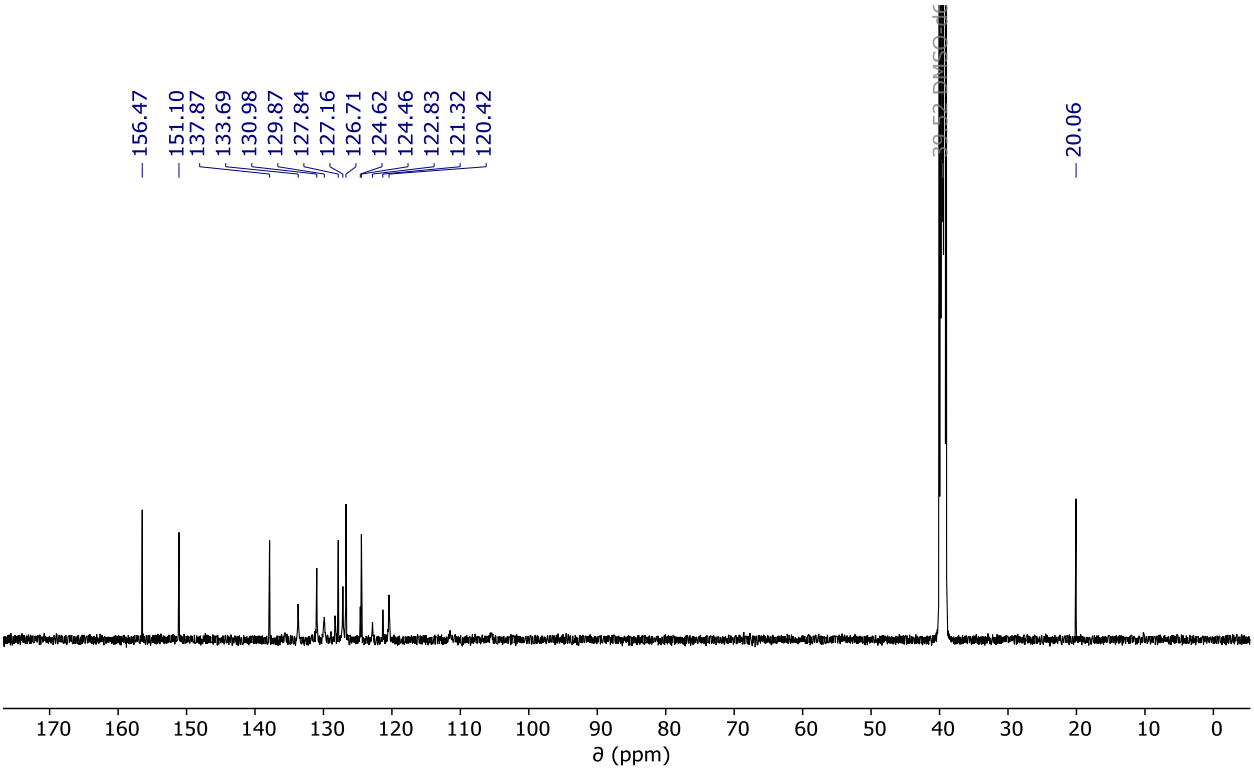

Figure 29. $^{13}C\{^{1}H\}$NMR (DMSO-d_6, 25 °C, 126 MHz) spectrum of [Ru(bpy)$_3$][**1**-Cu$_3$]

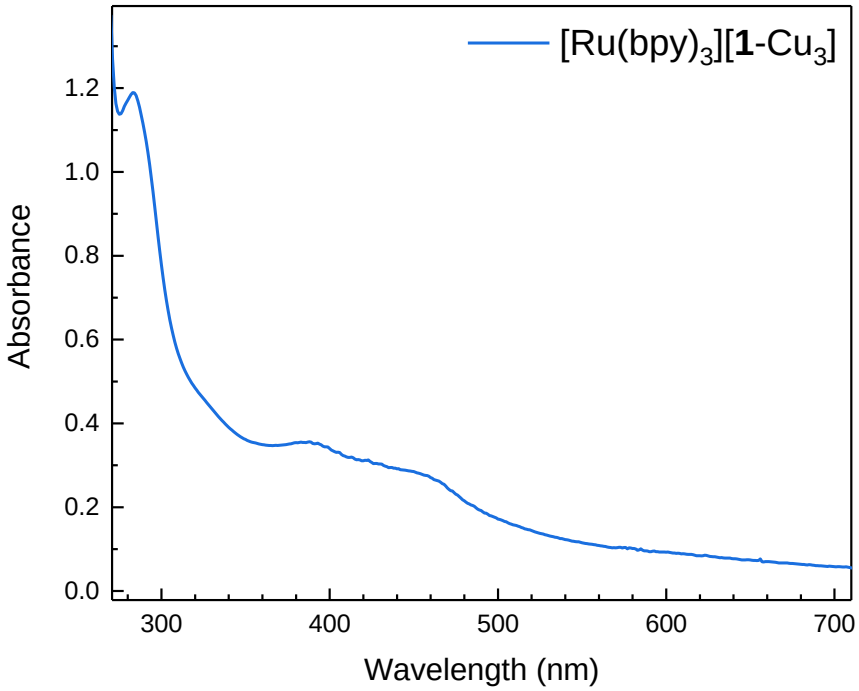

Figure 30. UV-Vis spectrum of [Ru(bpy)$_3$][**1**-Cu$_3$] in dimethylformamide

1.5.10 *Oxidation of [TBA][1-Cu_3]*

Inside the glovebox, [TBA][**1**-Cu_3] (0.100 g, 0.0316 mmol) and ferrocenium hexafluorophosphate (0.011 g, 0.0332 mmol) are weighed out into a vial with Teflon-coated stirbar. Dichloromethane (7 mL) is added to the vial, and the resulting dark brown solution is stirred at 25 °C for 1 hour. NMR analysis of the crude reaction mixture shows full conversion to **1**-Cu_3.

1.5.11 *Ligand coordination studies with [TBA][1-Cu_3]*

The general procedure for testing the possible coordination of ligands to the cluster is as follows: Inside the glovebox, [TBA][**1**-Cu_3] was dissolved in acetonitrile-d_3. To the solution was added an excess of the coordinating ligand (pyridine, tetrahydrofuran, trimethylphosphine, tert-butyl isocyanide), and the resulting mixture was homogenized. The ^{1}H NMR spectrum of the solution was measured, in all cases the data indicated no change in the spectral signature of the starting materials.

For testing the coordination of carbon monoxide to the cluster, a different procedure was used. [TBA][**1**-Cu_3] was dissolved in tetrahydrofuran in a 25 mL Schlenk flask with Teflon-coated stirbar, which was capped with a septum and attached to the Schlenk line outside the glovebox. The flask was evacuated and backfilled with carbon monoxide gas, and left to stir at room temperature under a CO atmosphere for 12 hours. The headspace of the flask was then purged for 15 minutes, and an aliquot taken for IR spectroscopic analysis. The FT-IR spectrum of a drop cast aliquot sample indicated no change from the spectrum of the starting material, and no diagnostic peaks belonging to CO were seen.

1.6 Electronic Paramagnetic Resonance Spectroscopy

EPR measurements were performed on a Bruker EMXnano EPR instrument. Samples were dissolved in toluene and cooled to 100 K during measurement. The resulting spectra were corrected for background by measuring a solvent blank and subtracting the resulting signal from the sample data. No signals could be discerned in the EPR spectra over a wide window.

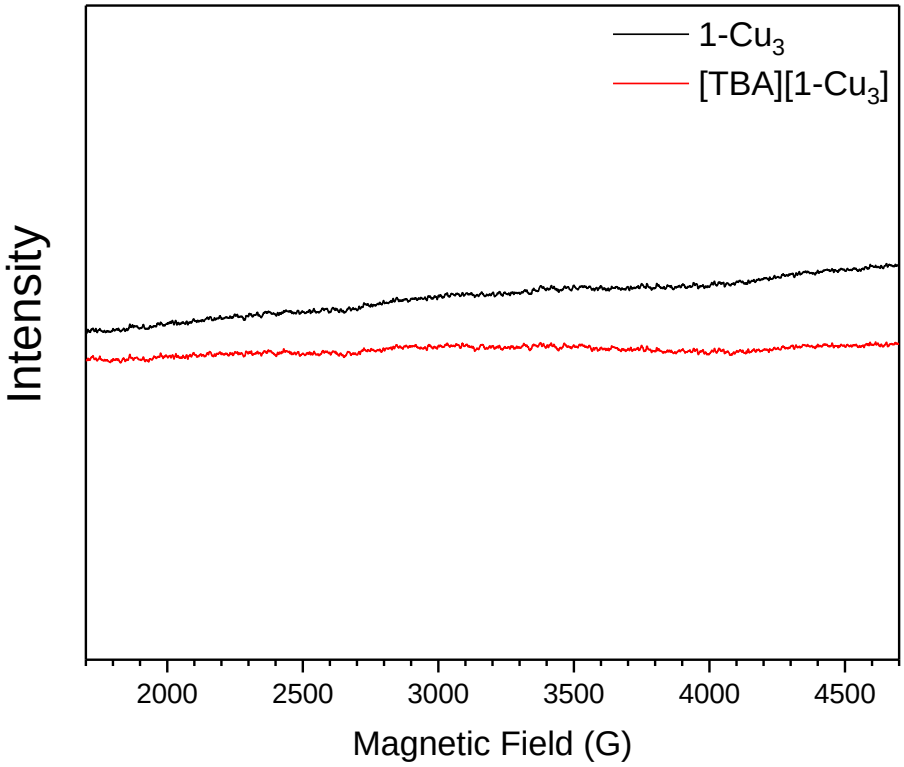

Figure 31. EPR spectra of **1**-Cu_3 and [TBA][**1**-Cu_3] in toluene at 100 K.

1.7 Paramagnetic ^{31}P NMR Studies

The observed experimental chemical shift of a paramagnetic compound is given by equation (1),[72,73]

$$\delta_T^{obs} = \delta^{dia} + \delta^{para} = \delta^{dia} + \frac{S(S+1)\beta_e}{3k_bT\gamma_N} gA + \delta^{TIP} \quad (1)$$

in which δ^{dia} and δ^{para} are the diamagnetic and paramagnetic contributions to the chemical shift respectively, δ^{TIP} is the temperature-independent paramagnetic contribution, S is total spin of the system, β_e is the Bohr magneton, k_b the Boltzmann constant, T the absolute temperature, γ_N the nuclear gyromagnetic ratio, g the g-tensor, and A the hyperfine tensor. Paramagnetic ^{31}P NMR spectra for **1**-Cu_3, [TBA][**1**-Cu_3], [Li(thf)$_4$]$_2$[**1**-Cu_3], [Li(CH_3CN)$_4$][Cp*$_2$Co]$_2$[**1**-Cu_3] were collected at 290, 300, 310, 320, and 330 K on a 500 MHz spectrometer. Additionally, spectra of [TBA][**1**-Cu_3] were measured over a larger temperature range (190-340K) to further study its paramagnetic temperature dependence. Temperatures were calibrated using a methanol standard.[74]

The observed relaxation times ($T_1 \approx$ 2-3 ms) of the paramagnetic ^{31}P NMR signals (Figures S27-29) allowed for data collection with short acquisition and delay times (10 and 50 ms, respectively). The NMR shifts were plotted as a function of 1/T and showed idealized Curie-Weiss behavior. Temperature independent NMR shifts were determined by applying linear fits to each data set and extrapolating the fit to a hypothetical infinite temperature (1/T = 0) to find the resulting value. As anticipated, the ^{31}P NMR signal of diamagnetic [**1**-Cu_3]$^{3-}$ did not exhibit a significant shift at different temperatures.

Table 1. Parameters from the linear fit of ^{31}P VT-NMR of [**1**-Cu_3]$^{n-}$

Compound	**Slope of linear fit (ppm K)**	**Temperature-independent ^{31}P NMR shift (ppm)**
1-Cu_3	-4.11 ± 0.09 * 10^5	182 ± 27
[**1**-Cu_3]$^-$	-4.25 ± 0.08 * 10^5	354 ± 25
[**1**-Cu_3]$^{2-}$	-2.12 ± 0.04 * 10^5	190 ± 13
[**1**-Cu_3]$^{3-}$	0	82.6

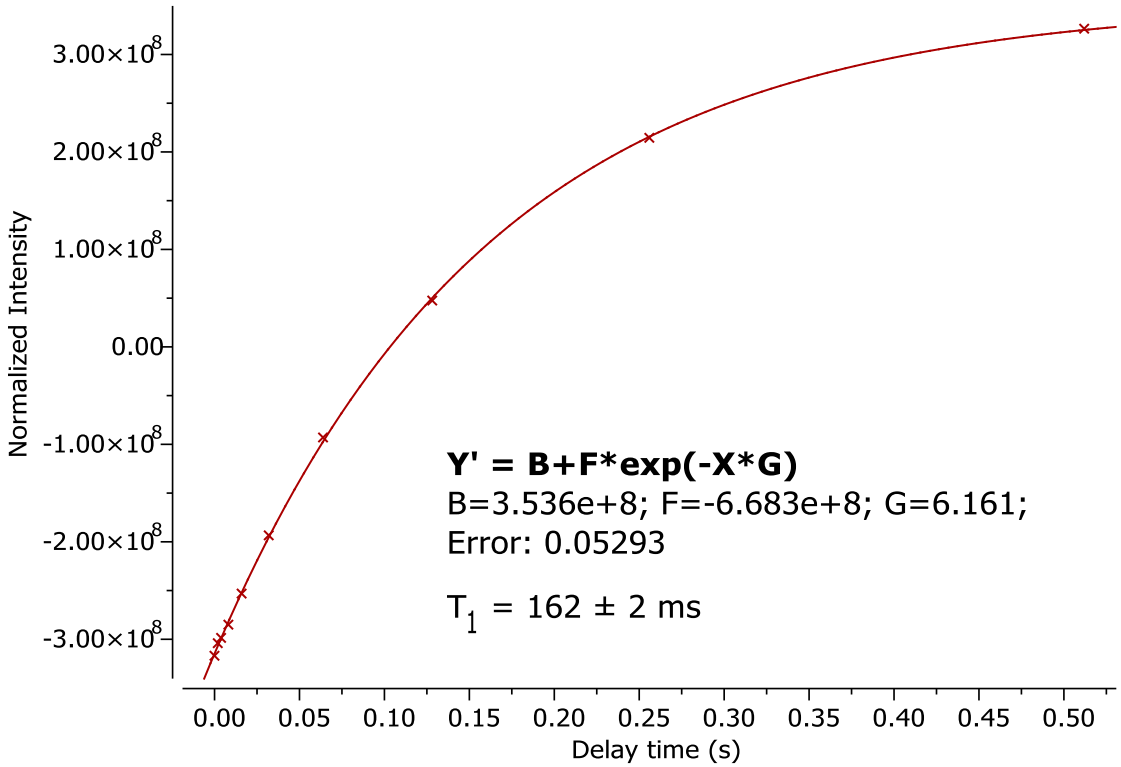

Figure 32. Results of inversion recovery experiments performed to determine the ^{31}P T_1 relaxation time of **1**-H_6 (chloroform-*d*, 25 °C, 283 MHz).

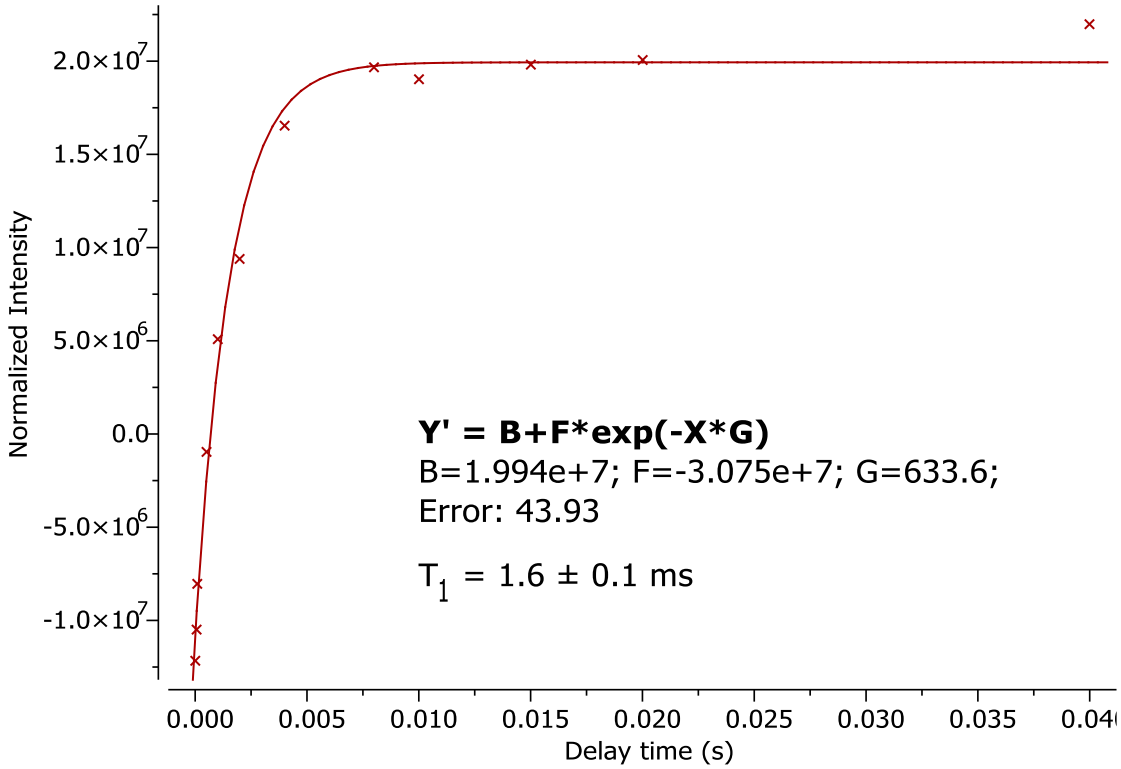

Figure 33. Results of inversion recovery experiments performed to determine the ^{31}P T_1 relaxation time of $[Li(thf)_4]_2$[**1**-Cu_3] (acetonitrile-d_3, 25 °C, 283 MHz)

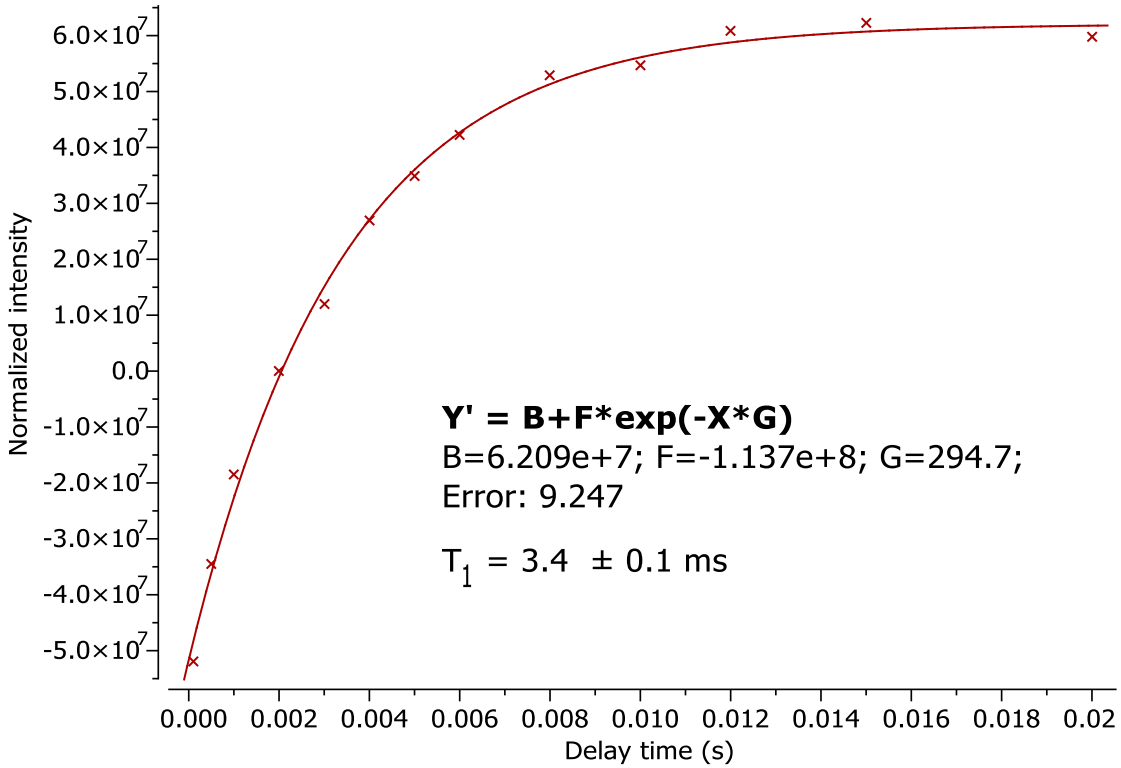

Figure 34. Results of inversion recovery experiments performed to determine the ^{31}P T_1 relaxation time of [TBA][**1**-Cu_3] (acetonitrile-d_3, 25 °C, 283 MHz)

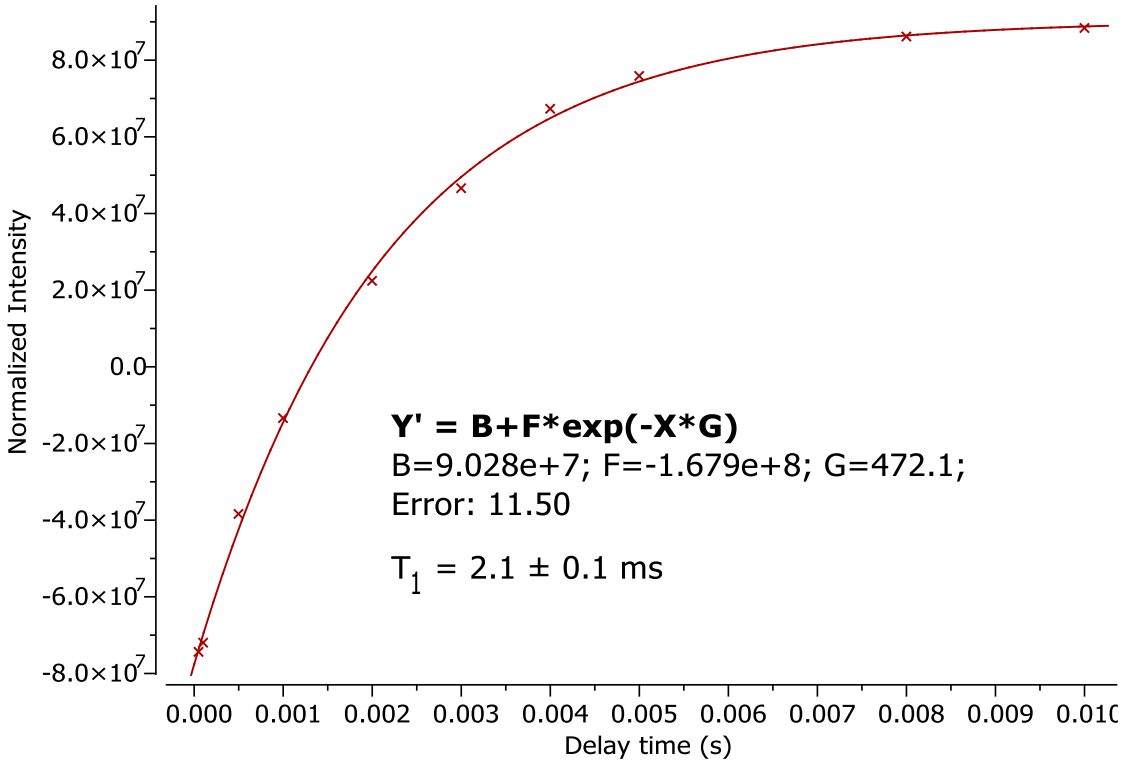

Figure 35. Results of inversion recovery experiments performed to determine the ^{31}P T_1 relaxation time of **1**-Cu_3 (dichloromethane-d_2, 25 °C, 283 MHz)

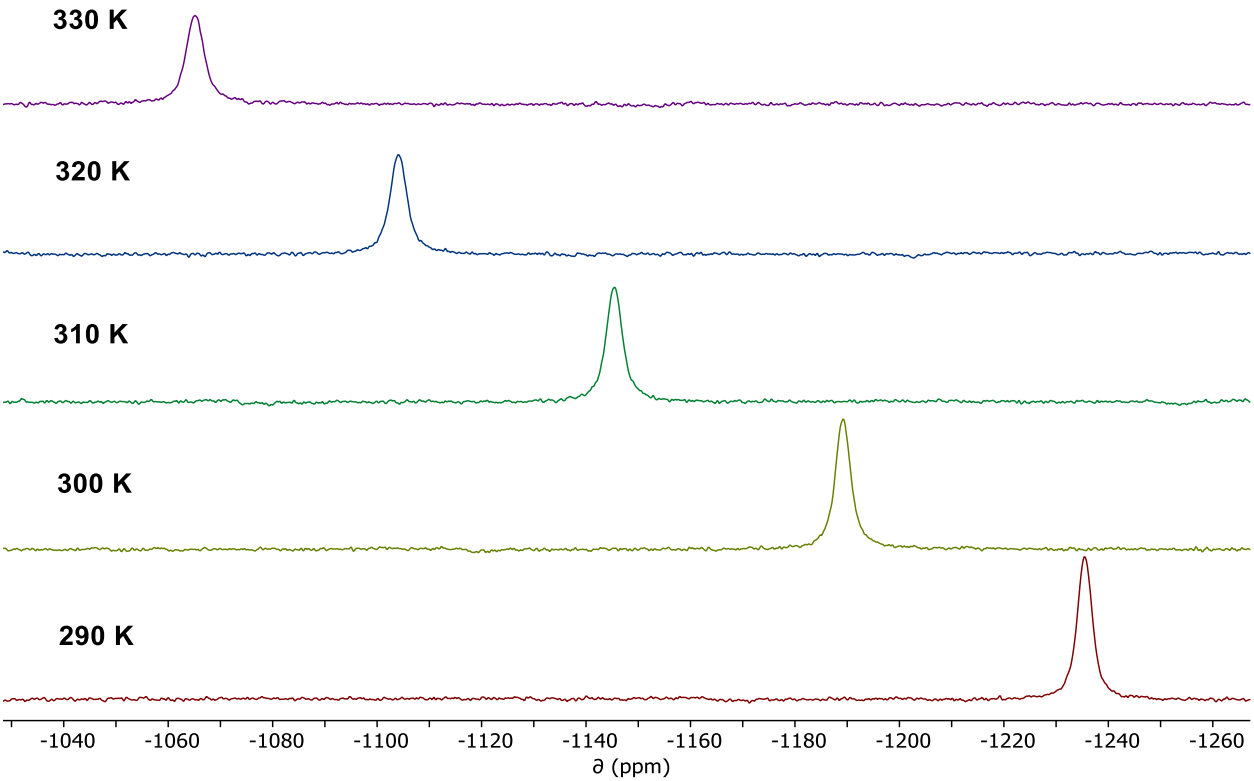

Figure 36. Variable-temperature ^{31}P NMR (Toluene, 202 MHz) spectra of **1**-Cu_3

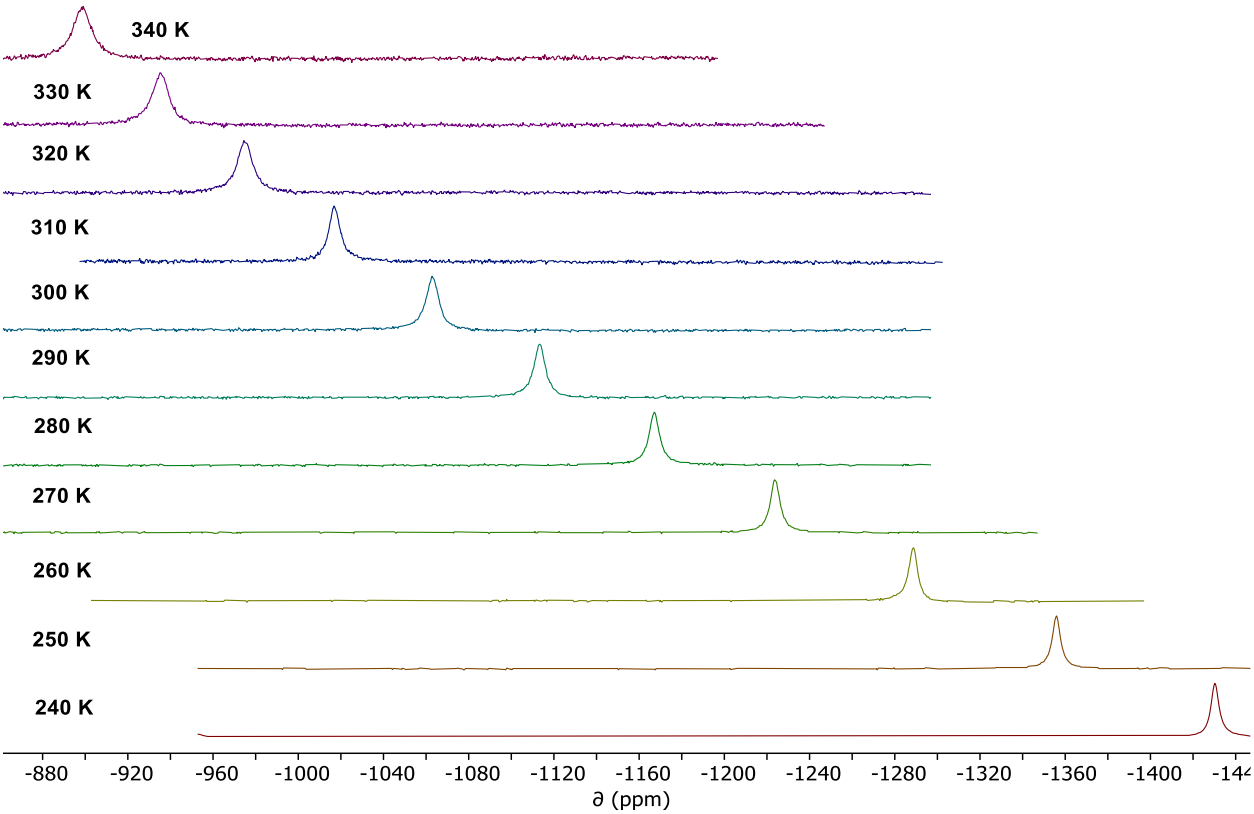

Figure 37. Variable-temperature ^{31}P NMR (acetonitrile-d_3, 202 MHz) spectra of [TBA][**1**-Cu_3]

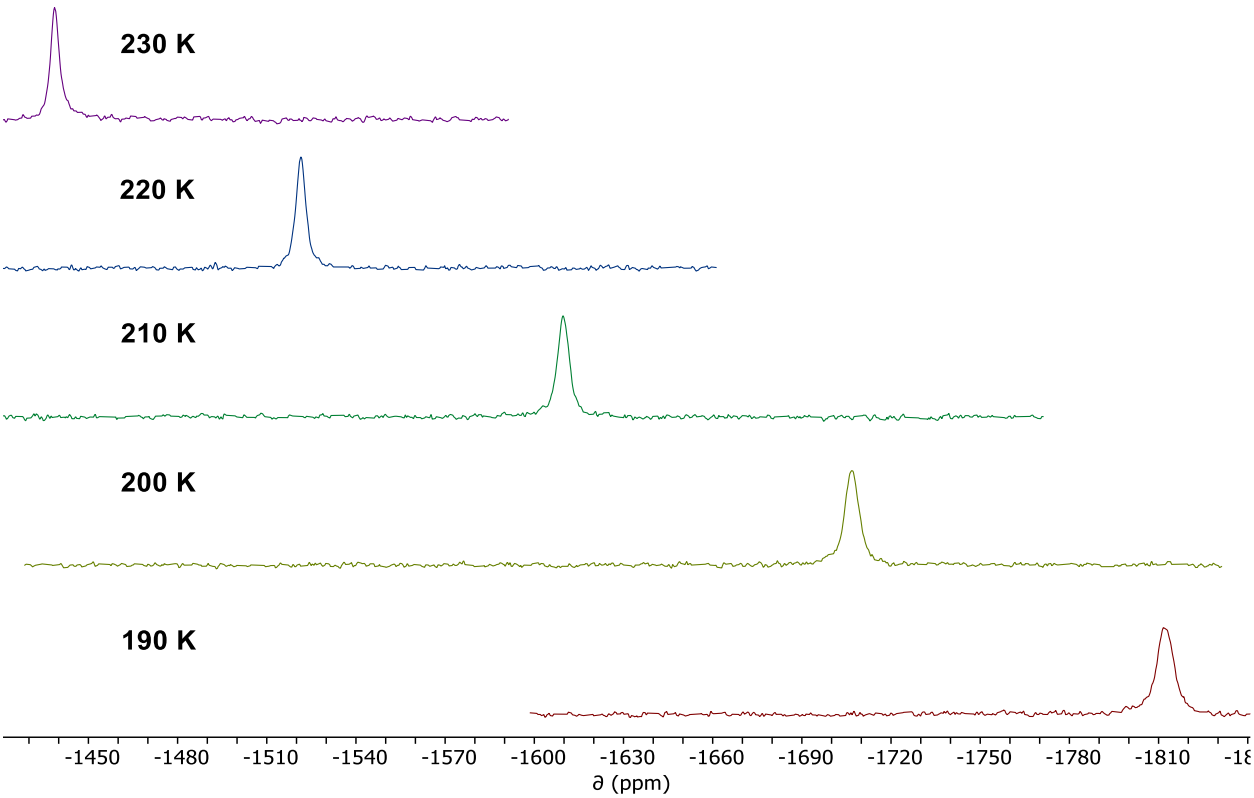

Figure 38. Variable-temperature ^{31}P NMR (THF, 202 MHz) spectra of [TBA][**1**-Cu_3]

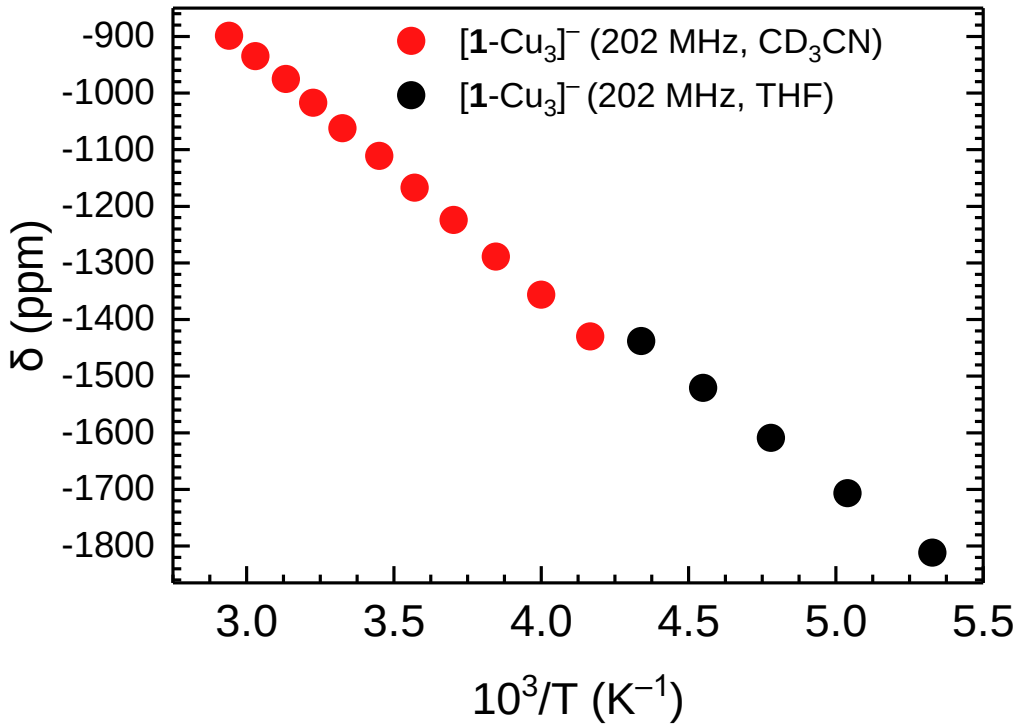

Figure 39. Plot of chemical shifts from ^{31}P VT-NMR (202 MHz, 190-340K) of [TBA][**1**-Cu_3].

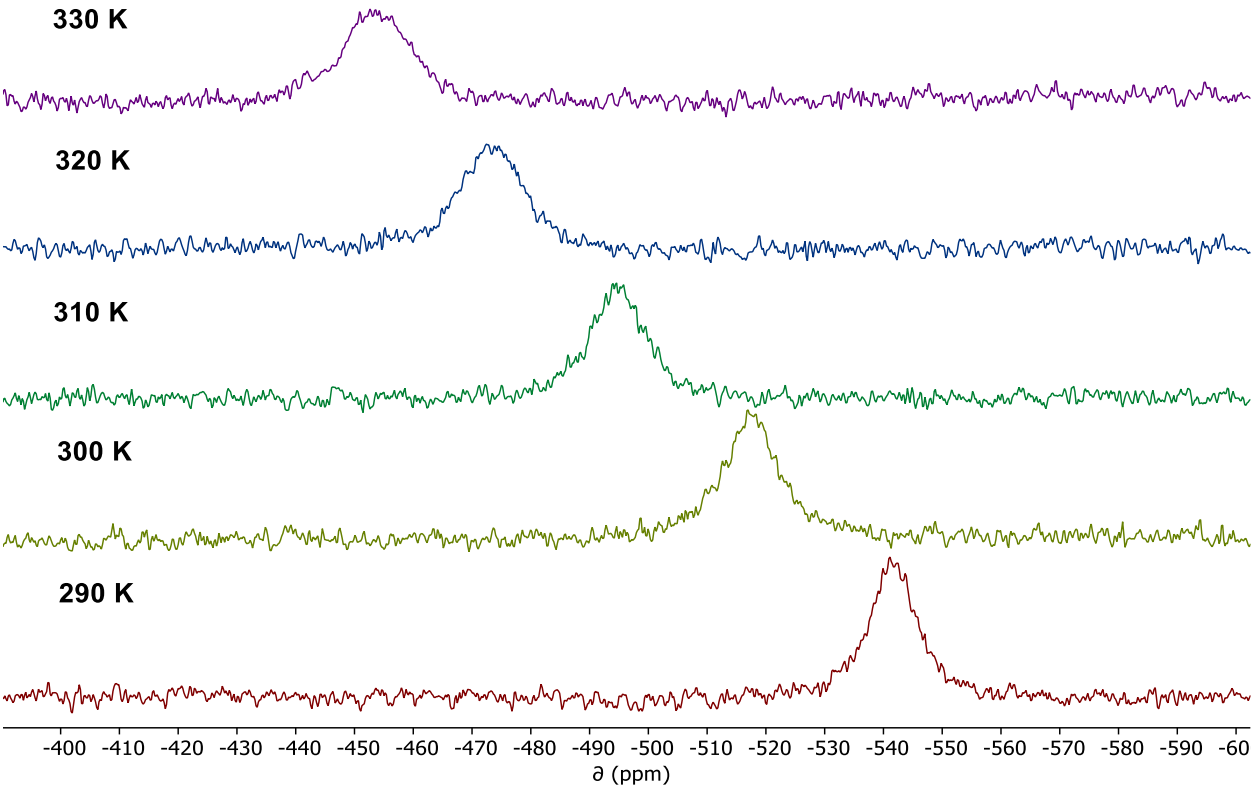

Figure 40. Variable-temperature ^{31}P NMR (acetonitrile-d_3, 202 MHz) spectra of $[Li(thf)_4]_2$[**1**-Cu_3]

1.8 Selenium X-ray Absorption Studies

Solid samples were shipped to the beamline in sealed vials, then prepared in an argon glovebox at Stanford Synchrotron Radiation Lightsource (SSRL). The samples were diluted to 1% Se by mass with BN (~2 mg analyte/50 mg BN) and were ground to a fine powder using a mortar and pestle inside the glovebox. BN was dried at >250 °C under vacuum (~1 × 10^{-3} Torr) for 24 h prior to use. The complexes were characterized by Se K-edge X-ray measurements. The X-ray absorption measurements were made at SSRL, under dedicated operating conditions (3.0 GeV, 5%, 500 mA using continuous top-off injections) on end station 7-3. With the use of a liquid-nitrogen-cooled double-crystal Si(220) (φ = 90) monochromator that employed collimating and focusing mirrors, a single energy was selected from the incident white beam. The beam was fully tuned 1 keV above the edge energy. Solid-state samples were loaded into a 1/64" thick aluminum plate with a 3 × 15 mm^2 oval window and screw holes. One side of the plate was covered with 0.5 mil Kapton tape, and the sample was evenly loaded in the window. The sample window was then

sealed with a second piece of 0.5 mil Kapton tape. The plate was fastened into the sample holder, removed from the glovebox, and immediately submerged in LN_2, then transported to the beamline (SSRL 7-3). At the beamline, the sample holder was attached to the sample rod while submerged in LN_2, then immediately inserted into the cryostat (Oxford Instruments) at 45° with respect to the beam against a flow of He gas. The sample chamber was cycled with vacuum and He gas 3 times, then the valve was closed and the measurements were performed in the cryostat under a He atmosphere at 10 K.

The horizontal beam slit sizes were 10 mm, and vertical slit sizes were 1 mm in all measurements. The cryostat was attached to beamline, which was equipped with three ionization chambers, through which nitrogen gas was continually flowed. One chamber was positioned before the helium beam pass and the cryostat to monitor the incident radiation (I0). The second chamber was positioned after the cryostat so that sample transmission (I1) could be evaluated against I0 and so that the absorption coefficient (μ) could be calculated as ln(I0/I1). The third chamber (I2) was positioned downstream from I1 so that the XANES of a calibration foil could be measured against I1. A PIPS detector under argon was placed on one side of the cryostat to detect the fluorescence from the samples. The energy was calibrated *in situ* to the energy of the first inflection point of the K-edge of Se^0 foil (12.658 keV). The end station is equipped with a beam shutter in which the sample is not exposed to the beam as the monochromator energy is tuned. Transmission data were acquired in triplicate and averaged. Background subtraction and normalization were performed in Athena.[75] The spectra were fitted using least-squares curve fitting as implemented in the LMFIT software package in python.[76] The edge jump was modeled using a step-like function, which was held constant across all spectra. Peaks were modeled using pseudo-Voigt functions, in which the Gaussian-Lorentzian fraction was fixed at 0.5.

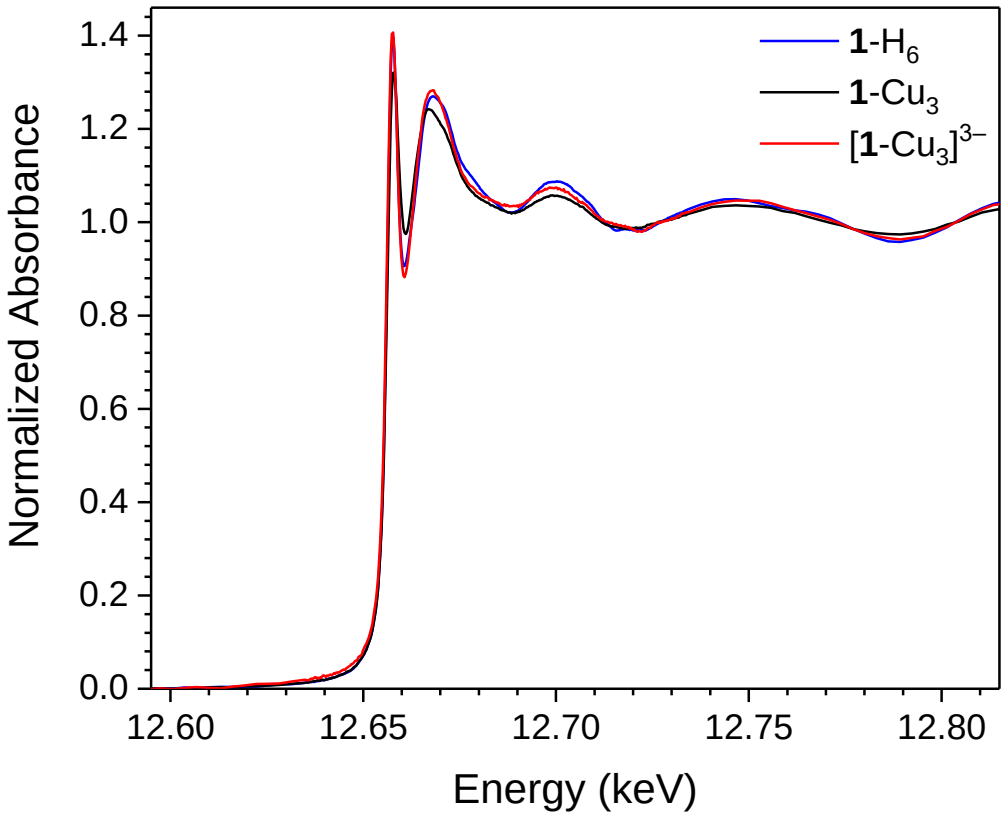

Figure 41. Overlaid selenium X-ray absorption spectra of selected cluster compounds

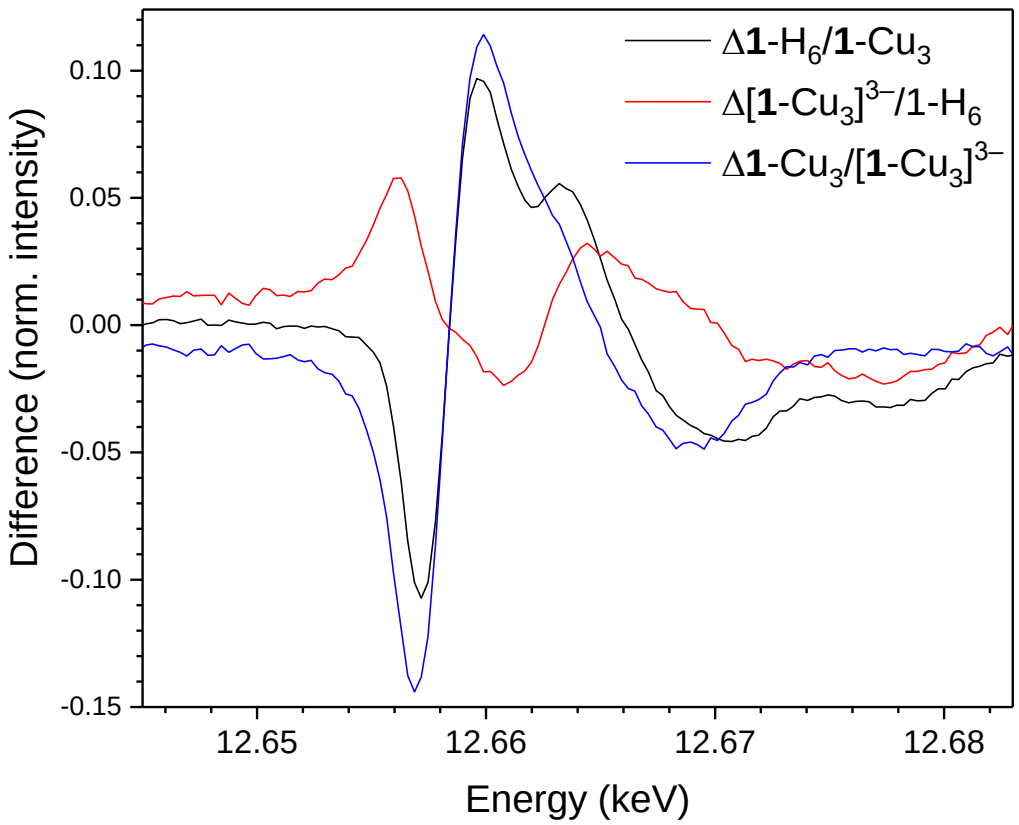

Figure 42. Difference plot of selenium X-ray absorption spectra of selected cluster compounds

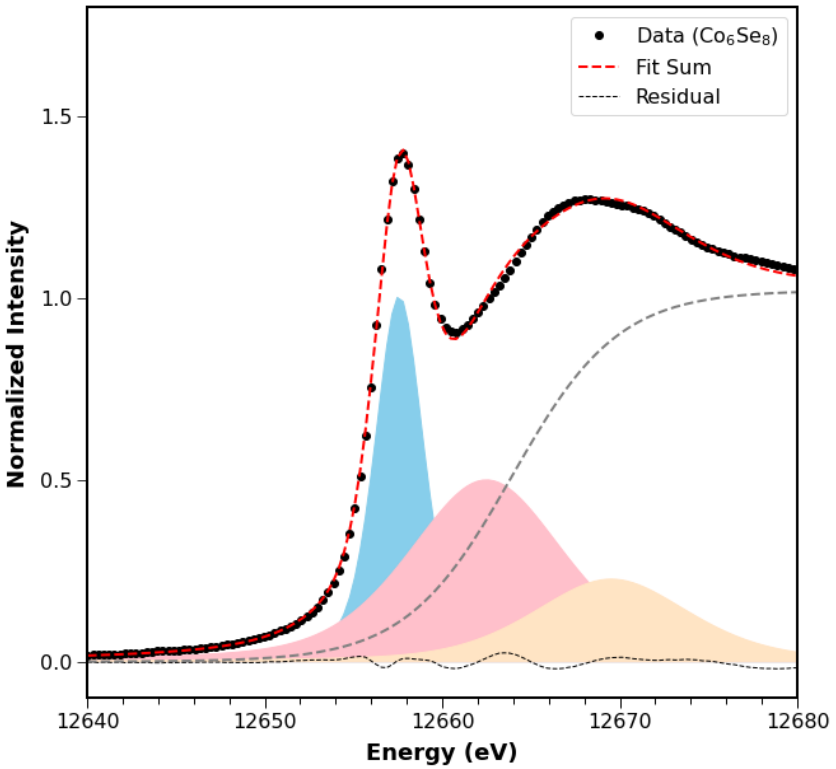

Figure 43. Fitted selenium X-ray absorption spectrum of **1**-H_6

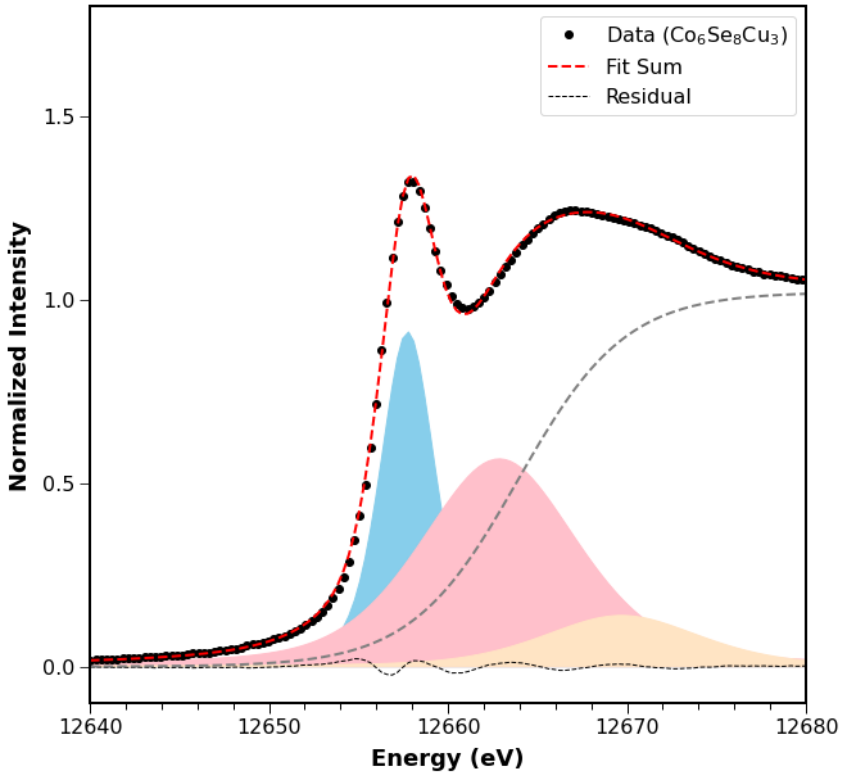

Figure 44. Fitted selenium X-ray absorption spectrum of **1**-Cu_3

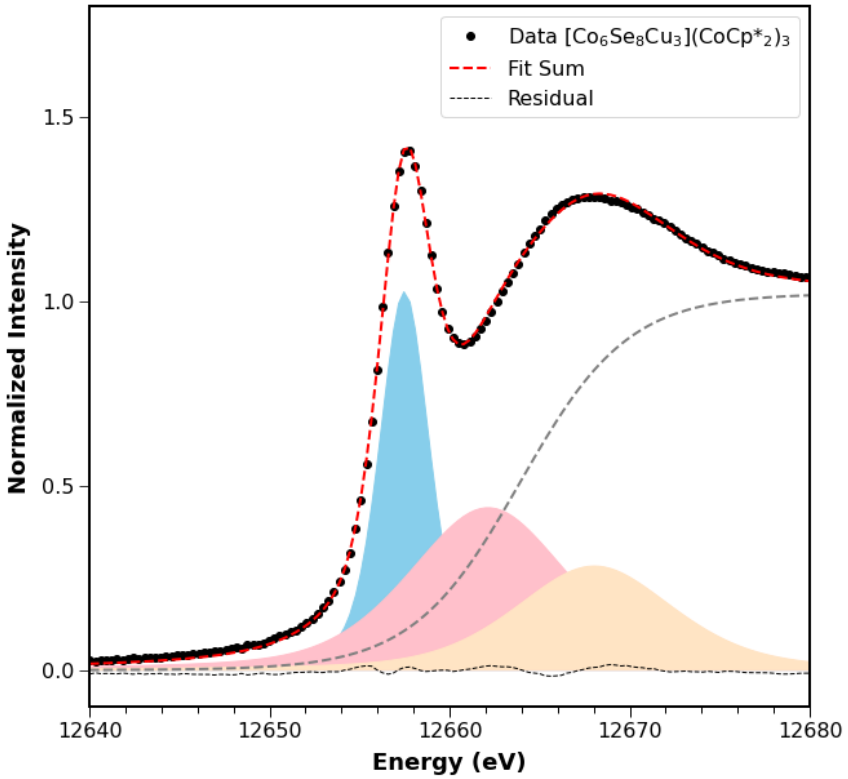

Figure 45. Fitted selenium X-ray absorption spectrum of [**1**-Cu_3]$^{3-}$

Table 2. Calculated parameters from fitted Se XAS data

	1-H_6	**1-Cu_3**	**[1-Cu_3]$^{3-}$**
P1 area	4.11(6)	4.16(5)	4.26(6)
P1 center	12657.58(1)	12657.75(1)	12657.50(1)
P2 area	6.59(8)	7.47(7)	5.80(11)
P2 center	12662.49(11)	12662.87(8)	12662.14(14)
P3 area	2.99(11)	1.84(9)	3.72(15)
P3 center	12669.52(15)	12669.67(20)	12668.04(13)
Maximum	12657.80(10)	12658.10(10)	12657.80(10)
Inflection	12656.29(10)	12656.29(10)	12656.29(10)

1.9 X-RAY DIFFRACTION STUDIES

Single crystals suitable for X-ray analysis were coated in deoxygenated paratone oil and mounted on a 20 µm CryoLoop™ (Hampton Research, 18 mm mount, 0.2 to 0.3 mm loop diameter). Data was collected at –173 °C on a Bruker APEX II single crystal X-ray diffractometer equipped with a Mo source unless noted otherwise. Unless indicated otherwise, all data was integrated and scaled using SAINT, SADABS within the APEX2 software package by Bruker.[77] Solution by direct methods (SHELXT[78] or SIR97[79,80]) produced a complete heavy atom phasing model consistent

with the proposed structure. Structures were completed by difference Fourier synthesis with SHELXL.[81–83] Scattering factors are from Waasmair and Kirfel.[84] Hydrogen atoms were placed in geometrically idealized positions and constrained to ride on their parent atoms with C–H distances in the range 0.95–1.00 Å. Isotropic thermal parameters U_{eq} were fixed such that they were $1.2U_{eq}$ of their parent atom U_{eq} for CHs and $1.5U_{eq}$ of their parent atom U_{eq} in case of methyl groups. All non-hydrogen atoms were refined anisotropically by full-matrix least-squares.

1.9.1 *[Li(thf)$_4$][1-Cu$_3$]*

Single crystals of suitable quality for X-ray diffraction were grown by vapor diffusion of diethyl ether into a solution of the cluster in tetrahydrofuran at room temperature. The compound crystallizes as a racemic mixture of enantiopure crystals. The highest quality crystal structure was collected on a racemic twin with a Hooft parameter of 0.498(1), but other structures were obtained from enantiopure crystals as well. Disordered THF and diethyl ether solvent was refined with SIMU restraints to stabilize thermal displacement parameters.

1.9.2 *[Li(thf)$_4$][Cp*$_2$Co]$_2$[1-Cu$_3$]*

Single crystals of suitable quality for X-ray diffraction were grown by vapor diffusion of diethyl ether into a solution of the cluster in tetrahydrofuran at –35 °C. The crystal was a pseudo-merohedral twin. There was severe disorder of the cations and solvent molecules, to the extent that the solvated lithium ion could not be modeled entirely. Multiple restraints (DELU, SAME, ISOR) were required to stabilize the refinement, and AFIX was used to fix the geometry of phenyl and Cp* groups in the model. Due to the low quality of the crystal structure resulting from extensive crystallographic disorder, the structure was only used to confirm connectivity.

1.9.3 *1-Cu$_3$*

Single crystals of suitable quality for X-ray diffraction were grown by vapor diffusion of diethyl ether into a solution of the cluster in tetrahydrofuran at room temperature. The exceedingly thin, plate-like habit of the crystals necessitated data collection at a diffractometer with a microfocus X-ray source. Specifically, the crystals were mailed to Bruker AXS and a Bruker D8 Venture with a Mo microfocus X-ray source and PHOTON III area detector was used to obtain this structure.

Disordered THF molecules and phenyl groups in the structure necessitated the usage of DELU, ISOR, and SAME restraints.

1.9.4 *[Ru(bpy)$_3$][1-Cu$_3$]*

Single crystals of suitable quality for X-ray diffraction were grown by vapor diffusion of acetonitrile into a solution of the compound in dimethylformamide at room temperature. The contribution of disordered acetonitrile and dimethylformamide to the diffraction pattern was removed with SQUEEZE. One of the bipyridine ligands in the $[Ru(bpy)_3]^{2+}$ cation was disordered over two positions, and one of the $(NTol)_2$–Cu sites on the clusters appeared to be disordered with $(NTol\text{-}H)_2$ in an 89:11 ratio of metallated to protonated ligand.

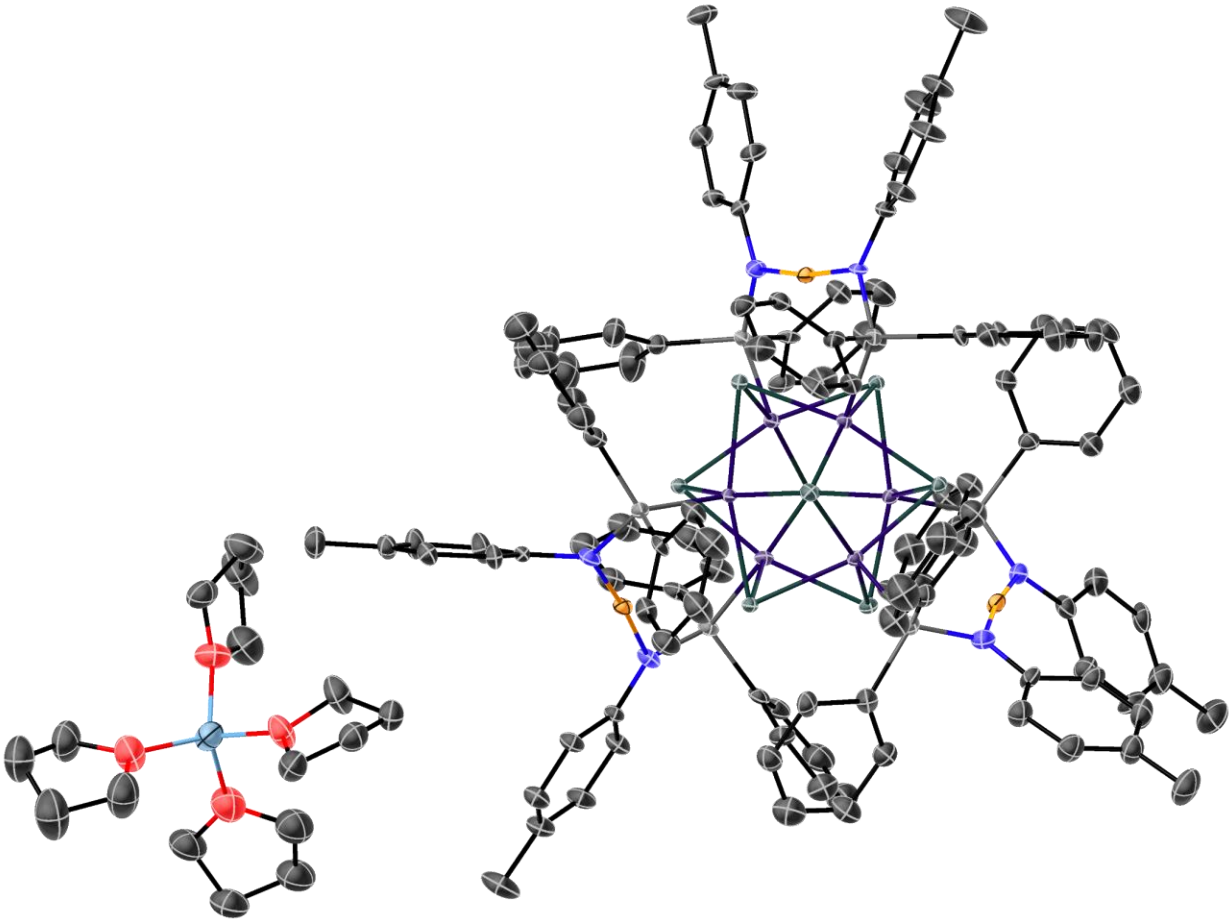

Figure 46. Solid-state structure of [Li(thf)$_4$][**1**-Cu$_3$] with thermal ellipsoids shown at a 50% probability level. All hydrogen atoms and isolated co-crystallized solvent molecules omitted for clarity.

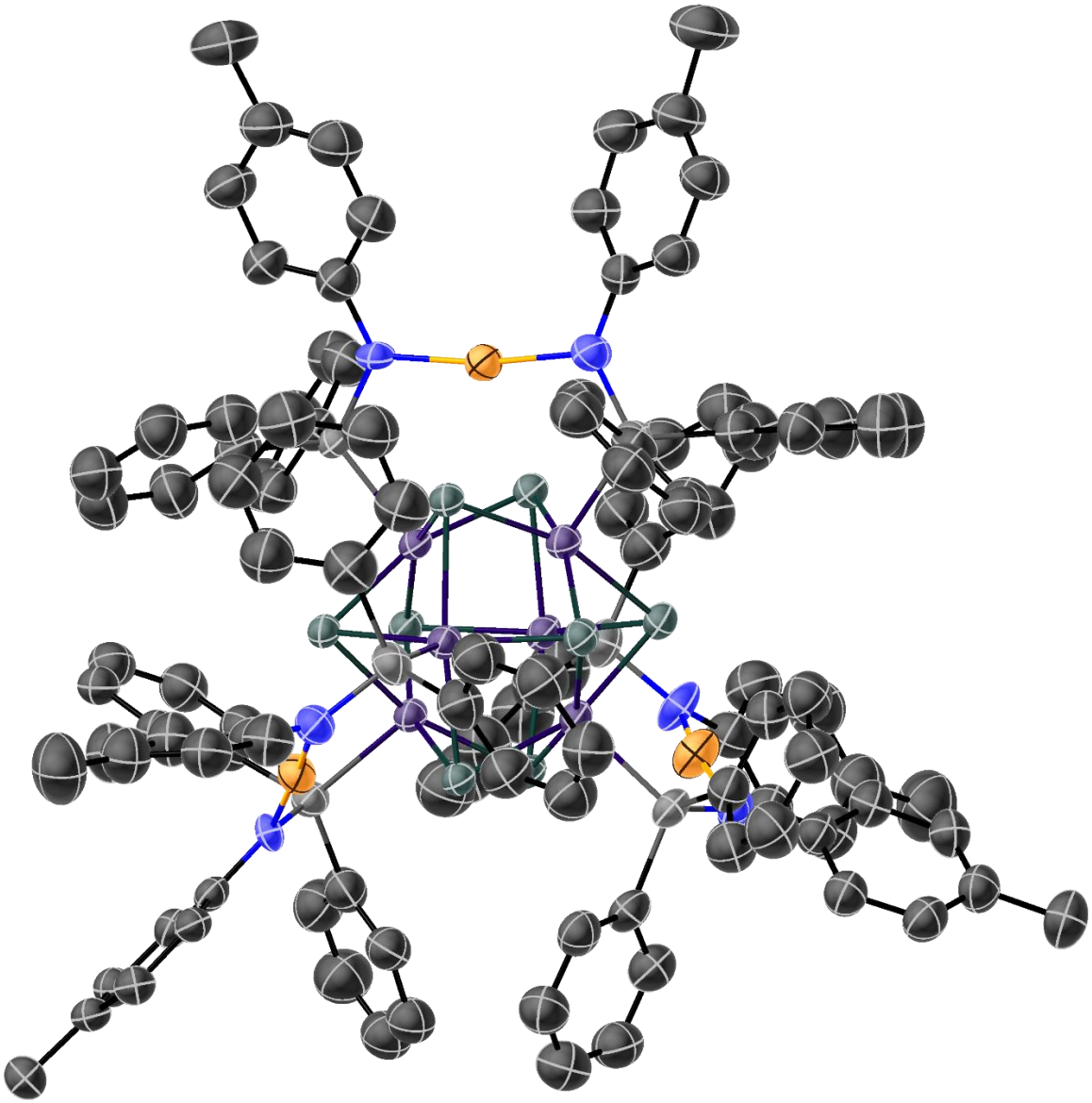

Figure 47. Solid-state structure of **1**-Cu_3 with thermal ellipsoids shown at a 50% probability level. All hydrogen atoms and co-crystallized solvent molecules omitted for clarity.

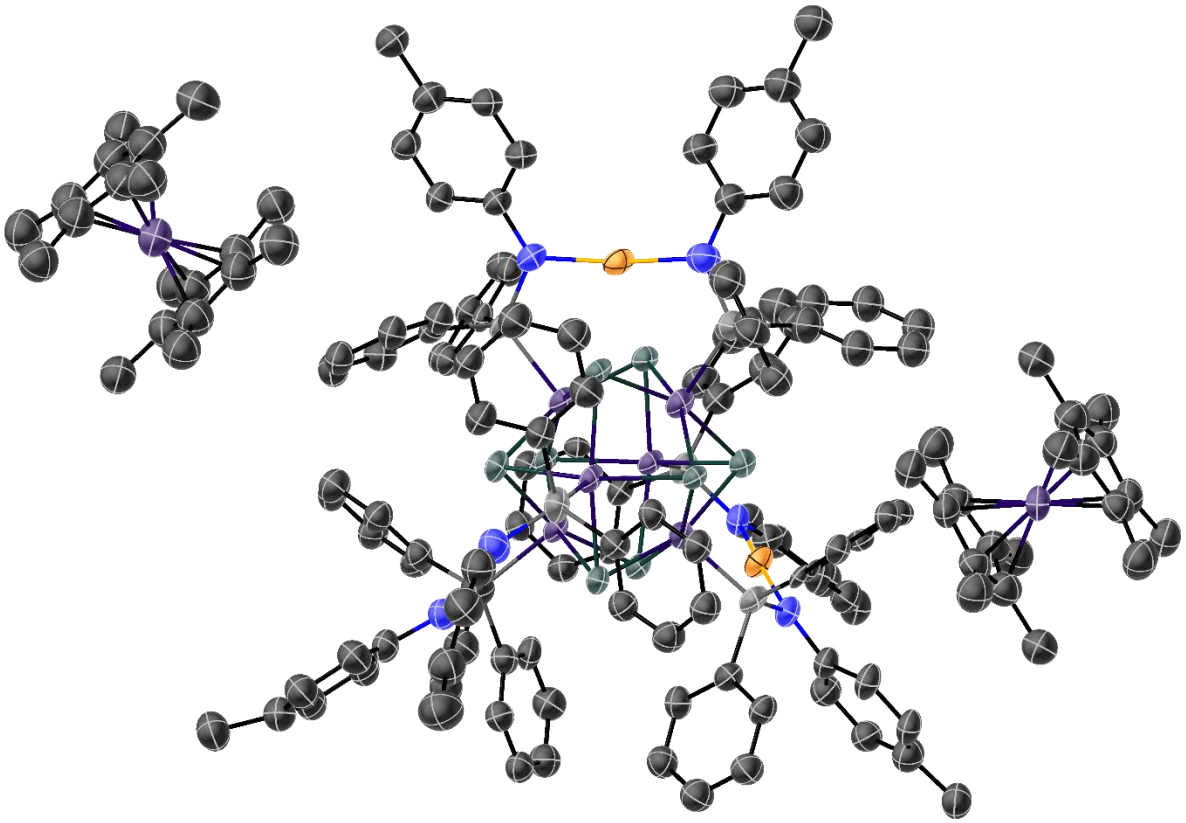

Figure 48. Solid-state structure of $[Li(thf)_4][Cp_2^*Co]_2[\mathbf{1}\text{-}Cu_3]$ with thermal ellipsoids shown at a 30% probability level. All hydrogen atoms and co-crystallized solvent molecules are omitted for clarity. Due to extensive disorder, the $[Li(thf)_4]^+$ ion could not be located definitively.

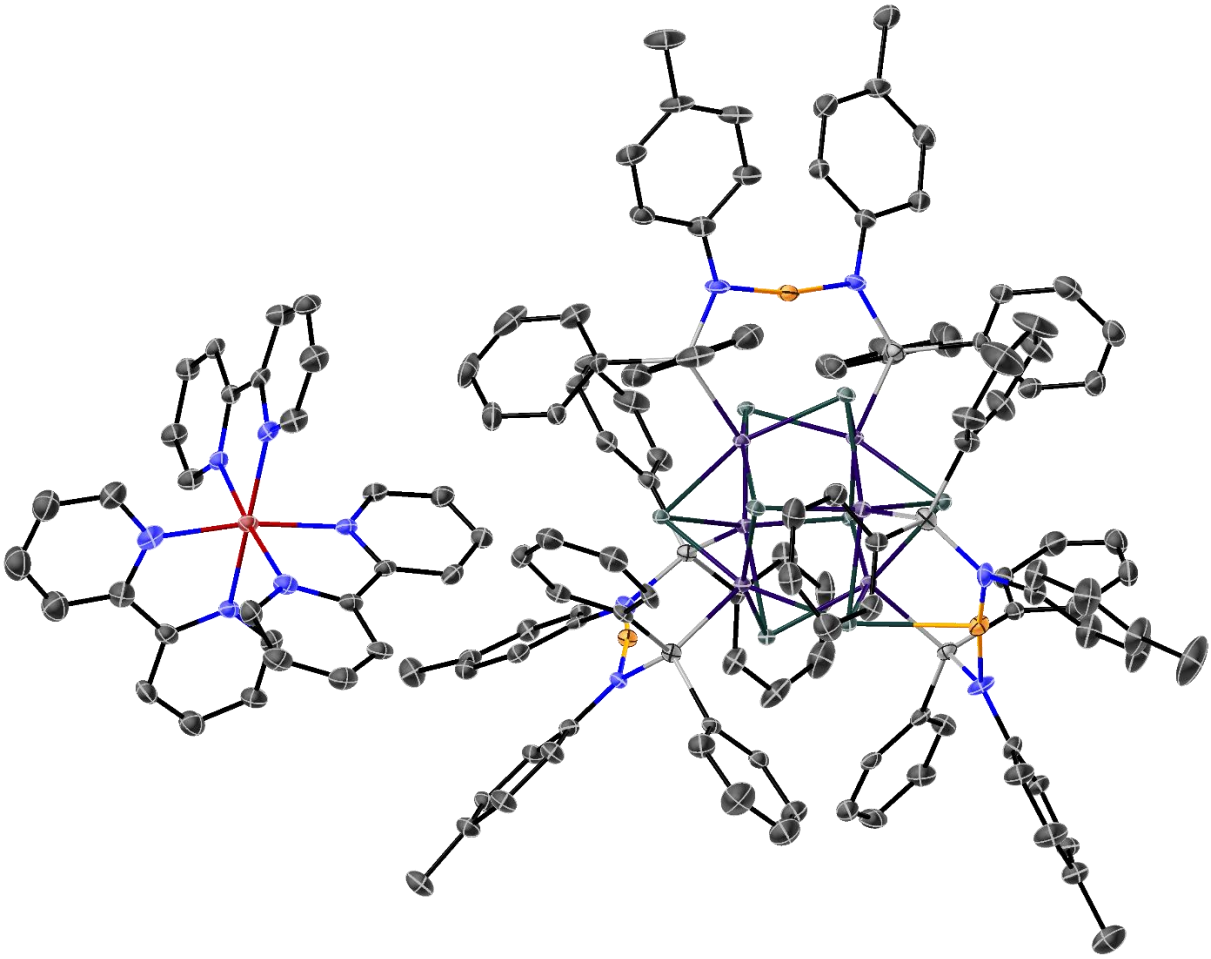

Figure 49. Solid -state structure of $[Ru(bpy)_3][\mathbf{1}\text{-}Cu_3]$ with thermal ellipsoids shown at a 50% probability level. All hydrogen atoms and co-crystallized solvent molecules are omitted for clarity

Table 3. Crystallographic information for $[Li(thf)_4][\mathbf{1}\text{-}Cu_3]$, $[Li(thf)_4][Cp^*_2Co]_2[\mathbf{1}\text{-}Cu_3]$, and $\mathbf{1}\text{-}Cu_3$

Compound	$[Li(thf)_4][\mathbf{1}\text{-}Cu_3]$	$[Li(thf)_4][Cp^*_2Co]_2$ $[\mathbf{1}\text{-}Cu_3]$	$\mathbf{1}\text{-}Cu_3$
Empirical formula	$C_{138}H_{151}Co_6Cu_3N_6O_4P_6Se_8$	$C_{160}H_{174}Cl_4Co_8Cu_3LiN_6OP_6Se_8$	$C_{118}H_{110}Co_6Cu_3N_6P_6Se_8$
CCDC Number	2351184	2351183	2351182
Formula weight	3358.68	3825.34	2989.81
Temperature (K)	100(2)	100(2)	120(2)
Wavelength (Å)	0.71073	0.71073	0.71073
Crystal system	Orthorhombic	Triclinic	Monoclinic
Space group	$P2_12_12_1$	P-1	$P2_1/n$
Flack parameter	0.498(1)	-	-
a (Å)	15.3064(8)	19.942(4)	27.432(4)
b (Å)	29.4018(16)	21.112(4)	15.2595(17)
c (Å)	30.3754(16)	21.411(4)	28.119(3)
α (°)	90	87.981(6)	90
β (°)	90	86.225(6)	94.878(4)
γ (°)	90	62.118(5)	90
Volume (Å^3)	13670.0(13)	7951(3)	11728(2)
Z	4	2	4
ρ^{calc} (g cm^{-1})	1.632	1.598	1.693
Absorption coefficient (mm^{-1})	3.422	3.214	3.974
F(000)	6734	3840	5916
Crystal size (mm^3)	0.200 x 0.060 x 0.040	0.140 x 0.140 x 0.140	0.070 x 0.036 x 0.005
Theta range for data collection (°)	1.341 to 29.130	0.953 to 25.019	1.991 to 25.418
Index ranges	$-20\leq h\leq 20$, $-40\leq k\leq 40$, $-41\leq l\leq 41$	$-21\leq h\leq 23$, $-24\leq k\leq 23$, $-23\leq l\leq 21$	$-33\leq h\leq 33$, $-18\leq k\leq 18$, $-29\leq l\leq 33$
Reflections collected	141221	41257	71846
Independent reflections	36759 [R(int) = 0.0741]	23295 [R(int) = 0.1039]	21574 [R(int) = 0.1761]
Completeness to theta = 25.000°	99.7%	83.1%	100.0%
Data / restraints / parameters	36759 / 1751 / 1712	23295 / 2913 / 1378	21574 / 2270 / 1616
Goodness-of-fit on F^2	1.216	1.028	0.992
Final R indices [I>2sigma(I)]	R1 = 0.0580, wR2 = 0.1170	R1 = 0.1728, wR2 = 0.3514	R1 = 0.0895, wR2 = 0.2098
R indices (all data)	R1 = 0.0642, wR2 = 0.1190	R1 = 0.3237, wR2 = 0.4483	R1 = 0.1972, wR2 = 0.2490
Largest diff. peak and hole (e$^-$Å^{-3})	1.100 and –1.256	2.319 and –2.366	1.136 and –1.037

Table 4. Crystallographic information for $[Ru(bpy)_3][\mathbf{1}\text{-}Cu_3]$

Compound	$[Ru(bpy)_3][\mathbf{1}\text{-}Cu_3]$
Empirical formula	$C_{144}H_{126}Co_6Cu_3N_{12}P_6RuSe_8$
CCDC Number	2351185
Formula weight	3644.62
Temperature (K)	100(2)
Wavelength (Å)	0.71073
Crystal system	Monoclinic
Space group	$P2_1/n$
a (Å)	15.6656(14)
b (Å)	18.4804(15)
c (Å)	55.074(5)
α (°)	90
β (°)	97.625(5)
γ (°)	90
Volume ($Å^3$)	15803(2)
Z	5
ρ^{calc} ($g\ cm^{-1}$)	1.532
Absorption coefficient (mm^{-1})	3.041
F(000)	7256
Crystal size (mm^3)	0.150 x 0.140 x 0.020
Theta range for data collection (°)	1.163 to 25.027
Index ranges	$-18\leq h\leq 18$, $-22\leq k\leq 22$, $-65\leq l\leq 65$
Reflections collected	109065
Independent reflections	27918 [R(int) = 0.0608]
Completeness to theta = 25.000°	100.0%
Data / restraints / parameters	27918 / 689 / 1848
Goodness-of-fit on F^2	1.218
Final R indices [I>2sigma(I)]	R1 = 0.0629, wR2 = 0.1186
R indices (all data)	R1 = 0.0757, wR2 = 0.1223
Largest diff. peak and hole ($e^-Å^{-3}$)	0.799 and –1.427

1.10 DFT CALCULATIONS

1.10.1 *Example inputs*

Example of geometry optimizations:

```
%nprocshared=40
%mem=128GB
%chk=Cu3_neutral_NoMe_def2SVP.chk
#p opt freq ubvp86/def2SVP scf=maxcycle=3072 gfinput pop=(full,nbo)
Cu3_neutral_NoMe_def2SVP.chk
0 2
*Coordinates from X-ray structure*
```

Example of single point calculations:

```
%nprocshared=40
%mem=128GB
%oldchk= Cu3_neutral_NoMe_def2SVP.chk
%chk=Cu3_neutral_NoMe_ccPVTZ.chk
#p ub3lyp IOp(3/76=1000001500) IOp(3/77=0720008000) IOp(3/78=0810010000) cc-pVTZ
guess=read geom=check scf=maxcycle=3072 gfinput pop=full IOp(6/82=1)
Cu3_neutral_NoMe_ccPVTZ.chk
0 2
```

1.10.2 *Selected calculation results*

Table 5. DFT optimized interatomic distances and angles for [**1**-Cu_3]^n (n = 0,–1,–2,–3)

Compound	Cu–N (Å)	Co–P (Å)	Co…Co (Å)	Co–Se (Å)
1-Cu$_3$	1.917-1.915	2.198-2.194	2.926-2.683	2.417-2.325
[**1-Cu$_3$**]$^-$	1.931-1.929	2.195-2.192	2.923-2.683	2.424-2.329
[**1-Cu$_3$**]$^{2-}$	1.943-1.937	2.185-2.152	2.990-2.659	2.432-2.321
[**1-Cu$_3$**]$^{3-}$	1.952-1.946	2.142-2.139	2.995-2.872	2.392-2.342

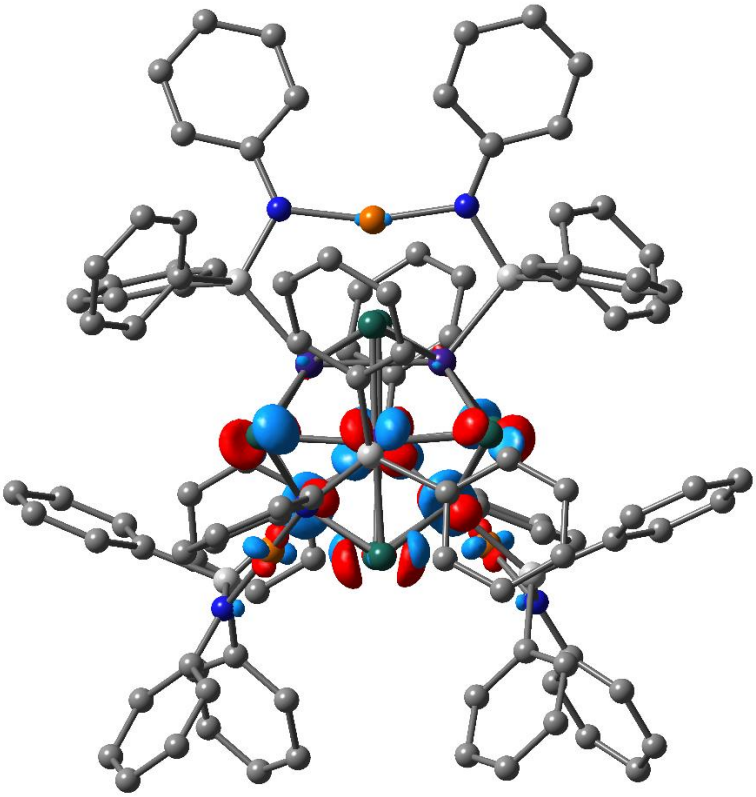

Figure 50. The LUMO of [**1**-Cu_3]$^-$ calculated at the DFT uB3LYP+/cc-PVTZ level of theory with hydrogen atoms omitted for clarity. Surface plotted at an isovalue of 0.05.

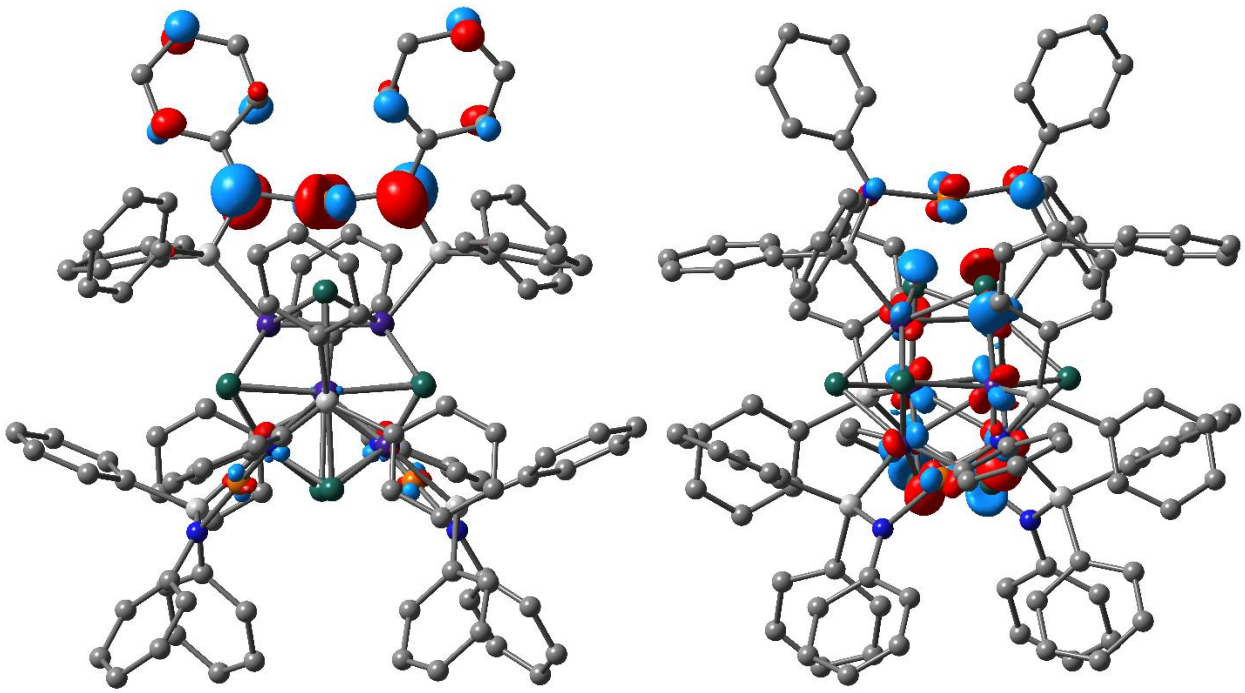

Figure 51. The pseudo-degenerate HOMO/HOMO-1 orbitals of [**1**-Cu_3]$^-$ calculated at the DFT uB3LYP+/cc-PVTZ level of theory with hydrogen atoms omitted for clarity. The orbitals on the left and right belong to the alpha and beta spin manifolds, respectively. Surfaces plotted at an isovalue of 0.05.

1.11 References

(1) Tedstone, A. A.; Lewis, D. J.; O'Brien, P. Synthesis, Properties, and Applications of Transition Metal-Doped Layered Transition Metal Dichalcogenides. *Chem. Mater.* **2016**, *28* (7), 1965–1974. https://doi.org/10.1021/acs.chemmater.6b00430.

(2) Morales-Guio, C. G.; Hu, X. Amorphous Molybdenum Sulfides as Hydrogen Evolution Catalysts. *Acc. Chem. Res.* **2014**, *47* (8), 2671–2681. https://doi.org/10.1021/ar5002022.

(3) Chianelli, R. R.; Berhault, G.; Torres, B. Unsupported Transition Metal Sulfide Catalysts: 100 Years of Science and Application. *Catal. Today* **2009**, *147* (3), 275–286. https://doi.org/10.1016/j.cattod.2008.09.041.

(4) Kibsgaard, J.; Tuxen, A.; Knudsen, K. G.; Brorson, M.; Topsøe, H.; Lægsgaard, E.; Lauritsen, J. V.; Besenbacher, F. Comparative Atomic-Scale Analysis of Promotional Effects by Late 3d-Transition Metals in MoS2 Hydrotreating Catalysts. *J. Catal.* **2010**, *272* (2), 195–203. https://doi.org/10.1016/j.jcat.2010.03.018.

(5) Harris, S.; Chianelli, R. R. Catalysis by Transition Metal Sulfides: A Theoretical and Experimental Study of the Relation between the Synergic Systems and the Binary

Transition Metal Sulfides. *J. Catal.* **1986**, *98* (1), 17–31. https://doi.org/10.1016/0021-9517(86)90292-7.

(6) Muetterties, E. L.; Rhodin, T. N.; Band, E.; Brucker, C. F.; Pretzer, W. R. Clusters and Surfaces. *Chem Rev* **1979**, *79* (2), 91–137. https://doi.org/10.1021/cr60322a001.

(7) Kibsgaard, J.; Jaramillo, T. F.; Besenbacher, F. Building an Appropriate Active-Site Motif into a Hydrogen-Evolution Catalyst with Thiomolybdate [Mo3S13]2− Clusters. *Nat. Chem.* **2014**, *6* (3), 248–253. https://doi.org/10.1038/nchem.1853.

(8) Kephart, J. A.; Mitchell, B. S.; Chirila, A.; Anderton, K. J.; Rogers, D.; Kaminsky, W.; Velian, A. Atomically Defined Nanopropeller Fe3Co6Se8(Ph2PNTol)6: Functional Model for the Electronic Metal–Support Interaction Effect and High Catalytic Activity for Carbodiimide Formation. *J. Am. Chem. Soc.* **2019**, *141* (50), 19605–19610. https://doi.org/10.1021/jacs.9b12473.

(9) Eaton, M. C.; Catalano, V. J.; Shearer, J.; Murray, L. J. Dinitrogen Insertion and Cleavage by a Metal–Metal Bonded Tricobalt(I) Cluster. *J. Am. Chem. Soc.* **2021**, *143* (15), 5649–5653. https://doi.org/10.1021/jacs.1c01840.

(10) Mitchell, B. S.; Chirila, A.; Kephart, J. A.; Boggiano, A. C.; Krajewski, S. M.; Rogers, D.; Kaminsky, W.; Velian, A. Metal–Support Interactions in Molecular Single-Site Cluster Catalysts. *J. Am. Chem. Soc.* **2022**, *144* (40), 18459–18469. https://doi.org/10.1021/jacs.2c07033.

(11) Amtawong, J.; Nguyen, A. I.; Tilley, T. D. Mechanistic Aspects of Cobalt–Oxo Cubane Clusters in Oxidation Chemistry. *J. Am. Chem. Soc.* **2022**, *144* (4), 1475–1492. https://doi.org/10.1021/jacs.1c11445.

(12) Jin, R.; Liu, X.; Zhao, S.; Xing, Y.; Jin, R. Shape Effect of Atomically Precise Au25 Nanoclusters on Catalytic CO Oxidation. *J. Phys. Chem. C* **2022**, *126* (40), 17114–17122. https://doi.org/10.1021/acs.jpcc.2c06066.

(13) Touchton, A. J.; Wu, G.; Hayton, T. W. [Ni $_{30}$ S $_{16}$ (PEt $_{3}$) $_{11}$]: An Open-Shell Nickel Sulfide Nanocluster with a “Metal-like” Core. *Chem. Sci.* **2022**, *13* (18), 5171–5175. https://doi.org/10.1039/D2SC00960A.

(14) Cesari, C.; Shon, J.-H.; Zacchini, S.; Berben, L. A. Metal Carbonyl Clusters of Groups 8–10: Synthesis and Catalysis. *Chem. Soc. Rev.* **2021**, *50* (17), 9503–9539. https://doi.org/10.1039/D1CS00161B.

(15) Beamer, A. W.; Buss, J. A. Synthesis, Structural Characterization, and CO $_{2}$ Reactivity of a Constitutionally Analogous Series of Tricopper Mono-, Di-, and Trihydrides. *J. Am. Chem. Soc.* **2023**, *145* (23), 12911–12919. https://doi.org/10.1021/jacs.3c04170.

(16) Cooney, S. E.; Walls, M. R. A.; Schreiber, E.; Brennessel, W. W.; Matson, E. M. Heterometal Dopant Changes the Mechanism of Proton-Coupled Electron Transfer at the

Polyoxovanadate-Alkoxide Surface. *J. Am. Chem. Soc.* **2024**, *146* (4), 2364–2369. https://doi.org/10.1021/jacs.3c14054.

(17) Mondal, S.; Zhang, W.; Zhang, S. Thermodynamics of Proton-Coupled Electron Transfer at Tricopper μ-Oxo/Hydroxo/Aqua Complexes. *J. Am. Chem. Soc.* **2024**, *146* (22), 15036–15044. https://doi.org/10.1021/jacs.3c14420.

(18) Lauritsen, J. V.; Kibsgaard, J.; Olesen, G. H.; Moses, P. G.; Hinnemann, B.; Helveg, S.; Nørskov, J. K.; Clausen, B. S.; Topsøe, H.; Lægsgaard, E.; Besenbacher, F. Location and Coordination of Promoter Atoms in Co- and Ni-Promoted MoS2-Based Hydrotreating Catalysts. *J. Catal.* **2007**, *249* (2), 220–233. https://doi.org/10.1016/j.jcat.2007.04.013.

(19) Arnanz, A.; Marcos, M.-L.; Delgado, S.; González-Velasco, J.; Moreno, C. Electronic Communication through a Poly-Yne Carbonyldicobalt Complex Containing an Open Linear Triosmium Cluster. *Dalt Trans* **2009**, No. 1, 168–176. https://doi.org/10.1039/b812195h.

(20) Kephart, J. A.; Romero, C. G.; Tseng, C.-C.; Anderton, K. J.; Yankowitz, M.; Kaminsky, W.; Velian, A. Hierarchical Nanosheets Built from Superatomic Clusters: Properties, Exfoliation and Single-Crystal-to-Single-Crystal Intercalation. *Chem. Sci.* **2020**, *11* (39), 10744–10751. https://doi.org/10.1039/D0SC03506H.

(21) Kephart, J. A.; Boggiano, A. C.; Kaminsky, W.; Velian, A. Inorganic Clusters as Metalloligands: Ligand Effects on the Synthesis and Properties of Ternary Nanopropeller Clusters. *Dalton Trans.* **2020**, *49* (45), 16464–16473. https://doi.org/10.1039/D0DT02416C.

(22) Mitchell, B. S.; Kaminsky, W.; Velian, A. Tuning the Electronic Structure of Atomically Precise Sn/Co/Se Nanoclusters via Redox Matching of Tin(IV) Surface Sites. *Inorg. Chem.* **2021**, *60* (9), 6135–6139. https://doi.org/10.1021/acs.inorgchem.1c00313.

(23) Kephart, J. A.; Mitchell, B. S.; Kaminsky, W.; Velian, A. Multi-Active Site Dynamics on a Molecular Cr/Co/Se Cluster Catalyst. *J. Am. Chem. Soc.* **2022**, *144* (21), 9206–9211. https://doi.org/10.1021/jacs.2c00234.

(24) Mitchell, B. S.; Krajewski, S. M.; Kephart, J. A.; Rogers, D.; Kaminsky, W.; Velian, A. Redox-Switchable Allosteric Effects in Molecular Clusters. *JACS Au* **2022**, *2* (1), 92–96. https://doi.org/10.1021/jacsau.1c00491.

(25) Kephart, J. A.; Zhou, D. Y.; Sandwisch, J.; Cajiao, N.; Krajewski, S. M.; Malinowski, P.; Chu, J.-H.; Neidig, M. L.; Kaminsky, W.; Velian, A. Caught in the Act of Substitution: Interadsorbate Effects on an Atomically Precise Fe/Co/Se Nanocluster. *ACS Cent. Sci.* **2024**, acscentsci.4c00210. https://doi.org/10.1021/acscentsci.4c00210.

(26) Johnson, B. J.; Antholine, W. E.; Lindeman, S. V.; Graham, M. J.; Mankad, N. P. A One-Hole Cu_4S Cluster with N_2O Reductase Activity: A Structural and Functional Model for Cu_Z*. *J. Am. Chem. Soc.* **2016**, *138* (40), 13107–13110. https://doi.org/10.1021/jacs.6b05480.

(27) Arnett, C. H.; Chalkley, M. J.; Agapie, T. A Thermodynamic Model for Redox-Dependent Binding of Carbon Monoxide at Site-Differentiated, High Spin Iron Clusters. *J. Am. Chem. Soc.* **2018**, *140* (16), 5569–5578. https://doi.org/10.1021/jacs.8b01825.

(28) Kim, Y.; Sridharan, A.; Suess, D. L. M. The Elusive Mononitrosylated [Fe4S4] Cluster in Three Redox States. *Angew. Chem. Int. Ed.* **2022**, *61* (47), e202213032. https://doi.org/10.1002/anie.202213032.

(29) Ghebreamlak, S.; Stoian, S. A.; Lees, N. S.; Cronin, B.; Smith, F.; Ross, M. O.; Telser, J.; Hoffman, B. M.; Duin, E. C. The Active-Site [4Fe-4S] Cluster in the Isoprenoid Biosynthesis Enzyme IspH Adopts Unexpected Redox States during Ligand Binding and Catalysis. *J. Am. Chem. Soc.* **2024**, *146* (6), 3926–3942. https://doi.org/10.1021/jacs.3c11674.

(30) Juda, C. E.; Handford, R. C.; Bartholomew, A. K.; Powers, T. M.; Gu, N. X.; Meyer, E.; Roth, N.; Chen, Y.; Zheng, S.-L.; Betley, T. A. Cluster Dynamics of Heterometallic Trinuclear Clusters during Ligand Substitution, Redox Chemistry, and Group Transfer Processes. *Chem. Sci.* **2024**, *15* (21), 8242–8248. https://doi.org/10.1039/D3SC03606E.

(31) Mitchell, B. S.; Chirila, A.; Anderton, K. J.; Kaminsky, W.; Velian, A. Probing Edge/Support Electronic Cooperativity in Single Edge Fe/Co6Se8 Clusters. *Inorg. Chem.* **2023**, *62* (26), 10497–10503. https://doi.org/10.1021/acs.inorgchem.3c01661.

(32) Evangelio, E.; Ruiz-Molina, D. Valence Tautomerism: New Challenges for Electroactive Ligands. *Eur. J. Inorg. Chem.* **2005**, *2005* (15), 2957–2971. https://doi.org/10.1002/ejic.200500323.

(33) Kundu, N.; Maity, M.; Chatterjee, P. B.; Teat, S. J.; Endo, A.; Chaudhury, M. Reporting a Unique Example of Electronic Bistability Observed in the Form of Valence Tautomerism with a Copper(II) Helicate of a Redox-Active Nitrogenous Heterocyclic Ligand. *J. Am. Chem. Soc.* **2011**, *133* (50), 20104–20107. https://doi.org/10.1021/ja2088986.

(34) Lonnon, D. G.; Lee, S. T.; Colbran, S. B. Valence Tautomerism and Coordinative Lability in Copper(II)−Imidazolyl−Semiquinonate Anion Radical Models for the CuB Center in Cytochrome c Oxidases. *J. Am. Chem. Soc.* **2007**, *129* (18), 5800–5801. https://doi.org/10.1021/ja068972f.

(35) O'Brien, E. S.; Trinh, M. T.; Kann, R. L.; Chen, J.; Elbaz, G. A.; Masurkar, A.; Atallah, T. L.; Paley, M. V.; Patel, N.; Paley, D. W.; Kymissis, I.; Crowther, A. C.; Millis, A. J.; Reichman, D. R.; Zhu, X.-Y.; Roy, X. Single-Crystal-to-Single-Crystal Intercalation of a Low-Bandgap Superatomic Crystal. *Nat. Chem.* **2017**, *9* (12), 1170–1174. https://doi.org/10.1038/nchem.2844.

(36) Banthia, S.; Samanta, A. Synthesis and Structure of Unusually Stable Linear Copper(I) Complexes with Blue Fluorescence. *Polyhedron* **2006**, *25* (11), 2269–2276. https://doi.org/10.1016/j.poly.2006.01.025.

(37) Zhang, Q.; Wilson, P.; Li, Z.; McHale, R.; Godfrey, J.; Anastasaki, A.; Waldron, C.; Haddleton, D. M. Aqueous Copper-Mediated Living Polymerization: Exploiting Rapid Disproportionation of CuBr with Me6TREN. *J. Am. Chem. Soc.* **2013**, *135* (19), 7355–7363. https://doi.org/10.1021/ja4026402.

(38) Connelly, N. G.; Geiger, W. E. Chemical Redox Agents for Organometallic Chemistry. *Chem. Rev.* **1996**, *96* (2), 877–910. https://doi.org/10.1021/cr940053x.

(39) Le Clainche, L.; Giorgi, M.; Reinaud, O. Synthesis and Characterization of a Novel Calix[4]Arene-Based Two-Coordinate Copper(I) Complex That Is Unusually Resistant to Dioxygen. *Eur. J. Inorg. Chem.* **2000**, *2000* (9), 1931–1933. https://doi.org/10.1002/1099-0682(200009)2000:9<1931::AID-EJIC1931>3.0.CO;2-H.

(40) Sanyal, I.; Karlin, K. D.; Strange, R. W.; Blackburn, N. J. Chemistry and Structural Studies on the Dioxygen-Binding Copper-1,2-Dimethylimidazole System. *J. Am. Chem. Soc.* **1993**, *115* (24), 11259–11270. https://doi.org/10.1021/ja00077a027.

(41) Sorrell, T. N.; Jameson, D. L. Synthesis, Structure, and Reactivity of Monomeric Two-Coordinate Copper(I) Complexes. *J. Am. Chem. Soc.* **1983**, *105* (19), 6013–6018. https://doi.org/10.1021/ja00357a009.

(42) *A Search for All Cu...N Bond Lengths in the Cambridge Structural Database (April 2024) Yielded 212141 Hits between 1.147 and 3.037 Å (Mean 2.0(1) Å).*; 2024.

(43) Xu, Y.; Chen, J.; Aydt, A. P.; Zhang, L.; Sergeyev, I.; Keeler, E. G.; Choi, B.; He, S.; Reichman, D. R.; Friesner, R. A.; Nuckolls, C.; Steigerwald, M. L.; Roy, X.; McDermott, A. E. Electron and Spin Delocalization in [Co6Se8(PEt3)6]0/+1 Superatoms. *ChemPhysChem* **2024**, *25* (2), e202300064. https://doi.org/10.1002/cphc.202300064.

(44) Wagner, C. L.; Tao, L.; Thompson, E. J.; Stich, T. A.; Guo, J.; Fettinger, J. C.; Berben, L. A.; Britt, R. D.; Nagase, S.; Power, P. P. Dispersion-Force-Assisted Disproportionation: A Stable Two-Coordinate Copper(II) Complex. *Angew. Chem. Int. Ed.* **2016**, *55* (35), 10444–10447. https://doi.org/10.1002/anie.201605061.

(45) Wagner, C. L.; Tao, L.; Fettinger, J. C.; Britt, R. D.; Power, P. P. Two-Coordinate, Late First-Row Transition Metal Amido Derivatives of the Bulky Ligand -N(SiPri3)Dipp (Dipp = 2,6-Diisopropylphenyl): Effects of the Ligand on the Stability of Two-Coordinate Copper(II) Complexes. *Inorg. Chem.* **2019**, *58* (13), 8793–8799. https://doi.org/10.1021/acs.inorgchem.9b01159.

(46) James, A. M.; Laxman, R. K.; Fronczek, F. R.; Maverick, A. W. Phosphorescence and Structure of a Tetrameric Copper(I)−Amide Cluster. *Inorg. Chem.* **1998**, *37* (15), 3785–3791. https://doi.org/10.1021/ic971341p.

(47) *A Search for All Cu...Se Bond Lengths in the Cambridge Structural Database (March 2024) Yielded 4798 Hits between 2.163 and 3.170 Å (Mean 2.5(1) Å).*; 2024.

(48) Hughbanks, T.; Hoffmann, R. Molybdenum Chalcogenides: Clusters, Chains, and Extended Solids. The Approach to Bonding in Three Dimensions. *J. Am. Chem. Soc.* **1983**, *105* (5), 1150–1162. https://doi.org/10.1021/ja00343a014.

(49) Choi, B.; Yu, J.; Paley, D. W.; Trinh, M. T.; Paley, M. V.; Karch, J. M.; Crowther, A. C.; Lee, C.-H.; Lalancette, R. A.; Zhu, X.; Kim, P.; Steigerwald, M. L.; Nuckolls, C.; Roy, X. Van Der Waals Solids from Self-Assembled Nanoscale Building Blocks. *Nano Lett.* **2016**, *16* (2), 1445–1449. https://doi.org/10.1021/acs.nanolett.5b05049.

(50) *A Search for All Co...Co Bond Lengths in the Cambridge Structural Database (March 2024) Yielded 8297 Hits between 1.978 and 3.219 Å (Mean 2.5(2) Å).*; 2024.

(51) Bridgeman, A. J.; Cavigliasso, G.; Ireland, L. R.; Rothery, J. The Mayer Bond Order as a Tool in Inorganic Chemistry. *J. Chem. Soc. Dalton Trans.* **2001**, No. 14, 2095–2108. https://doi.org/10.1039/B102094N.

(52) Hernández Sánchez, R.; Champsaur, A. M.; Choi, B.; Wang, S. G.; Bu, W.; Roy, X.; Chen, Y.-S.; Steigerwald, M. L.; Nuckolls, C.; Paley, D. W. Electron Cartography in Clusters. *Angew. Chem. Int. Ed.* **2018**, *57* (42), 13815–13820. https://doi.org/10.1002/anie.201806426.

(53) Zhu, Y.; Guo, J.; Qiu, X.; Zhao, S.; Tang, Z. Optical Activity of Chiral Metal Nanoclusters. *Acc. Mater. Res.* **2021**, *2* (1), 21–35. https://doi.org/10.1021/accountsmr.0c00057.

(54) Pérez-García, L.; Amabilino, D. B. Spontaneous Resolution under Supramolecular Control. *Chem. Soc. Rev.* **2002**, *31* (6), 342–356. https://doi.org/10.1039/B201099M.

(55) Evans, D. F. 400. The Determination of the Paramagnetic Susceptibility of Substances in Solution by Nuclear Magnetic Resonance. *J. Chem. Soc. Resumed* **1959**, 2003–2005. https://doi.org/10.1039/jr9590002003.

(56) F. H. Köhler. *Paramagnetic Complexes in Solution: The NMR Approach. In Encyclopedia of Magnetic Resonance*; John Wiley & Sons, Ltd: Chichester, U.K., 2011.

(57) Mugiraneza, S.; Hallas, A. M. Tutorial: A Beginner's Guide to Interpreting Magnetic Susceptibility Data with the Curie-Weiss Law. *Commun. Phys.* **2022**, *5* (1), 1–12. https://doi.org/10.1038/s42005-022-00853-y.

(58) Wilcke, S. L.; Lee, Y.-J.; Cairns, E. J.; Reimer, J. A. Covalency Measurements via NMR in Lithium Metal Phosphates. *Appl. Magn. Reson.* **2007**, *32* (4), 547–563. https://doi.org/10.1007/s00723-007-0032-1.

(59) Palstra, T. T. M.; Steigerwald, M. L.; Ramirez, A. P.; Kwon, Y.-U.; Stuczynski, S. M.; Schneemeyer, L. F.; Waszczak, J. V.; Zaanen, J. Electron Correlations on a Mesoscopic Scale: Magnetic Properties of Transition Metal Telluride Cluster Compounds. *Phys. Rev. Lett.* **1993**, *71* (11), 1768–1771. https://doi.org/10.1103/PhysRevLett.71.1768.

(60) Van Vleck, J. H.; Frank, A. The Effect of Second Order Zeeman Terms on Magnetic Susceptibilities in the Rare Earth and Iron Groups. *Phys. Rev.* **1929**, *34* (11), 1494–1496. https://doi.org/10.1103/PhysRev.34.1494.

(61) Aleshin, D. Y.; Nikovskiy, I.; Novikov, V. V.; Polezhaev, A. V.; Melnikova, E. K.; Nelyubina, Y. V. Room-Temperature Spin Crossover in a Solution of Iron(II) Complexes with N,N′-Disubstituted Bis(Pyrazol-3-Yl)Pyridines. *ACS Omega* **2021**, *6* (48), 33111–33121. https://doi.org/10.1021/acsomega.1c05463.

(62) Perryman, J. T.; Hyler, F. P.; Ortiz-Rodríguez, J. C.; Mehta, A.; Kulkarni, A. R.; Velázquez, J. M. X-Ray Absorption Spectroscopy Study of the Electronic Structure and Local Coordination of 1st Row Transition Metal-Promoted Chevrel-Phase Sulfides. *J. Coord. Chem.* **2019**.

(63) Hyler, F. P.; Bille, B. A. W.; Ortíz-Rodríguez, J. C.; Sanz-Matias, A.; Roychoudhury, S.; Perryman, J. T.; Patridge, C. J.; Singstock, N. R.; Musgrave, C. B.; Prendergast, D.; Velázquez, J. M. X-Ray Absorption Spectroscopy Insights on the Structure Anisotropy and Charge Transfer in Chevrel Phase Chalcogenides. *Phys. Chem. Chem. Phys.* **2022**, *24* (28), 17289–17294. https://doi.org/10.1039/D1CP04851A.

(64) Kompch, A.; Sahu, A.; Notthoff, C.; Ott, F.; Norris, D. J.; Winterer, M. Localization of Ag Dopant Atoms in CdSe Nanocrystals by Reverse Monte Carlo Analysis of EXAFS Spectra. *J. Phys. Chem. C* **2015**, *119* (32), 18762–18772. https://doi.org/10.1021/acs.jpcc.5b04399.

(65) Yao, S. A.; Lancaster, K. M.; Götz, A. W.; DeBeer, S.; Berry, J. F. X-Ray Absorption Spectroscopic, Crystallographic, Theoretical (DFT) and Chemical Evidence for a Chalcogen–Chalcogen Two-Center/Three-Electron Half Bond in an Unprecedented "Subselenide" Se23− Ligand. *Chem. – Eur. J.* **2012**, *18* (30), 9179–9183. https://doi.org/10.1002/chem.201201291.

(66) Henthorn, J. T.; DeBeer, S. Selenium Valence-to-Core X-Ray Emission Spectroscopy and Kβ HERFD X-Ray Absorption Spectroscopy as Complementary Probes of Chemical and Electronic Structure. *Inorg. Chem.* **2022**, *61* (6), 2760–2767. https://doi.org/10.1021/acs.inorgchem.1c02802.

(67) Lu, T.; Chen, F. Multiwfn: A Multifunctional Wavefunction Analyzer. *J. Comput. Chem.* **2012**, *33* (5), 580–592. https://doi.org/10.1002/jcc.22885.

(68) Reber, A. C.; Chauhan, V.; Khanna, S. N. Symmetry and Magnetism in Ni9Te6 Clusters Ligated by CO or Phosphine Ligands. *J. Chem. Phys.* **2017**, *146* (2), 024302. https://doi.org/10.1063/1.4973609.

(69) Puttreddy, R.; Hutchison, J. A.; Gorodetski, Y.; Harrowfield, J.; Rissanen, K. Enantiomer Separation of Tris(2,2′-Bipyridine)Ruthenium(II): Interaction of a D3-Symmetric Cation with a C2-Symmetric Anion. *Cryst. Growth Des.* **2015**, *15* (4), 1559–1563. https://doi.org/10.1021/acs.cgd.5b00053.

(70) Evans, D. F. 400. The Determination of the Paramagnetic Susceptibility of Substances in Solution by Nuclear Magnetic Resonance. *J. Chem. Soc. Resumed* **1959**, 2003. https://doi.org/10.1039/jr9590002003.

(71) Frisch, M. J.; Trucks, G. W.; Schlegel, H. B.; Scuseria, G. E.; Robb, M. A.; Cheeseman, J. R.; Scalmani, G.; Barone, V.; Petersson, G. A.; Nakatsuji, H.; Li, X.; Caricato, M.; Marenich, A. V.; Bloino, J.; Janesko, B. G.; Gomperts, R.; Mennucci, B.; Hratchian, H. P.; Ortiz, J. V.; Izmaylov, A. F.; Sonnenberg, J. L.; Williams; Ding, F.; Lipparini, F.; Egidi, F.; Goings, J.; Peng, B.; Petrone, A.; Henderson, T.; Ranasinghe, D.; Zakrzewski, V. G.; Gao, J.; Rega, N.; Zheng, G.; Liang, W.; Hada, M.; Ehara, M.; Toyota, K.; Fukuda, R.; Hasegawa, J.; Ishida, M.; Nakajima, T.; Honda, Y.; Kitao, O.; Nakai, H.; Vreven, T.; Throssell, K.; Montgomery Jr., J. A.; Peralta, J. E.; Ogliaro, F.; Bearpark, M. J.; Heyd, J. J.; Brothers, E. N.; Kudin, K. N.; Staroverov, V. N.; Keith, T. A.; Kobayashi, R.; Normand, J.; Raghavachari, K.; Rendell, A. P.; Burant, J. C.; Iyengar, S. S.; Tomasi, J.; Cossi, M.; Millam, J. M.; Klene, M.; Adamo, C.; Cammi, R.; Ochterski, J. W.; Martin, R. L.; Morokuma, K.; Farkas, O.; Foresman, J. B.; Fox, D. J. Gaussian 16 Rev. C.01, 2016.

(72) Kaupp, M.; Köhler, F. H. Combining NMR Spectroscopy and Quantum Chemistry as Tools to Quantify Spin Density Distributions in Molecular Magnetic Compounds. *Coord. Chem. Rev.* **2009**, *253* (19), 2376–2386. https://doi.org/10.1016/j.ccr.2008.12.020.

(73) Roquette, P.; Maronna, A.; Reinmuth, M.; Kaifer, E.; Enders, M.; Himmel, H.-J. Combining NMR of Dynamic and Paramagnetic Molecules: Fluxional High-Spin Nickel(II) Complexes Bearing Bisguanidine Ligands. *Inorg. Chem.* **2011**, *50* (5), 1942–1955. https://doi.org/10.1021/ic102420x.

(74) Karschin, N.; Krenek, S.; Heyer, D.; Griesinger, C. Extension and Improvement of the Methanol-D4 NMR Thermometer Calibration. *Magn. Reson. Chem. MRC* **2022**, *60* (2), 203–209. https://doi.org/10.1002/mrc.5216.

(75) Ravel, B.; Newville, M. ATHENA, ARTEMIS, HEPHAESTUS: Data Analysis for X-Ray Absorption Spectroscopy Using IFEFFIT. *J. Synchrotron Radiat.* **2005**, *12* (4), 537–541. https://doi.org/10.1107/S0909049505012719.

(76) Newville, M.; Stensitzki, T.; Allen, D. B.; Ingargiola, A. LMFIT: Non-Linear Least-Square Minimization and Curve-Fitting for Python, 2014. https://doi.org/10.5281/zenodo.11813.

(77) *Bruker APEX2 (Version 2.1-4), SAINT (Version 7.34A), SADABS (Version 2007/4), 2007 BrukerAXS Inc, Madison, Wisconsin, USA.*

(78) *Sheldrick, G.M. Acta Cryst. 2015 A71, 3-8.*

(79) *Altomare, A.; Burla, C.; Camalli, M.; Cascarano, G. L.; Giacovazzo, C.; Guagliardi, A.; Moliterni, A.G.G.; Polidori, G.; Spagna, R. J. Appl. Crystallogr., 1999, 32, 115-119.*

(80) *Altomare, A.; Cascarano, G. L.; Giacovazzo, C.; Guagliardi, A. J. Appl. Crystallogr., 1993, 26, 343-350.*

(81) *Sheldrick, G. M. SHELXL-97, Program for the Refinement of Crystal Structures, 1997, University of Göttingen, Germany.*

(82) *Sheldrick, G. M. Acta Cryst. 2015, C71, 3–8.*

(83) *Mackay, S.; Edwards, C.; Henderson, A.; Gilmore, C.; Stewart, N.; Shankland, K.; Donald, A. MaXus: A Computer Program for the Solution and Refinement of Crystal Structures from Diffraction Data, 1997, University of Glasgow, Scotland.*

(84) *Waasmaier, D.; Kirfel, A. Acta Cryst., 1995, 51, 416-430.*

Chapter 2. PROBING THE SYNTHETIC LIMITS OF THE $Co_6Se_8L_6$ SYSTEM WITH BIFUNCTIONAL PHOSPHINE LIGANDS

2.1 ABSTRACT

The $M_6X_8L_6$ family of octahedral clusters represents an important bridge between molecular systems and materials science, offering opportunities for designing functional nanoscale systems. While our previous work established the utility of Ph2PNHTol ligands in creating ternary nanocluster systems, expanding the range of phosphine ligands promises to unlock new reactivity patterns and properties. Here, we report the synthesis and characterization of a series of $Co_6Se_8L_6$ clusters featuring bifunctional phosphine ligands, where L includes various heteroatom-containing groups such as alcohols, ethers, thioethers, and amines. These clusters were obtained in moderate yields through the reaction of dicobalt octacarbonyl with the corresponding phosphine selenides. Single crystal X-ray diffraction revealed that while Co–Se distances remain remarkably consistent across the series, Co–P and Co…Co distances vary significantly with ligand identity and cluster oxidation state. The introduction of hydrogen-bonding functionalities dramatically influences cluster solubility, with phosphinoalcohol-decorated clusters showing selective solubility in polar aprotic solvents. Although attempts to generate ternary clusters through deprotonation and transmetallation were unsuccessful, likely due to coordination polymer formation, this work establishes the broad compatibility of bifunctional phosphine ligands with the $Co_6Se_8L_6$ framework and provides insight into structure-property relationships and importance of precise ligand design in these systems.

2.2 INTRODUCTION

At the intersection of molecular chemistry and nanoscale engineering lie the $M_6X_8L_6$ family of octahedral clusters (M = metal, X = chalcogen, L = ligand). In our exploration of the field, we have focused on the development of ternary nanoclusters of this type capable of supporting transition metal edge sites, pushing the envelope of the structural paradigm. Our initial efforts settled on the usage of the $Ph_2PNHTol$ (Tol = 4-tolyl) ligand, the geometry and amide functionality of which allows for facile transmetallation and formation of edge sites with templated low-coordinate geometry, all while retaining solubility in common organic solvents.[1–3] However, venturing

beyond this ligand promises to open new avenues of research with these ternary nanoclusters, such as better stability to ambient conditions (especially water), transmetallation with different transition metals, and new catalytic reactivity. As such, we decided to synthesize several new nanoclusters through synthetic variation of the capping phosphine ligands to probe their usage in future studies.

The presence of tunable heteroatom functionality in phosphine ligands offers a powerful handle for tuning the properties of octahedral clusters. While traditional phosphines provide reliable metal coordination through their P-donor sites, incorporating additional functional groups like hydroxyl, amine, or thioether moieties alter the fundamental characteristics of metal coordination and opens new possibilities for surface reactivity and cluster stability. The majority of studies concerning $M_6X_8L_6$ (L = phosphine) clusters utilize inert trialkyl or triaryl phosphines, generally for solubility reasons and/or compatibility with harsh synthetic conditions.[4–11] The scattered examples of functional phosphine ligands in such systems have demonstrated their ability to engender water solubility, form polymeric networks via ligand reactivity, or allow for incorporation into electronic devices.[12–15] In our design, maintaining two phenyl groups on phosphorus ensures structural rigidity and crystallinity, while strategic modification of the third substituent allows us to introduce these diverse functionalities. This approach enables us to dramatically alter the cluster's chemical behavior compared to our initial $Ph_2PNHTol$ system, while still benefiting from the stability of the Co–P bond.

2.3 Results and Discussion

2.3.1 *Motivation and selection of phosphines*

We aimed to specifically target phosphine ligands which would engender edge site binding modes unlike those seen previously. Specifically, ligands allowing for tripodal coordination geometries were desired, leading to the testing of ligands with spacer groups (e.g. $–(CH_2)_n$-) between the diphenylphosphine group and the heteroatom functional group. In the opposite vein, diphenylphosphine itself (Ph_2PH) was chosen as a candidate due to it possibly providing a more intimate edge metal binding motif, where the cluster-bound secondary phosphine is deprotonated and transmetalated to give a ternary nanocluster with a direct M–P bond. Furthermore, ligands with neutral ligand binding modes (namely ethers and thioethers) were incorporated onto the

cluster surface to extend the diversity of available coordination motifs. Overall, many of the phosphine archetypes have been previously studied in transition metal coordination complexes and described as hemilabile due to their bifunctionality.[16–18]

2.3.2 *Synthetic Approaches to $Co_6Se_8L_6$ Formation*

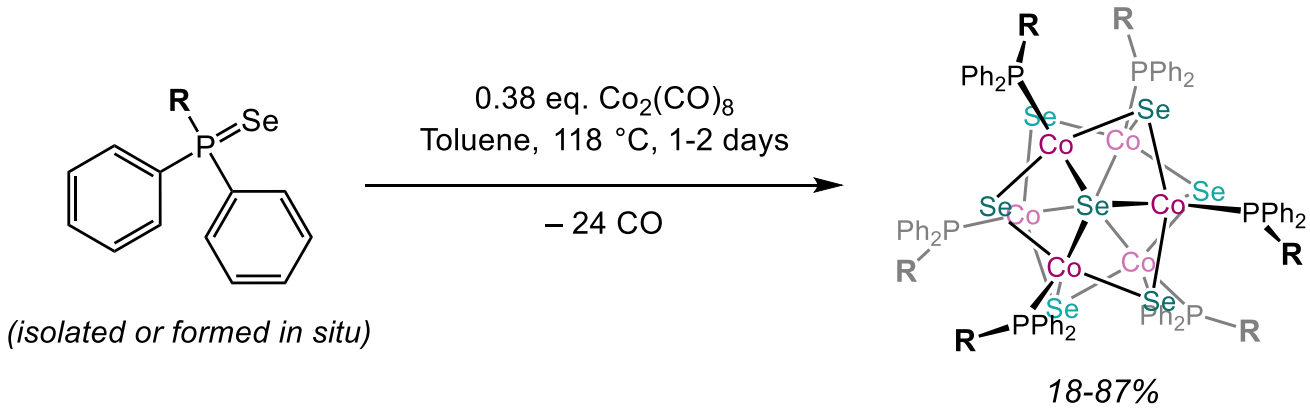

R = H, STol, CH_2NHTol, CH_2OH, CH_2CH_2OH, CH_2OCH_3, $CH_2C_4H_7O$

Scheme 3. Generalized Synthesis of $Co_6Se_8(Ph_2R)_6$ clusters.

Systemic exploration yielded seven new nanoclusters that were successfully synthesized in yields ranging from 13 to 87% (Scheme 3, Section 2.5). Each cluster is of the general formula $Co_6Se_8(Ph_2R)_6$, where R is varied to form an array of phosphine ligands with different functionalities. The various phosphines were synthesized via literature procedures as needed.[19–23] In most cases, the phosphine was converted to the phosphine selenide to increase the air stability and handling characteristics of the phosphines, most of which are viscous liquids as the phosphine but solids as the selenide. Synthetic procedures and characterization for any previously unreported compounds are in section 2.5. Refluxing dicobalt octacarbonyl with the respective phosphine selenide (or the phosphine and elemental selenium) in toluene generally yields the homoleptic cluster after 1-2 days. We found this approach to be broadly applicable to all phosphine ligands that were tested.

2.3.3 *General Properties of the Nanoclusters*

In general, the $Co_6Se_8L_6$ clusters are present as dark brown air-stable solids. Nuclear Mass Resonance (NMR) spectroscopy generally indicates that the clusters are highly symmetric in

solution, with a single signal for all six phosphine ligands. The ^{31}P NMR signal for the neutral homoleptic clusters is located within the range of 30-100 ppm, with the singular peak being quite broad in any case ($\nu_{1/2}$ = 175-800 Hz for the neutral clusters, up to 2800 Hz for oxidized clusters). The solubilities of the clusters vary drastically and can be rationalized by comparing their respective functional groups. In the most extreme case of the phosphinoalcohol ligated clusters, the material has negligible solubility in most solvents, with the exception being highly polar aprotic solvents such as dimethylformamide or dimethyl sulfoxide. Water does not solubilize the phosphinoalcohol clusters to any degree, likely due to the presence of hydrophobic phenyl groups on the cluster's exterior.

As single-crystal structures would reveal, extensive hydrogen bonding from the -OH groups to the solvent are responsible for the solubility of the phosphinoalcohol clusters in these solvents. Solid state-structures also indicate that, in the case of $Co_6Se_8(Ph_2PCH_2CH_2OH)_6$, inter-cluster hydrogen bonding is still present even with a large amount of dimethylformamide in the lattice. On the other hand, the trimethylsilylated versions of these phosphinoalcohol clusters have excellent solubility in a variety of moderately polar solvents such as dichloromethane and tetrahydrofuran, explained by the replacement of polar hydrogen-bonding -OH groups with lipophilic -$SiMe_3$ groups. The silylation of the isolated phosphinoalcohol clusters proceeds swiftly upon treatment with trimethylsilyl chloride (Section 2.5.13), exemplifying the potential for the on-cluster reactivity and derivatization of phosphine ligands.

The presence of the diphenyl moiety in each cluster, while conferring crystallinity, does appear to be a primary culprit for one of the practical drawbacks of the clusters described in this study, namely low solubility. For example, the $Co_6Se_8(Ph_2PH)_6$ cluster is only slightly soluble in toluene and dichloromethane despite its low dipole moment and hydrocarbon exterior. Based on the solid-state crystal structure, we hypothesize that π-π interactions resulting from the interdigitation of the phenyl rings are the main culprit. In fact, compared to the previously reported $Co_6Se_8(Ph_2PNHTol)_6$ cluster, both the $Co_6Se_8(Ph_2PCH_2NHTol)_6$ and $Co_6Se_8(Ph_2PSTol)_6$ clusters have substantially lower solubilities, possibly due to the greater flexibility and separation of the tolyl group from the cluster core due to the extra spacer group and longer P–S vs P–N distance, respectively. A similar predicament was reported in the study of $W_6S_8L_6$ (R_2PR', R = phenyl or ethyl, R' = thiophene) clusters, where the compounds with diphenylphosphine-derived ligands had prohibitively low solubilities.[15]

2.3.4 *Structural Parameter Comparison*

Crystallography of the clusters proved feasible throughout the entire series, allowing for a thorough comparison of the effects of ligand substitution on the family of nanoclusters (Table 3, Section 2.6). In some cases, the cluster was crystallized in oxidized form with a weakly coordinating anion such as PF_6^- as the counterion.

Table 6. Structural parameters for homoleptic clusters with general formula $Co_6Se_8L_6$. Some clusters were crystallized in oxidized form and are marked accordingly.

Phosphine	**Average Co–P distance (Å)**	**Average Co…Co distance (Å)**	**Average Co–Se distance (Å)**
$Ph_2PNHTol$[a]	2.129(10)	2.944(8)	2.346(4)
$Ph_2PNHTol$[a] ***[cluster oxidized]***	2.161(2)	2.90(16)	2.341(4)
Ph_2PCH_2NHTol	2.152(10)	2.991(4)	2.344(7)
Ph_2PSTol	2.113(3)	2.95(11)	2.343(3)
Ph_2PCH_2OH	2.146(9)	2.94(10)	2.339(3)
$Ph_2PCH_2OCH_3$	2.131(4)	2.95(15)	2.345(3)
$Ph_2PCH_2O(Si(CH_3)_3)$ ***[cluster oxidized]***	2.166(10)	2.91(13)	2.346(19)
$Ph_2PCH_2O(Si(CH_3)_3)$ ***[cluster dioxidized]***	2.184(3)	2.85(2)	2.341(4)
$Ph_2PCH_2H_2OH$	2.138(3)	2.969(4)	2.344(3)
$Ph_2PCH_2CH_2O(SiMe_3)$	2.184(3)	2.85(2)	2.38(4)
$Ph_2PCH_2(C_4H_7O)$	2.151(3)	2.89(2)	2.333(5)
Ph_2PH	2.119(8)	2.907(7)	2.337(2)
Ph_2PH ***[cluster oxidized]***	2.143(13)	2.87(17)	2.337(3)

[a]Previously reported structures[8]

Firstly, it is obvious that the significant structural variations are expressed through the Co…Co and Co–P distances, with the Co–Se distances being very consistently around 2.34 Å,

even when comparing the neutral vs. oxidized clusters. This paradigm was similarly observed in the series of $[Cu_3Co_6Se_8(Ph_2PNTol)_6]^{n+}$ (n = 0, 1, 2, 3) nanoclusters.[24] The average Co–P distances spans a range of 2.113-2.184 Å and generally serves as a proxy for the electron deficiency of the cluster core, with longer distances correlating to greater deficiency, although steric effects are also significant. For example, both $Co_6Se_8(Ph_2PSTol)_6$ and $[Co_6Se_8(Ph_2NHTol)_6]^+$ have longer Co–P distances than in $Co_6Se_8(Ph_2NHTol)_6$, due to the lower electronegativity of S vs. N and one-electron oxidation respectively. Meanwhile, Ph_2PH is ostensibly one of the more electron-deficient phosphines in this series, but has one of the shortest Co–P distances due to having the least demanding steric profile. The trends in Co…Co distances are less obvious, with a rise in oxidation state resulting in substantial contraction of the Co_6 octahedron, with the effect of ligand identity on Co…Co distances more difficult to trace.

2.3.5 *Challenges with cluster deprotonation and transmetallation*

One of the most obvious avenues for further synthesis starting from the nanoclusters is the metalation to form ternary nanoclusters with transition metal edge sites. However, we consistently encountered major issues with any attempt at deprotonation of the clusters. The treatment of the phosphinoalcohol clusters with strong base, for instance, invariably resulted in the immediate precipitation of a dark brown solid which could not be dissolved in any tested solvent. The identity of the solid is most likely a coordination polymer of deprotonated clusters bridged by the cation of the strong base, although the precipitate has resisted attempts at definitive characterization. It is likely that the sterically unprotected nature of the phosphinoalcohol ligands makes irreversible catenation of the corresponding metal alkoxide facile, precluding isolation of a molecular species.

Other issues were encountered when polymerization was unlikely, such as in the sterically protected $Co_6Se_8(Ph_2PCH_2NHTol)_6$. Treatment of the cluster resulted in decomposition of the compound and was attributed to the breaking of the P–C bond, which was previously reported in the free ligand.[21] Less direct approaches to metalation proved similarly challenging. The trimethylsilyl-protected clusters with L = $Ph_2PCH_2OSi(CH_3)_3$ and $Ph_2PCH_2CH_2OSi(CH_3)_3$ were treated with strong Lewis acids such as $FeCl_3$ or $NbCl_5$ in hopes of simultaneously deprotecting the silyl group and metalating the now-exposed alkoxide. However, the only species that could be isolated from these reactions was starting material or oxidized cluster, such as the dioxidized cluster $[Co_6Se_8(Ph_2PCH_2CH_2OSi(CH_3)_3)_6][FeCl_4]_2$ obtained in the case of treatment with $FeCl_3$.

2.4 Conclusion

The compatibility of bifunctional substituted phosphines with the conditions of $Co_6Se_8L_6$ synthesis is demonstrated, with exposed, highly protic functional groups such as primary alcohols giving no issue during synthesis. While the successful incorporation of diverse bifunctional phosphines demonstrates the synthetic robustness of these clusters, their subsequent reactivity highlights critical challenges in nanocluster design. The dramatic influence of surface functionality on cluster properties, particularly the formation of extensive hydrogen bonding networks in phosphinoalcohol clusters, suggests opportunities for engineering specific intermolecular interactions. A central lesson is that steric protection must be sufficient to prevent coordination polymer formation while maintaining reactivity at desired sites. In a related vein, obstructing the uniformity of the surface ligand geometry to prevent π-π stacking also appears to be strongly beneficial for conferring favorable solubility in common solvents. These insights provide a foundation for rational design of next-generation nanoclusters, suggesting that future work should focus on ligand systems with carefully positioned steric bulk and a deliberate level of surface heterogeneity.

2.5 Synthetic Details and Characterization of Products

2.5.1 *General Information*

All syntheses were conducted under a dinitrogen atmosphere using a standard Schlenk line or an LC Technology Solutions glovebox equipped with a freezer set to −35 °C. All glassware was dried at 160 °C for a minimum of 12 h prior to use.

Solvents were purchased from Fisher Scientific and degassed, dried and purified using solvent purification columns housed in a stainless-steel cabinet and dispensed by a stainless-steel Schlenk line manufactured by JC Meyer Solvent Systems. Tetrahydrofuran (THF), diethyl ether (Et_2O), and methylene chloride (DCM) are passed through two packed columns of neutral alumina. *n*-Pentane, benzene, and toluene are passed through a column packed with alumina, and one containing Q5 reactant, a copper(II) oxide oxygen scavenger. All solvents were passed through an in-line, 2 μm filter, then stored over activated 3Å molecular sieves in the glovebox. 3Å molecular sieves were purchased from Sigma Aldrich and activated under vacuum at 300 °C

for 48 h. Anhydrous pyridine (99.8%) was purchased from Sigma Aldrich and stored over activated 3Å molecular sieves for 72 h prior to use.

Deuterated solvents were purchased from Sigma Aldrich, degassed and dried over activated 3Å molecular sieves in the glovebox for a minimum of 72 h. $Co_2(CO)_8$ (stabilized with 2-5% hexanes, Strem Chemicals, Inc.) was stored in the glovebox freezer, and used as received. Selenium (99.5%, powder, ~325 mesh, Fisher Scientific), diphenylphosphine (Sigma Aldrich), and *n*-butyl lithium (2.5 M in hexanes, Sigma Aldrich) were used as received. UV-vis-*n*IR absorption spectra were acquired using a Varian Cary 5000 UV-Vis-*n*IR spectrophotometer, in *n*IR quartz cuvettes (Spectrocell Inc., 10 mm path length, 220–3500 nm spectral window). Attenuated total reflectance infrared (ATR-IR) spectra were recorded on a Bruker Alpha IR instrument equipped with a Platinum ATR accessory housed within a nitrogen glovebox. NMR spectra were acquired at 25 °C unless indicated otherwise on Bruker 300 or 500 MHz spectrometers. ^{1}H NMR spectra were referenced to residual deuterated solvent peaks.

2.5.2 *Synthesis of Ph_2PCH_2NHTol*

A modified literature procedure was followed.[21] Outside of the glovebox, a 50 mL Schlenk flask with Teflon-coated stir bar was charged with paraformaldehyde (0.182 g, 6.06 mmol) and capped with a rubber septum. The interior of the flask was degassed and backfilled with nitrogen. Diphenylphosphine (1.07 g, 1.00 mL, 5.37 mmol) was taken up in a syringe and injected into the flask. The resulting suspension is heated to 110 °C in an oil bath with stirring. Within 30 minutes, the suspension changes to a clear liquid. After cooling the flask to room temperature, dichloromethane (10 mL) is injected into the flask, making sure to rinse the walls of the flask. The flask is cooled to -78 C° in a dry ice/acetone bath and injected with *para*-toluidine dissolved in dichloromethane. The mixture is stirred and placed under dynamic vacuum overnight, slowly warming to room temperature. The flask is taken into the glovebox and the clear liquid filtered through Celite before removing the solvent under vacuum, resulting in isolation of a clear viscous liquid. The liquid is then crystallized by diluting with a small amount of dichloromethane (approx. 1 mL) and layering with pentane (15 mL) before cooling the mixture in the freezer. The next day, the resulting crystals are isolated via vacuum filtration and washed with pentane, giving the product as a white solid (0.900 g, 2.95 mmol, 51%). ^{1}H NMR (benzene-d_6, 500 MHz) δ: 7.47-7.36 (m, 4H, PPh_2 *m*-Ar***H***), 7.12-7.01 (m, 6H, PPh_2, *o*,*p*-Ar***H***), 6.95 (d, *J*=8.1 Hz, 2H, tolyl *m*-Ar***H***), 6.39 (d, *J*=8.4 Hz, 2H, tolyl *o*-Ar***H***), 3.65 (dd, *J*=5.9, 4.1 Hz, 2H, C***H***$_2$), 3.42 (q, *J*=5.5 Hz, 1H, N***H***), 2.17 (s, 3H, tolyl C***H***$_3$). ^{31}P NMR (benzene-d_6, 121 MHz) δ: -18.9.

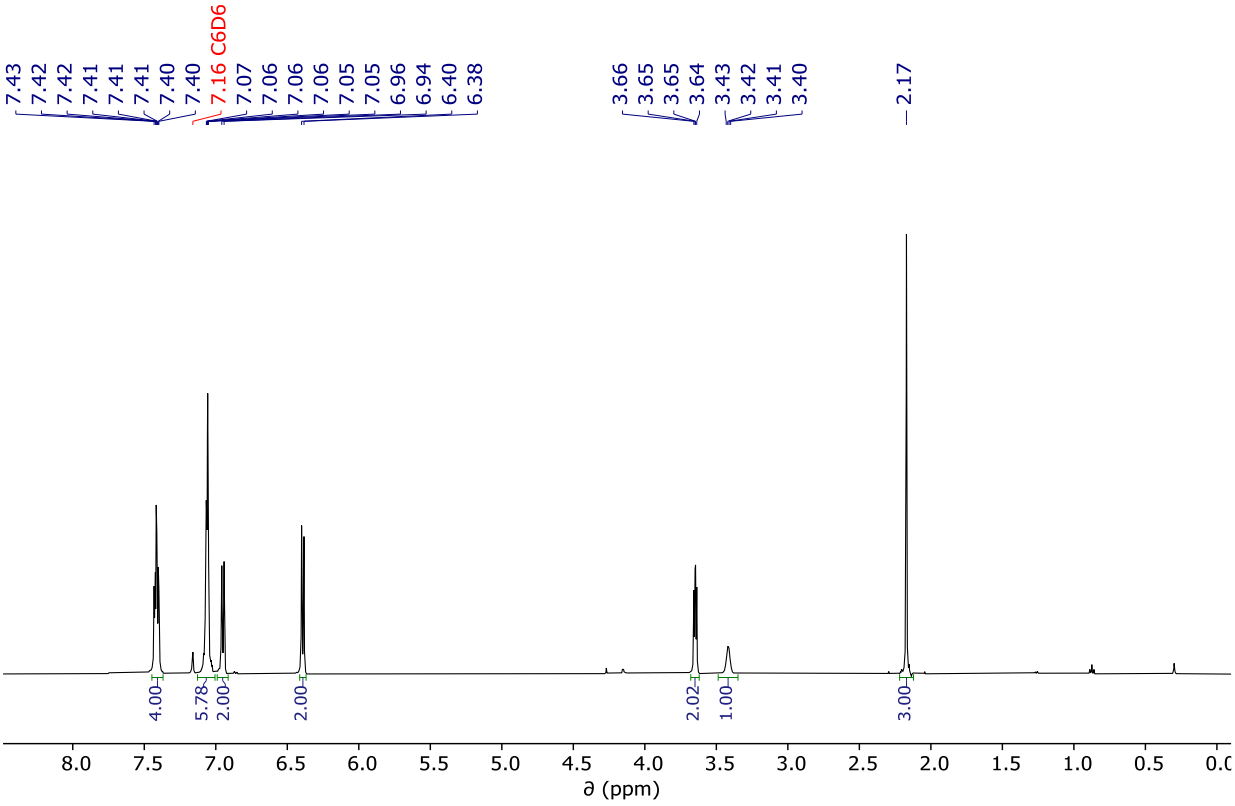

Figure 52. ^{1}H NMR (C_6D_6, 25 °C, 500 MHz) spectrum of Ph_2PCH_2NHTol

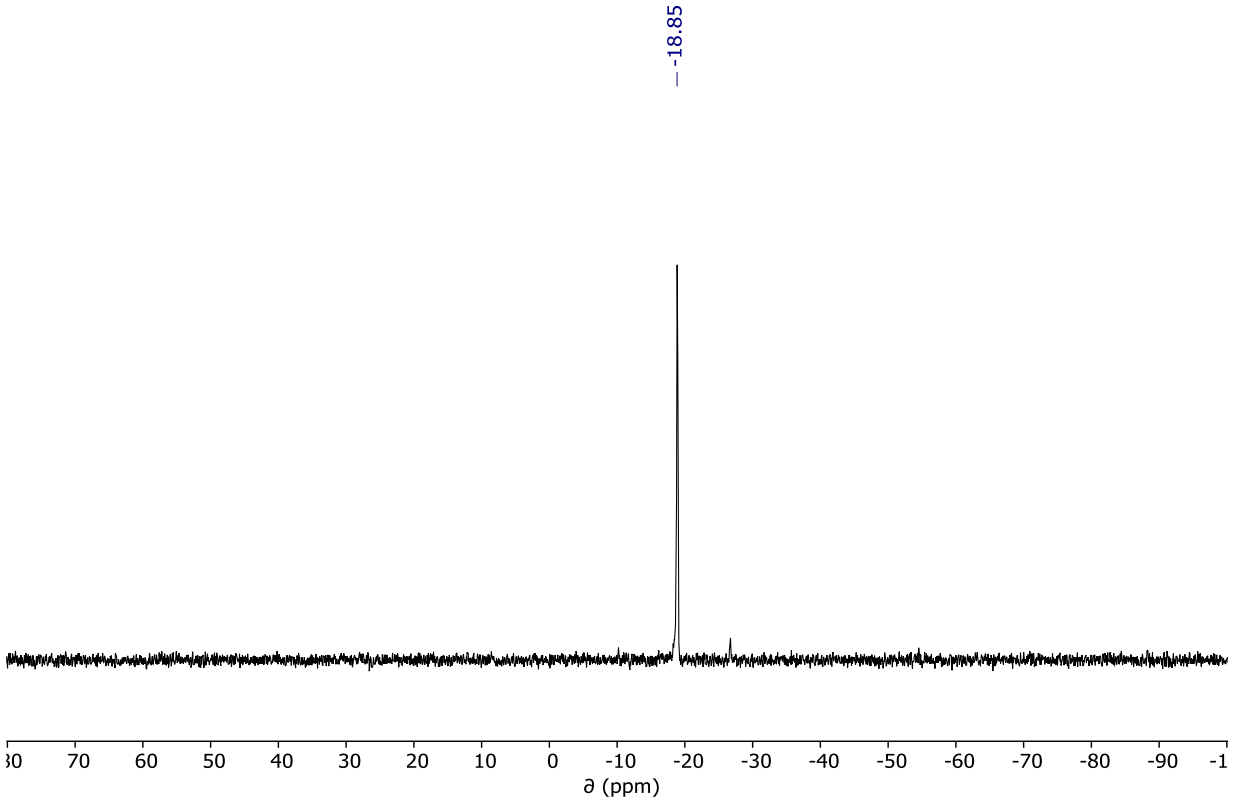

Figure 53. ^{31}P NMR (C_6D_6, 25 °C, 202 MHz) spectrum of Ph_2PCH_2NHTol

2.5.3 *Synthesis of Ph_2PSeCH_2OH*

Outside of the glovebox, a 50 mL Schlenk flask with Teflon-coated stir bar was charged with paraformaldehyde (0.190 g, 6.33 mmol) and capped with a rubber septum. The interior of the flask was degassed and backfilled with nitrogen. Diphenylphosphine (1.07 g, 1.0 mL, 5.75 mmol) was taken up in a syringe and injected into the flask. The resulting suspension is heated to 110 °C in an oil bath with stirring. Within 30 minutes, the suspension changes to a clear liquid. After cooling the flask to room temperature, dichloromethane (10 mL) is injected into the flask, making sure to rinse the walls of the flask. The flask is then charged with selenium powder (0.545 g, 6.90 mmol), and stirred at room temperature for 1 hour. The flask is taken into the glovebox and the clear liquid filtered through Celite before removing the solvent under vacuum, resulting in isolation of a clear viscous liquid (1.647 g, 5.58 mmol, 97%). ^{31}P NMR ($CDCl_3$, 121 MHz) δ: -36.8.

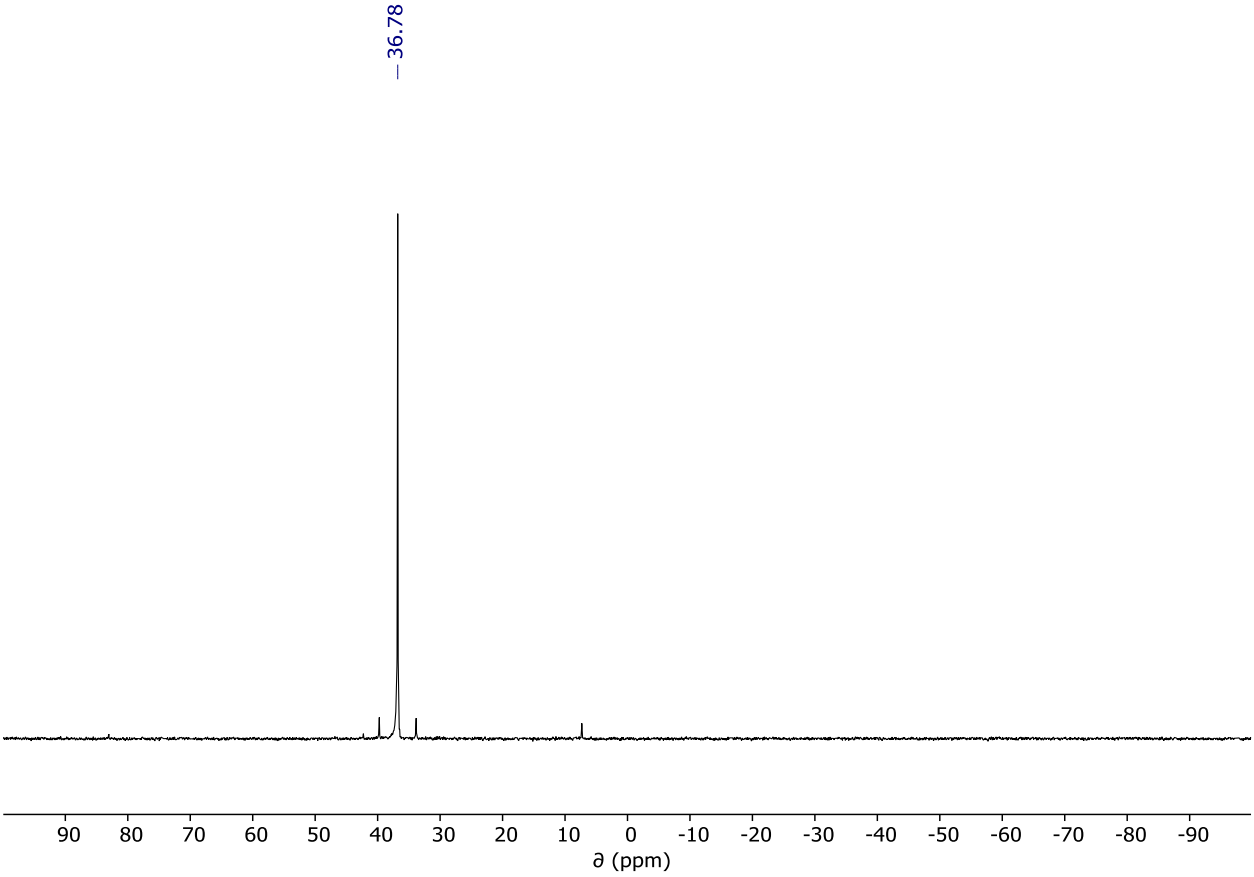

Figure 54. ^{31}P NMR ($CDCl_3$, 25 °C, 202 MHz) spectrum of Ph_2PSeCH_2OH

2.5.4 *Synthesis of $Ph_2PSeCH_2CH_2OH$*

Inside the glovebox, diphenylphosphine (2.327 g, 12.5 mmol) and 2-bromoethanol (1.562 g, 12.5 mmol) are weighed out into separate vials and diluted with 15 mL tetrahydrofuran each. The solutions are combined in a 100 mL Schlenk flask, which is then capped with a rubber septum and brought out of the glovebox before being put under nitrogen flow on the Schlenk line. The flask is then cooled in an ice bath. Once the flask has cooled, a solution of n-butyllithium in hexanes (2.5 M, 10 mL, 25.0 mmol) is injected dropwise into the flask, ultimately resulting in a pale yellow-orange solution. The solution is left to stir in the ice bath for two hours. The ice bath is removed, and selenium powder (1.480 g, 18.7 mmol) is added to the flask, which is left to stir at room temperature for one hour. The solvent is then removed from the dark red solution using the Schlenk line vacuum. The residue is extracted with dichloromethane (30 mL) and quenched with excess ammonium chloride. The suspension is filtered through Celite and concentrated until nearly dry, then diluted with diethyl ether (25 mL). The ether solution is washed with water in a separatory funnel and dried over sodium sulfate. The ether solution is concentrated on the rotovap, yielding the product as an orange oil (1.663 g, 5.38 mmol, 43%). If desired, the product can be converted to an off-white powder by dilution with a small amount of toluene and ether, followed by dilution with pentane and cooling in the fridge. ^{1}H NMR (benzene-d_6, 300 MHz) δ: 7.78-7.63 (m, 4H), 6.95 (m, 6H), 3.85 (dt, J=19.9, 6.0 Hz, 2H), 2.78 (s, 1H), 2.42 (dt, J=11.0, 6.0 Hz, 2H). ^{31}P NMR (benzene-d_6, 121 MHz) δ: 41.25.

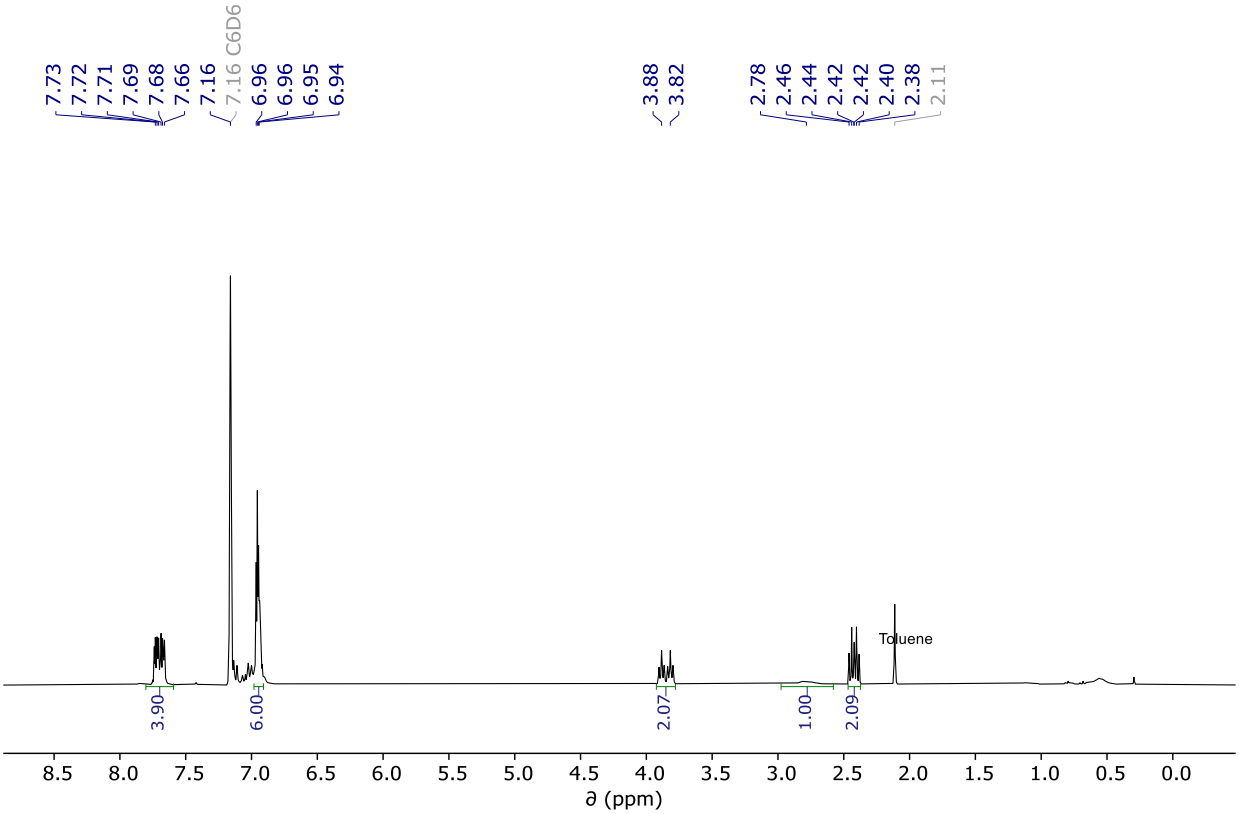

Figure 55. ^{1}H NMR (C_6D_6, 25 °C, 300 MHz) spectrum of $Ph_2PSeCH_2CH_2OH$

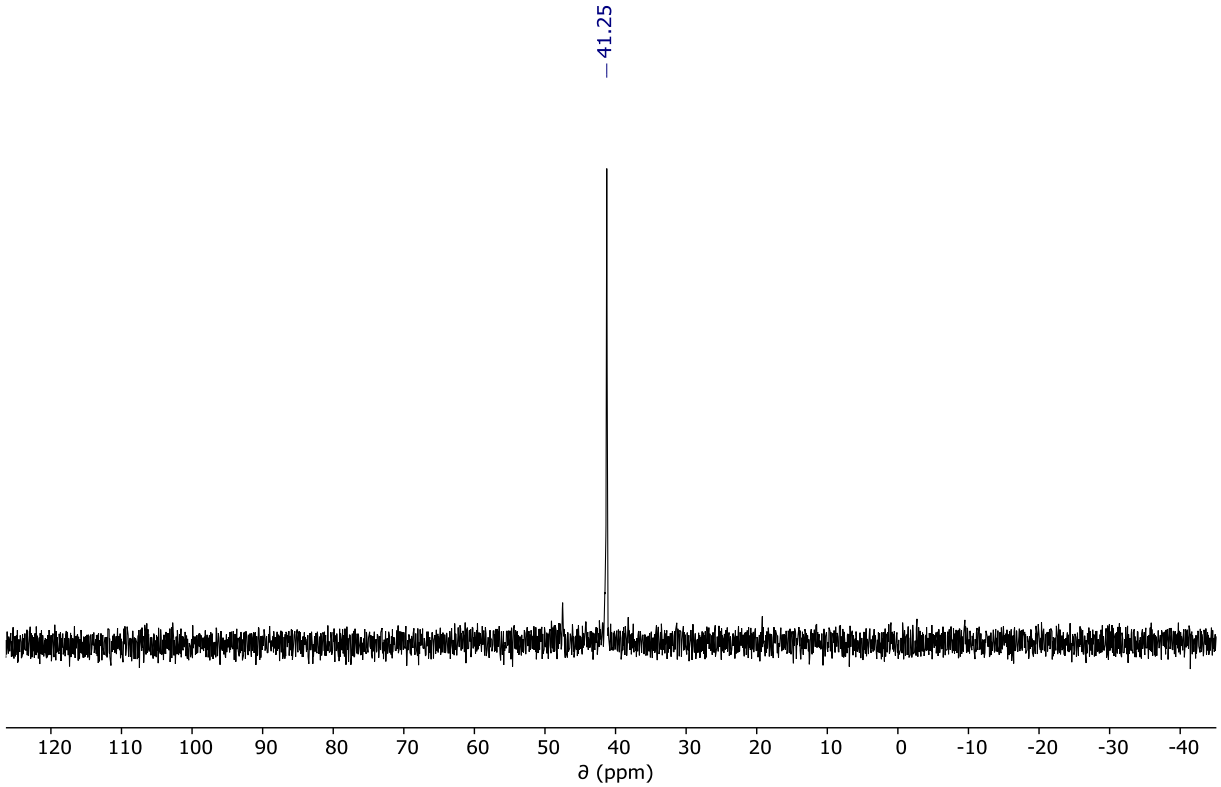

Figure 56. ^{31}P NMR (C_6D_6, 25 °C, 101 MHz) spectrum of $Ph_2PSeCH_2CH_2OH$

2.5.5 *Synthesis of Ph_2PSTol*

Inside the glovebox, a 500 mL Schlenk flask with Teflon-coated stirbar was charged with potassium hydride (1.292 g, 32.2 mmol) and diethyl ether (150 mL). The flask is capped with a rubber septum and brought out of the glovebox and attached to the Schlenk line. An addition funnel is connected to the flask and purged with nitrogen. 4-Methylbenzenethiol (4.000 g, 32.2 mmol) is dissolved in diethyl ether (24 mL) and the resulting solution is transferred to the addition funnel via syringe. The thiol solution is added dropwise to the stirring suspension of potassium hydride while stirring, resulting in the formation of a milky suspension. After stirring overnight while venting through the Schlenk line, a solution of chlorodiphenylphosphine (7.105 g, 32.2 mmol) in diethyl ether (24 mL) is added to the addition funnel. The flask is cooled in an ice bath, then the chlorodiphenylphosphine solution is added dropwise to the mixture while stirring. The ice bath was removed and the reaction mixture left to warm to room temperature and stir for 3 hours. The solvent is removed from the mixture under vacuum and the flask returned to the glovebox, where the residue is extracted with toluene (80 mL). The extract is filtered through Celite and the solvent removed from the filtrate under vacuum, yielding the product as a colorless liquid (9.031 g). ^{1}H NMR ($CDCl_3$, 500 MHz) δ: 7.60 (m, 4H), 7.37 (m, 8H), 7.07 (d, J = 7.8 Hz, 2H), 2.31 (s, 3H). ^{31}P NMR ($CDCl_3$, 202 MHz) δ: -33.98.

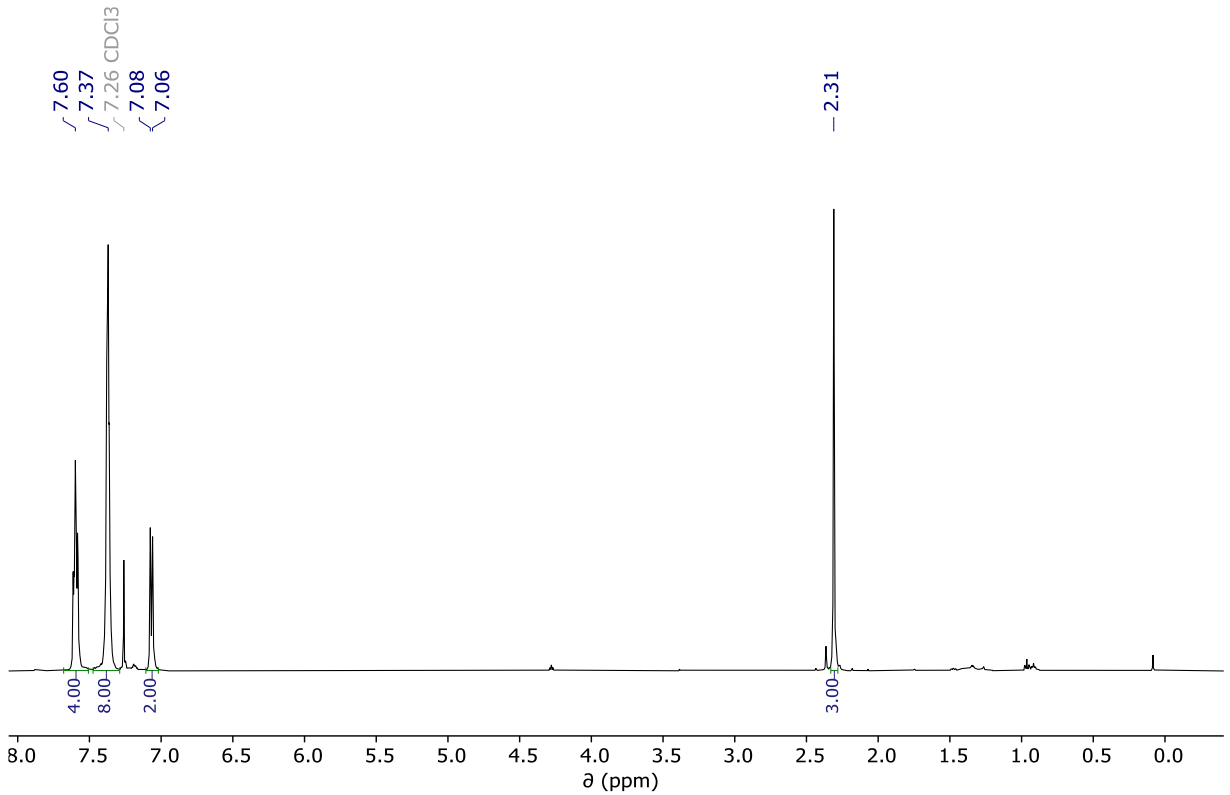

Figure 57. ^{1}H NMR ($CDCl_3$, 25 °C, 500 MHz) spectrum of Ph_2PSTol

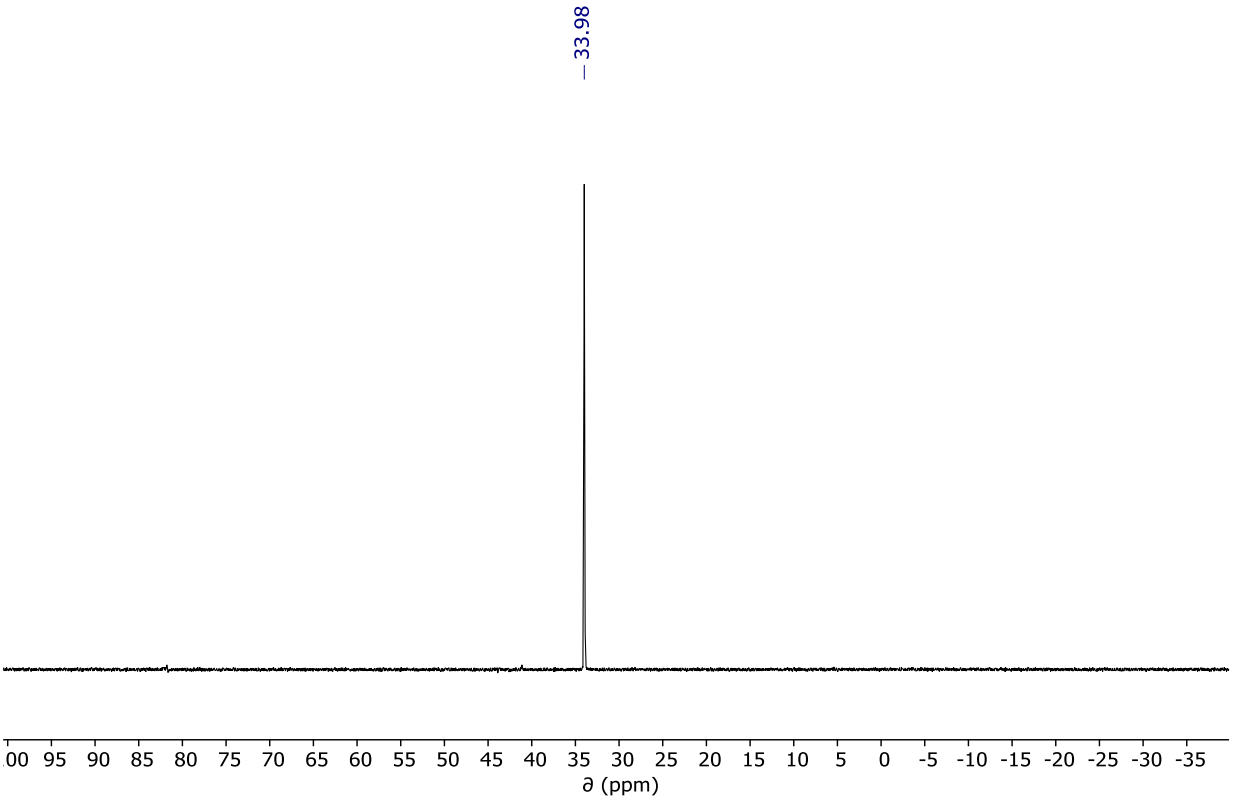

Figure 58. ^{31}P NMR ($CDCl_3$, 25 °C, 202 MHz) spectrum of Ph_2PSTol

2.5.6 *Synthesis of $Ph_2P(Se)STol$*

Inside the glovebox, a 250 mL Schlenk flask with Teflon-coated stirbar was charged with selenium powder (1.476 g, 18.7 mmol) and Ph_2PSTol (5.240 g, 17.0 mmol). Toluene (100 mL) was added to the flask, which was then capped with a rubber septum and taken out of the glovebox. The reaction was heated to 100 °C in an oil bath and stirred for 2 hours. After cooling the mixture to room temperature, the reaction mixture was filtered through Celite, yielding a light yellow solution. The solution was concentrated, then agitated after adding pentane (50 mL) to induce precipitation of the product. The product was isolated via vacuum filtration and washed with pentane, yielding the phosphine selenide as a fine off-white powder (4.681 g, 12.1 mmol, 71%). ^{1}H NMR ($CDCl_3$, 500 MHz) δ: 7.95 (dd, *J* = 14.1, 7.0 Hz, 4H) 7.50-7.43 (m, 6H), 7.19 (dd, *J* = 7.9 Hz, 2H), 7.05 (d, *J* = 7.9 Hz, 2H), 2.30 (s, 3H). ^{31}P NMR ($CDCl_3$, 202 MHz) δ: -57.76.

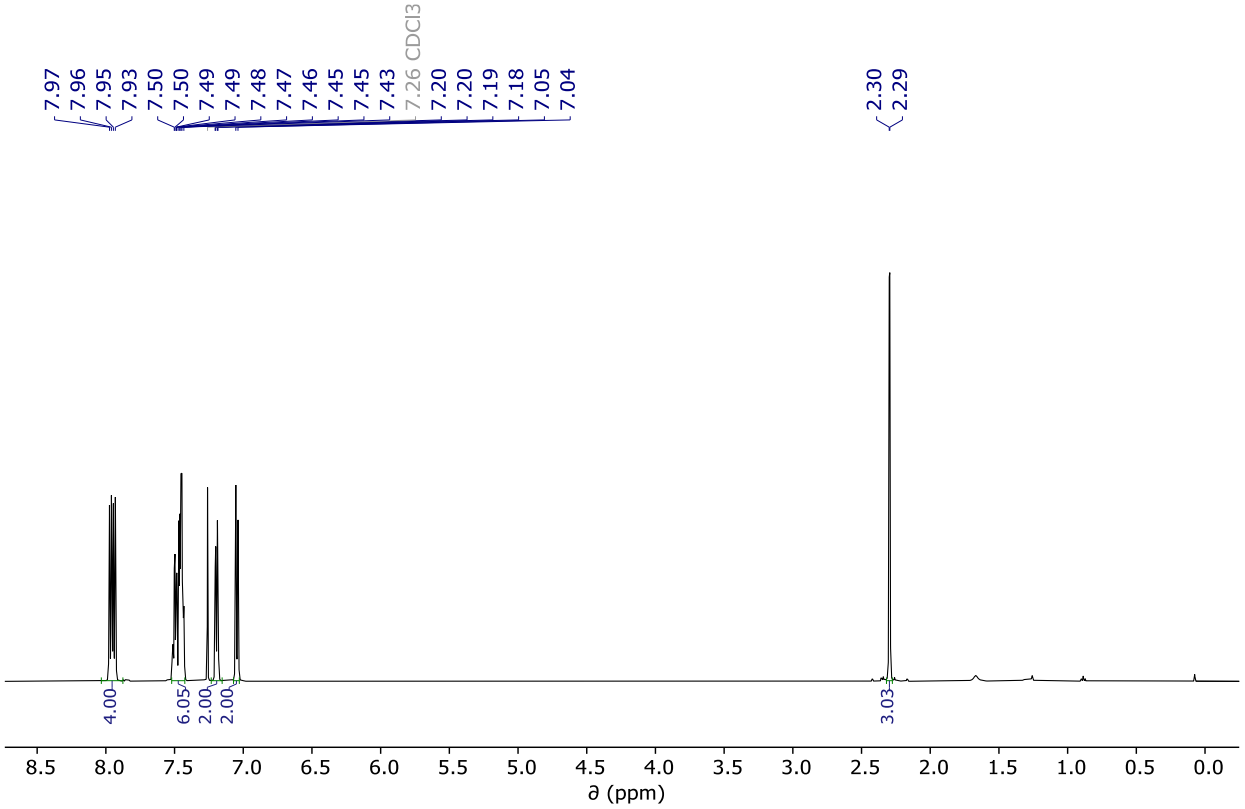

Figure 59. ^{1}H NMR ($CDCl_3$, 25 °C, 500 MHz) spectrum of $Ph_2P(Se)STol$

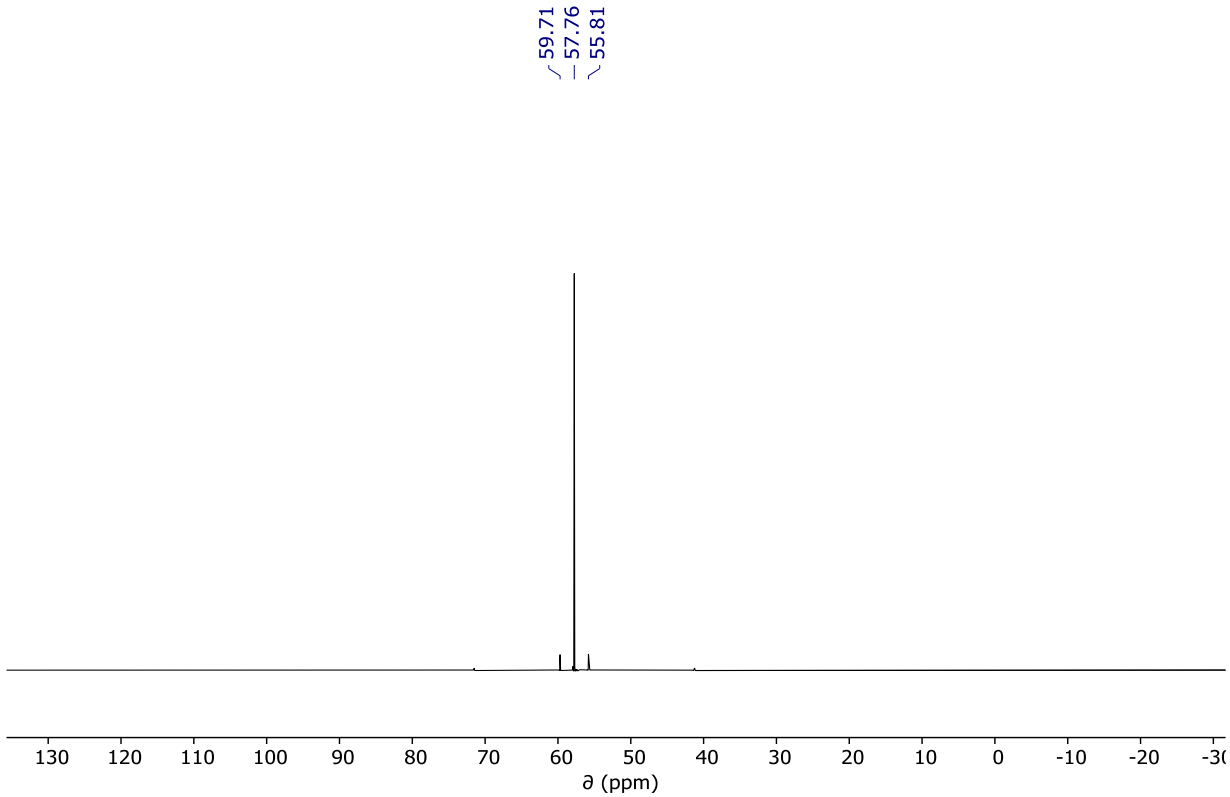

Figure 60. ^{31}P NMR ($CDCl_3$, 25 °C, 202 MHz) spectrum of $Ph_2P(Se)STol$

2.5.7 *Synthesis of $Co_6Se_8(Ph_2PCH_2NHTol)_6$*

Inside the glovebox, a 100 mL Schlenk flask with Teflon-coated stirbar was charged with selenium powder (1.034 g, 13.1 mmol) and Ph_2PCH_2NHTol (3.000 g, 9.82 mmol). Dicobalt octacarbonyl (1.680 g, 4.91 mmol) is added to the flask, which is promptly capped with a rubber septum and taken out of the glovebox and attached to the Schlenk line. Once the flask is under nitrogen flow, toluene (15 mL) is injected into the flask, resulting in effervescence and formation of a dark red solution. The mixture is left to stir at room temperature for 30 minutes, then heated to 115 °C in an oil bath, resulting in further darkening of the solution. After 18 hours of heating, the reaction is cooled to room temperature and returned to the glovebox. The solvent is removed under vacuum, and the black residue is dissolved in dichloromethane (20 mL) and filtered through Celite. The solvent is removed under vacuum and the residue dissolved in a minimal amount of warm toluene. The solution is cooled to room temperature and layered with approximately three times the volume of pentane and cooled to -35 °C overnight. The precipitate is collected on a medium-pore frit the next day and washed with pentane, yielding the product as a dark brown solid (2.260 g, 0.802

mmol, 49%). ^{1}H NMR (benzene-d_6, 500 MHz) δ: 7.69 (s, 24 H), 6.99 (s, 36 H), 6.83 (d, *J*=7.9 Hz, 12 H), 6.30 (d, *J*=7.9 Hz, 12H), 4.59 (s 6H), 4.01 (s, 12 H), 2.14 (s, 18 H). ^{31}P NMR (benzene-d_6, 121 MHz) δ: 74.98 ($\nu_{1/2}$ = 200 Hz).

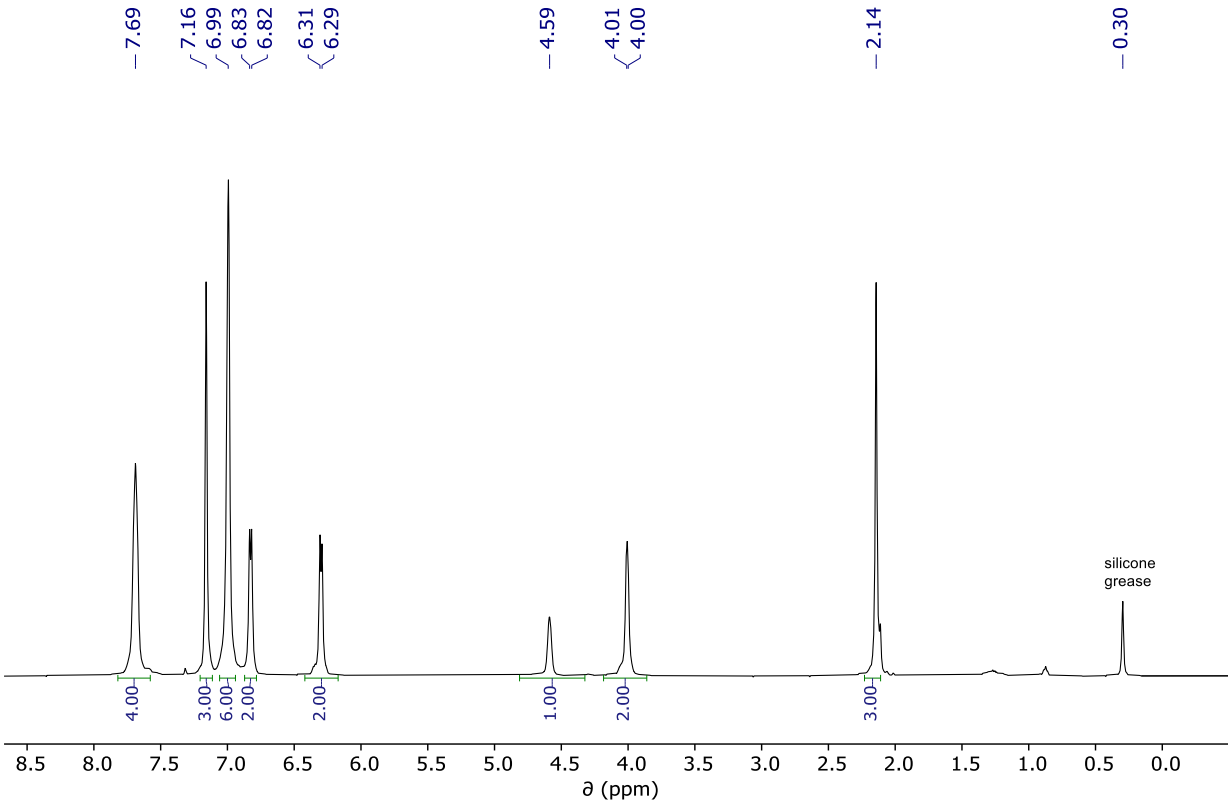

Figure 61. ^{1}H NMR (C_6D_6, 25 °C, 300 MHz) spectrum of $Co_6Se_8(Ph_2PCH_2NHTol)_6$

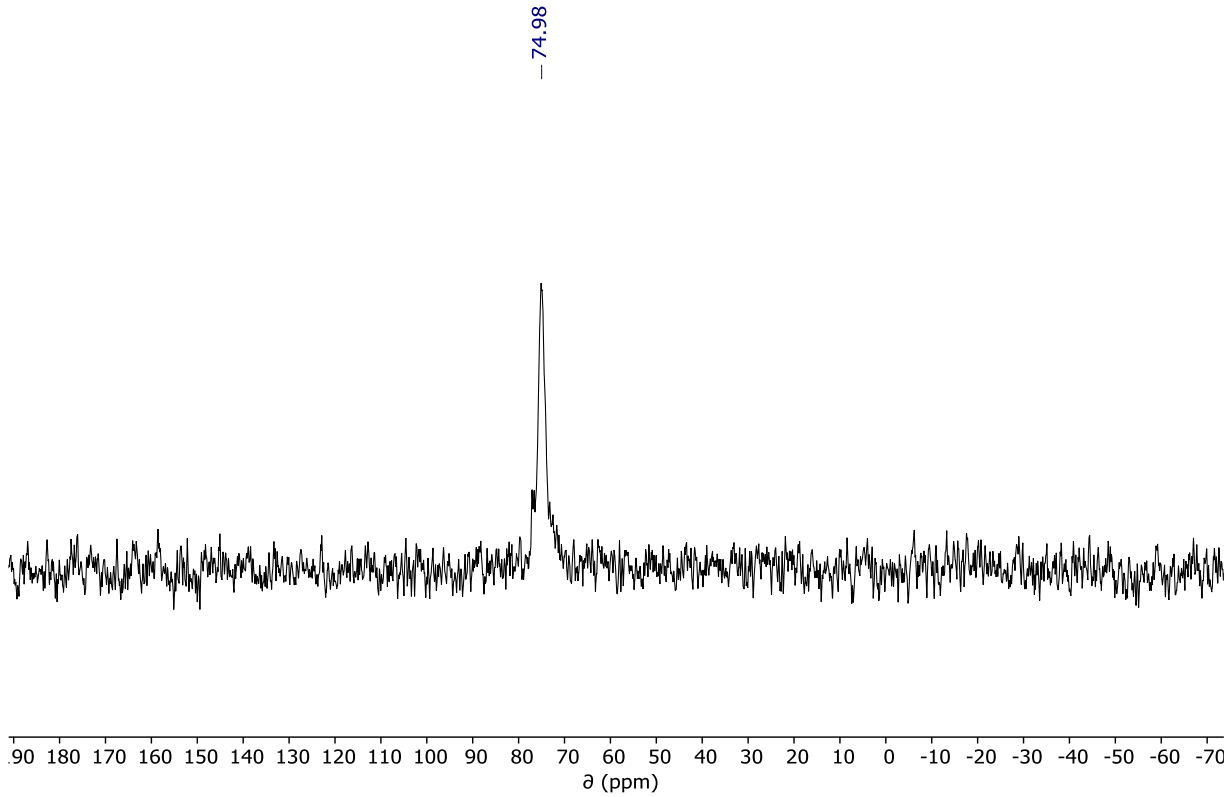

Figure 62. ^{31}P NMR (C_6D_6, 25 °C, 121 MHz) spectrum of $Co_6Se_8(Ph_2PCH_2NHTol)_6$

2.5.8 *Synthesis of $Co_6Se_8(Ph_2PCH_2OH)_6$*

Inside the glovebox, a 50 mL Schlenk flask with Teflon-coated stirbar was charged with selenium powder (0.082 g, 1.04 mmol) and dicobalt octacarbonyl (0.713 g, 2.09 mmol). The flask is capped with a rubber septum and brought out of the glovebox and attached to the Schlenk line. Once the flask is under nitrogen flow, a solution of Ph_2PCH_2OH (1.333 g, 6.17 mmol) in toluene injected into the flask, resulting in effervescence and formation of a dark red solution. The mixture is left to stir at room temperature for 30 minutes, then heated to 115 °C in an oil bath, resulting in further darkening of the solution. After 18 hours of heating, the reaction is cooled to room temperature and returned to the glovebox. The mixture is diluted with diethyl ether (20 mL) and filtered through a medium-pore frit. The dark brown solids on the frit are washed liberally with toluene and diethyl ether prior to isolation of the product (1.380 g, 0.605 mmol, 87%). ^{1}H NMR (DMSO-d_6, 300 MHz) δ: 7.40-7.11 (m, 60H, Ar***H***), 5.20 (q, *J*=4.5 Hz, 6H, O***H***), 4.11 (s, 12H, C***H***$_2$). ^{31}P NMR (DMSO-d_6, 121 MHz) δ: 68.37 ($\nu_{1/2}$ = 175 Hz).

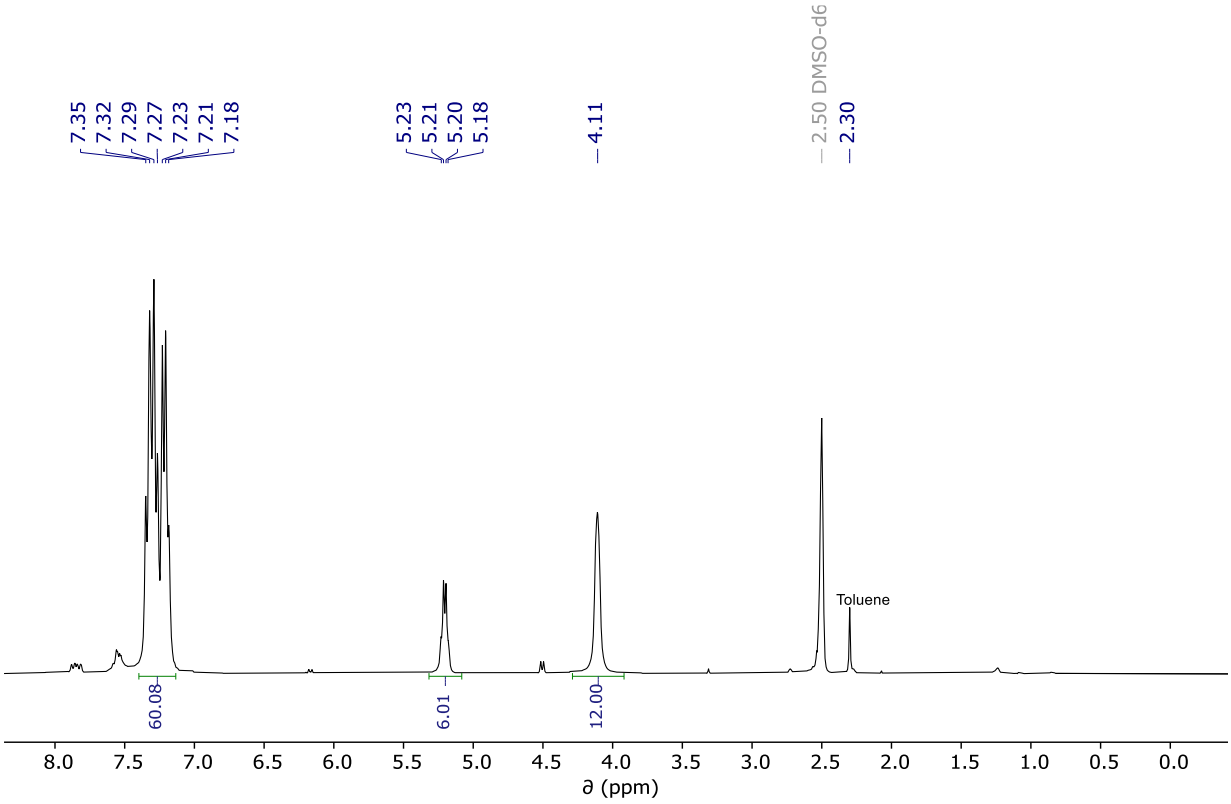

Figure 63. ^{1}H NMR (DMSO-d_6, 25 °C, 500 MHz) spectrum of $Co_6Se_8(Ph_2PCH_2OH)_6$

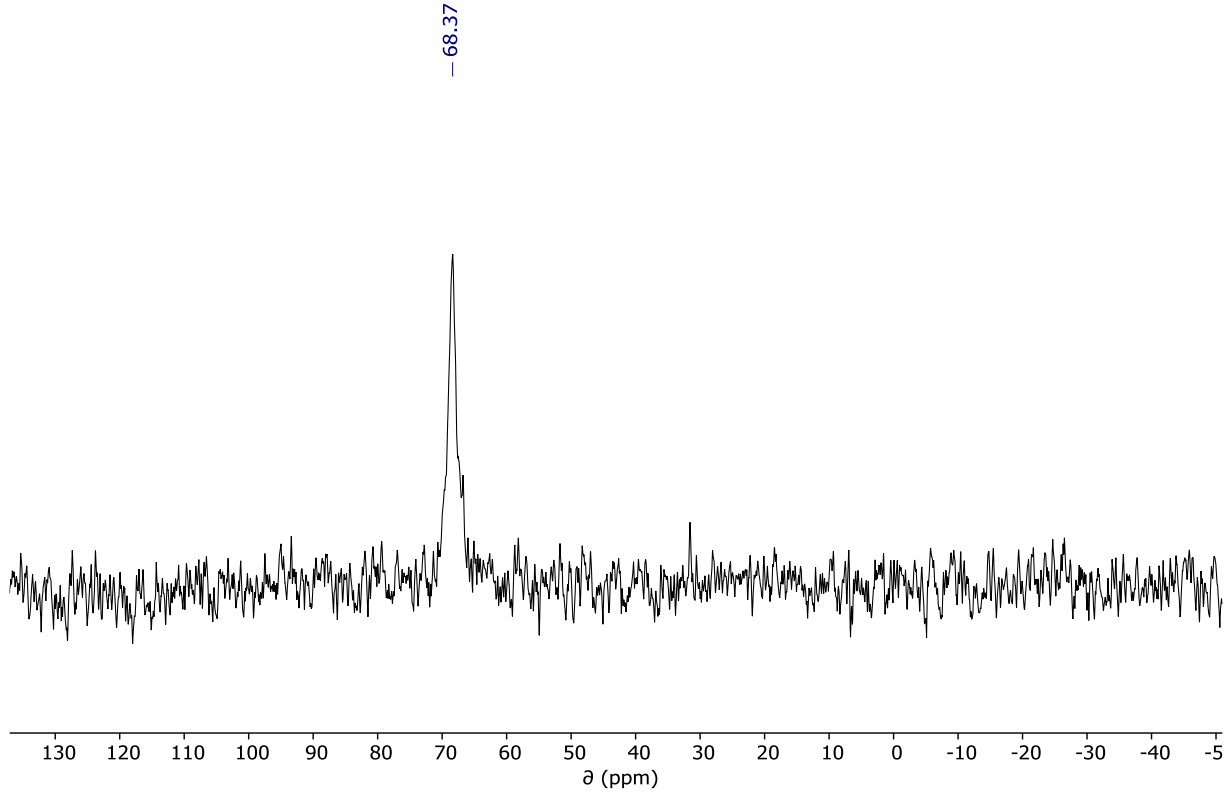

Figure 64. ^{31}P NMR (DMSO-d_6, 25 °C, 121 MHz) spectrum of $Co_6Se_8(Ph_2PCH_2OH)_6$

2.5.9 *Synthesis of $Co_6Se_8(Ph_2PCH_2OSiMe_3)_6$*

Inside the glovebox, a 100 mL Schlenk flask with Teflon-coated stirbar was charged with selenium powder (1.460 g, 2.15 mmol) and dicobalt octacarbonyl (2.371 g, 4.33 mmol). The flask is capped with a rubber septum and brought out of the glovebox and attached to the Schlenk line. Once the flask is under nitrogen flow, a solution of $Ph_2PCH_2OSiMe_3$ (2.900 g, 12.6 mmol) in toluene injected into the flask, resulting in effervescence and formation of a dark red-brown solution. The mixture is left to stir at room temperature for 30 minutes, then heated to 118 °C in an oil bath, resulting in further darkening of the solution. After 16 hours of heating, another solution of $Ph_2PCH_2OSiMe_3$ (0.667 g, 2.31 mmol) in toluene was injected into the flask. After another 24 hours of heating, the reaction was cooled to room temperature and returned to the glovebox. The reaction mixture is filtered through a medium porosity fritted funnel and the resulting black solids were washed with acetonitrile (25 mL), then diethyl ether (40 mL), yielding the product as a fine, dark brown powder (4.469 g, 1.65 mmol, 71%). ^{1}H NMR (C_6D_6, 300 MHz) δ: 7.61 (m, 4H), 6.92 (m, 10H), 4.38 (s, 2H), -0.39 (s, 9H). ^{31}P NMR (C_6D_6, 121 MHz) δ: 71.36 ($\nu_{1/2}$ = 300 Hz).

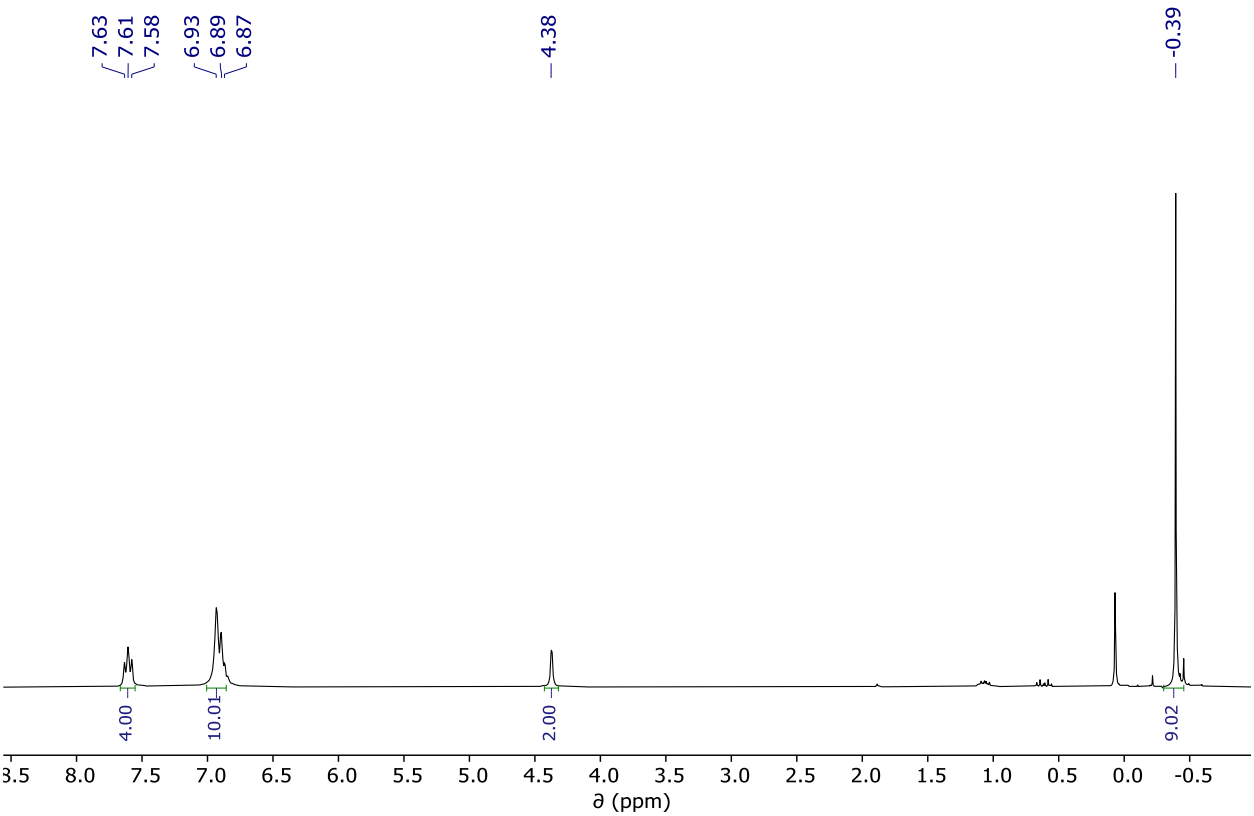

Figure 65. ^{1}H NMR (benzene-d_6, 25 °C, 300 MHz) spectrum of $Co_6Se_8(Ph_2PCH_2OSiMe_3)_6$

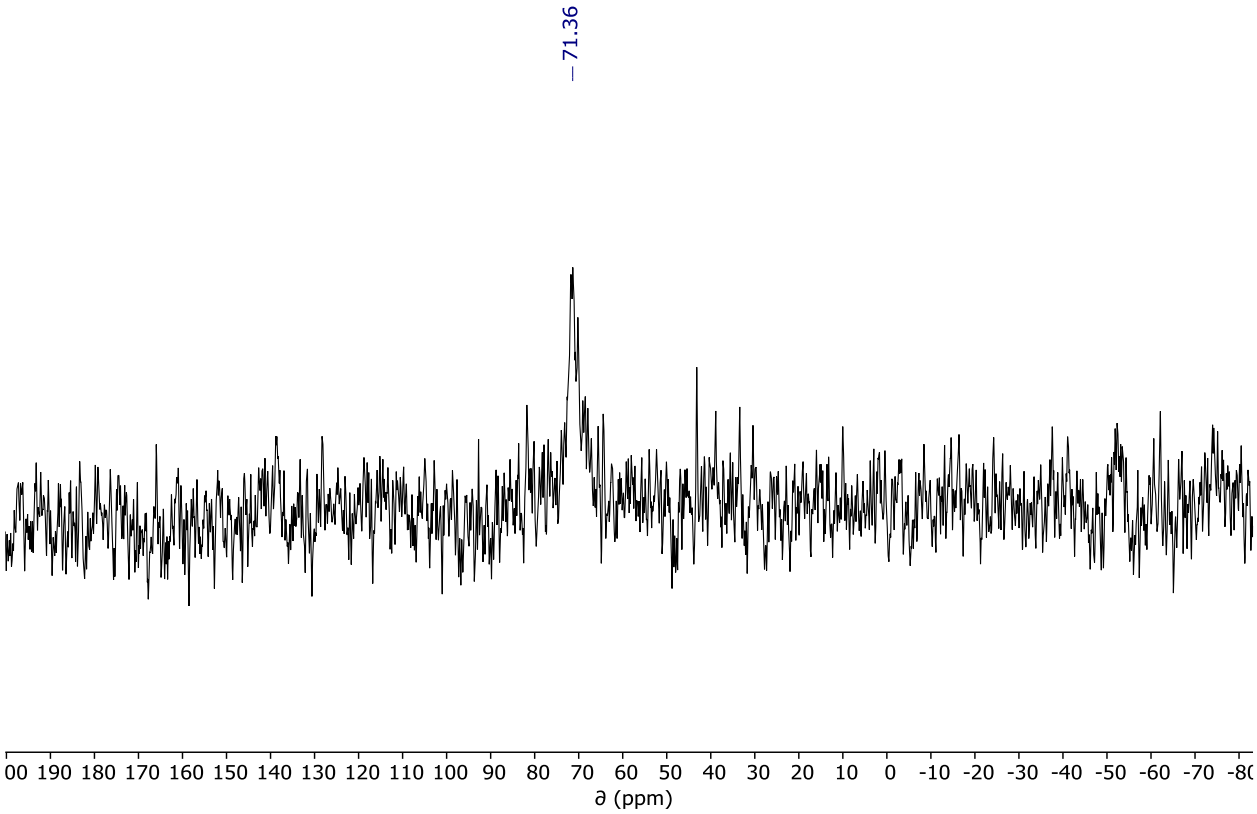

Figure 66. ^{31}P NMR (benzene-d_6, 25 °C, 121 MHz) spectrum of $Co_6Se_8(Ph_2PCH_2OSiMe_3)_6$

2.5.10 *Synthesis of $[Co_6Se_8(Ph_2PCH_2OSiMe_3)_6][PF_6]$*

In a 20 mL vial with Teflon-coated stirbar, $Co_6Se_8(Ph_2PCH_2OSi(CH_3)_3)_6$ (1.000 g, 0.368 mmol) and ferrocenium hexafluorophosphate (0.122 g, 0.369 mmol) are combined with dichloromethane (18 mL) and stirred at room temperature for 1 hour. The solution is concentrated to half the initial volume and cooled in the freezer to –35 °C, then layered with diethyl ether (20 mL). After letting the mixture sit in the freezer overnight, the resulting crystals are isolated via vacuum filtration and washed with diethyl ether, yielding the product as dark brown crystals (0.792 g, 0.277 mmol, 75%). ^{1}H NMR ($CDCl_3$, 300 MHz) δ: 7.60 (t, *J*=7.6 Hz, 2H), 7.14 (d, *J*=7.6 Hz, 4H), 6.80 (t, *J*=7.5 Hz, 4H), -0.26 (s, 9H). ^{31}P NMR ($CDCl_3$, 121 MHz) δ: -144.26, -353.79 ($\nu_{1/2}$ = 850 Hz).

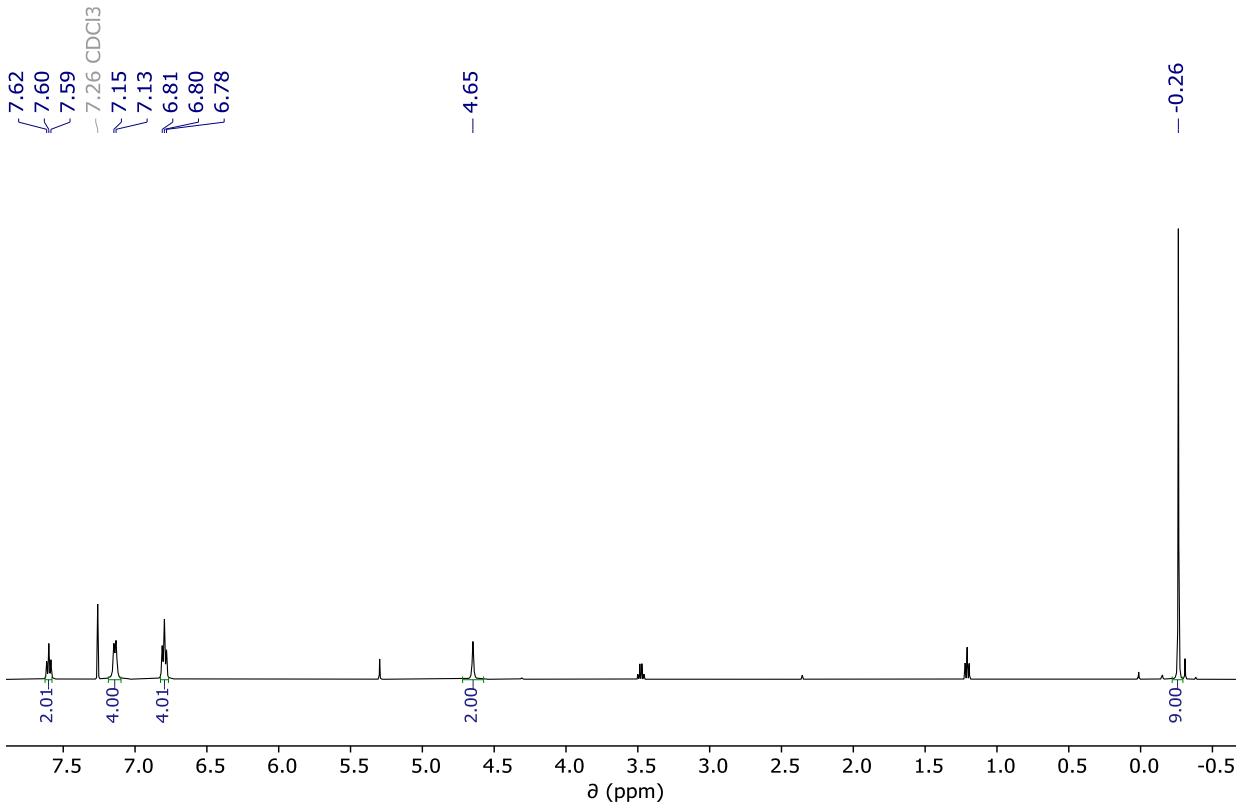

Figure 67. ^{1}H NMR ($CDCl_3$, 25 °C, 300 MHz) spectrum of $[Co_6Se_8(Ph_2PCH_2OSiMe_3)_6][PF_6]$

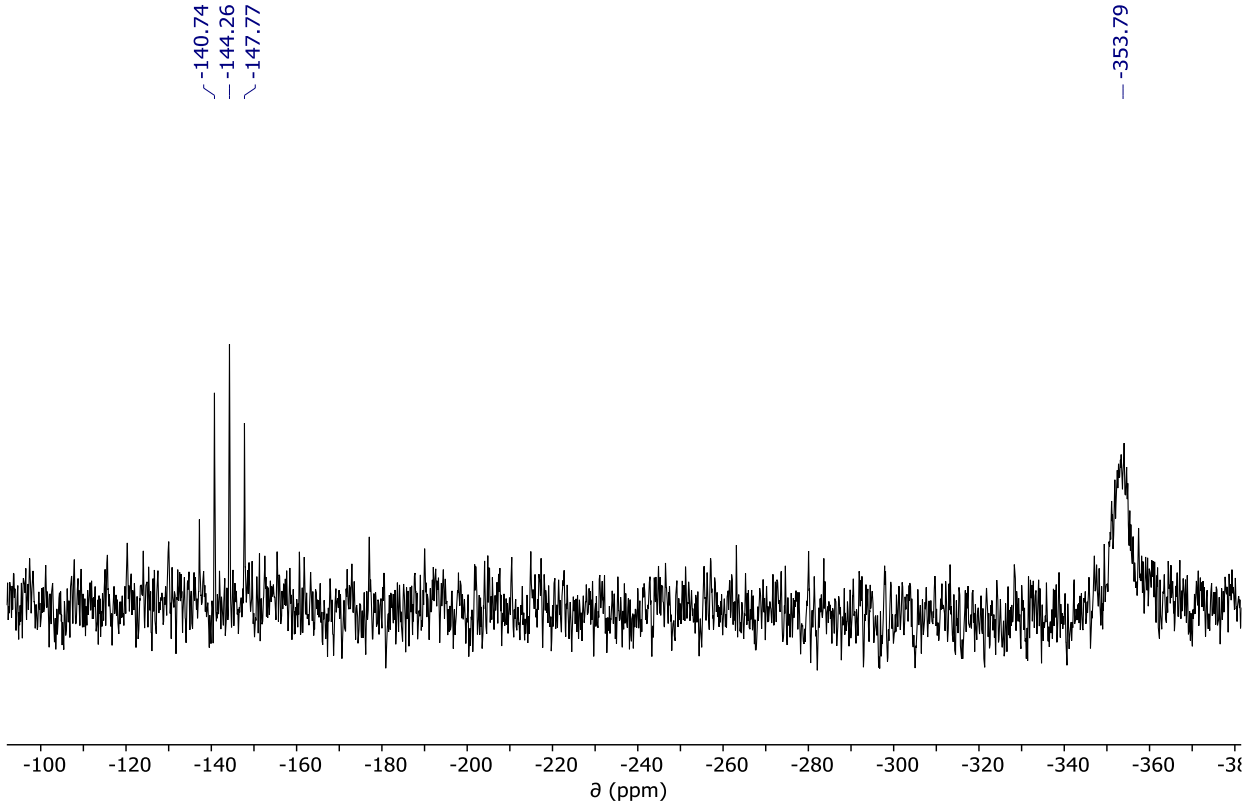

Figure 68. ^{31}P NMR ($CDCl_3$, 25 °C, 121 MHz) spectrum of $[Co_6Se_8(Ph_2PCH_2OSiMe_3)_6][PF_6]$

2.5.11 *Synthesis of $Co_6Se_8(Ph_2PCH_2OCH_3)_6$*

Inside the glovebox, a 50 mL Schlenk flask with Teflon-coated stirbar, dicobalt octacarbonyl (0.816 g, 2.39 mmol) and selenium (0.503 g, 6.37 mmol) were added. The flask is capped with a rubber septum and attached to the Schlenk line. Once the flask is under nitrogen flow, a solution of $Ph_2PCH_2OCH_3$ (1.100 g) in toluene is injected into the flask, resulting in effervescence and formation of a dark red-brown solution. The mixture is left to stir at room temperature for 30 minutes, then heated to reflux in an oil bath. After stirring at reflux overnight, another solution of the phosphine (0.100 g) in toluene is injected into the flask, which is heated for another 24 hours. The reaction mixture is cooled to room temperature and the solvent removed under vacuum. The resulting residue is dissolved in warm dichloromethane (50 mL) and filtered through Celite. The solution is concentrated to 1/3 the initial volume and layered with diethyl ether (60 mL) at room temperature. ^{1}H NMR (CD_2Cl_2, 500 MHz) δ: 7.43 (t, *J*=8.8 Hz, 4H), 7.27 (t, *J*=7.3 Hz, 2H), 7.19 (t, *J*=7.3 Hz, 4H), 4.00 (s, 2H), 3.02 (s, 3H).

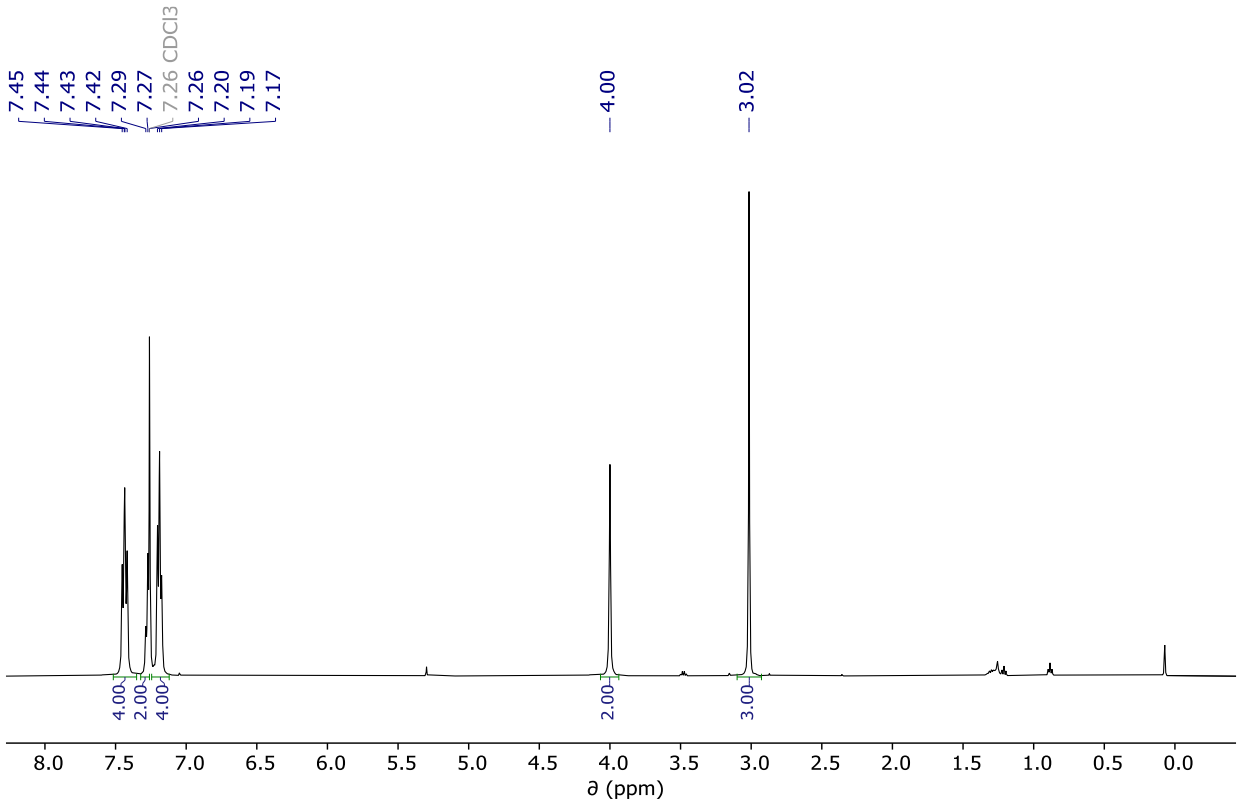

Figure 69. ^{1}H NMR (CD_2Cl_2, 25 °C, 500 MHz) spectrum of $Co_6Se_8(Ph_2PCH_2OCH_3)_6$

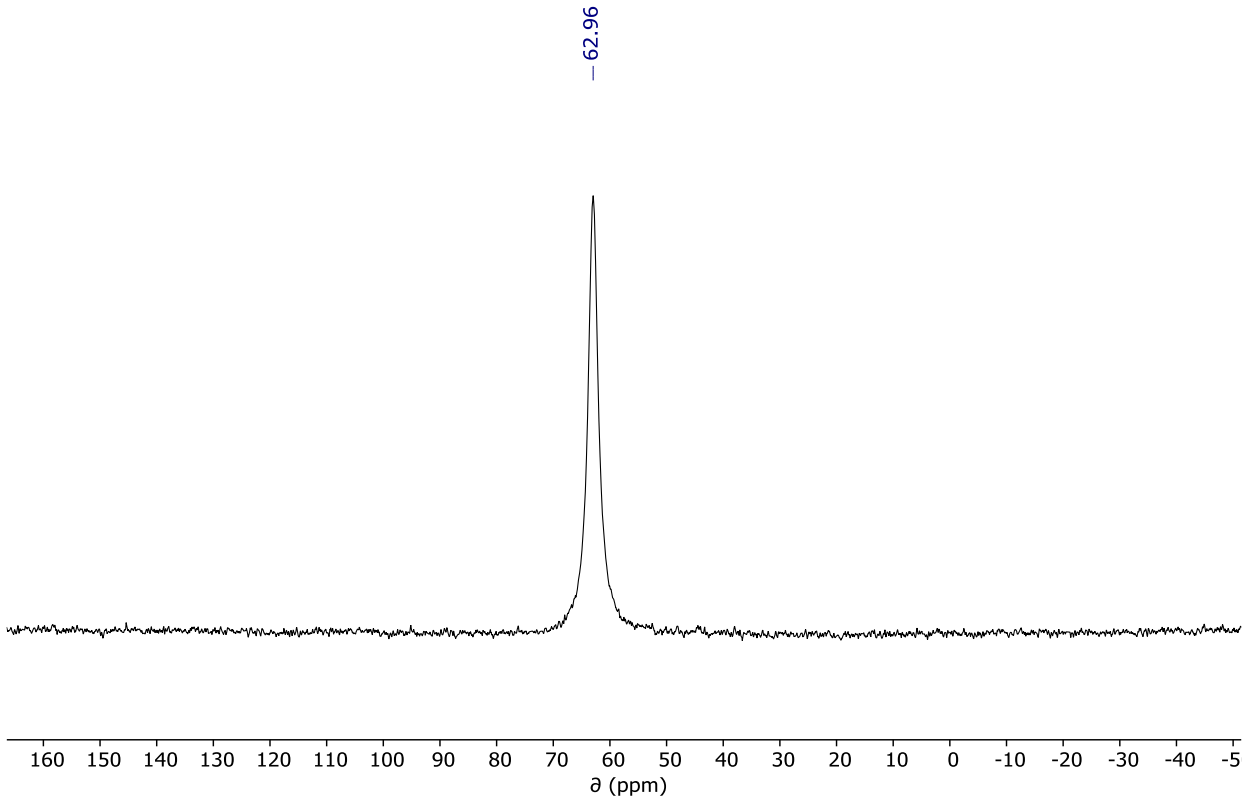

Figure 70. ^{31}P NMR ($CDCl_3$, 25 °C, 202 MHz) spectrum of $Co_6Se_8(Ph_2PCH_2OCH_3)_6$

2.5.12 *Synthesis of $Co_6Se_8(Ph_2PCH_2CH_2OH)_6$*

Inside the glovebox, a 100 mL Schlenk flask with Teflon-coated stirbar was charged with selenium powder (0.170 g, 2.15 mmol) and dicobalt octacarbonyl (1.480 g, 4.33 mmol). The flask is capped with a rubber septum and brought out of the glovebox and attached to the Schlenk line. Once the flask is under nitrogen flow, a solution of $Ph_2PCH_2CH_2OH$ (2.900 g, 12.6 mmol) in toluene injected into the flask, resulting in effervescence and formation of a dark red-brown solution. The mixture is left to stir at room temperature for 30 minutes, then heated to 118 °C in an oil bath, resulting in further darkening of the solution. After 18 hours of heating, the reaction is cooled to room temperature and returned to the glovebox. The mixture is diluted with diethyl ether (20 mL) and filtered through a medium-pore frit. The dark brown solids on the frit are washed liberally with toluene, dichloromethane, and diethyl ether prior to isolation of the product (2.282 g, 0.964 mmol, 67%). ^{1}H NMR (DMSO-d_6, 300 MHz) δ: 7.27 (m, 60H, Ar***H***), 4.56 (s, 2H, O***H***), 4.43, (s, 4H, O***H***), 3.03, (s, 12H, C***H***$_2$), 2.53 (s, 12H, C***H***$_2$). ^{31}P NMR (DMSO-d_6, 121 MHz) δ: 48.7 ($\nu_{1/2}$ =

190 Hz).

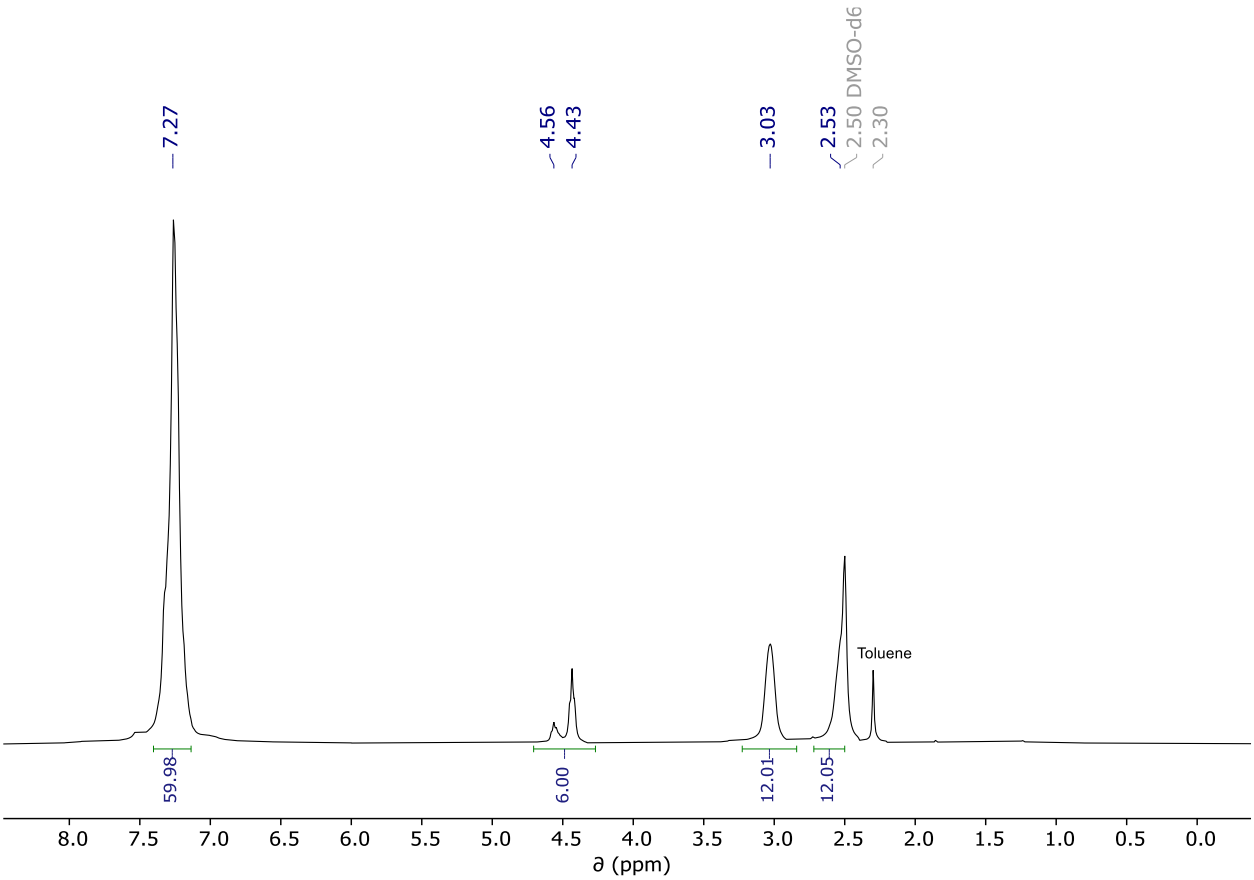

Figure 71. ^{1}H NMR (DMSO-d_6, 25 °C, 300 MHz) spectrum of $Co_6Se_8(Ph_2PCH_2CH_2OH)_6$

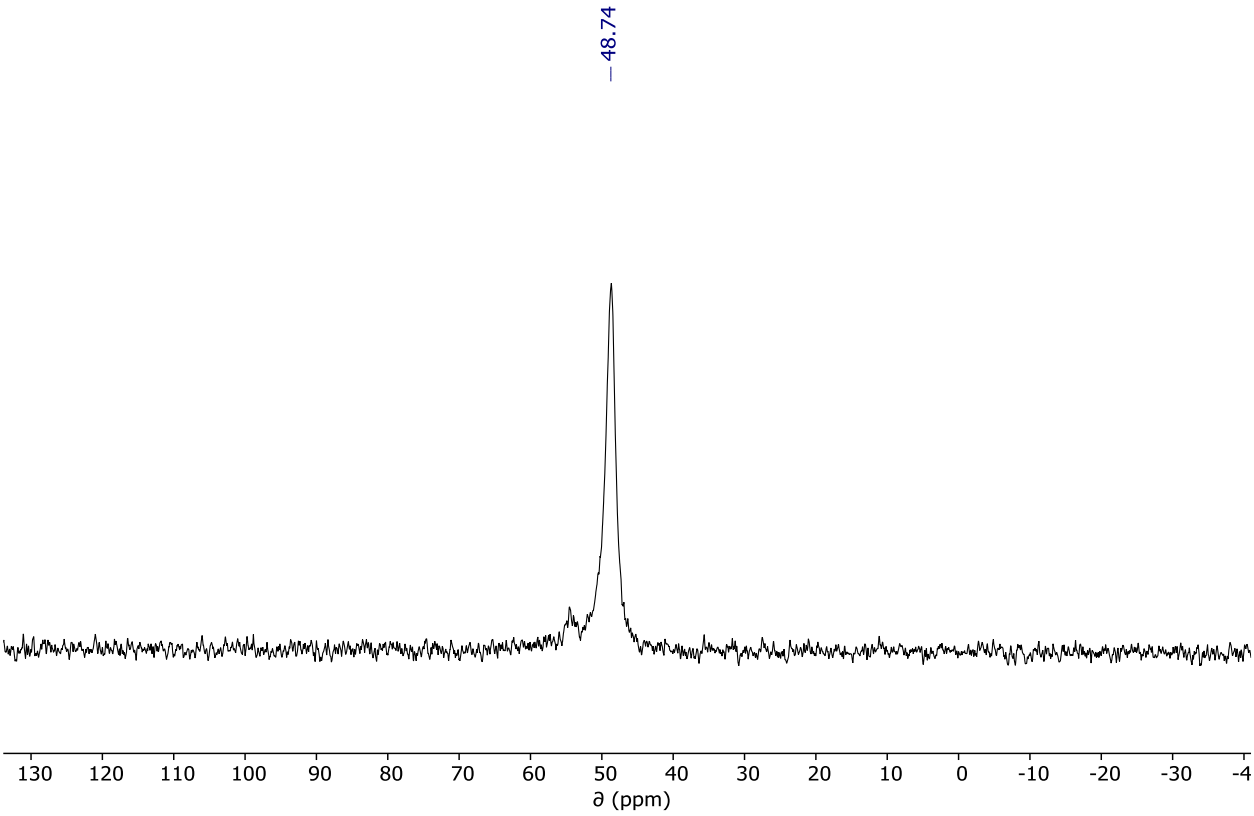

Figure 72. ^{31}P NMR (DMSO-d_6, 25 °C, 121 MHz) spectrum of $Co_6Se_8(Ph_2PCH_2CH_2OH)_6$

2.5.13 *Synthesis of $[Co_6Se_8(Ph_2PCH_2CH_2OH)_6][PF_6]$*

To a 50 ml Schlenk flask with Teflon-coated stirbar, $Co_6Se_8(Ph_2PCH_2CH_2OH)_6$ (1.000 g, 0.423 mmol) and acetonitrile (20 mL) were added. Ferrocenium hexafluorophosphate (0.133 g, 0.402 mmol) was dissolved in acetonitrile and the resulting solution added to the reaction flask, resulting in formation of a dark brown solution. The mixture was stirred for one hour at room temperature, then filtered through Celite. The filtrate was concentrated to half of the initial volume and combined with toluene (10 mL) before being stored at -35 °C overnight. The resulting precipitate is isolated by filtration through a medium-pore frit and washed with toluene (10 mL) and diethyl ether (20 mL), giving the product as a dark brown powder (0.892 g, 0.355 mmol, 84%). ^{1}H NMR (CD_3CN, 300 MHz) δ: 7.63 (t, 12H, *p*-Ar***H***), 7.06 (d, 24H, *o*-Ar***H***), 6.92 (t, 24H, *m*-Ar***H***), 2.84 (s, 12H, C***H***$_2$OH), 2.64, (s, 6H, O***H***), 1.21 (s, 12H, PC***H***$_2$). ^{31}P NMR (CD_3CN, 121 MHz) δ: -144.5 (p, J = 704.8 Hz), -408.2 ($\nu_{1/2}$ = 1900 Hz).

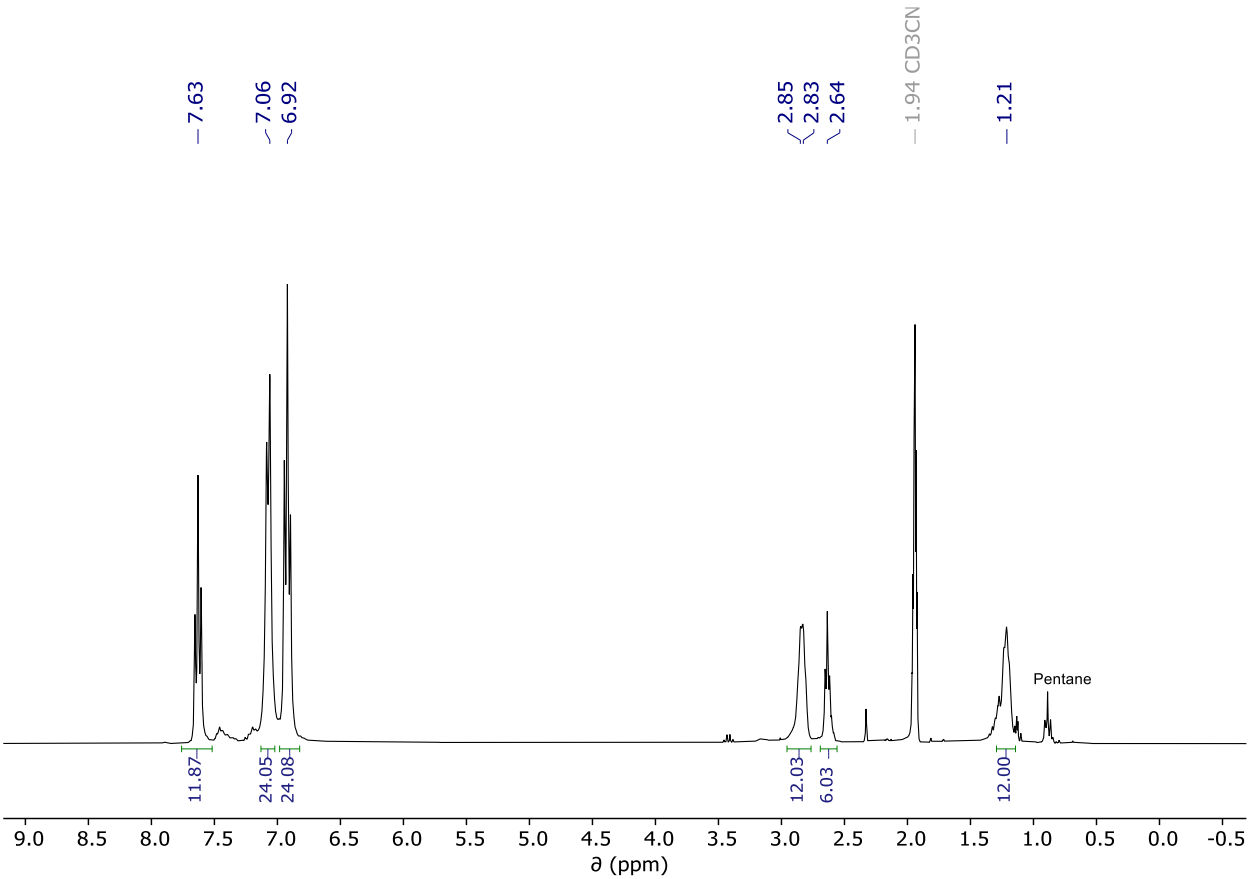

Figure 73. ^{1}H NMR (CD_3CN, 25 °C, 300 MHz) spectrum of $[Co_6Se_8(Ph_2PCH_2CH_2OH)_6][PF_6]$

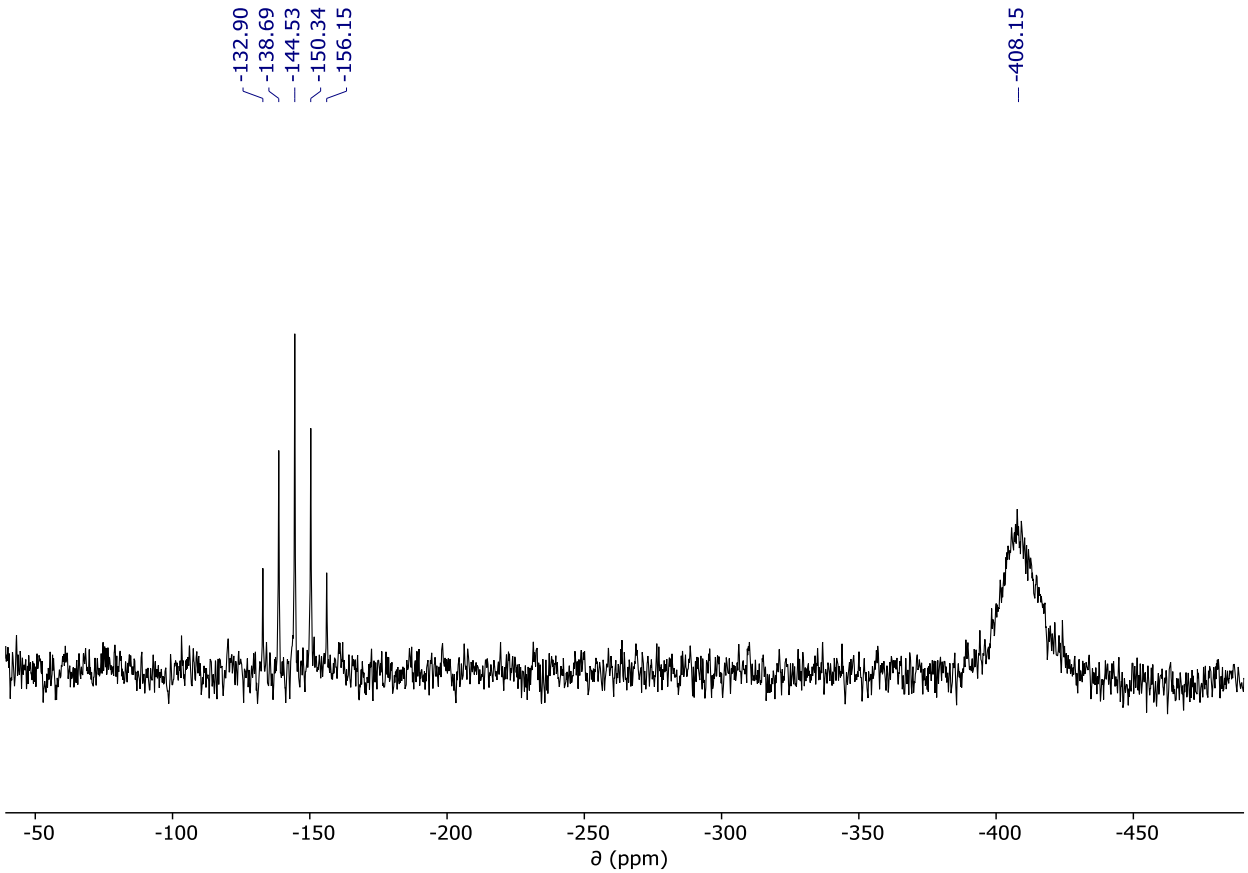

Figure 74. ^{31}P NMR (CD_3CN, 25 °C, 121 MHz) spectrum of $[Co_6Se_8(Ph_2PCH_2CH_2OH)_6][PF_6]$

2.5.14 *Synthesis of $Co_6Se_8(Ph_2PCH_2CH_2O(SiMe_3))_6$*

To a 20 mL vial with Teflon-coated stir bar, $Co_6Se_8(Ph_2PCH_2CH_2OH)_6$ (0.633 g, 0.267 mmol) and dichloromethane are added, forming a brown suspension. Pyridine (0.212 g, 0.22 mL, 2.68 mmol) is added to the mixture, which is then cooled to –35 °C in the freezer. The cold suspension is stirred, and trimethylsilyl chloride is added dropwise to the mixture. Less than 15 minutes later, the mixture is now a homogenous red-brown solution. The solvent is removed from the reaction mixture under vacuum, and the resulting residue is dissolved in a 1:1 mixture of toluene/pentane and filtered through Celite. The solvent is removed from the filtrate under vacuum, and following trituration with pentane the product is isolated as a dark brown solid (0.666 g, 0.238 mmol, 89%). ^{1}H NMR ($CDCl_3$, 300 MHz) δ: 7.45-7.24 (m, 10H), 3.40 (m, 2H), 2.71 (m, 2H), 0.00 (s, 9H). ^{31}P NMR ($CDCl_3$, 121 MHz) δ: -49.07 ($\nu_{1/2}$ = 330 Hz)

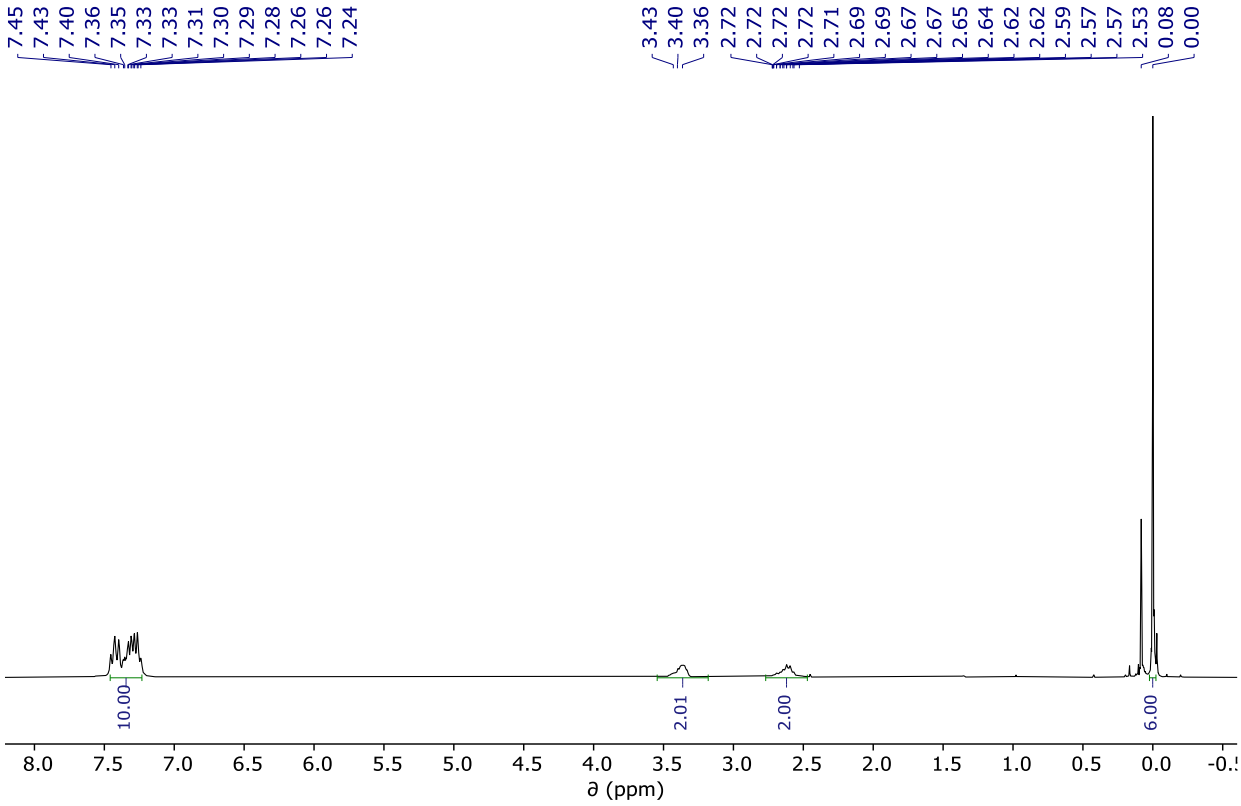

Figure 75. ^{1}H NMR ($CDCl_3$, 25 °C, 300 MHz) spectrum of $Co_6Se_8(Ph_2PCH_2CH_2O(SiMe_3))_6$

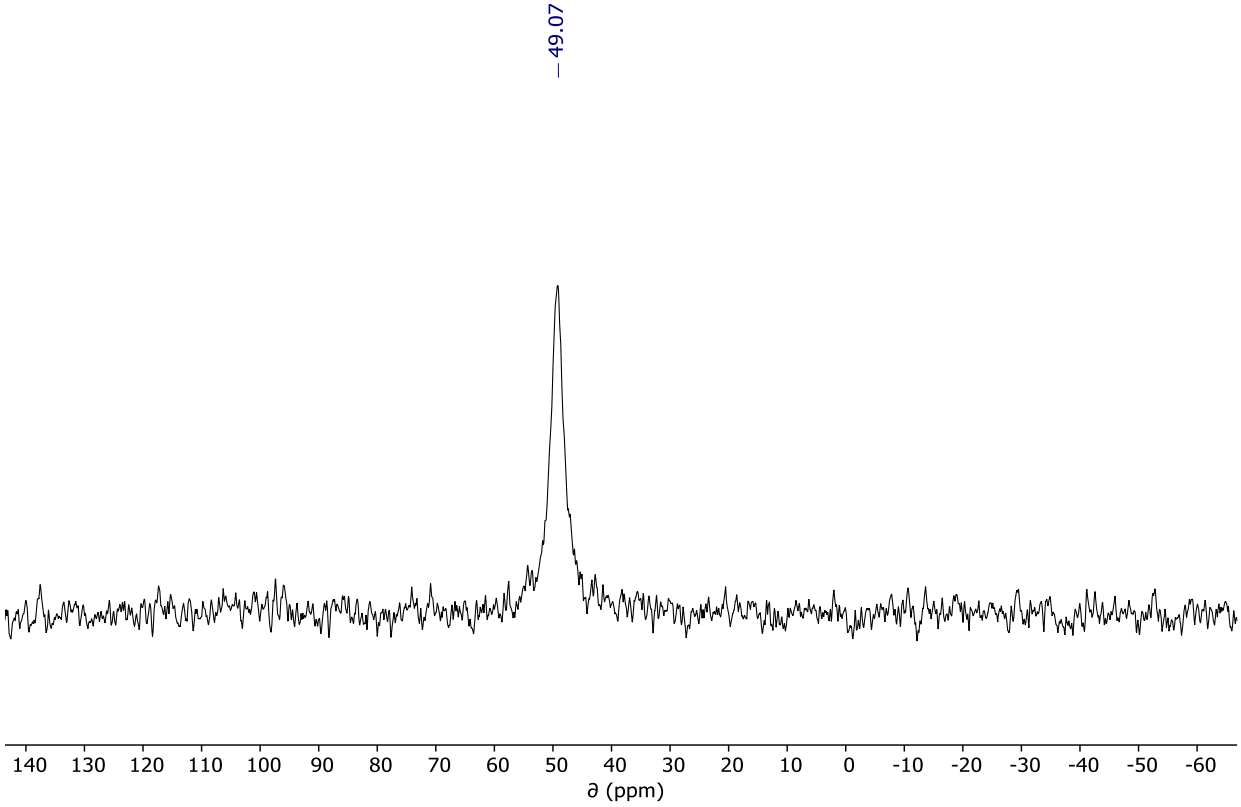

Figure 76. ^{31}P NMR ($CDCl_3$, 25 °C, 121 MHz) spectrum of $Co_6Se_8(Ph_2PCH_2CH_2O(SiMe_3))_6$

2.5.15 *Synthesis of $Co_6Se_8(Ph_2PH)_6$*

To a 100 mL Schlenk flask with Teflon-coated stirbar, diphenylphosphine selenide (5.200 g, 19.6 mmol) and dicobalt octacarbonyl (2.515 g, 7.35 mmol) are added. The flask was capped with a rubber septum and moved out of the glovebox and attached to a Schlenk line. With the flask venting through the Schlenk line, toluene (24 mL) is injected into the flask while stirring, resulting in evolution of gas and formation of a dark red-brown solution. The mixture was left to stir at room temperature for 30 minutes while venting, then was heated to reflux. After 16 hours of reflux, diphenylphosphine was injected into the reaction flask, which was left to continue stirring at reflux for 24 hours. The flask was then cooled and returned to the glovebox, where the reaction mixture was filtered through Celite. After washing the Celite with dichloromethane, the filtrate was concentrated until it took on a thick consistency. This residue was then dissolved in dichloromethane (30 mL) and layered with diethyl ether (130 mL) and left to sit at room temperature for 16 hours. The product is isolated via vacuum filtration as dark brown crystals and washed with diethyl ether (2.216 g, 1.05 mmol, 43%). ^{1}H NMR ($CDCl_3$, 300 MHz) δ: 8.05 (s, 3H), 7.41 (m, 24H), 7.24 (m, 12H), 7.15 (m, 24H), 6.83 (s, 3H). ^{31}P NMR ($CDCl_3$, 121 MHz) δ: ($\nu_{1/2}$ = 900 Hz)

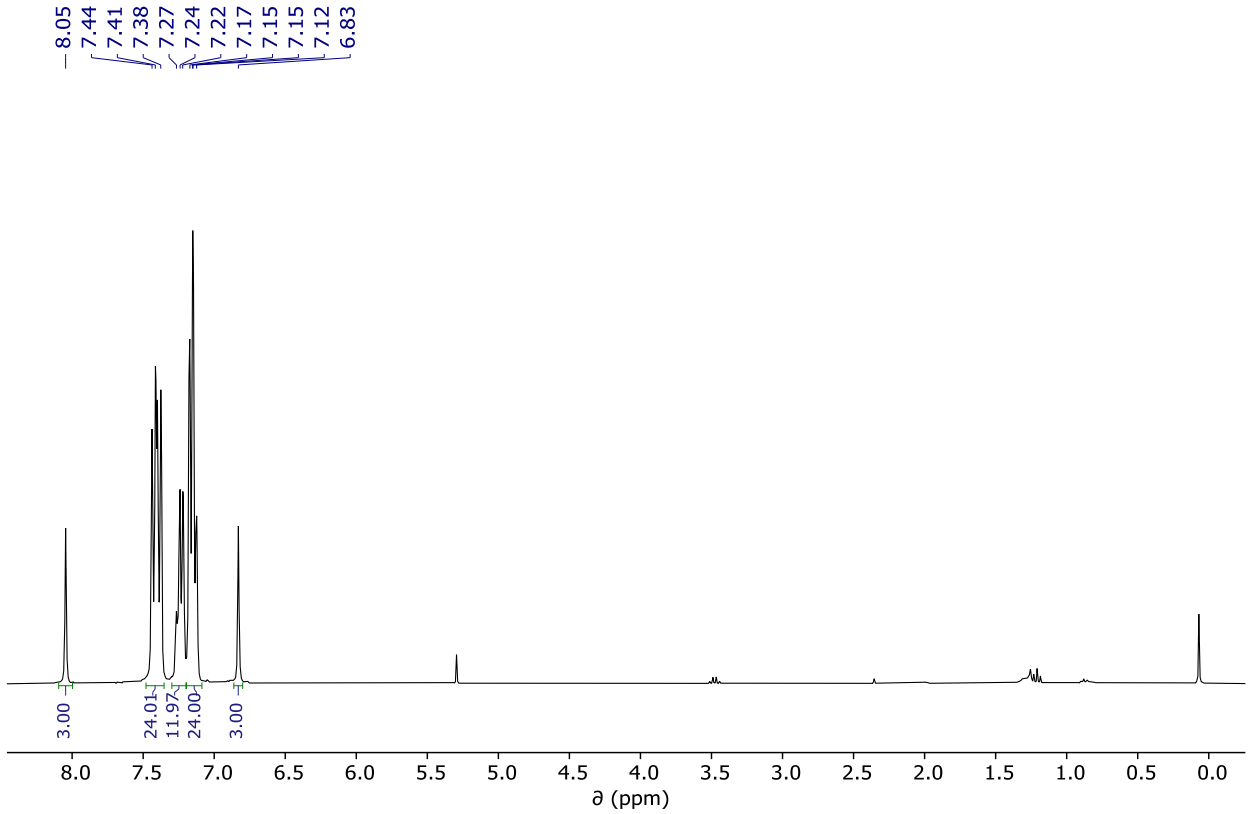

Figure 77. ^{1}H NMR ($CDCl_3$, 25 °C, 500 MHz) spectrum of $Co_6Se_8(Ph_2PH)_6$

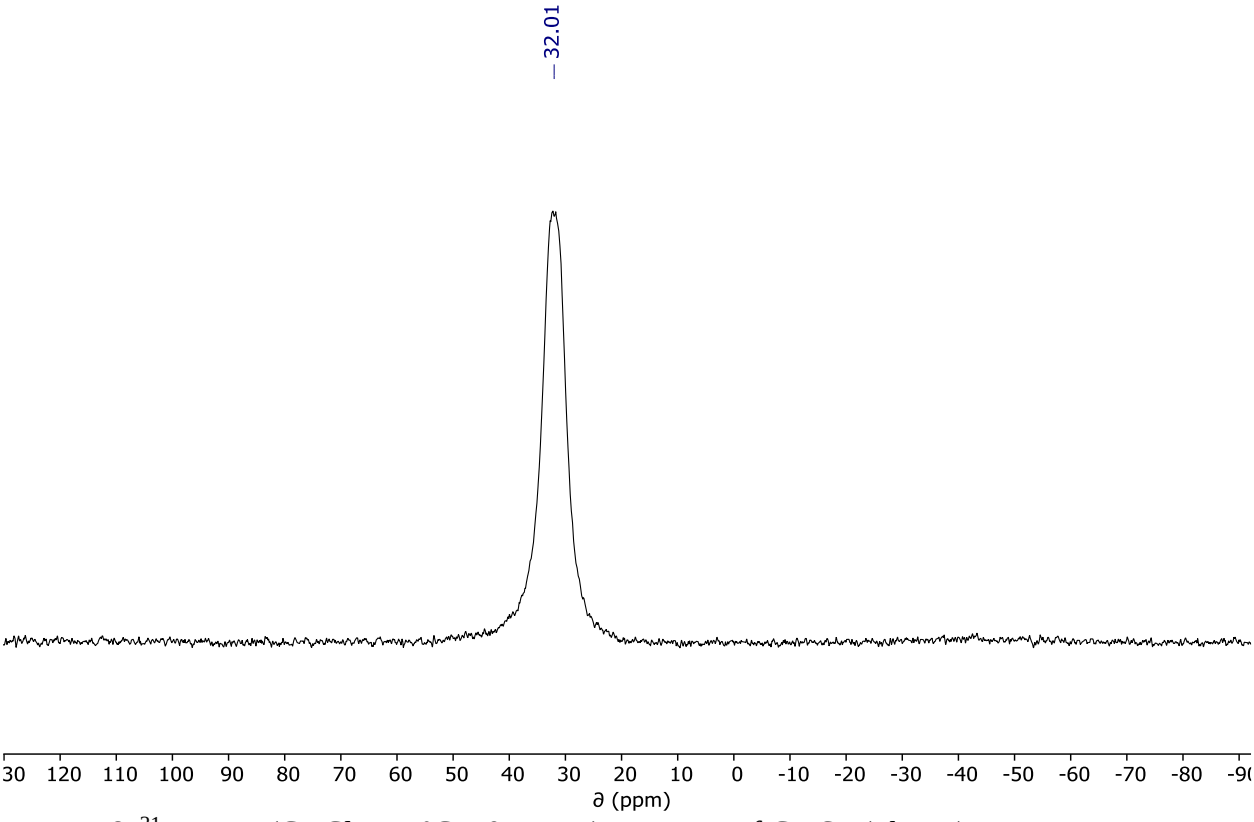

Figure 78. ^{31}P NMR ($CDCl_3$, 25 °C, 202 MHz) spectrum of $Co_6Se_8(Ph_2PH)_6$

2.5.16 *Synthesis of $[Co_6Se_8(Ph_2PH)_6][PF_6]$*

To a 20 mL vial with Teflon-coated stirbar, $Co_6Se_8(Ph_2PH)_6$ (0.300 g, mmol) and acetonitrile (7 mL) were added, forming a brown suspension. A solution of ferrocenium hexafluorophosphate (0.047 g, 0.142 mmol) in acetonitrile is added to the reaction mixture, resulting in gradual dissolution of the cluster as it reacts. After an hour of stirring at room temperature, the mixture is filtered through Celite and concentrated to half the initial volume and cooled to –35 °C in the freezer overnight. The resulting crystals are isolated via vacuum filtration and washed liberally with diethyl ether, yielding the product as black crystals (0.232 g, 72%). ^{31}P NMR (Tetrahydrofuran, 121 MHz) δ: -457.36 ($\nu_{1/2}$ = 2800 Hz).

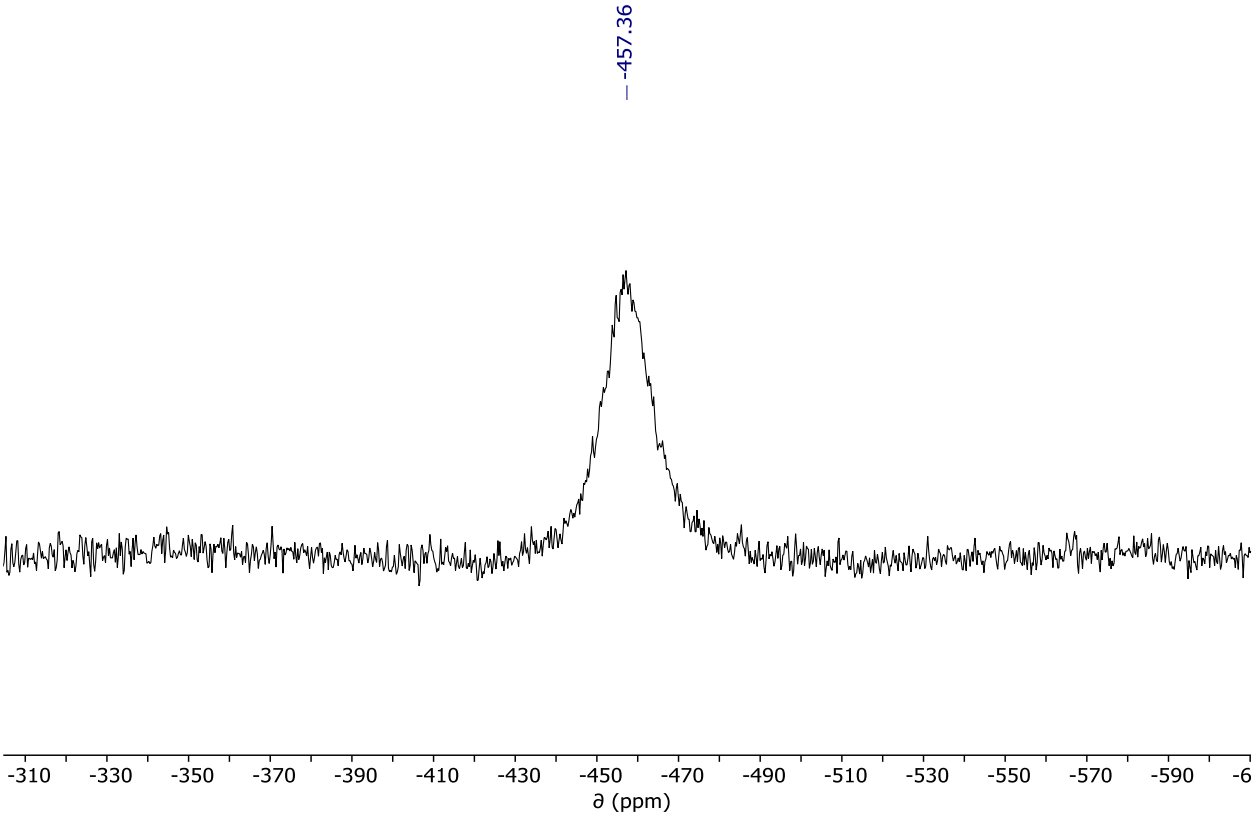

Figure 79. ^{31}P NMR (Tetrahydrofuran, 25 °C, 500 MHz) spectrum of $[Co_6Se_8(Ph_2PH)_6][PF_6]$

2.5.17 *Synthesis of $Co_6Se_8(Ph_2PSTol)_6$*

To a 100 mL Schlenk flask with Teflon-coated stirbar, dicobalt octacarbonyl (1.324 g, 3.87 mmol) was added, and the flask capped with a rubber septum. The flask was taken out of the glovebox and attached to the Schlenk line and put under flow of nitrogen. With the flask sidearm open to

vent through the Schlenk line, a solution of $Ph_2P(Se)STol$ (4.000 g) in toluene (20 mL) was injected into the flask, resulting in evolution of gas and formation of a dark- red-brown solution. The mixture was stirred at room temperature for 20 minutes, then gradually heated to reflux. The solution was left to reflux and stir overnight while venting through the Schlenk line. The reaction was cooled and the solvent removed under vacuum, yielding a dark brown residue which was dissolved in minimal dichloromethane. The mixture was filtered through Celite, and after washing the Celite with warm dichloromethane the filtrate was concentrated to a total volume of ~20 mL. After laying the solution with diethyl ether and letting sit at room temperature overnight, crystalline precipitate forms which is isolated by vacuum filtration, yielding the product as a dark brown solid (0.670 g, 18%). ^{1}H NMR ($CDCl_3$, 500 MHz) δ: 7.43 (m, 4H), 7.20 (t, *J* = 7.8 Hz, 2H), 7.09 (t, *J* = 7.8 Hz, 4H)) 6.66 (dd, *J* = 7.8, 27 Hz, 4H), 2.14 (s, 3H). ^{31}P NMR ($CDCl_3$, 202 MHz) δ: 101.48 ($\nu_{1/2}$ = 290 Hz).

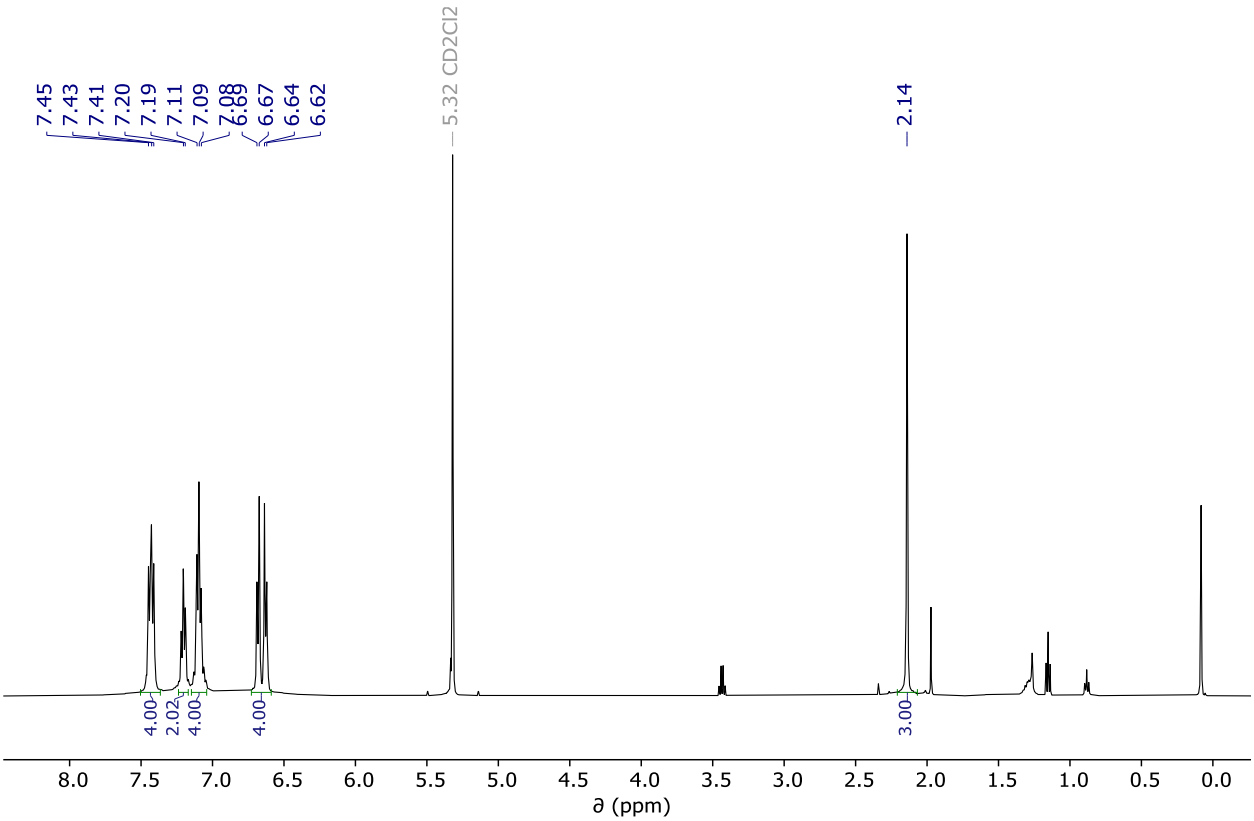

Figure 80. ^{1}H NMR (CD_2Cl_2, 25 °C, 500 MHz) spectrum of $Co_6Se_8(Ph_2PSTol)_6$

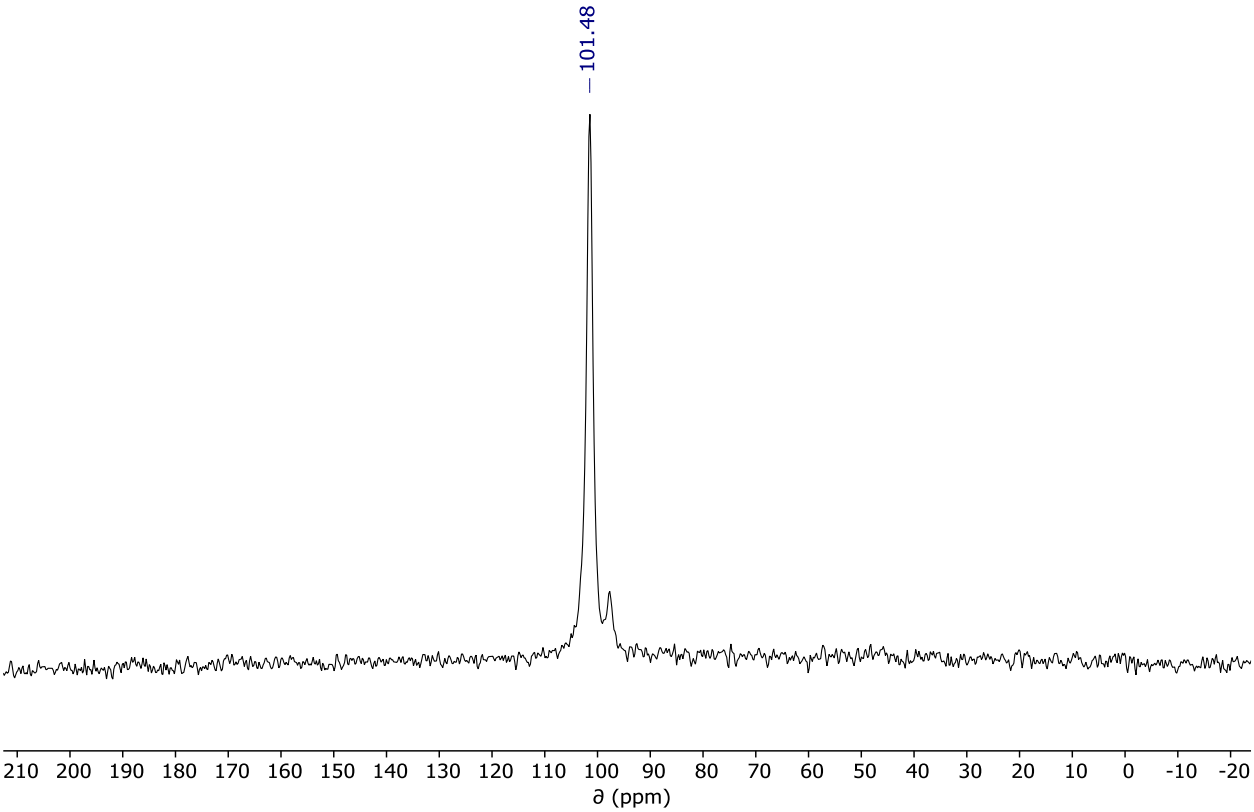

Figure 81. ^{31}P NMR (CD_2Cl_2, 25 °C, 202 MHz) spectrum of $Co_6Se_8(Ph_2PSTol)_6$

2.5.18 *Synthesis of $Co_6Se_8(Ph_2PCH_2(C_4H_7O))_6$*

To a 100 mL Schlenk flask with Teflon-coated stirbar, dicobalt octacarbonyl (2.130 g, 6.23 mmol) was added, and the flask capped with a rubber septum. The flask was taken out of the glovebox and attached to the Schlenk line and put under flow of nitrogen. With the flask sidearm open to vent through the Schlenk line, a solution of $Ph_2PSeCH_2C_4H_7O$ (5.800 g) in toluene (20 mL) was injected into the flask, resulting in evolution of gas and formation of a dark- red-brown solution. The mixture was stirred at room temperature for 30 minutes, then gradually heated to reflux. The solution was left to reflux and stir overnight while venting through the Schlenk line. The next day, $Ph_2PCH_2C_4H_7O$ is dissolved in toluene and injected into the reaction mixture, which was stirred for 16 more hours at reflux. The flask is then cooled and the solvent removed under vacuum. The resulting residue is dissolved in warm dichloromethane and filtered through Celite. After washing the Celite with a small amount of warm dichloromethane, the filtrate is concentrated to a volume of ~70 mL and layered with diethyl ether (130 mL) and stored in the freezer for 2 days. The resulting precipitate is isolated via vacuum filtration, and after washing with diethyl ether the

product is isolated as a dark brown powder. ^{1}H NMR (CD_2Cl_2, 500 MHz) δ: 7.39 (m, 4H), 7.25 (m, 2H), 7.18 (m 4H), ^{31}P NMR (CD_2Cl_2, 202 MHz) δ: -52.66 ($\nu_{1/2}$ = 370 Hz).

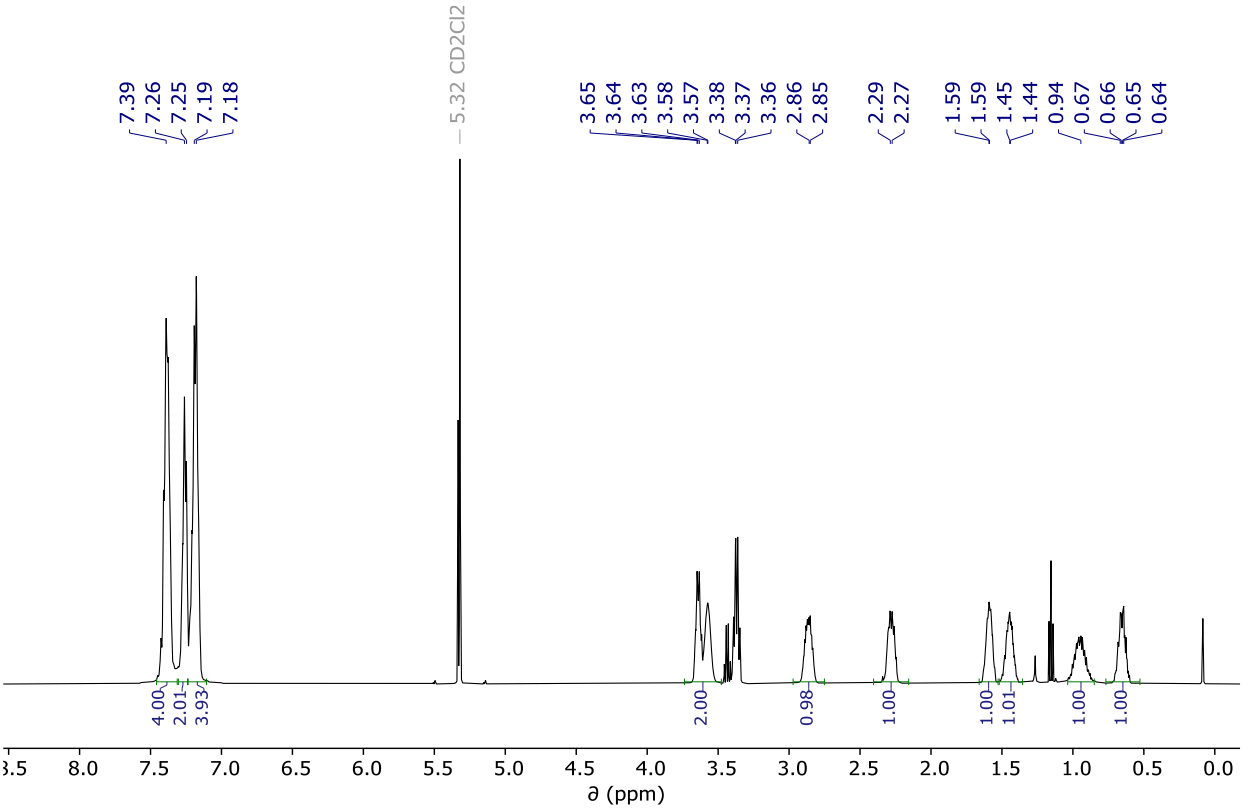

Figure 82. ^{1}H NMR (CD_2Cl_2, 25 °C, 500 MHz) spectrum of $Co_6Se_8(Ph_2PCH_2(C_4H_7O))_6$

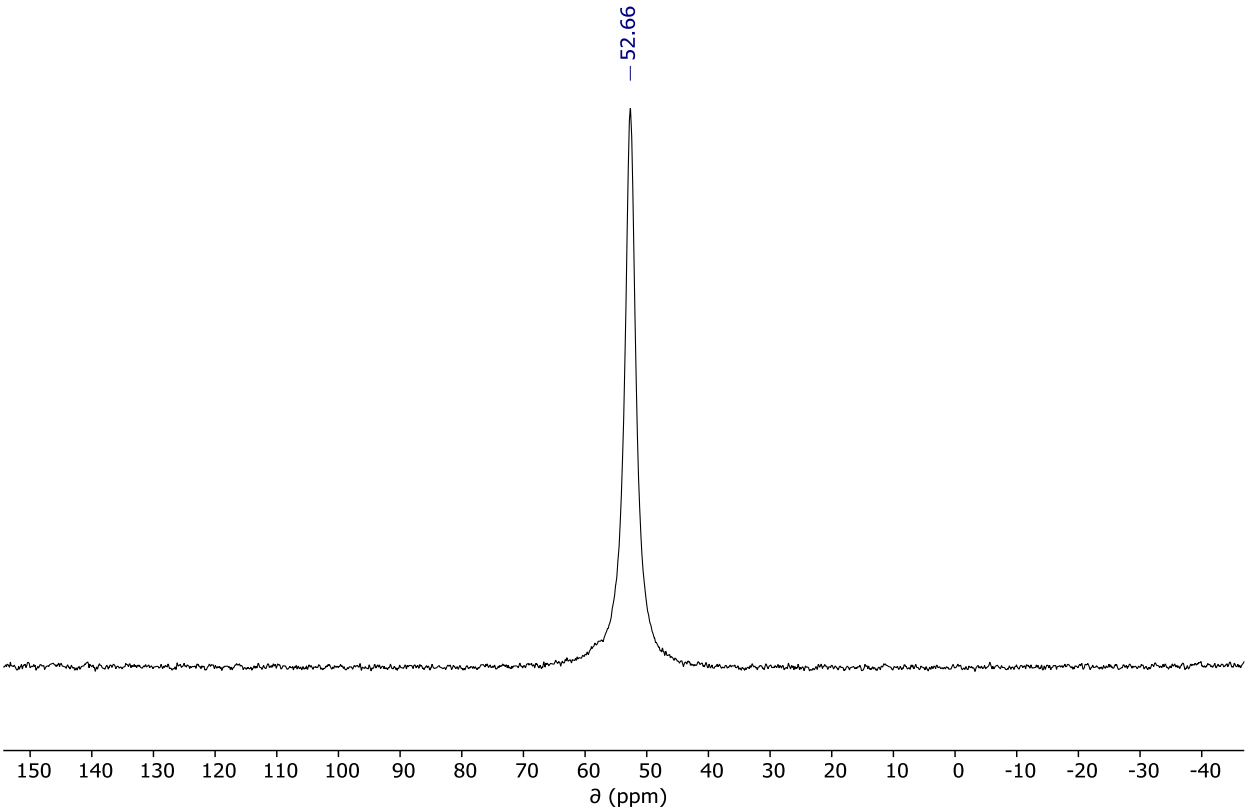

Figure 83. ^{31}P NMR (CD_2Cl_2, 25 °C, 202 MHz) spectrum of $Co_6Se_8(Ph_2PCH_2(C_4H_7O))_6$

2.6 X-RAY DIFFRACTION STUDIES

Single crystals suitable for X-ray analysis were coated in deoxygenated paratone oil and mounted on a 20 µm CryoLoop™ (Hampton Research, 18 mm mount, 0.2 to 0.3 mm loop diameter). Data was collected either at –173 °C or –183 °C on a Bruker APEX II or Nonius Kappa CCD FR590 single crystal X-ray diffractometer, respectively, each equipped with a Mo source, as indicated for each sample. Unless indicated otherwise, all data was integrated and scaled using SAINT, SADABS within the APEX2 software package by Bruker.[77] Solution by direct methods (SHELXT[78] or SIR97[79,80]) produced a complete heavy atom phasing model consistent with the proposed structure. Structures were completed by difference Fourier synthesis with SHELXL.[81–83] Scattering factors are from Waasmair and Kirfel.[84] Hydrogen atoms were placed in geometrically idealized positions and constrained to ride on their parent atoms with C–H distances in the range 0.95–1.00 Å. Isotropic thermal parameters U_{eq} were fixed such that they were $1.2U_{eq}$ of their parent atom U_{eq} for CHs and $1.5U_{eq}$ of their parent atom U_{eq} in case of methyl groups. All non-hydrogen atoms were refined anisotropically by full-matrix least-squares.

2.6.1 *$Co_6Se_8(Ph_2PCH_2NHTol)_6$*

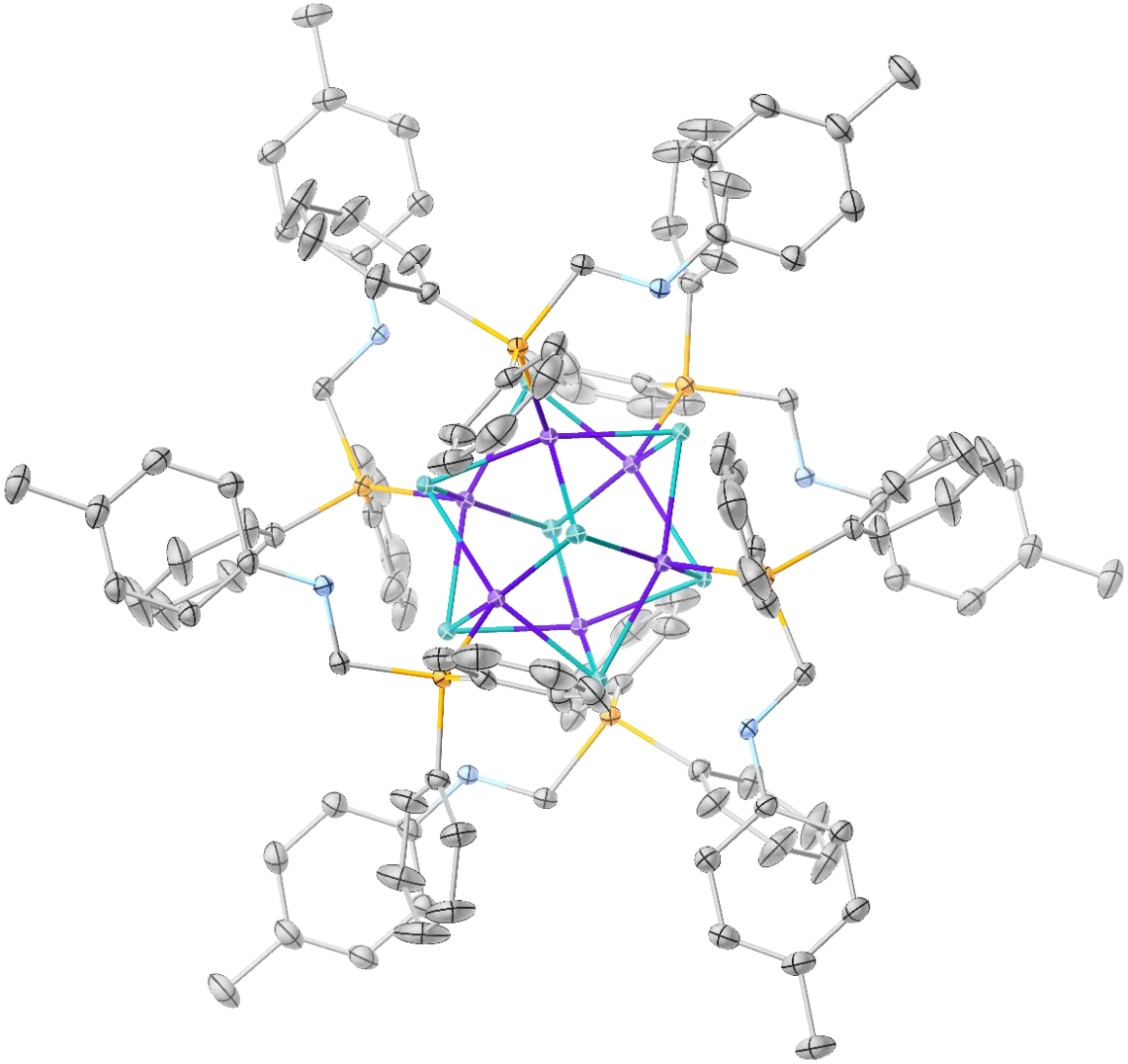

Figure 84. Solid-state structure of $Co_6Se_8(Ph_2PCH_2NHTol)_6$ with thermal ellipsoids shown at a 50% probability level. All hydrogen atoms and co-crystallized solvent molecules omitted for clarity.

Single crystals of suitable quality for X-ray diffraction were grown by vapor diffusion of *n*-pentane into a solution of the cluster in toluene at room temperature. The N-H proton was refined freely, as the data was of excellent quality.

2.6.2 *$Co_6Se_8(Ph_2PCH_2OH)_6$*

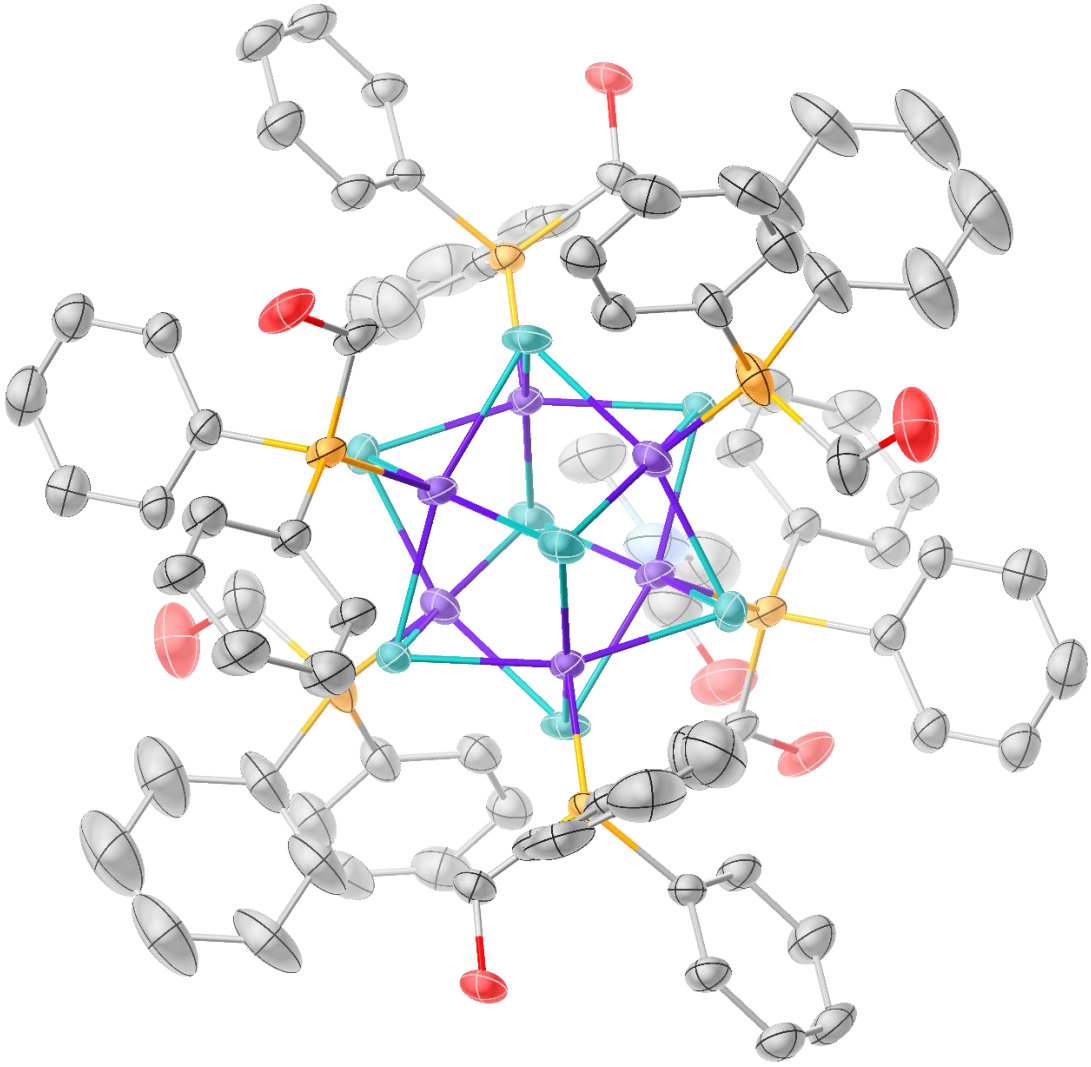

Figure 85. Solid-state structure of $Co_6Se_8(Ph_2PCH_2OH)_6$ with thermal ellipsoids shown at a 50% probability level. All hydrogen atoms and co-crystallized solvent molecules omitted for clarity.

Single crystals of suitable quality for X-ray diffraction were grown by layering diethyl ether onto a solution of the cluster in *N*,*N*-dimethylformamide at -35 °C. Each phosphine ligand exhibits significant positional disorder, which is correlated with similar disorder in the dimethylformamide molecules in the lattice that hydrogen bond to the ligands. This disorder was managed using RIGU, FLAT, and EADP restraints on the organic moieties in the structure.

2.6.3 *$Co_6Se_8(Ph_2PCH_2OCH_3)_6$*

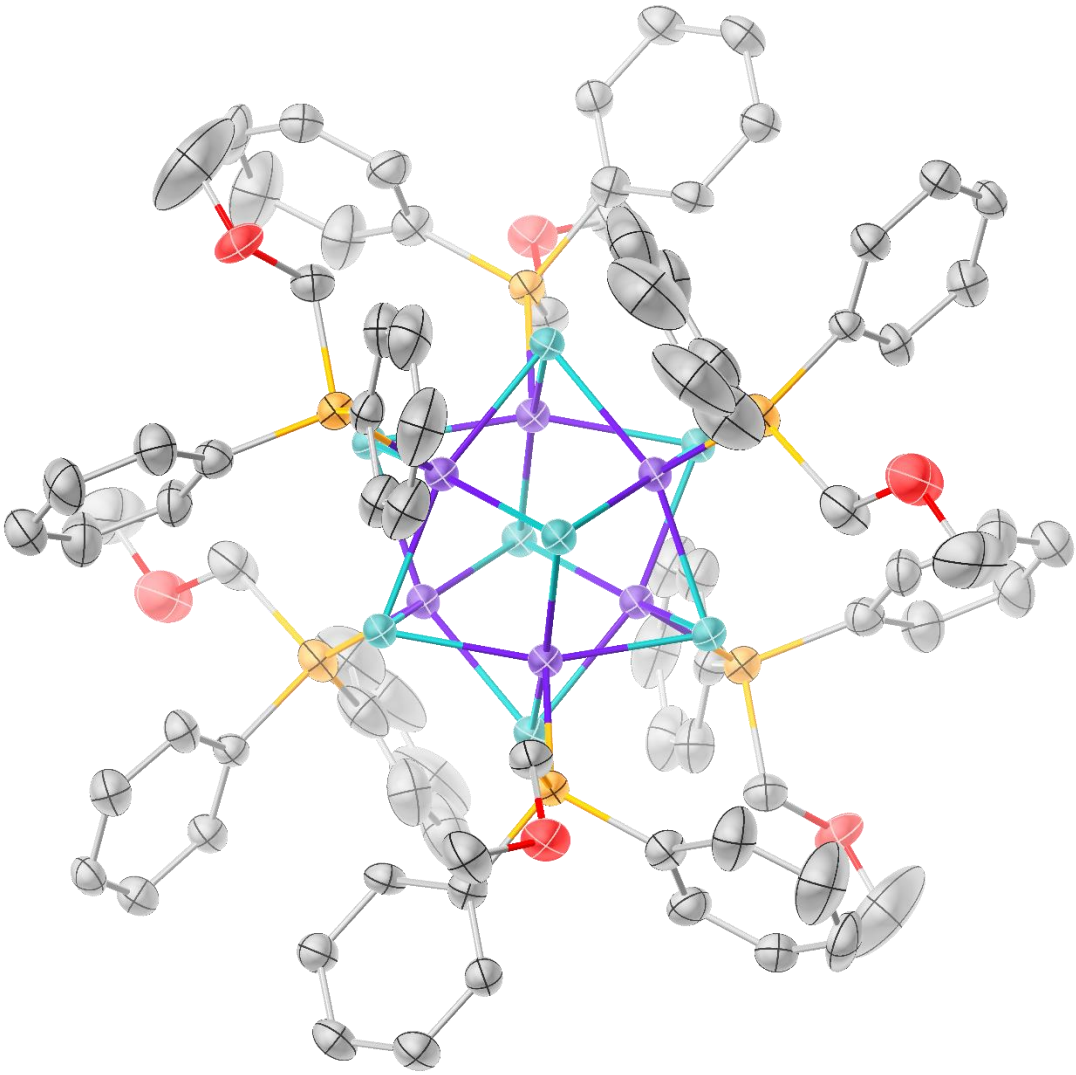

Figure 86. Solid-state structure of $Co_6Se_8(Ph_2PCH_2OCH_3)_6$ with thermal ellipsoids shown at a 50% probability level. All hydrogen atoms and co-crystallized solvent molecules omitted for clarity.

Single crystals of suitable quality for X-ray diffraction were grown by layering diethyl ether onto a solution of the cluster in dichloromethane at room temperature.

2.6.4 *[$Co_6Se_8(Ph_2PCH_2OSi(CH_3)_3)_6$][$PF_6$]*

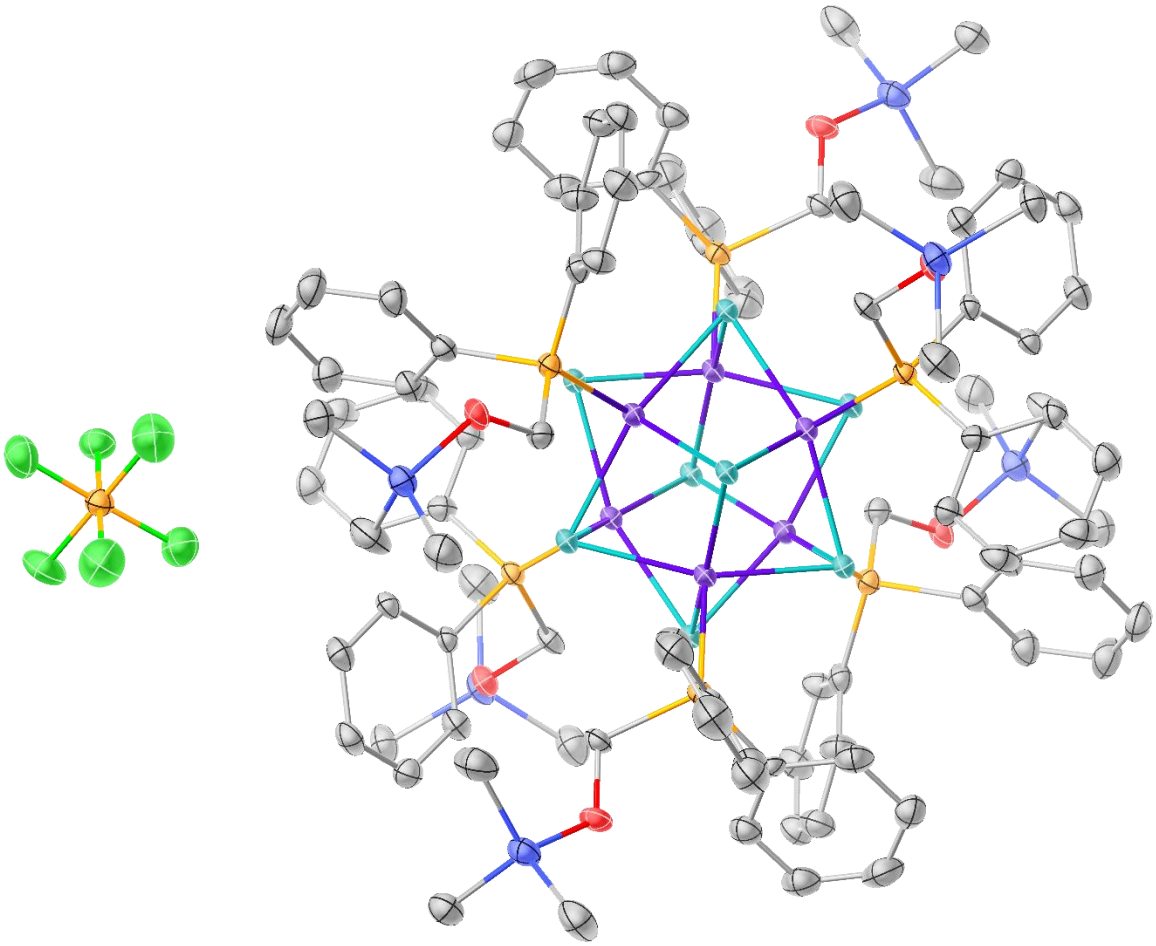

Figure 87. Solid-state structure of $Co_6Se_8(Ph_2PCH_2OSi(CH_3)_3)_6$ with thermal ellipsoids shown at a 50% probability level. All hydrogen atoms and co-crystallized solvent molecules omitted for clarity.

Single crystals of suitable quality for X-ray diffraction were grown by layering diethyl ether onto a solution of the cluster in dichloromethane at –35 °C. Within the structure, it was found that the PF_6 anion was substitutionally disordered with a molecule of dichloromethane with an occupancy of 0.5 for either moiety. Since the structure is centrosymmetric, this means there is one cluster unit for each $[PF_6]^-$.

2.6.5 *[Co$_6$Se$_8$(Ph$_2$PCH$_2$OSi(CH$_3$)$_3$)$_6$][FeCl$_4$]$_2$*

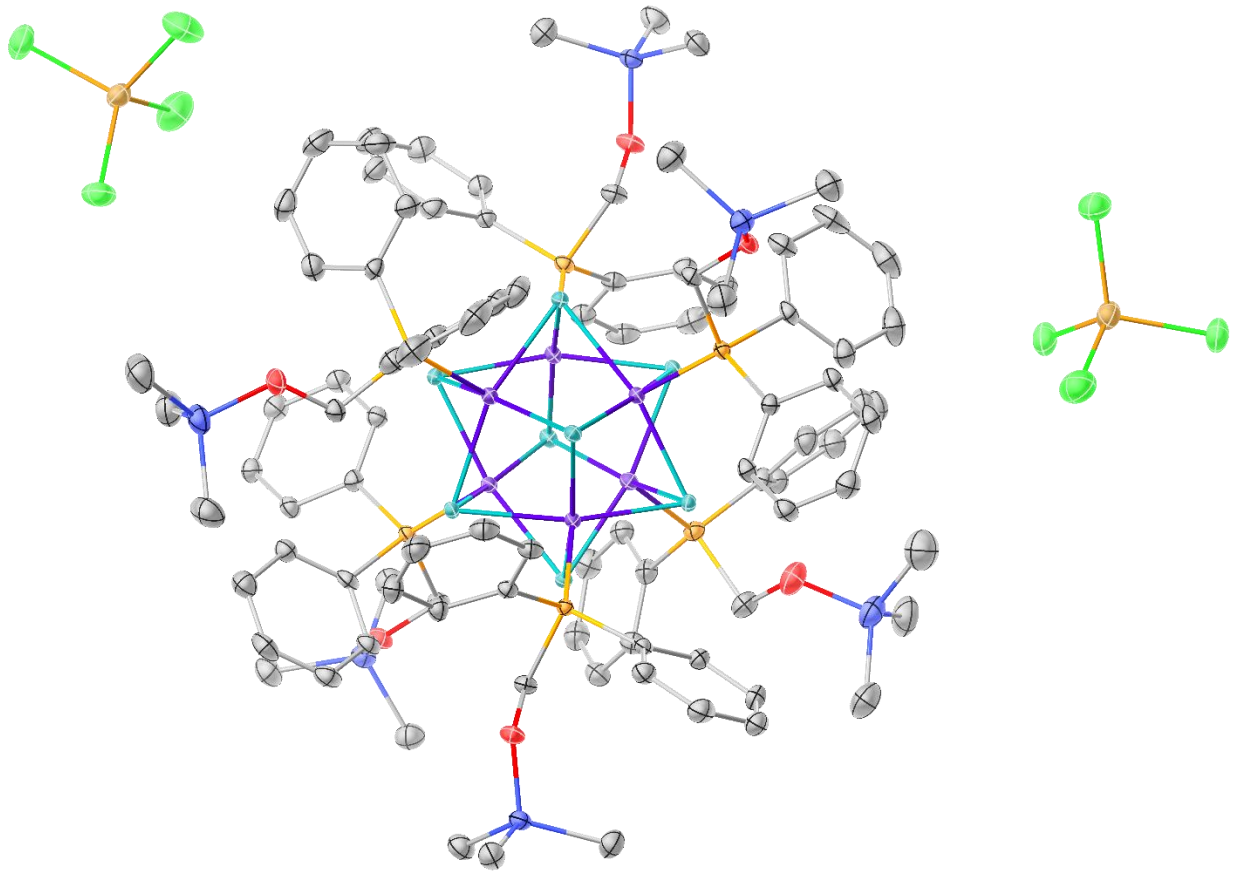

Figure 88. Solid-state structure of $Co_6Se_8(Ph_2PCH_2OSi(CH_3)_3)_6$ with thermal ellipsoids shown at a 50% probability level. All hydrogen atoms and co-crystallized solvent molecules omitted for clarity.

Single crystals of suitable quality for X-ray diffraction were grown by layering diethyl ether onto a mixture of $Co_6Se_8(Ph_2PCH_2OSi(CH_3)_3)_6$ and $FeCl_3$ in dichloromethane at –35 °C.

2.6.6 *$Co_6Se_8(Ph_2PCH_2CH_2OH)_6$*

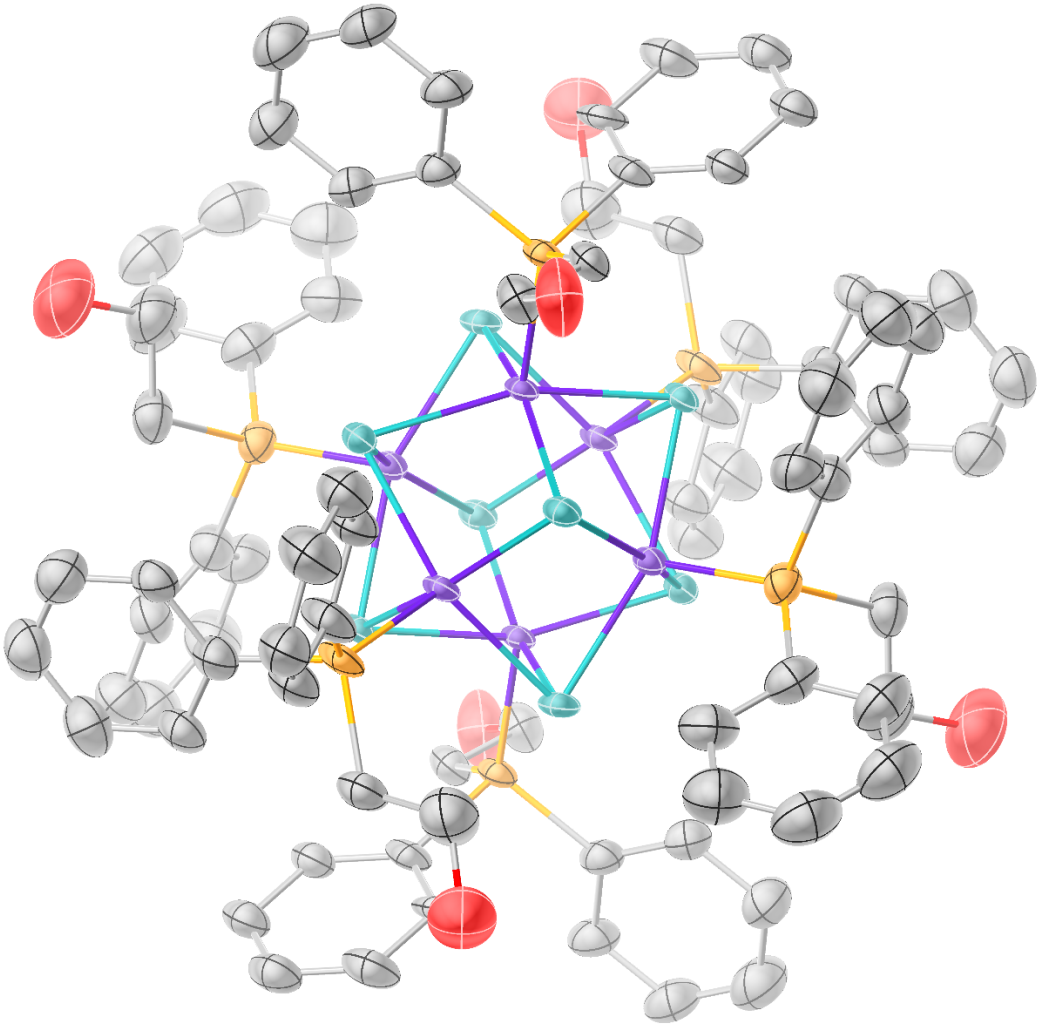

Figure 89. Solid-state structure of $Co_6Se_8(Ph_2PCH_2CH_2OH)_6$ with thermal ellipsoids shown at a 50% probability level. All hydrogen atoms and co-crystallized solvent molecules omitted for clarity.

Single crystals of suitable quality for X-ray diffraction were grown by layering diethyl ether onto a solution of the cluster in *N*,*N*-dimethylformamide at -35 °C.

2.6.7 *$Co_6Se_8(Ph_2PCH_2CH_2OSi(CH_3)_3)_6$*

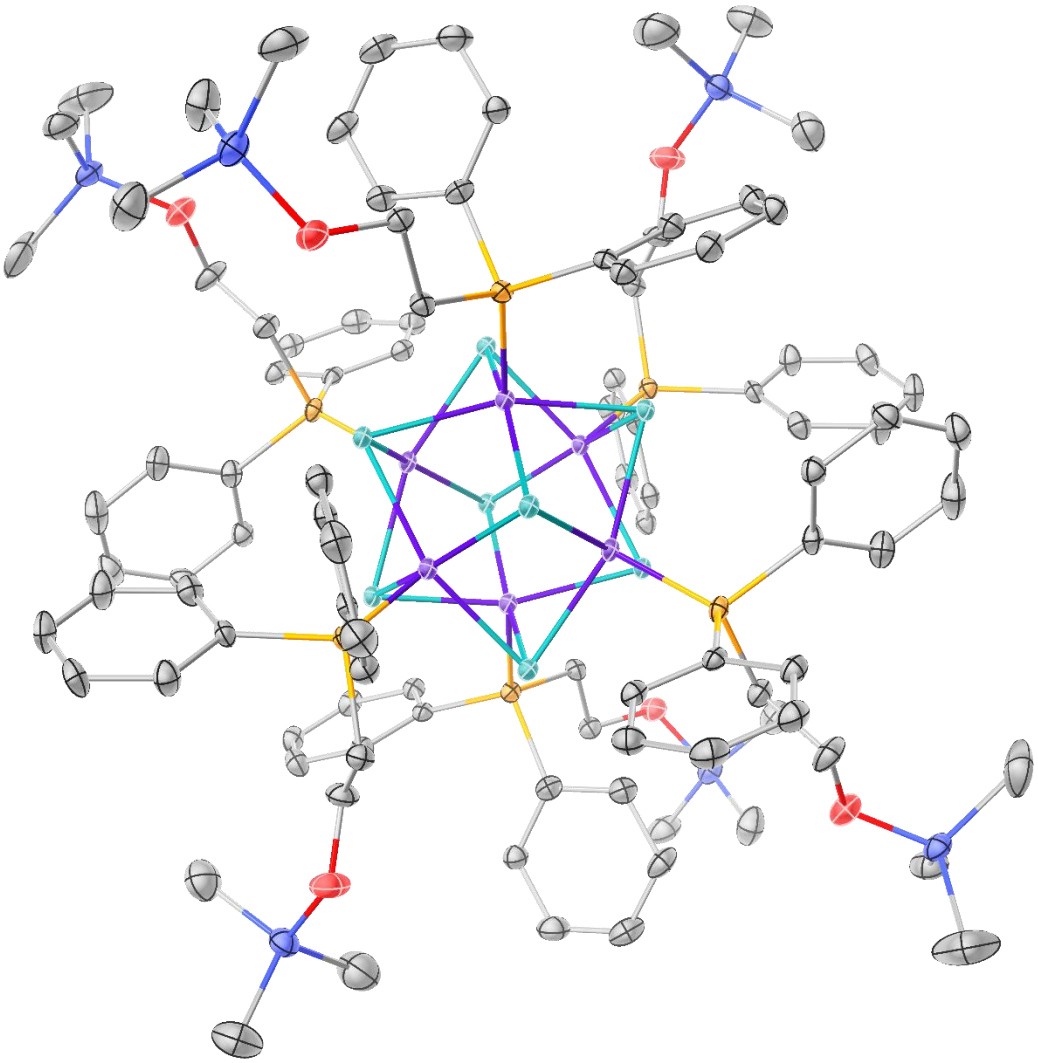

Figure 90. Solid-state structure of $Co_6Se_8(Ph2PCH_2CH2OSi(CH_3)_3)_6$ with thermal ellipsoids shown at a 50% probability level. All hydrogen atoms and co-crystallized solvent molecules omitted for clarity.

Single crystals of suitable quality for X-ray diffraction were grown by layering pentane onto a solution of the cluster in dichloromethane at room temperature.

2.6.8 *$Co_6Se_8(Ph_2PH)_6$*

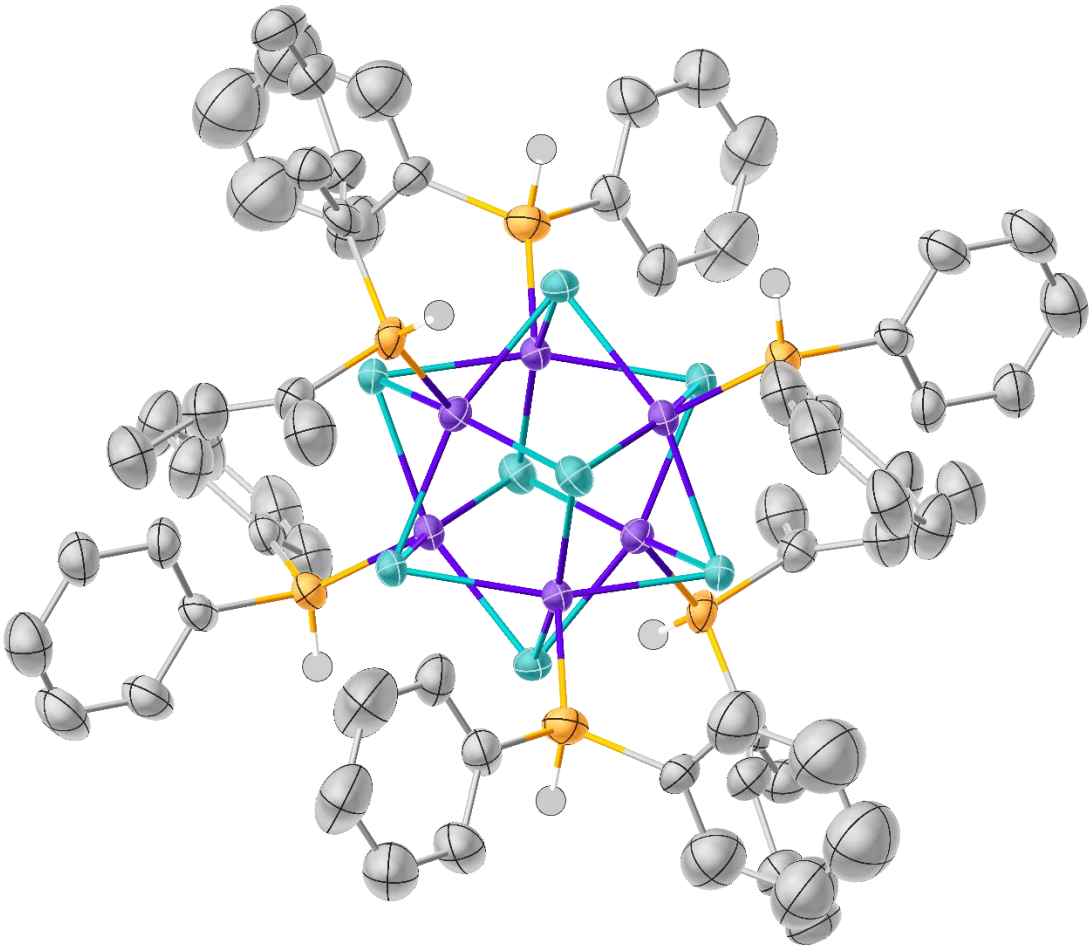

Figure 91. Solid-state structure of $Co_6Se_8(Ph_2PH)_6$ with thermal ellipsoids shown at a 50% probability level. All hydrogen atoms and co-crystallized solvent molecules omitted for clarity, except for P-H hydrogen atoms (drawn as 2D spheres).

Single crystals of suitable quality for X-ray diffraction were grown by layering diethyl ether onto a solution of the cluster in dichloromethane at room temperature. The P-H hydrogen atoms were located from the difference map and refined semi-freely, with their distances restrained with the SADI command.

2.6.9 *[Co$_6$Se$_8$(Ph$_2$PH)$_6$][PF$_6$]*

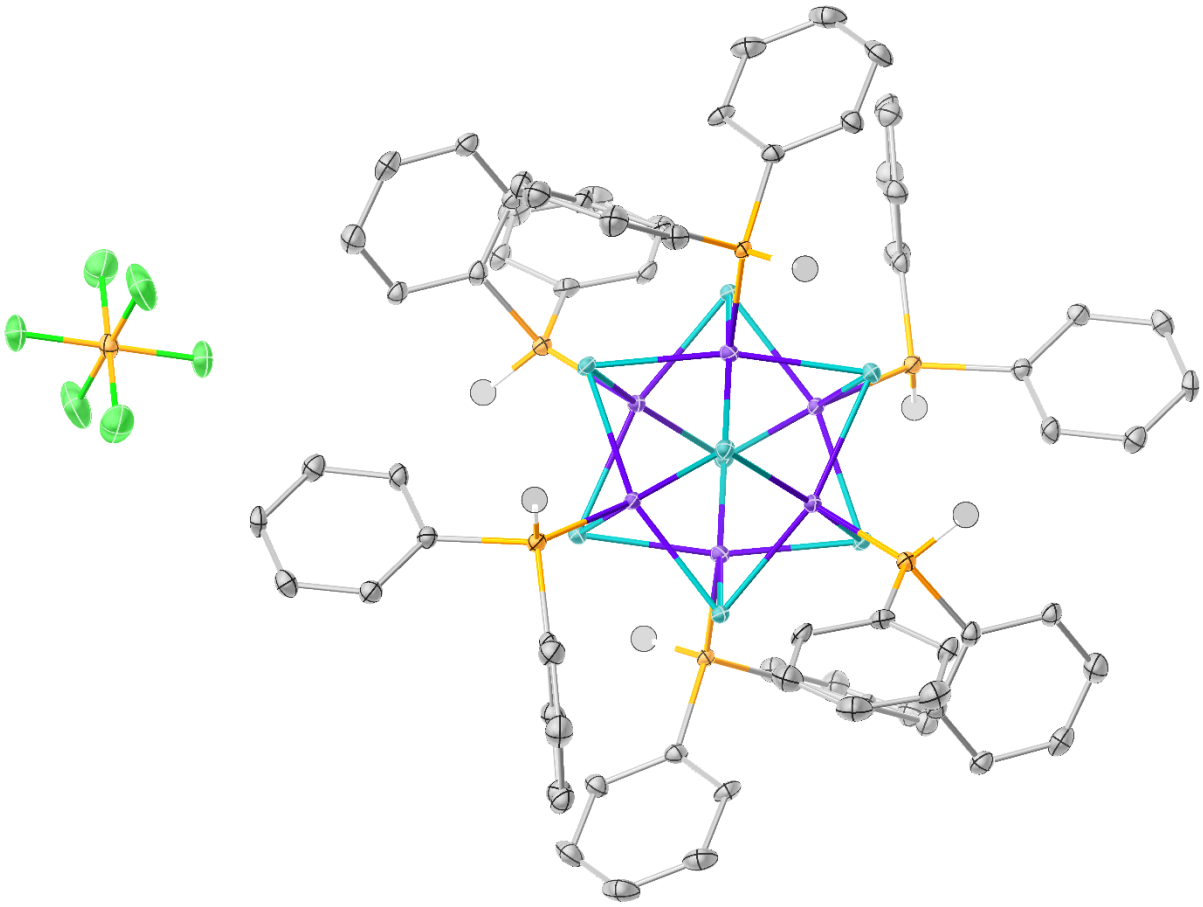

Figure 92. Solid-state structure of [Co$_6$Se$_8$(Ph$_2$PH)$_6$][PF$_6$] with thermal ellipsoids shown at a 50% probability level. All hydrogen atoms and co-crystallized solvent molecules omitted for clarity, except for P-H hydrogen atoms (drawn as 2D spheres).

Single crystals of suitable quality for X-ray diffraction were grown by cooling an acetonitrile solution of the cluster to –35 °C for two days. The P-H hydrogen atoms were located from the difference map and refined freely.

2.6.10 *$Co_6Se_8(Ph_2PSTol)_6$*

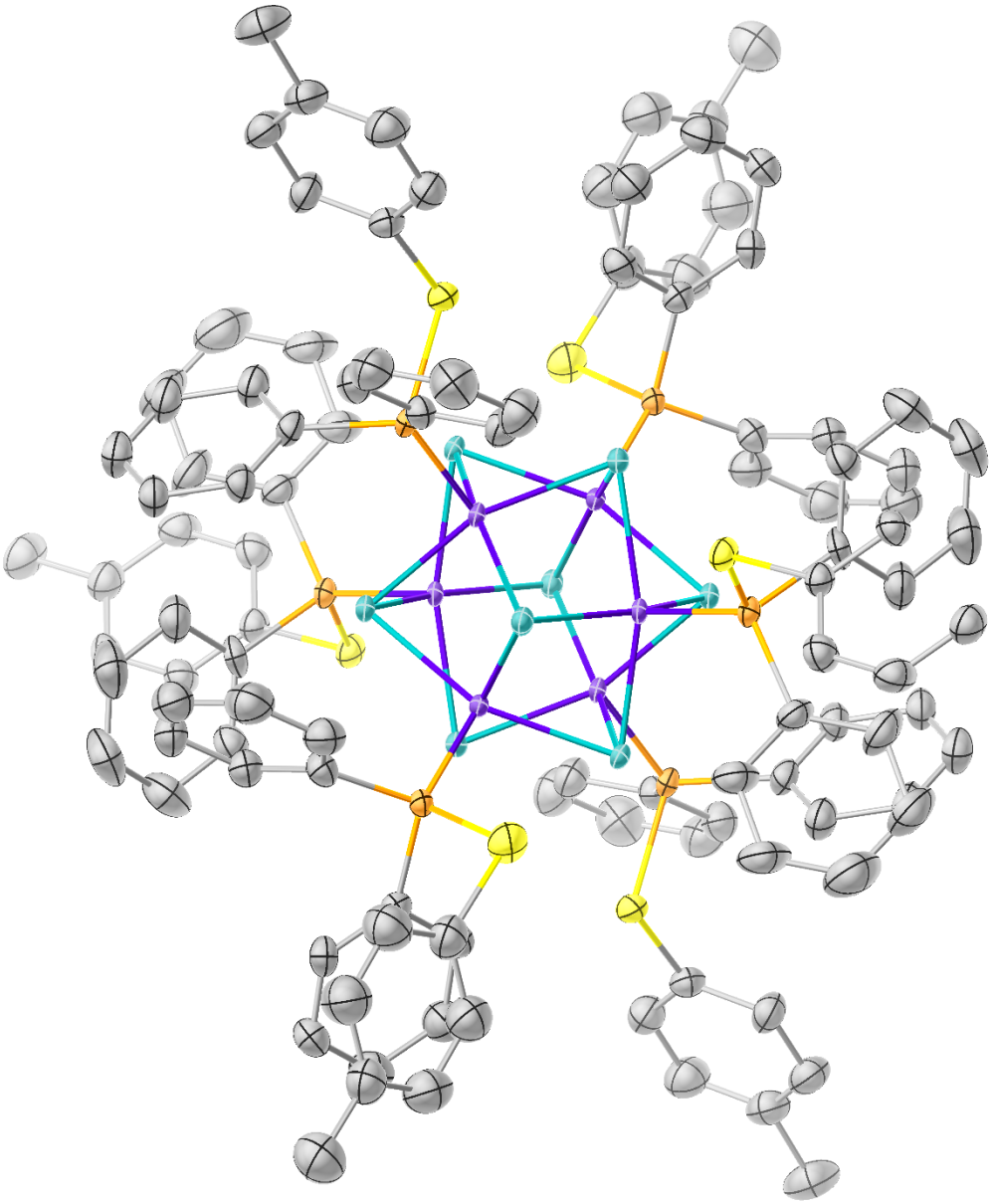

Figure 93. Solid-state structure of $Co_6Se_8(Ph_2PSTol)_6$ with thermal ellipsoids shown at a 50% probability level. All hydrogen atoms and co-crystallized solvent molecules omitted for clarity.

Single crystals of suitable quality for X-ray diffraction were grown by layering pentane onto a solution of the cluster in dichloromethane at room temperature.

2.6.11 *$Co_6Se_8(Ph_2PCH_2C_4H_7O)_6$*

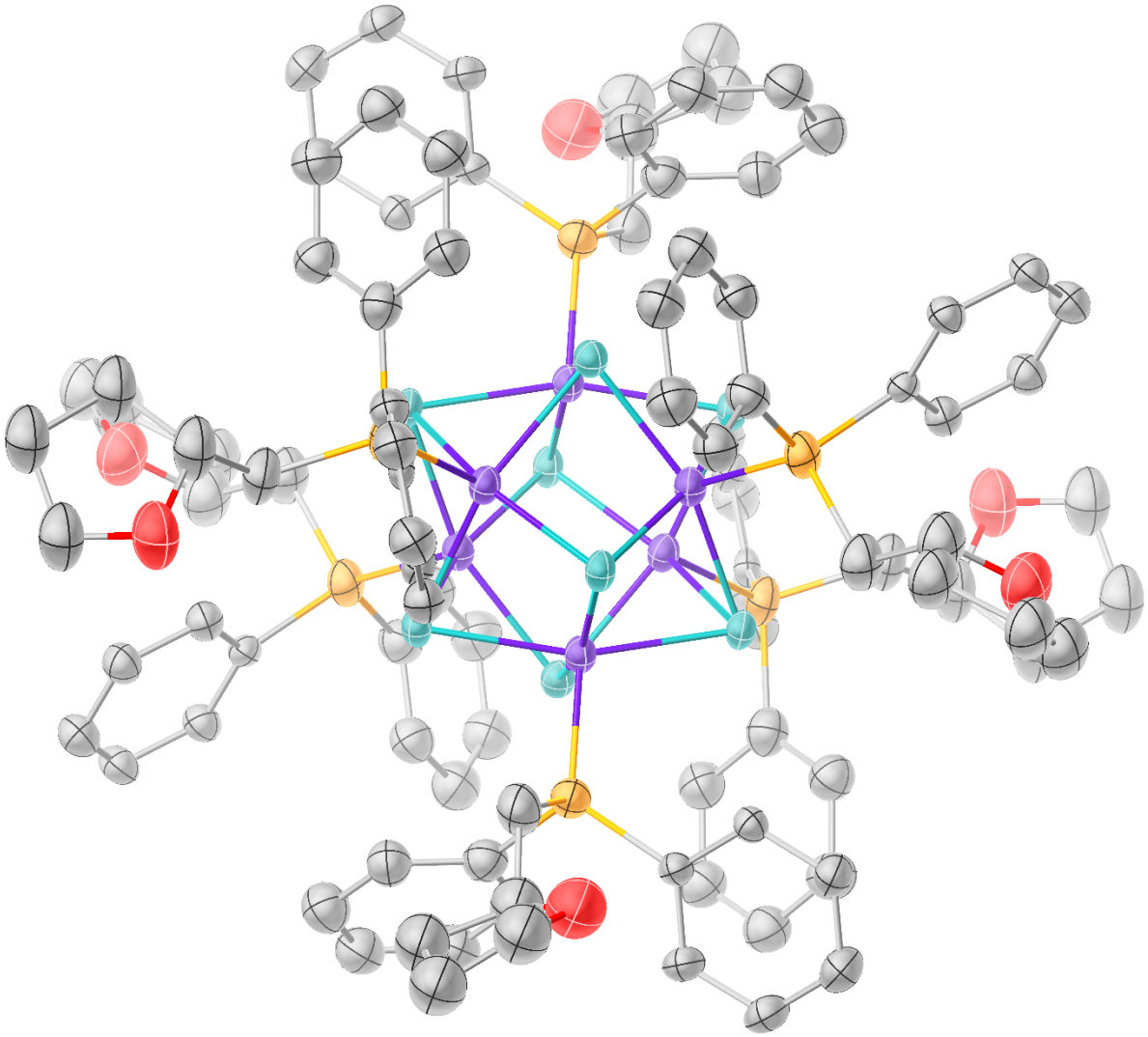

Figure 94. Solid-state structure of $Co_6Se_8(Ph_2PCH_2C_4H_7O)_6$ with thermal ellipsoids shown at a 30% probability level. All hydrogen atoms and co-crystallized solvent molecules omitted for clarity. Only a single enantiomer of the disordered phosphine is shown.

Single crystals of suitable quality for X-ray diffraction were grown by layering diethyl ether onto a solution of the cluster in dichloromethane at room temperature. The phosphine ligand was disordered due to the presence of both enantiomers of the ligand, requiring the usage of DELU, ISOR, and SIMU restraints.

Table 7. Crystallographic information for $Co_6Se_8(Ph_2PCH_2NHTol)_6$, $Co_6Se_8(Ph_2PCH_2OH)_6$, and $Co_6Se_8(Ph_2PCH_2CH_2OH)_6$

Compound	$Co_6Se_8(Ph_2PCH_2NHTol)_6$	$Co_6Se_8(Ph_2PCH_2OH)_6$	$Co_6Se_8(Ph_2PCH_2CH_2OH)_6$
Empirical formula	$C_{134}H_{136}Co_6N_6P_6Se_8$	$C_{102}H_{134}Co_6N_8O_{14}P_6Se_8$	$C_{106}H_{142}Co_6N_8O_{13}P_6Se_8$
CCDC Number	-	-	-
Formula weight	3001.56	2867.24	2879.33
Temperature (K)	100(2)	100(2)	100(2)
Wavelength (Å)	0.71073	0.71073	0.71073
Crystal system	Trigonal	Monoclinic	Triclinic
Space group	R -3 :H	C2/c	P -1
a (Å)	19.0324(7)	29.2699(12)	16.2849(9)
b (Å)	19.0324(7)	14.6169(5)	18.5339(12)
c (Å)	29.7609(12)	30.0860(18)	19.4856(12)
α (°)	90	90	95.494(4)
β (°)	90	115.714(2)	91.628(3)
γ (°)	120	90	91.872(3)
Volume (Å^3)	9336.1(8)	11597.2(9)	5848.1(6)
Z	3	4	2
ρ^{calc} (g cm^{-1})	1.602	1.642	1.635
Absorption coefficient (mm^{-1})	3.250	3.493	3.463
F(000)	4518	5752	2896
Crystal size (mm^3)	0.300 x 0.200 x 0.150	0.260 x 0.070 x 0.070	0.200 x 0.070 x 0.050
Theta range for data collection (°)	1.412 to 30.547	1.502 to 28.401	1.050 to 25.156
Index ranges	$-27\leq h\leq 27$, $-27\leq k\leq 27$, $0\leq l\leq 42$	$-39\leq h\leq 39$, $-19\leq k\leq 19$, $-40\leq l\leq 40$	$-19\leq h\leq 19$, $-22\leq k\leq 22$, $-23\leq l\leq 23$
Reflections collected	18992	28446	41445
Independent reflections	6364 [R(int) = 0.0208]	14529 [R(int) = 0.0353]	20733 [R(int) = 0.0695]
Completeness to theta = 25.000°	100.0%	99.9%	98.9 %
Data / restraints / parameters	6364 / 102/ 279	14529 / 1515/ 795	20733 / 1918 / 1209
Goodness-of-fit on F^2	1.077	1.104	1.089
Final R indices [I>2sigma(I)]	R1 = 0.0363, wR2 = 0.0667	R1 = 0.0616, wR2 = 0.1303	R1 = 0.0814, wR2 = 0.1912
R indices (all data)	R1 = 0.0377, wR2 = 0.0748	R1 = 0.0951, wR2 = 0.1445	R1 = 0.1325, wR2 = 0.2288
Largest diff. peak and hole (e$^-$Å^{-3})	0.924 and –0.389	1.490 and –0.702	2.551 and –1.023

Table 8. Crystallographic information for $Co_6Se_8(Ph_2PCH_2OCH_3)_6$, $[Co_6Se_8(Ph_2PCH_2OSi(CH_3)_3)_6][PF_6]$, and $[Co_6Se_8(Ph_2PCH_2OSi(CH_3)_3)_6][PF_6]$

Compound	$Co_6Se_8(Ph_2PCH_2OCH_3)_6$	$[Co_6Se_8(Ph_2PCH_2OSi(CH_3)_3)_6][PF_6]$	$[Co_6Se_8(Ph_2PCH_2OSi(CH_3)_3)_6][FeCl_4]_2$
Empirical formula	$C_{84}H_{90}Co_6O_6P_6Se_8$	$C_{97}H_{128}Cl_2Co_6F_6O_6P_7Se_8Si_6$	$C_{98}H_{130}Cl_{12}Co_6Fe_2O_6P_6Se_8Si_6$
CCDC Number	-	-	-
Formula weight	2366.63	2945.48	3280.73
Temperature (K)	100(2)	100(2)	100(2)
Wavelength (Å)	0.71073	0.71073	0.71073
Crystal system	Triclinic	Triclinic	Triclinic
Space group	P -1	P -1	P -1
a (Å)	13.1751(8)	14.7932(17)	16.9630(12)
b (Å)	13.6400(9)	14.9151(15)	18.9606(13)
c (Å)	13.9207(13)	15.8051(17)	21.5838(14)
α (°)	118.690(4)	78.187(4)	77.890(3)
β (°)	98.176(6)	64.925(4)	78.966(3)
γ (°)	96.400(4)	67.936(4)	70.924(4)
Volume ($Å^3$)	2125.2(3)	2923.0(6)	6357.8(8)
Z	1	1	2
ρ^{calc} (g cm^{-1})	1.849	1.673	1.714
Absorption coefficient (mm^{-1})	4.735	3.583	3.705
F(000)	1166	1469	3260
Crystal size (mm^3)	0.070 x 0.050 0.050	0.460 x 0.240 x 0.120	0.300 x 0.300 x 0.100
Theta range for data collection (°)	1.596 to 25.350	1.425 to 28.279	1.151 to 28.354
Index ranges	$-15\leq h\leq 15$, $-16\leq k\leq 16$, $-16\leq l\leq 16$	$-19\leq h\leq 19$, $-19\leq k\leq 19$, $-20\leq l\leq 20$	$-22\leq h\leq 22$, $-25\leq k\leq 25$, $-28\leq l\leq 28$
Reflections collected	42961	28756	63031
Independent reflections	7691 [R(int) = 0.1129]	14421 [R(int) = 0.0801]	31610 [R(int) = 0.0312
Completeness to theta = 25.000°	99.0 %	100.0 %	99.9%
Data / restraints / parameters	7691 / 623/ 557	14421 / 36 / 676	31610 / 51 / 1347
Goodness-of-fit on F^2	1.029	0.970	1.027
Final R indices [I>2sigma(I)]	R1 = 0.0590, wR2 = 0.1398	R1 = 0.0461, wR2 = 0.0833	R1 = 0.0423, wR2 = 0.1096
R indices (all data)	R1 = 0.0858, wR2 = 0.1589	R1 = 0.1017, wR2 = 0.1016	R1 = 0.0652, wR2 = 0.1234
Largest diff. peak and hole ($e^-Å^{-3}$)	1.788 and –1.213	0.719 and –0.824	1.779 and –1.408

Table 9. Crystallographic information for $Co_6Se_8(Ph_2PCH_2CH_2OSi(CH_3)_3)_6$, $Co_6Se_8(Ph_2PCH_2C_4H_7O)_6$, $Co_6Se_8(Ph_2PSTol)_6$

Compound	$Co_6Se_8(Ph_2PCH_2CH_2OSi(CH_3)_3)_6$	$Co_6Se_8(Ph_2PCH_2C_4H_7O)_6$	$Co_6Se_8(Ph_2PSTol)_6$
Empirical formula	$C_{102}H_{138}Co_6O_6P_6Se_8Si_6$	$C_{102}H_{114}Co_6O_6P_6Se_8$	$C_{117}H_{108}Cl_6Co_6P_6S_6Se_8$
CCDC Number	-	-	-
Formula weight	2799.74	2607.01	3090.17
Temperature (K)	100(2)	100(2)	100(2)
Wavelength (Å)	0.71073	0.71073	0.71073
Crystal system	Triclinic	Trigonal	Triclinic
Space group	P -1	R -3 c :H	P -1
a (Å)	13.3378(7)	15.1045(13)	13.9575(16)
b (Å)	14.3357(6)	15.1045(13)	15.2262(18)
c (Å)	16.2044(8)	93.178(10)	16.5780(19)
α (°)	110.412(2)°	90	117.257(6)
β (°)	100.541(3)°	90	101.046(6)
γ (°)	91.348(3)°	120	92.305(6)
Volume ($Å^3$)	2842.0(2)	18410(4)	3040.7(6)
Z	1	6	1
ρ^{calc} (g cm^{-1})	1.636	1.411	1.688
Absorption coefficient (mm^{-1})	3.614	3.286	3.554
F(000)	1406	7788	1532
Crystal size (mm^3)	0.130 x 0.070 x 0.070	120 x 0.060 x 0.020	0.170 x 0.160 0.110
Theta range for data collection (°)	1.370 to 28.479	1.311 to 25.349	1.422 to 25.027
Index ranges	$-17\leq h\leq 17$, $-19\leq k\leq 19$, $-21\leq l\leq 21$	$-18\leq h\leq 18$, $-18\leq k\leq 17$, $-112\leq l\leq 113$	$-16\leq h\leq 16$, $-18\leq k\leq 18$, $-19\leq l\leq 19$
Reflections collected	28279	145553	84997
Independent reflections	14246 [R(int) = 0.0470]	3767 [R(int) = 0.1155]	10478 [R(int) = 0.08662]
Completeness to theta = 25.000°	100.0 %	100.0 %	97.4%
Data / restraints / parameters	14246 / 102 / 639	3767 / 542 / 308	10478 / 796 / 683
Goodness-of-fit on F^2	0.993	1.101	1.075
Final R indices [I>2sigma(I)]	R1 = 0.0343, wR2 = 0.0619	R1 = 0.0762, wR2 = 0.1628	R1 = 0.0781, wR2 = 0.2007
R indices (all data)	R1 = 0.650, wR2 = 0.0709	R1 = 0.1115, wR2 = 0.1875	R1 = 0.1011, wR2 = 0.2241
Largest diff. peak and hole ($e^-Å^{-3}$)	0.617 and –0.586	1.171 and –0.930	2.378 and –1.490

Table 10. Crystallographic information for $Co_6Se_8(Ph_2PH)_6$ and $[Co_6Se_8(Ph_2PH)_6][PF_6]$

Compound	$Co_6Se_8(Ph_2PH)_6$	$[Co_6Se_8(Ph_2PH)_6][PF_6]$
Empirical formula	$C_{74}H_{70}Cl_4Co_6P_6Se_8$	$C_{72}H_{66}Co_6F_6P_7Se_8$
CCDC Number	-	-
Formula weight	2272.18	2247.29
Temperature (K)	100(2)	100(2)
Wavelength (Å)	0.71073	0.71073
Crystal system	Orthorhombic	Triclinic
Space group	P c c n	P -1
a (Å)	25.5525(17)	10.7729(10)
b (Å)	25.7316(17)	13.0021(11)
c (Å)	11.8903(8)	13.5766(12)
α (°)	110.412(2)°	89.200(4)
β (°)	100.541(3)°	82.754(4)
γ (°)	91.348(3)°	84.852(4)
Volume ($Å^3$)	7818.0(9)	1878.9(3)
Z	4	1
ρ^{calc} (g cm^{-1})	1.930	1.986
Absorption coefficient (mm^{-1})	5.270	5.375
F(000)	4424	1091
Crystal size (mm^3)	0.570 x 0.100 x 0.100	0.600 x 0.500 x 0.200
Theta range for data collection (°)	1.123 to 28.301	1.573 to 26.372
Index ranges	$-34\leq h\leq 34$, $-34\leq k\leq 34$, $-15\leq l\leq 15$	$-13\leq h\leq 13$, $-16\leq k\leq 16$, $-16\leq l\leq 16$
Reflections collected	18522	15003
Independent reflections	9689 [R(int) = 0.0555]	7610 [R(int) = 0.0496]
Completeness to theta = 25.000°	99.8 %	99.3 %
Data / restraints / parameters	9689 / 319 / 411	7610 / 127 / 532
Goodness-of-fit on F^2	1.157	1.004
Final R indices [I>2sigma(I)]	R1 = 0.1035, wR2 = 0.2059	R1 = 0.0418, wR2 = 0.0924
R indices (all data)	R1 = 0.1616, wR2 = 0.2221	R1 = 0.0468, wR2 = 0.0963
Largest diff. peak and hole ($e^-Å^{-3}$)	1.524 and –1.247	1.990 and –1.737

2.7 REFERENCES

(1) Kephart, J. A.; Mitchell, B. S.; Chirila, A.; Anderton, K. J.; Rogers, D.; Kaminsky, W.; Velian, A. Atomically Defined Nanopropeller Fe3Co6Se8(Ph2PNTol)6: Functional Model for the Electronic Metal–Support Interaction Effect and High Catalytic Activity for Carbodiimide Formation. *J. Am. Chem. Soc.* **2019**, *141* (50), 19605–19610. https://doi.org/10.1021/jacs.9b12473.

(2) Kephart, J. A.; Boggiano, A. C.; Kaminsky, W.; Velian, A. Inorganic Clusters as Metalloligands: Ligand Effects on the Synthesis and Properties of Ternary Nanopropeller Clusters. *Dalton Trans.* **2020**, *49* (45), 16464–16473. https://doi.org/10.1039/D0DT02416C.

(3) Mitchell, B. S.; Chirila, A.; Kephart, J. A.; Boggiano, A. C.; Krajewski, S. M.; Rogers, D.; Kaminsky, W.; Velian, A. Metal–Support Interactions in Molecular Single-Site Cluster Catalysts. *J. Am. Chem. Soc.* **2022**, *144* (40), 18459–18469. https://doi.org/10.1021/jacs.2c07033.

(4) Xu, Y.; Chen, J.; Aydt, A. P.; Zhang, L.; Sergeyev, I.; Keeler, E. G.; Choi, B.; He, S.; Reichman, D. R.; Friesner, R. A.; Nuckolls, C.; Steigerwald, M. L.; Roy, X.; McDermott, A. E. Electron and Spin Delocalization in [Co6Se8(PEt3)6]0/+1 Superatoms. *ChemPhysChem* **2024**, *25* (2), e202300064. https://doi.org/10.1002/cphc.202300064.

(5) Thiele, G.; You, Z.; Dehnen, S. Molecular CHEVREL-like Clusters [(RhPPh3)6(M3-Se)8] and [Pd6(M3-Te)8]4–. *Inorg. Chem.* **2015**, *54* (6), 2491–2493. https://doi.org/10.1021/ic502409r.

(6) Cecconi, F.; Ghilardi, C. A.; Midollini, S.; Orlandini, A.; Zanello, P. Redox Behaviour of the Iron–Sulphur Cluster [Fe6(M3-S)8(PEt3)6]2+. Synthesis and Crystal Structure of the New Paramagnetic Monopositive Species [Fe6(M3-S)8(PEt3)6]+ as Its [PF6]– Salt. *J. Chem. Soc. Dalton Trans.* **1987**, No. 4, 831–835. https://doi.org/10.1039/DT9870000831.

(7) Champsaur, A. M.; Velian, A.; Paley, D. W.; Choi, B.; Roy, X.; Steigerwald, M. L.; Nuckolls, C. Building Diatomic and Triatomic Superatom Molecules. *Nano Lett.* **2016**, *16* (8), 5273–5277. https://doi.org/10.1021/acs.nanolett.6b02471.

(8) Saito, T.; Yamamoto, N.; Nagase, T.; Tsuboi, T.; Kobayashi, K.; Yamagata, T.; Imoto, H.; Unoura, K. Molecular Models of the Superconducting Chevrel Phases: Syntheses and Structures of [Mo6X8(PEt3)6] and [PPN][Mo6X8(PEt3)6] (X = S, Se; PPN = (Ph3P)2N). *Inorg. Chem.* **1990**, *29* (4), 764–770. https://doi.org/10.1021/ic00329a039.

(9) Goddard, C. A.; Long, J. R.; Holm, R. H. Synthesis and Characterization of Four Consecutive Members of the Five-Member [Fe6S8(PEt3)6]N+ (n = 0−4) Cluster Electron Transfer Series. *Inorg. Chem.* **1996**, *35* (15), 4347–4354. https://doi.org/10.1021/ic960052i.

(10) Kamiguchi, S.; Imoto, H.; Saito, T.; Chihara, T. Syntheses, Structures, FAB Mass Spectra, and Magnetic Properties of Chromium Chalcogenide Cluster Complexes [Cr6Se8(PEt3)6], [Cr6Se8(H)(PEt3)6], and [Cr6S8(H)(PEt3)6]. *Inorg. Chem.* **1998**, *37* (26), 6852–6857. https://doi.org/10.1021/ic9807700.

(11) Mironov, Yu. V.; Kozhomuratova, Zh. S.; Naumov, D. Yu.; Fedorov, V. E. Synthesis and Structure of a New Molecular Octahedral Cluster Complex Mo6Se8(Ph3P)6·2H2O. *J. Struct. Chem.* **2007**, *48* (2), 383–387. https://doi.org/10.1007/s10947-007-0058-0.

(12) Novikova, E. D.; Gassan, A. D.; Ivanov, A. A.; Vorotnikov, Y. A.; Shestopalov, M. A. Neutral Mo6Q8-Clusters with Terminal Phosphane Ligands – a Route to Water-Soluble Molecular Units of Chevrel Phases. *New J. Chem.* **2022**, *46* (5), 2218–2223. https://doi.org/10.1039/D1NJ05802A.

(13) Gunasekaran, S.; Reed, D. A.; Paley, D. W.; Bartholomew, A. K.; Venkataraman, L.; Steigerwald, M. L.; Roy, X.; Nuckolls, C. Single-Electron Currents in Designer Single-Cluster Devices. *J. Am. Chem. Soc.* **2020**, *142* (35), 14924–14932. https://doi.org/10.1021/jacs.0c04970.

(14) Roy, X.; Schenck, C. L.; Ahn, S.; Lalancette, R. A.; Venkataraman, L.; Nuckolls, C.; Steigerwald, M. L. Quantum Soldering of Individual Quantum Dots. *Angew. Chem. Int. Ed.* **2012**, *51* (50), 12473–12476. https://doi.org/10.1002/anie.201206301.

(15) Perruchas, S.; Flores, S.; Jousselme, B.; Lobkovsky, E.; Abruña, H.; DiSalvo, F. J. [W6S8] Octahedral Tungsten Clusters Functionalized with Thiophene Derivatives: Toward Polymerizable Building Blocks. *Inorg. Chem.* **2007**, *46* (21), 8976–8987. https://doi.org/10.1021/ic7010748.

(16) Jeffrey, J. C.; Rauchfuss, T. B. Metal Complexes of Hemilabile Ligands. Reactivity and Structure of Dichlorobis(o-(Diphenylphosphino)Anisole)Ruthenium(II). *Inorg. Chem.* **1979**, *18* (10), 2658–2666. https://doi.org/10.1021/ic50200a004.

(17) Jiménez, M. V.; Pérez-Torrente, J. J.; Bartolomé, M. I.; Oro, L. A. Convenient Methods for the Synthesis of a Library of Hemilabile Phosphines. *Synthesis* **2009**, *2009*, 1916–1922. https://doi.org/10.1055/s-0028-1088060.

(18) Jiménez, M. V.; Bartolomé, M. I.; Pérez-Torrente, J. J.; Lahoz, F. J.; Oro, L. A. Rhodium(I) Complexes with Hemilabile Phosphines: Rational Design for Efficient Oxidative Amination Catalysts. *ChemCatChem* **2012**, *4* (9), 1298–1310. https://doi.org/10.1002/cctc.201200101.

(19) Kühl, O.; Blaurock, S.; Sieler, J.; Hey-Hawkins, E. Metallatriphos Complexes: Synthesis and Molecular Structure of [TpZr(OCH2PPh2)3] (Tp=tris(Pyrazolyl)Hydroborate) and Formation of the Heterodinuclear Complex [TpZr(μ-OCH2PPh2)3Mo(CO)3] with Bridging Phosphinoalkoxide Ligands. *Polyhedron* **2001**, *20* (17), 2171–2177. https://doi.org/10.1016/S0277-5387(01)00811-7.

(20) Acton, A. L.; Leroux, F.; Feula, A.; Melia, K.; Sambrook, M. R.; Hayes, W.; Russell, A. T. Self-Immolative Systems for the Disclosure of Reactive Electrophilic Alkylating Agents. *Chem. Commun.* **2019**, *55* (36), 5219–5222. https://doi.org/10.1039/C8CC09728C.

(21) Payet, E.; Auffrant, A.; Le Goff, X. F.; Floch, P. L. Phosphine- and Thiophosphorane-Amine Ligands: Lithiation and Coordination to Rh(I). *J. Organomet. Chem.* **2010**, *695* (10), 1499–1506. https://doi.org/10.1016/j.jorganchem.2010.03.006.

(22) Reeves, B. J.; Boardman, B. M. Synthesis and Characterization of Thienyl Phosphines and Thienyl Phosphine Chalcogenides. *Polyhedron* **2014**, *73*, 118–123. https://doi.org/10.1016/j.poly.2014.02.030.

(23) Lindner, E.; Rauleder, H.; Scheytt, C.; Mayer, H. A.; Hiller, W.; Fawzi, R.; Wegner, P. Neuartige Basische Liganden Für Die Homogenkatalytische Homologisierung von Methanol Zu Ethanol, II [1]. Synthese Und Komplexchemisches Verhalten Potentiell Zwei- Und Dreizähniger P–N- Und P–O-Haltiger Chelatliganden / Novel Basic Ligands for the Homogeneous Catalytic Homologation of Methanol to Ethanol, II [1]. Synthesis and Complex Chemical Behaviour of Potential Bi- and Tridentate P–N and P–O Containing Chelate Ligands. *Z. Für Naturforschung B* **1984**, *39* (5), 632–642. https://doi.org/10.1515/znb-1984-0518.

(24) Krajewski, S. M.; Love, R. J. Jr.; Kephart, J. A.; Boggiano, A. C.; La Pierre, H. S.; Kaminsky, W.; Velian, A. Exploring Charge Redistribution at the Cu/Co6Se8 Interface. *Inorg. Chem.* **2024**, *63* (43), 20388–20397. https://doi.org/10.1021/acs.inorgchem.4c02639.

(25) *Bruker APEX2 (Version 2.1-4), SAINT (Version 7.34A), SADABS (Version 2007/4), 2007 BrukerAXS Inc, Madison, Wisconsin, USA.*

(26) *Sheldrick, G.M. Acta Cryst. 2015 A71, 3-8.*

(27) *Altomare, A.; Burla, C.; Camalli, M.; Cascarano, G. L.; Giacovazzo, C.; Guagliardi, A.; Moliterni, A.G.G.; Polidori, G.; Spagna, R. J. Appl. Crystallogr., 1999, 32, 115-119.*

(28) *Altomare, A.; Cascarano, G. L.; Giacovazzo, C.; Guagliardi, A. J. Appl. Crystallogr., 1993, 26, 343-350.*

(29) *Sheldrick, G. M. SHELXL-97, Program for the Refinement of Crystal Structures, 1997, University of Göttingen, Germany.*

(30) *Sheldrick, G. M. Acta Cryst. 2015, C71, 3–8.*

(31) *Mackay, S.; Edwards, C.; Henderson, A.; Gilmore, C.; Stewart, N.; Shankland, K.; Donald, A. MaXus: A Computer Program for the Solution and Refinement of Crystal Structures from Diffraction Data, 1997, University of Glasgow, Scotland.*

(32) *Waasmaier, D.; Kirfel, A. Acta Cryst., 1995, 51, 416-430.*

VITA

Sebastian grew up in Arlington, Massachusetts, and in May 2020 he graduated from the University of Colorado, Boulder with an undergraduate degree in Chemistry and minor in Philosophy. During his time at CU Boulder working for Prof. Michael Marshak, he became enthralled with both inorganic synthesis and crystallography, eventually becoming the chemistry department's unofficial crystallographer. After graduating from CU, he began his graduate studies at the University of Washington in 2020. At UW, Sebastian joined the lab of Prof. Alexandra Velian and began working on the synthesis and characterization of inorganic nanoclusters. In his third year of graduate school, he also began working as the student crystallographer of the UW Chemistry department, working with Dr. Habil Werner Kaminsky to collaborate with various users across the university to obtain high-quality crystal structures. As a graduate student, Sebastian received the ARCS Seattle Chapter Fellowship and the Clean Energy Institute Graduate Fellowship. He had the opportunity during graduate school to attend and present at several conferences, including an ACS National Meeting, a Gordon Research Conference, the MIT/Bruker symposium, and two ORCAS conferences. In March 2025, Sebastian received a Doctor of Philosophy degree in Chemistry from UW. Outside of lab, Sebastian enjoys finding and hiking new trails, watching baseball, and practicing photography.